TOWARDS IMPROVED METHODS FOR DETERMINING POROUS MEDIA MULTIPHASE FLOW FUNCTIONS

A Thesis

by

SONG XUE

Submitted to the Office of Graduate Studies of
Texas A&M University
in partial fulfillment of the requirements for the degree of

MASTER OF SCIENCE

May 2004

Major Subject: Chemical Engineering

TOWARDS IMPROVED METHODS FOR DETERMINING POROUS MEDIA MULTIPHASE FLOW FUNCTIONS

A Thesis

by

SONG XUE

Submitted to Texas A&M University
in partial fulfillment of the requirements
for the degree of

MASTER OF SCIENCE

Approved as to style and content by:

A. Ted Watson (Co-Chair of Committee)	John C. Slattery (Co-Chair of Committee)
Randall L. Eubank (Member)	Kenneth R. Hall (Head of Department)

May 2004

Major Subject: Chemical Engineering

ABSTRACT

Towards Improved Methods for Determining Porous Media

Multiphase Flow Functions. (May 2004)

Song Xue, B.S., Zhejiang University ;

M.S., Zhejiang University

Co–Chairs of Advisory Committee: Dr. A. Ted Watson
Dr. John C. Slattery

The mathematical modeling and simulation of the flow of fluid through porous media are important in many areas. Relative permeability and capillary pressure functions are macroscopic properties that are defined within the mathematic model. Accurate determinations of these functions are of great importance.

An established inverse methodology provides the most accurate estimates of the unknown functions from the available data. When the inverse method is used to determine the flow functions, the media properties, absolute permeability and porosity are typically represented by single average values for the entire sample. Fortunately, an advanced core analysis tools utilizing nuclear magnetic resonance (NMR) spectroscopy and imaging (MRI) to determine complete distributions of porosity and permeability has been developed. The process for determining multiphase properties from experimental data is implemented with the computer program SENDRA. This program is built around a two-dimension, two-phase simulator. In this thesis, the computer code is extended to represent all three spatial coordinate directions so that the porosity and permeability distributions in three-dimensional space can be taken into account. Taking the sample's heterogeneity into account is expected to obtain

more accurate multiphase property. Three synthetic experiments are used to show the erroneous estimation of flow functions associated with the homogeneity assumption.

A proposal approach is used to predict the relative permeability of wetting phase using NMR relaxation data. Several sets of three-dimensional NMR experiments are performed. Three-dimensional saturation distribution and relaxation are determined. Relative permeability of wetting phase are calculated by applying an empirical relation. This approach provides a *in situ* measurement of relative permeability of wetting phase from NMR data.

To Mom, Dad and Jianzhong

ACKNOWLEDGMENTS

I would first like to express my gratitude to Dr. A. Ted Watson for leading and guiding me through my research. I would also like to thank the remaining members of my committee, Dr. John C. Slattery and Dr. Randy Eubank, for their time and suggestions. Special thanks go out to Dr. Rudi Michalak who provided guidance on all the required NMR experiments and thesis. I would also like to thank Dr. Jack Phan and Jinsoo Uh for their continual assistance, collaboration and support throughout this research. I would like to thank Jingjun Zhou for his help in preparation the paperwork required at Texas A&M University.

Many people have been around and supported me during my graduate studies. These are at Texas A&M University, Li Zhu, Zhifang Ren, Wenyan He, Yisan Li, Yu Chen, Fang Xu, Hao Xu and Ping Yan. At Colorado State University, these are Zhen Yu, Qing Zhao, Binbing Han, Ying Lu and Li Zhang.

I would like to thank my parents and my husband for their support to me throughout this journey.

TABLE OF CONTENTS

Page

LIST OF FIGURES

FIGURE Page

FIGURE Page

FIGURE Page

FIGURE Page

FIGURE Page

FIGURE Page

FIGURE Page

LIST OF TABLES

TABLE Page

CHAPTER I

INTRODUCTION

The mathematical modeling and simulation of the flow of fluid through porous media are important in many areas, including petroleum engineering, soil science and environmental engineering. Multiphase flow is typically modeled by a continuum representation in space and time based on local volume averaging (Slattery, 1981). Relative permeability and capillary pressure functions, commonly referred to as flow functions, are macroscopic properties that are defined within the mathematic model. Accurate determinations of these functions, which are functions of state variables (saturations), are of great importance.

It is a difficult task to determine the highly nonlinear relationships between multiphase properties and saturations. A number of approaches have been reported to determine the flow functions. The network modeling approach, which uses a network of pores, percolation theory and pore-scale displacement mechanisms to represent the flow in porous media, has been used extensively to compute relative permeabilities and capillary pressure (Mani and Mohanty, 1999; Maximenko and Kadet, 2000; Reeves and Celia, 1996). The advantage of the network modeling is that the flow functions can be directly calculated and the effects of fluid properties and underlying pore structure on the flow functions can be quickly assessed (Mani and Mohanty, 1999). However, the predictive properties of this approach, the accurate determination of the flow functions, are limited to idealized simple systems since an accurate characterization of complicated pore morphology is not available (Blunt, 2001).

Another approach to obtain multiphase properties is performing estimation from

---

This thesis follows the style and format of *AIChE Journal*.

measurements made during dynamic fluid displacement experiments on core samples. The estimation methods of the relative permeability and capillary pressure functions may be classified as steady and unsteady methods (Richmond and Watson, 1990). In the steady method and the two-fluid system, the two phases are injected at a certain volumetric ratio until both the pressure drop across the core and the composition of the effluent stabilize. The saturations of the two fluids in the core are then determined typically by weighing the core or by performing mass balance calculations for each phase. The relative permeabilities are calculated from the flow equations. Unfortunately, the steady method is time consuming and expensive (Akin and Demiral, 1998). Furthermore, this method is based on the assumption of uniform saturation by neglecting the capillary end effect which creates a higher saturation near the downstream of the flow than for the remainder of test sample (Dana and Skoczylas, 2002; Mitlin et al., 1998).

In the unsteady method, flow functions are estimated from the pressure drop data and production data. One type of method uses centrifugal acceleration and buoyancy as the driving force. This type of experiment provides a stable displacement (Nordtvedt et al., 1993), and the capillary pressure and relative permeabilities can be measured on three or six core samples simultaneously. However, the properly designed equipment and technique in this experiment is complex and expensive (Hirasaki et al., 1992). The other type of the method uses pressure as the driving force, where the injected fluid has a higher pressure at the inlet than at the outlet of the core sample. The Johnson-Bossler-Naumann (JBN) method (Johnson et al., 1959) is the most widely used technique for relative permeabilities estimation. The relative permeabilities are calculated explicitly from the experiment data according to a mathematical relationship. It suffers from the simplification of avoiding the capillary pressure effect and can not simultaneously estimate both relative permeability and

capillary pressure functions (Watson et al., 1998).

An inverse methodology, which can be used to estimate the multiphase flow functions simultaneously from a variety of experiment scenarios, has been developed, tested, and reported (Watson et al., 1988; Nordtvedt et al., 1993; Kulkarni et al., 1998; Watson et al., 1998). This method is not limited by the form of the mathematical model and provides the most accurate estimates of the unknown functions from the available data. A significant feature of this method is that the capillary pressure can be taken into account in the estimation process. A mathematical model required in this methodology should sufficiently represent the fluid-flow experiment and include the properties to be estimated. The flow functions are adjusted until the numerical solutions of the mathematical model for the process match the experimental data.

For the most common methods used when determining the flow functions, the media properties, absolute permeability and porosity, are represented by single average values for the entire sample (Watson et al., 1984; Kulkarni et al., 1998), *i.e.*, the porous media are assumed homogeneous. A recent study (Valestrand et al., 2002) shows numerically that such assumptions result in highly erroneous estimates of the flow functions since the natural porous media and core samples are likely to be heterogeneous. While the data collected from the experiment are influenced by the samples' heterogeneity, assuming homogeneity will result in serious estimation errors. It would be a better option to include the variation of absolute permeability and porosity when estimating the flow functions. This opinion has been addressed by several authors (Valestrand et al., 2002; Mejia et al., 1995). Valenstrand et al. (2002) tried to estimate the absolute permeability simultaneously, which is spatially varying, with relative permeabilities. The ill-posed nature of their models resulted in non-uniqueness problem which was particularly important when only production data were used. Moreover, the variation in porosity was neglected in the above cited

references. A more realistic case is where the absolute permeability and porosity are both spatially dependent.

The information regarding the exact detail of the rock heterogeneities, which are required by the mathematical model, can be basically unavailable. Fortunately, advanced core analysis tools utilizing nuclear magnetic resonance (NMR) spectroscopy and imaging (MRI) to determine complete distributions of porosity and permeability within heterogeneous core samples have been developed and tested (Borgia et al., 1996; Seto et al., 2001; Watson et al., 2001; Watson et al., 2002). Once the porosity and permeability distributions are determined, it is desirable to include all these information into the mathematical model.

However, a numerical simulator which utilizes the inverse methodology to determine relative permeability and capillary pressure curves is limited to two dimensions. This situation results in the inability of representation the distribution of the properties in the third direction. It is necessary to extend the numerical code in order to include the third spatial dimension. After extending the code from two dimensions to three dimensions, the modified code is in the need of validation. Once the three-dimensional simulator is available, all three spatial variations can be taken into account in the mathematical model. It is believed that taking the sample's heterogeneity into account will result in accurate multiphase property determination (Valestrand et al., 2002).

NMR is an increasing popular well-logging tool in petroleum industry because it can provide the *in situ* measurement of the petrophysical properties of the porous media. An empirical relation is provided to calculate wetting phase relative permeability from average NMR relaxation rates determined at different saturations (Chen et al., 1994). This simple relation could prove valuable for determination of relative permeability *in situ* from logging data. However, single average saturation and

relaxation values were applied in calculation by assuming uniform saturation distribution in the sample (Chen et al., 1994). It is more suitable to perform a series of three-dimensional NMR experiments and determine the relative permeability from three-dimensional saturation and relaxation rate data.

Objective of this thesis is to complete the simulator used for determination of flow functions by extending the code into three dimensions so that the entire sample heterogeneity can be considered, and utilizing the empirical relation for the determination of relative permeability from three-dimensional NMR observable properties.

Chapter II describes the methodology to estimate the multiphase properties. The process for determining multiphase properties from experimental data is implemented with a computer program, SENDRA (Petec Software & Services, 2000). This program is built around a two-dimensional, two-phase simulator. In this Chapter, the computer code is extended to represent all three spatial coordinate directions so that the entire porosity and permeability distributions are accounted for in estimation of multiphase flow properties. The validity of the extended SENDRA is verified with the original two-dimensional representation. The estimates of flow functions associated with the homogeneity assumption are investigated by three examples, utilizing data from three independent synthetic experiments.

In Chapter III, the proposal empirical relation between wetting phase relative permeability and relaxation rate (Chen et al., 1994) is presented. In order to determine the relative permeability, saturation and relaxation distributions are required. The methodology used to determine multi-dimensional saturation and relaxation distribution in porous media has been developed (Hollenshead, 2001). Quantitative analysis of NMR images is conducted to obtain the intrinsic magnetization and relaxation time at each position. The intrinsic magnetization, the magnetization at equilibrium before the relaxation takes place, is proportional to the local amount of

fluid and is used to determine the saturation distribution throughout the sample. The relative permeability of wetting phase is determined according to the empirical relation by using the three-dimensional saturation and relaxation data.

CHAPTER II

ESTIMATION OF POROUS MEDIA FLOW FUNCTIONS

Multiphase flow functions are required to simulate the flow of multiple fluid phases through porous media. These are normally determined from experimental data measured during displacement experiments on laboratory core samples. Conventionally, these estimates are based on the assumption that the porosity and permeability are uniform within the sample. Spatial variation in those properties, which are known to exist, will lead to associated errors in the estimates of the multiphase flow functions. The process for determining multiphase properties from a displacement experimental data is implemented in the computer program, SENDRA (Petec Software & Services, 2000). This program is limited to two-dimension. In order to account for all three spatial variations in the process of estimation, the computer code needs to be extended.

In this chapter, a regression-based estimation methodology that is used to determine flow functions is presented (Watson et al., 1988; Nordtvedt et al., 1993; Kulkarni et al., 1998; Watson et al., 1998). The two-dimensional numerical code is extended to three dimensions. The validation of the extended code is presented. Three synthetic experiments are used to show the erroneous estimates of flow functions associated with the homogeneity assumption.

A. Introduction

The relative permeabilities and capillary pressure are saturation dependent functions and of great importance for proper understanding of the multiphase flow in porous media. Over the past more than 10 years, an inverse methodology, in which a simulator is utilized for matching experimental data, has been developed, tested and

reported (Watson et al., 1988; Nordtvedt et al., 1993; Kulkarni et al., 1998; Watson et al., 1998). In this approach, the relative permeabilities and capillary pressure are estimated simultaneously. The method has proven to be successful.

B. Background

The estimation methodology has been developed to determine multiphase properties. There are several key elements in this methodology. A mathematical model is selected to represent the two-phase flow experiment. The mathematical model on which the estimation procedure is based should be sufficiently complete to include all the important physical effects that occurred in the experiment. Suitable functional representations have to be chosen for the multiphase flow functions. The determination of the coefficients within the functional representations will involve solving the inverse problem by matching the calculated data with the measured data from the experiment. The mathematical model will be described in Subsection 2. The suitable function representation and determination of the coefficients will be described in Subsection 3.

1. The Two-Phase Displacement Experiment

A dynamic displacement experiment is conducted, in which a single fluid is injected at a specific flow rate into a porous media initially saturated with the other fluid phase. The transient pressure drop and production are measured. The saturation distribution can be measured by involving NMR technique. The mathematical model is selected to represent the two-phase displacement experiment. The multiphase properties are determined by matching the calculated data with the measured data from the experiment.

2. The Mathematical Model

Two-phase immiscible flow through porous media is modeled by an extension of Darcy's law for single-phase flow through porous media. The following two equations are obtained by combining the Darcy equation with the continuity equation for each fluid phase (Aziz and Settari, 1979):

$$\nabla \cdot [\frac{\rho_{nw} K k_{r,nw}}{\mu_{nw}} (\nabla p_{nw} - \rho_{nw} g \nabla z)] + q_{nw} = \frac{\partial (\phi \rho_{nw} S_{nw})}{\partial t} \tag{2.1}$$

$$\nabla \cdot [\frac{\rho_{w} K k_{r,w}}{\mu_{w}} (\nabla p_{w} - \rho_{w} g \nabla z)] + q_{w} = \frac{\partial (\phi \rho_{w} S_{w})}{\partial t}, \tag{2.2}$$

where subscripts nw and w refer to the non-wetting and wetting phase respectively. In addition, the state variables, fluid-phase saturations and pressure, are related through the following two equations

$$p_c(S_w) = p_{nw} - p_w \tag{2.3}$$

$$S_{nw} + S_w = 1. \tag{2.4}$$

Together with boundary and initial conditions, Eqs. (2.1)-(2.4) provide a mathematical model of three-dimensional, two-phase fluid flow in porous media.

Several properties have to be specified in the above model. The densities and viscosities are fluid properties that can be measured independently. The porosity ϕ and absolute permeability K are effective media properties corresponding to local volume average. Methods used to determine porosity and/or absolute permeability are reported by involving MRI (Seto et al., 2001; Watson et al., 2001; Watson et al., 2002; Borgia et al., 1996). The relative permeabilities, $k_{r,nw}$, $k_{r,w}$, and capillary pressure, P_c, are multiphase properties. They are functions of the fluid saturation. The determination of these multiphase flow functions is the objective to be estimated through an inverse problem. q_{nw} and q_w are local source/sink terms which used to

account for the local fluid production/depletion (for example, fluid flows into/out the sample through a small hole.)

In order to solve the differential equations describing flow, it is necessary to specify appropriate boundary conditions. There are two kinds of boundary conditions realized in our experimental study: specified total fluid rate q_T injected through the inlet face Γ_1 and specified pressure maintained at the outlet face Γ_2.

In our experiment study, only one phase (for example, say non-wetting phase) is injected. Therefore, the boundary condition at the inlet end are

$$\int_{\Gamma} \frac{Kk_{r,nw}}{\mu_{nw}} (\nabla p_{nw} - \rho_{nw} g \nabla h)\, d\Gamma = q_{nw,T} \quad \text{at inlet } \Gamma_1, \tag{2.5}$$

$$\nabla p_w - \rho_w g \nabla h = 0 \quad \text{at inlet } \Gamma_1 \tag{2.6}$$

For the pressure specified boundary, if both fluids flow across the outlet (Kulkarni et al., 1998), we have

$$p_{nw} = p_{end} \quad \text{at outlet } \Gamma_2, \tag{2.7}$$

$$p_w = p_{end} \quad \text{at outlet } \Gamma_2. \tag{2.8}$$

If only one fluid phase flows across the outlet (for example, say non-wetting phase), we have

$$p_{nw} = p_{end} \quad \text{at outlet } \Gamma_2, \tag{2.9}$$

$$\nabla p_w - \rho_w g \nabla h = 0 \quad \text{at outlet } \Gamma_2. \tag{2.10}$$

The fluid will flow out of the sample when it's potential gradient is greater than zero,

$$\nabla p_f - \rho_f g \nabla h > 0 \quad \text{at outlet } \Gamma_2 \tag{2.11}$$

Both fluids will come out of the sample only when the potential gradients of both

fluids satisfy

$$\nabla p_{nw} - \rho_{nw} g \nabla h > 0 \quad \text{at outlet } \Gamma_2, \tag{2.12}$$

$$\nabla p_w - \rho_w g \nabla h = \nabla p_{nw} - \rho_w g \nabla h - \nabla p_c > 0 \quad \text{at outlet } \Gamma_2. \tag{2.13}$$

If there is no local fluid production/depletion, then

$$q_f = 0 \tag{2.14}$$

3. The Inverse Problem

The first step in the inverse problem is to select an adequate functional representation for the unknown flow functions. B-splines are a good choice for representing such nonparametric functions because, with sufficient number of knots, they can accurately represent any continuous smooth function (Schumaker, 1981). The following Eqs. (2.15)-(2.16) are the function representations using B-splines:

$$k_{r,f}(S_w) = \sum_{j=1}^{N_f} C_j^f B_j^m(S_w, \overrightarrow{y}^f), \tag{2.15}$$

$$p_c(S_w) = \sum_{j=1}^{N_c} C_j^c B_j^m(S_w, \overrightarrow{y}^c) \tag{2.16}$$

where the B-splines representations are specified by the order m, the spline coefficients C, and the extended partitions $\overrightarrow{y}$. The vector of unknown parameters becomes:

$$\mathbf{p} = [C_1^w, \ldots, C_{N_w}^w, C_1^{nw}, \ldots, C_{N_{nw}}^{nw}, C_1^c, \ldots, C_{N_c}^c]. \tag{2.17}$$

For a given representation (*i.e.*, order m and extended partition $\overrightarrow{y}$), the unknown parameters are chosen by minimizing an objective function in the form:

$$\min_{\mathbf{p}} J(\mathbf{p}) = [\overrightarrow{Y_m} - \overrightarrow{Y_s}(\mathbf{p})]^T \mathbf{W} [\overrightarrow{Y_m} - \overrightarrow{Y_s}(\mathbf{p})] \tag{2.18}$$

subject to the constraints:

$$\mathbf{Gp} \geq \mathbf{g}, \tag{2.19}$$

the idea being that the simulated data should reconcile those data actually measured. $\overrightarrow{Y_m}$ is the vector containing the measured experimental data, $\overrightarrow{Y_s}$ is the vector containing the corresponding values calculated by numerical simulation of the displacement process through mathematical model represented by Eqs. (2.1)-(2.4), **G** is the matrix specifying the linear inequality constraints **g** on the parameters, and **W** is the weighting matrix, a diagonal matrix with entries equal to the inverse of the estimated variances of the data measurement errors. The value of **p** that minimizes Eq. (2.18) is obtained by an implementation of Marquardt-Levenberg algorithm with linear inequality constraints. A numerical simulator, SENDRA, developed by PETEC Software & Services in FORTRAN, which utilizes the methodology, is capable of estimating relative permeability and capillary pressure curves by matching a set of laboratory data with those generated by the SENDRA (Petec Software & Services, 2000).

In order to fully represent the effects of heterogeneities (porosity and permeability), it is necessary that all three spatial dimensions should be taken into consideration in the simulation of the experiment. Originally, SENDRA is a two-dimensional, two-phase simulator (Petec Software & Services, 2000). It is necessary to extend the SENDRA code to include the third spatial dimension.

C. Extension to Three Dimensions

An unconditionally stable fully implicit finite-difference method is used in this work to calculate pressures and saturations. The original version of SENDRA represents only two spatial directions. A block-centered grid system is considered. The system is

expanded into three-dimensions. The system domain has $(N_x \times N_y \times N_z)$ grid blocks, instead of $(N_x \times N_y \times 1)$ grid blocks for two-dimensional SENDRA, where each block is represented by (i, j, k), $i = 1, 2, ..., N_x, j = 1, 2, ...N_y$, and $k = 1, 2, ..., N_z$. The equations for oil and water are solved simultaneously.

Using the finite difference scheme with the block centered grid system, the discretized form for Eqs. 2.1- 2.2 can be written into the following form. Here, the z-component of derivatives is added for the three-dimensional case:

$$\Delta_x T_{nw,x}(\Delta_x \Phi_{nw,x}) + \Delta_y T_{nw,y}(\Delta_y \Phi_{nw,y}) + \Delta_z T_{nw,z}(\Delta_z \Phi_{nw,z}) = V_b \Delta_t(\phi \rho_{nw} S_{nw}) - q_{nw} \tag{2.20}$$

$$\Delta_x T_{wx}(\Delta_x \Phi_{wx}) + \Delta_y T_{wy}(\Delta_y \Phi_{wy}) + \Delta_z T_{wz}(\Delta_z \Phi_{wz}) = V_b \Delta_t(\phi \rho_w S_w) - q_w \tag{2.21}$$

where $\Phi_{nw} = p_{nw} + \rho_{nw} gh$, $\Phi_w = p_w + \rho_w gh$, Δ_x, Δ_y, Δ_z are spatial difference operators, and Δ_t is a time difference operator. The transmissibilities T_{nw} and T_w are defined as $T_{nw} = \frac{K k_{r,nw} A}{\mu_{nw} \Delta l}$, $T_w = \frac{K k_{r,w} A}{\mu_w \Delta l}$ respectively. A is the cross section area of the block, and Δl is the length of the block along the l direction. q_{nw} and q_w are the local mass flow rates of source/sink. After replacing the derivatives by difference quotients, we have:

$$\frac{\partial}{\partial x}\left(T_f \frac{\partial \Phi_f}{\partial x}\right)\bigg|_{i,j,k} = \frac{T_{f,i+\frac{1}{2},j,k}\left(\Phi_{f,i+1,j,k} - \Phi_{f,i,j,k}\right) - T_{f,i-\frac{1}{2},j,k}\left(\Phi_{f,i,j,k} - \Phi_{f,i-1,j,k}\right)}{(\Delta x)^2} \tag{2.22}$$

$$\frac{\partial}{\partial y}\left(T_f \frac{\partial \Phi_f}{\partial y}\right)\bigg|_{i,j,k} = \frac{T_{f,i,j+\frac{1}{2},k}\left(\Phi_{f,i,j+1,k} - \Phi_{f,i,j,k}\right) - T_{f,i,j-\frac{1}{2},k}\left(\Phi_{f,i,j,k} - \Phi_{f,i,j-1,k}\right)}{(\Delta y)^2} \tag{2.23}$$

$$\frac{\partial}{\partial z}\left(T_f \frac{\partial \Phi}{\partial z}\right)\bigg|_{i,j,k} = \frac{T_{f,i,j,k+\frac{1}{2}}\left(\Phi_{f,i,j,k+1} - \Phi_{f,i,j,k}\right) - T_{f,i,j,k-\frac{1}{2}}\left(\Phi_{f,i,j,k} - \Phi_{f,i,j,k-1}\right)}{(\Delta z)^2} \tag{2.24}$$

Here, the transmissibility with $\frac{1}{2}$ index is calculated by harmonic means of the values

of the two adjacent blocks, for example,

$$T_{f,i+\frac{1}{2},j,k} = \left(\frac{KA\rho_f}{\triangle x \mu_f}\right)_{i+\frac{1}{2},j,k} (k_{r,f})_{i+\frac{1}{2},j,k}, \tag{2.25}$$

where

$$\left(\frac{KA\rho_f}{\triangle x \mu_f}\right)_{i+\frac{1}{2},j,k} = \frac{2}{\left(\frac{\triangle x \mu_f}{KA\rho_f}\right)_{i,j,k} + \left(\frac{\triangle x \mu_f}{KA\rho_f}\right)_{i+1,j,k}}$$

and the relative permeability $(k_{r,f})_{i+\frac{1}{2},j,k}$ is specified with the upstream value,

$$(k_{r,f})_{i+\frac{1}{2},j,k} = (k_{r,f})_{i,j,k} \cdot \Omega + (k_{r,f})_{i+1,j,k} \cdot (1-\Omega),$$

$$\Omega = \begin{cases} 0 & \Phi_{f,i+1,j,k} - \Phi_{f,i,j,k} > 0 \\ 1 & \Phi_{f,i+1,j,k} - \Phi_{f,i,j,k} < 0 \end{cases}.$$

We define the functions:

$$f(\mathbf{X}) = \left\{ \Delta_x \left(T_f \Delta_x \Phi_f\right) + \Delta_y \left(T_f \Delta_y \Phi_f\right) + \Delta_z \left(T_f \Delta_z \Phi_f\right) \right\}_{i,j,k}^{n+1} \tag{2.26}$$

$$h(\mathbf{X}) = \frac{V_b}{\Delta t}\left\{ \left(\phi \rho_f S_f\right)_{i,j,k}^{n+1} - \left(\phi \rho_f S_f\right)_{i,j,k}^{n} \right\} - \left(q_f\right)_{(i,j,k)}^{n+1} \tag{2.27}$$

where $\mathbf{X} \equiv \begin{bmatrix} p_o \\ S_w \end{bmatrix}$ is a solution need to be solved, and p_o and S_w are oil pressure and water saturation, respectively. n means these values are at time $t = t_n$. In basic equations (2.1 and 2.2), the state quantities are the pressures and saturations of each fluid phase, as a functions of position and time. For two-phase system, the saturation and pressure of one phase can be calculated through Eq. 2.3-2.4 with known values of the other phase. Therefore, $\mathbf{X}$ is the solution we need to solve.

The equations 2.20-2.21 then can be rewritten into the form:

$$\begin{aligned}\{R(\mathbf{X})\}^n &= \{f(\mathbf{X})\} - \{h(\mathbf{X})\} \\ &= \left\{ \Delta_x \left(T_f \Delta_x \Phi_f\right) + \Delta_y \left(T_f \Delta_y \Phi_f\right) + \Delta_z \left(T_f \Delta_z \Phi_f\right) \right\}_{i,j,k}^{n+1} \\ &- \frac{V_b}{\Delta t} \left\{ \left(\phi \rho_f S_f\right)_{i,j,k}^{n+1} - \left(\phi \rho_f S_f\right)_{i,j,k}^{n} \right\} + \left(q_f\right)_{(i,j,k)}^{n+1} \\ &= 0,\end{aligned} \tag{2.28}$$

By applying Taylor expansion, we have

$$R(\mathbf{X})^{n+1} = 0 \tag{2.29}$$

$$\left\{ \frac{\partial R(\mathbf{X})}{\partial \mathbf{X}} \right\}^n \delta \mathbf{X} = -R(\mathbf{X})^n, \tag{2.30}$$

where

$$\partial \mathbf{X} = \begin{bmatrix} p_o^{n+1} - p_o^n \\ S_w^{n+1} - S_w^n \end{bmatrix} \tag{2.31}$$

is the change in the unknown between two time iteration levels.

The partial differential Eq. 2.30 contains non-linear terms. These are treated by use of Newton-Raphson iteration method:

$$\left(T_f \Phi_f\right)^{n+1} = \left(T_f \Phi_f\right)^n + \frac{\partial}{\partial p_o} \left(T_f \Phi_f\right)^n \delta p_o + \frac{\partial}{\partial S_w} \left(T_f \Phi_f\right)^n \delta S_w \tag{2.32}$$

$$\left(\phi \rho_f S_f\right)_{i,j,k}^{n+1} - \left(\phi \rho_f S_f\right)_{i,j,k}^{n} = \frac{\partial}{\partial p_o} \left(\phi \rho_f S_f\right)_{i,j,k}^{n} \delta p_o + \frac{\partial}{\partial S_w} \left(\phi \rho_f S_f\right)_{i,j,k}^{n} \delta S_w \tag{2.33}$$

The pressure dependent terms, *i.e.*, viscosities are weak non-linear terms and expansion is neglected (Petec Software & Services, 2000). Thus

$$\frac{\partial}{\partial p_o} \left(T_o \Phi_o\right) = T_o, \tag{2.34}$$

$$\frac{\partial}{\partial S_w} \left(T_o \Phi_o\right) = \left(\frac{K A \rho_o}{\triangle x \mu_o}\right) \frac{\partial k_{r,o}}{\partial S_w} \Phi_o. \tag{2.35}$$

The expansion of the water equation follows the same manner:

$$\frac{\partial}{\partial p_o}(T_w\Phi_w) = T_w, \tag{2.36}$$

$$\frac{\partial}{\partial S_w}(T_w\Phi_w) = (\frac{KA\rho_w}{\triangle x\mu_w})\frac{\partial k_{r,w}}{\partial S_w}\Phi_w - T_w\frac{\partial p_c}{\partial S_w}. \tag{2.37}$$

And the derivatives in Eq. 2.33 are calculated:

$$\frac{\partial}{\partial p_o}\left(\phi\rho_o S_o\right) = (1-S_w)\left(\phi\frac{\partial\rho_o}{\partial p_o} + \rho_o\frac{\partial\phi}{\partial p_o}\right) \tag{2.38}$$

$$\frac{\partial}{\partial S_w}\left(\phi\rho_o S_o\right) = -\phi\rho_o \tag{2.39}$$

$$\frac{\partial}{\partial p_o}\left(\phi\rho_w S_w\right) = S_w\left(\phi\frac{\partial\rho_w}{\partial p_o} + \rho_w\frac{\partial\phi}{\partial p_o}\right) \tag{2.40}$$

$$\frac{\partial}{\partial S_w}\left(\phi\rho_w S_w\right) = \phi\rho_w \tag{2.41}$$

1. Expansion for the Inner Blocks

For the inner block (i,j,k) in Figure 1, if there is no local fluid depletion/production, the sink/source term $(q_f)_{(i,j,k)}$ equals to zero. The general form for the right hand side of Eq. 2.30 for the inner block (i,j,k) is expressed as

$$\begin{aligned} -\left\{R(\mathbf{X})\right\}_{i,j,k} = &-\Big\{\ \Delta_x\left(T_f\Delta_x\Phi_f\right) + \Delta_y\left(T_f\Delta_y\Phi_f\right) + \Delta_z\left(T_f\Delta_z\Phi_f\right)\ \Big\}_{i,j,k}^{n+1} \\ &+ \frac{V_b}{\Delta t}\Big\{\ \left(\phi\rho_f S_f\right)_{i,j,k}^{n+1} - \left(\phi\rho_f S_f\right)_{i,j,k}^{n}\ \Big\} \end{aligned} \tag{2.42}$$

The general form of the oil phase for the left hand side expansion of the Eq. 2.30

for the block (i,j,k) is expressed as

$$\begin{aligned}
\left\{\frac{\partial R(\mathbf{X})}{\partial \mathbf{X}}\right\}^n \delta\mathbf{X} = \frac{\partial}{\partial \mathbf{X}}\Big\{\ \Delta_x\left(T_o\Delta_x\Phi_o\right) + \Delta_y\left(T_o\Delta_y\Phi_o\right) + \Delta_z\left(T_o\Delta_z\Phi_o\right)\ \Big\}_{i,j,k}^{n+1}\delta\mathbf{X} \\
- \left(\frac{V_b}{\Delta t}\right)\frac{\partial}{\partial \mathbf{X}}\Big\{\ \left(\phi\rho_o S_o\right)_{i,j,k}^{n+1} - \left(\phi\rho_o S_o\right)_{i,j,k}^{n}\ \Big\}\delta\mathbf{X} \\
= \frac{\partial}{\partial \mathbf{X}}\left\{\frac{T_{o,i+\frac{1}{2},j,k}\left(\Phi_{o,i+1,j,k} - \Phi_{o,i,j,k}\right) - T_{o,i-\frac{1}{2},j,k}\left(\Phi_{o,i,j,k} - \Phi_{o,i-1,j,k}\right)}{\left(\Delta x\right)^2}\right\}^{n+1}\delta\mathbf{X} \\
+ \frac{\partial}{\partial \mathbf{X}}\left\{\frac{T_{o,i,j+\frac{1}{2},k}\left(\Phi_{o,i,j+1,k} - \Phi_{o,i,j,k}\right) - T_{o,i,j-\frac{1}{2},k}\left(\Phi_{o,i,j,k} - \Phi_{o,i,j-1,k}\right)}{\left(\Delta y\right)^2}\right\}^{n+1}\delta\mathbf{X} \\
+ \frac{\partial}{\partial \mathbf{X}}\left\{\frac{T_{o,i,j,k+\frac{1}{2}}\left(\Phi_{o,i,j,k+1} - \Phi_{o,i,j,k}\right) - T_{o,i,j,k-\frac{1}{2}}\left(\Phi_{o,i,j,k} - \Phi_{o,i,j,k-1}\right)}{\left(\Delta z\right)^2}\right\}^{n+1}\delta\mathbf{X} \\
- \left(\frac{V_b}{\Delta t}\right)\frac{\partial}{\partial \mathbf{X}}\Big\{\ \left(\phi\rho_o S_o\right)_{i,j,k}^{n+1} - \left(\phi\rho_o S_o\right)_{i,j,k}^{n}\ \Big\}\delta\mathbf{X}, \qquad (2.43)
\end{aligned}$$

$$
\begin{aligned}
&\left\{\frac{\partial R(\mathbf{X})}{\partial \mathbf{X}}\right\}^{n}\delta\mathbf{X} = \\
&\qquad\left\{T_{o,i-\frac{1}{2},j,k}\delta p_{o,i-1,j,k} - (T_{o,i-\frac{1}{2},j,k}+T_{o,i+\frac{1}{2},j,k})\delta p_{o,i,j,k} + T_{o,i+\frac{1}{2},j,k}\delta p_{o,i+1,j,k}\right\}^{n+1}\frac{1}{(\Delta x)^2} \\
&+\left\{T_{o,i,j-\frac{1}{2},k}\delta p_{o,i,j-1,k} - (T_{o,i,j-\frac{1}{2},k}+T_{o,i,j+\frac{1}{2},k})\delta p_{o,i,j,k} + T_{o,i,j+\frac{1}{2},k}\delta p_{o,i,j+1,k}\right\}^{n+1}\frac{1}{(\Delta y)^2} \\
&+\left\{T_{o,i,j,k-\frac{1}{2}}\delta p_{o,i,j,k-1} - (T_{o,i,j,k}+T_{o,i,j+\frac{1}{2},k-\frac{1}{2}})\delta p_{o,i,j,k} + T_{o,i,j,k+\frac{1}{2}}\delta p_{o,i,j,k+1}\right\}^{n+1}\frac{1}{(\Delta z)^2} \\
&+\Big\{\left(\frac{KA\rho_o}{\triangle x\mu_o}\right)_{i-\frac{1}{2},j,k}\left(\frac{\partial k_{r,o}}{\partial S_w}\right)_{i-1,j,k}(\Phi_{o,i-1,j,k}-\Phi_{o,i,j,k})\delta S_{w,i-1,j,k} \\
&+(\frac{KA\rho_o}{\triangle x\mu_o})_{i-\frac{1}{2},j,k}\left(\frac{\partial k_{r,o}}{\partial S_w}\right)_{i,j,k}(\Phi_{o,i-1,j,k}-\Phi_{o,i,j,k})\delta S_{w,i,j,k} \\
&+\left(\frac{KA\rho_o}{\triangle x\mu_o}\right)_{i+\frac{1}{2},j,k}\left(\frac{\partial k_{r,o}}{\partial S_w}\right)_{i,j,k}(\Phi_{o,i+1,j,k}-\Phi_{o,i,j,k})\delta S_{w,i,j,k} \\
&+\left(\frac{KA\rho_o}{\triangle x\mu_o}\right)_{i+\frac{1}{2},j,k}\left(\frac{\partial k_{r,o}}{\partial S_w}\right)_{i+1,j,k}(\Phi_{o,i+1,j,k}-\Phi_{o,i,j,k})\delta S_{w,i+1,j,k}\Big\}^{n+1}\frac{1}{(\Delta x)^2} \\
&+\Big\{\left(\frac{KA\rho_o}{\triangle x\mu_o}\right)_{i,j-\frac{1}{2},k}\left(\frac{\partial k_{r,o}}{\partial S_w}\right)_{i,j-1,k}(\Phi_{o,i,j-1,k}-\Phi_{o,i,j,k})\delta S_{w,i,j-1,k} \\
&+\left(\frac{KA\rho_o}{\triangle x\mu_o}\right)_{i,j-\frac{1}{2},k}\left(\frac{\partial k_{r,o}}{\partial S_w}\right)_{i,j,k}(\Phi_{o,i,j-1,k}-\Phi_{o,i,j,k})\delta S_{w,i,j,k} \\
&+\left(\frac{KA\rho_o}{\triangle x\mu_o}\right)_{i,j+\frac{1}{2},k}\left(\frac{\partial k_{r,o}}{\partial S_w}\right)_{i,j,k}(\Phi_{o,i,j+1,k}-\Phi_{o,i,j,k})\delta S_{w,i,j,k} \\
&+\left(\frac{KA\rho_o}{\triangle x\mu_o}\right)_{i,j+\frac{1}{2},k}\left(\frac{\partial k_{r,o}}{\partial S_w}\right)_{i,j+1,k}(\Phi_{o,i,j+1,k}-\Phi_{o,i,j,k})\delta S_{w,i,j+1,k}\Big\}^{n+1}\frac{1}{(\Delta y)^2} \\
&+\Big\{\left(\frac{KA\rho_o}{\triangle x\mu_o}\right)_{i,j,k-\frac{1}{2}}\left(\frac{\partial k_{r,o}}{\partial S_w}\right)_{i,j,k-1}(\Phi_{o,i,j,k-1}-\Phi_{o,i,j,k})\delta S_{w,i,j,k-1} \\
&+\left(\frac{KA\rho_o}{\triangle x\mu_o}\right)_{i,j,k-\frac{1}{2}}\left(\frac{\partial k_{r,o}}{\partial S_w}\right)_{i,j,k}(\Phi_{o,i,j,k-1}-\Phi_{o,i,j,k})\delta S_{w,i,j,k} \\
&+\left(\frac{KA\rho_o}{\triangle x\mu_o}\right)_{i,j,k+\frac{1}{2}}\left(\frac{\partial k_{r,o}}{\partial S_w}\right)_{i,j,k}(\Phi_{o,i,j,k+1}-\Phi_{o,i,j,k})\delta S_{w,i,j,k} \\
&+\left(\frac{KA\rho_o}{\triangle x\mu_o}\right)_{i,j,k+\frac{1}{2}}\left(\frac{\partial k_{r,o}}{\partial S_w}\right)_{i,j,k+1}(\Phi_{o,i,j,k+1}-\Phi_{o,i,j,k})\delta S_{w,i,j,k+1}\Big\}^{n+1}\frac{1}{(\Delta z)^2} \\
&-\left\{\frac{V_b}{\Delta t}(1-S_w)\left(\phi\frac{\partial\rho_o}{\partial p_o}+\rho_o\frac{\partial\phi}{\partial p_o}\right)\right\}^{n+1}\delta p_{o,i,j,k} - \left\{\frac{V_b}{\Delta t}\left(-\phi\rho_o\right)\right\}^{n+1}\delta S_{w,i,j,k}.
\end{aligned}
\tag{2.44}
$$

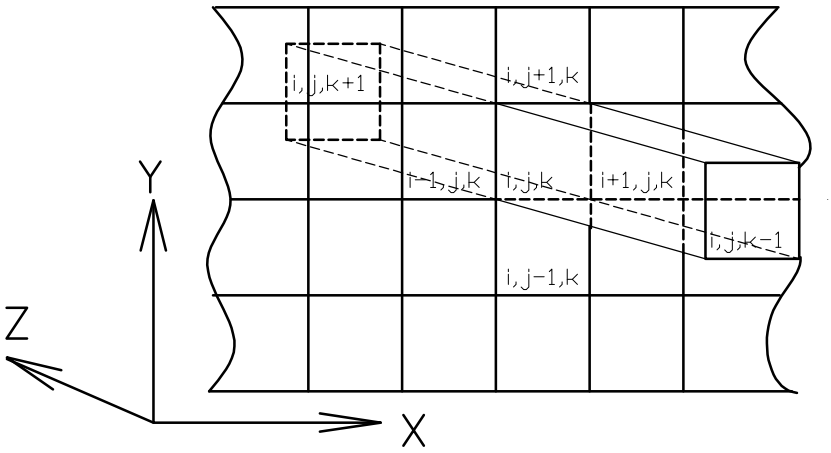

Fig. 1. The Grid Block System of the Sample

The general form of the water phase for the left hand side expansion of the

Eq. 2.30 for the block (i,j,k) is express as

$$\begin{aligned}
\left\{\frac{\partial R(\mathbf{X})}{\partial \mathbf{X}}\right\}^n \delta\mathbf{X} = & \frac{\partial}{\partial \mathbf{X}}\Big\{ \Delta_x\left(T_w \Delta_x \Phi_w\right) + \Delta_y\left(T_w \Delta_y \Phi_w\right) + \Delta_z\left(T_w \Delta_z \Phi_w\right) \Big\}_{i,j,k}^{n+1} \delta\mathbf{X} \\
& - \left(\frac{V_b}{\Delta t}\right) \frac{\partial}{\partial \mathbf{X}}\Big\{ \left(\phi \rho_w S_w\right)_{i,j,k}^{n+1} - \left(\phi \rho_w S_w\right)_{i,j,k}^{n} \Big\} \delta\mathbf{X} \\
= & \frac{\partial}{\partial \mathbf{X}} \left\{ \frac{T_{w,i+\frac{1}{2},j,k}\left(\Phi_{w,i+1,j,k} - \Phi_{w,i,j,k}\right) - T_{w,i-\frac{1}{2},j,k}\left(\Phi_{w,i,j,k} - \Phi_{w,i-1,j,k}\right)}{\left(\Delta x\right)^2} \right\}^{n+1} \delta\mathbf{X} \\
+ & \frac{\partial}{\partial \mathbf{X}} \left\{ \frac{T_{w,i,j+\frac{1}{2},k}\left(\Phi_{w,i,j+1,k} - \Phi_{w,i,j,k}\right) - T_{w,i,j-\frac{1}{2},k}\left(\Phi_{w,i,j,k} - \Phi_{w,i,j-1,k}\right)}{\left(\Delta y\right)^2} \right\}^{n+1} \delta\mathbf{X} \\
+ & \frac{\partial}{\partial \mathbf{X}} \left\{ \frac{T_{w,i,j,k+\frac{1}{2}}\left(\Phi_{w,i,j,k+1} - \Phi_{w,i,j,k}\right) - T_{w,i,j,k-\frac{1}{2}}\left(\Phi_{w,i,j,k} - \Phi_{w,i,j,k-1}\right)}{\left(\Delta z\right)^2} \right\}^{n+1} \delta\mathbf{X} \\
- & \left(\frac{V_b}{\Delta t}\right) \frac{\partial}{\partial \mathbf{X}}\Big\{ \left(\phi \rho_w S_w\right)_{i,j,k}^{n+1} - \left(\phi \rho_w S_w\right)_{i,j,k}^{n} \Big\} \delta\mathbf{X}, \qquad (2.45)
\end{aligned}$$

$$
\begin{aligned}
&\left\{\frac{\partial R(\mathbf{X})}{\partial \mathbf{X}}\right\}^{n}\delta\mathbf{X} = \\
&\quad\left\{T_{w,i-\frac{1}{2},j,k}\delta p_{o,i-1,j,k} - (T_{w,i-\frac{1}{2},j,k}+T_{w,i+\frac{1}{2},j,k})\delta p_{o,i,j,k} + T_{w,i+\frac{1}{2},j,k}\delta p_{o,i+1,j,k}\right\}^{n+1}\frac{1}{(\Delta x)^2} \\
&+\left\{T_{w,i,j-\frac{1}{2},k}\delta p_{o,i,j-1,k} - (T_{w,i,j-\frac{1}{2},k}+T_{w,i,j+\frac{1}{2},k})\delta p_{o,i,j,k} + T_{w,i,j+\frac{1}{2},k}\delta p_{o,i,j+1,k}\right\}^{n+1}\frac{1}{(\Delta y)^2} \\
&+\left\{T_{w,i,j,k-\frac{1}{2}}\delta p_{o,i,j,k-1} - (T_{w,i,j,k}+T_{w,i,j+\frac{1}{2},k-\frac{1}{2}})\delta p_{o,i,j,k} + T_{w,i,j,k+\frac{1}{2}}\delta p_{o,i,j,k+1}\right\}^{n+1}\frac{1}{(\Delta z)^2} \\
&+\left\{\frac{1}{(\Delta x)^2}\left\{\left(\frac{KA\rho_w}{\triangle x\mu_w}\right)_{i-\frac{1}{2},j,k}\left(\frac{\partial k_{r,o}}{\partial S_w}\right)_{i,j,k}(\Phi_{w,i-1,j,k}-\Phi_{w,i,j,k}) - \left(T_w\frac{\partial p_c}{\partial S_w}\right)_{i,j,k}\right\}\delta S_{w,i,j,k}\right. \\
&+\left\{\left(\frac{KA\rho_w}{\triangle x\mu_w}\right)_{i-\frac{1}{2},j,k}\left(\frac{\partial k_{r,o}}{\partial S_w}\right)_{i-1,j,k}(\Phi_{w,i-1,j,k}-\Phi_{w,i,j,k}) - \left(T_w\frac{\partial p_c}{\partial S_w}\right)_{i-1,j,k}\right\}\delta S_{w,i-1,j,k} \\
&+\left\{\left(\frac{KA\rho_w}{\triangle x\mu_w}\right)_{i+\frac{1}{2},j,k}\left(\frac{\partial k_{r,o}}{\partial S_w}\right)_{i,j,k}(\Phi_{w,i+1,j,k}-\Phi_{w,i,j,k}) - \left(T_w\frac{\partial p_c}{\partial S_w}\right)_{i,j,k}\right\}\delta S_{w,i,j,k} \\
&+\left.\left\{\left(\frac{KA\rho_w}{\triangle x\mu_w}\right)_{i+\frac{1}{2},j,k}\left(\frac{\partial k_{r,o}}{\partial S_w}\right)_{i+1,j,k}(\Phi_{w,i+1,j,k}-\Phi_{w,i,j,k}) - \left(T_w\frac{\partial p_c}{\partial S_w}\right)_{i+1,j,k}\right\}\delta S_{w,i+1,j,k}\right\}^{n+1} \\
&+\left\{\frac{1}{(\Delta y)^2}\left\{\left(\frac{KA\rho_w}{\triangle x\mu_w}\right)_{i,j-\frac{1}{2},k}\left(\frac{\partial k_{r,o}}{\partial S_w}\right)_{i,j,k}(\Phi_{w,i,j-1,k}-\Phi_{w,i,j,k}) - \left(T_w\frac{\partial p_c}{\partial S_w}\right)_{i,j,k}\right\}\delta S_{w,i,j,k}\right. \\
&+\left\{\left(\frac{KA\rho_w}{\triangle x\mu_w}\right)_{i,j-\frac{1}{2},k}\left(\frac{\partial k_{r,o}}{\partial S_w}\right)_{i,j-1,k}(\Phi_{w,i,j-1,k}-\Phi_{w,i,j,k}) - \left(T_w\frac{\partial p_c}{\partial S_w}\right)_{i,j-1,k}\right\}\delta S_{w,i,j-1,k} \\
&+\left\{\left(\frac{KA\rho_w}{\triangle x\mu_w}\right)_{i,j+\frac{1}{2},k}\left(\frac{\partial k_{r,o}}{\partial S_w}\right)_{i,j,k}(\Phi_{w,i,j+1,k}-\Phi_{w,i,j,k}) - \left(T_w\frac{\partial p_c}{\partial S_w}\right)_{i,j,k}\right\}\delta S_{w,i,j,k} \\
&+\left.\left\{\left(\frac{KA\rho_w}{\triangle x\mu_w}\right)_{i,j+\frac{1}{2},k}\left(\frac{\partial k_{r,o}}{\partial S_w}\right)_{i,j+1,k}(\Phi_{w,i,j+1,k}-\Phi_{w,i,j,k}) - \left(T_w\frac{\partial p_c}{\partial S_w}\right)_{i,j+1,k}\right\}\delta S_{w,i,j+1,k}\right\}^{n+1} \\
&+\left\{\frac{1}{(\Delta z)^2}\left\{\left(\frac{KA\rho_w}{\triangle x\mu_w}\right)_{i,j,k-\frac{1}{2}}\left(\frac{\partial k_{r,o}}{\partial S_w}\right)_{i,j,k}(\Phi_{w,i,j,k-1}-\Phi_{w,i,j,k}) - \left(T_w\frac{\partial p_c}{\partial S_w}\right)_{i,j,k}\right\}\delta S_{w,i,j,k}\right. \\
&+\left\{\left(\frac{KA\rho_w}{\triangle x\mu_w}\right)_{i,j,k-\frac{1}{2}}\left(\frac{\partial k_{r,o}}{\partial S_w}\right)_{i,j,k-1}(\Phi_{w,i,j,k-1}-\Phi_{w,i,j,k}) - \left(T_w\frac{\partial p_c}{\partial S_w}\right)_{i,j,k-1}\right\}\delta S_{w,i,j,k-1} \\
&+\left\{\left(\frac{KA\rho_w}{\triangle x\mu_w}\right)_{i,j,k+\frac{1}{2}}\left(\frac{\partial k_{r,o}}{\partial S_w}\right)_{i,j,k}(\Phi_{w,i,j,k+1}-\Phi_{w,i,j,k}) - \left(T_w\frac{\partial p_c}{\partial S_w}\right)_{i,j,k}\right\}\delta S_{w,i,j,k} \\
&+\left.\left\{\left(\frac{KA\rho_w}{\triangle x\mu_w}\right)_{i,j,k+\frac{1}{2}}\left(\frac{\partial k_{r,o}}{\partial S_w}\right)_{i,j,k+1}(\Phi_{w,i,j,k+1}-\Phi_{w,i,j,k}) - \left(T_w\frac{\partial p_c}{\partial S_w}\right)_{i,j,k+1}\right\}\delta S_{w,i,j,k+1}\right\}^{n+1} \\
&-\left\{\frac{V_b}{\Delta t}S_w\left(\phi\frac{\partial\rho_w}{\partial p_w}+\rho_w\frac{\partial\phi}{\partial p_w}\right)\right\}^{n+1}\delta p_{o,i,j,k} - \left\{\frac{V_b}{\Delta t}(\phi\rho_w)\right\}^{n+1}\delta S_{w,i,j,k}. \qquad (2.46)
\end{aligned}
$$

For simplification, we define the functions:

$$\mathbf{A_1} = \left\{T_{o,i-\frac{1}{2},j,k}\right\}^{n+1}, \qquad \mathbf{K_1} = \left\{T_{o,i,j+\frac{1}{2},k}\right\}^{n+1},$$

$$\mathbf{B_1} = \left\{T_{o,i+\frac{1}{2},j,k}\right\}^{n+1}, \qquad \mathbf{M_1} = \left\{T_{o,i,j,k-\frac{1}{2}}\right\}^{n+1},$$

$$\mathbf{I_1} = \left\{T_{o,i,j-\frac{1}{2},k}\right\}^{n+1}, \qquad \mathbf{O_1} = \left\{T_{o,i,j,k+\frac{1}{2}}\right\}^{n+1},$$

$$\mathbf{C_1} = \frac{1}{(\Delta x)^2}\left\{ \left(\frac{KA\rho_o}{\triangle x \mu_o}\right)_{i-\frac{1}{2},j,k} \left(\frac{\partial k_{r,o}}{\partial S_w}\right)_{i-1,j,k} (\Phi_{o,i-1,j,k} - \Phi_{o,i,j,k}) \right\}^{n+1},$$

$$\mathbf{C_2} = \frac{1}{(\Delta x)^2}\left\{ \left(\frac{KA\rho_o}{\triangle x \mu_o}\right)_{i+\frac{1}{2},j,k} \left(\frac{\partial k_{r,o}}{\partial S_w}\right)_{i,j,k} (\Phi_{o,i-1,j,k} - \Phi_{o,i,j,k}) \right\}^{n+1},$$

$$\mathbf{C_3} = \frac{1}{(\Delta x)^2}\left\{ \left(\frac{KA\rho_o}{\triangle x \mu_o}\right)_{i+\frac{1}{2},j,k} \left(\frac{\partial k_{r,o}}{\partial S_w}\right)_{i,j,k} (\Phi_{o,i+1,j,k} - \Phi_{o,i,j,k}) \right\}^{n+1},$$

$$\mathbf{C_4} = \frac{1}{(\Delta x)^2}\left\{ \left(\frac{KA\rho_o}{\triangle x \mu_o}\right)_{i+\frac{1}{2},j,k} \left(\frac{\partial k_{r,o}}{\partial S_w}\right)_{i+1,j,k} (\Phi_{o,i+1,j,k} - \Phi_{o,i,j,k}) \right\}^{n+1},$$

$$\mathbf{J_1} = \frac{1}{(\Delta y)^2}\left\{ \left(\frac{KA\rho_o}{\triangle x \mu_o}\right)_{i,j-\frac{1}{2},k} \left(\frac{\partial k_{r,o}}{\partial S_w}\right)_{i,j-1,k} (\Phi_{o,i,j-1,k} - \Phi_{o,i,j,k}) \right\}^{n+1},$$

$$\mathbf{J_2} = \frac{1}{(\Delta y)^2}\left\{ \left(\frac{KA\rho_o}{\triangle x \mu_o}\right)_{i,j-\frac{1}{2},k} \left(\frac{\partial k_{r,o}}{\partial S_w}\right)_{i,j,k} (\Phi_{o,i,j-1,k} - \Phi_{o,i,j,k}) \right\}^{n+1},$$

$$\mathbf{J_3} = \frac{1}{(\Delta y)^2}\left\{ \left(\frac{KA\rho_o}{\triangle x \mu_o}\right)_{i,j+\frac{1}{2},k} \left(\frac{\partial k_{r,o}}{\partial S_w}\right)_{i,j,k} (\Phi_{o,i,j+1,k} - \Phi_{o,i,j,k}) \right\}^{n+1},$$

$$\mathbf{J_4} = \frac{1}{(\Delta y)^2}\left\{ \left(\frac{KA\rho_o}{\triangle x \mu_o}\right)_{i,j+\frac{1}{2},k} \left(\frac{\partial k_{r,o}}{\partial S_w}\right)_{i,j+1,k} (\Phi_{o,i,j+1,k} - \Phi_{o,i,j,k}) \right\}^{n+1},$$

$$\mathbf{N_1} = \frac{1}{(\Delta z)^2}\left\{ \left(\frac{KA\rho_o}{\triangle x \mu_o}\right)_{i,j,k-\frac{1}{2}} \left(\frac{\partial k_{r,o}}{\partial S_w}\right)_{i,j,k-1} (\Phi_{o,i,j,k-1} - \Phi_{o,i,j,k}) \right\}^{n+1},$$

$$\mathbf{N_2} = \frac{1}{(\Delta z)^2}\left\{ \left(\frac{KA\rho_o}{\triangle x \mu_o}\right)_{i,j,k-\frac{1}{2}} \left(\frac{\partial k_{r,o}}{\partial S_w}\right)_{i,j,k} (\Phi_{o,i,j,k-1} - \Phi_{o,i,j,k}) \right\}^{n+1},$$

$$\mathbf{N_3} = \frac{1}{(\Delta z)^2}\left\{ \left(\frac{KA\rho_o}{\triangle x \mu_o}\right)_{i,j,k+\frac{1}{2}} \left(\frac{\partial k_{r,o}}{\partial S_w}\right)_{i,j,k} (\Phi_{o,i,j,k+1} - \Phi_{o,i,j,k}) \right\}^{n+1},$$

$$\mathbf{N_4} = \frac{1}{(\Delta z)^2}\left\{ \left(\frac{KA\rho_o}{\triangle x \mu_o}\right)_{i,j,k+\frac{1}{2}} \left(\frac{\partial k_{r,o}}{\partial S_w}\right)_{i,j,k+1} (\Phi_{o,i,j,k+1} - \Phi_{o,i,j,k}) \right\}^{n+1},$$

$$\mathbf{E_1} = \frac{V_b}{\Delta t}\left\{ (1 - S_w)\left(\phi \frac{\partial \rho_o}{\partial p_o} + \rho_o \frac{\partial \phi}{\partial p_o}\right) \right\}^{n+1}, \quad \mathbf{E_2} = \frac{V_b}{\Delta t}\left\{ (-\phi \rho_o) \right\}^{n+1},$$

and

$$\mathbf{A_2} = \left\{T_{w,i-\frac{1}{2},j,k}\right\}^{n+1}, \qquad \mathbf{K_2} = \left\{T_{w,i,j+\frac{1}{2},k}\right\}^{n+1},$$

$$\mathbf{B_2} = \left\{T_{w,i+\frac{1}{2},j,k}\right\}^{n+1}, \qquad \mathbf{M_2} = \left\{T_{w,i,j,k-\frac{1}{2}}\right\}^{n+1},$$

$$\mathbf{I_2} = \left\{T_{w,i,j-\frac{1}{2},k}\right\}^{n+1}, \qquad \mathbf{O_2} = \left\{T_{w,i,j,k+\frac{1}{2}}\right\}^{n+1},$$

$$\mathbf{D_1} = \frac{1}{(\Delta x)^2}\left\{ \left(\frac{KA\rho_w}{\triangle x \mu_w}\right)_{i-\frac{1}{2},j,k} \left(\frac{\partial k_{r,o}}{\partial S_w}\right)_{i-1,j,k} (\Phi_{w,i-1,j,k} - \Phi_{w,i,j,k}) - \left(T_w \frac{\partial p_c}{\partial S_w}\right)_{i-1,j,k} \right\}^{n+1},$$

$$\mathbf{D_2} = \frac{1}{(\Delta x)^2}\left\{ \left(\frac{KA\rho_w}{\triangle x \mu_w}\right)_{i-\frac{1}{2},j,k} \left(\frac{\partial k_{r,o}}{\partial S_w}\right)_{i,j,k} (\Phi_{w,i-1,j,k} - \Phi_{w,i,j,k}) - \left(T_w \frac{\partial p_c}{\partial S_w}\right)_{i,j,k} \right\}^{n+1},$$

$$\mathbf{D_3} = \frac{1}{(\Delta x)^2}\left\{ \left(\frac{KA\rho_w}{\triangle x \mu_w}\right)_{i+\frac{1}{2},j,k} \left(\frac{\partial k_{r,o}}{\partial S_w}\right)_{i,j,k} (\Phi_{w,i+1,j,k} - \Phi_{w,i,j,k}) - \left(T_w \frac{\partial p_c}{\partial S_w}\right)_{i,j,k} \right\}^{n+1},$$

$$\mathbf{D_4} = \frac{1}{(\Delta x)^2}\left\{ \left(\frac{KA\rho_w}{\triangle x \mu_w}\right)_{i+\frac{1}{2},j,k} \left(\frac{\partial k_{r,o}}{\partial S_w}\right)_{i+1,j,k} (\Phi_{w,i+1,j,k} - \Phi_{w,i,j,k}) - \left(T_w \frac{\partial p_c}{\partial S_w}\right)_{i+1,j,k} \right\}^{n+1},$$

$$\mathbf{L_1} = \frac{1}{(\Delta y)^2}\left\{ \left(\frac{KA\rho_w}{\triangle x \mu_w}\right)_{i,j-\frac{1}{2},k} \left(\frac{\partial k_{r,o}}{\partial S_w}\right)_{i,j-1,k} (\Phi_{w,i,j-1,k} - \Phi_{w,i,j,k}) - \left(T_w \frac{\partial p_c}{\partial S_w}\right)_{i,j-1,k} \right\}^{n+1},$$

$$\mathbf{L_2} = \frac{1}{(\Delta y)^2}\left\{ \left(\frac{KA\rho_w}{\triangle x \mu_w}\right)_{i,j-\frac{1}{2},k} \left(\frac{\partial k_{r,o}}{\partial S_w}\right)_{i,j,k} (\Phi_{w,i,j-1,k} - \Phi_{w,i,j,k}) - \left(T_w \frac{\partial p_c}{\partial S_w}\right)_{i,j,k} \right\}^{n+1},$$

$$\mathbf{L_3} = \frac{1}{(\Delta y)^2}\left\{ \left(\frac{KA\rho_w}{\triangle x \mu_w}\right)_{i,j+\frac{1}{2},k} \left(\frac{\partial k_{r,o}}{\partial S_w}\right)_{i,j,k} (\Phi_{w,i,j+1,k} - \Phi_{w,i,j,k}) - \left(T_w \frac{\partial p_c}{\partial S_w}\right)_{i,j,k} \right\}^{n+1},$$

$$\mathbf{L_4} = \frac{1}{(\Delta y)^2}\left\{ \left(\frac{KA\rho_w}{\triangle x \mu_w}\right)_{i,j+\frac{1}{2},k} \left(\frac{\partial k_{r,o}}{\partial S_w}\right)_{i,j+1,k} (\Phi_{w,i,j+1,k} - \Phi_{w,i,j,k}) - \left(T_w \frac{\partial p_c}{\partial S_w}\right)_{i,j+1,k} \right\}^{n+1},$$

$$\mathbf{P_1} = \frac{1}{(\Delta z)^2}\left\{ \left(\frac{KA\rho_w}{\triangle x \mu_w}\right)_{i,j,k-\frac{1}{2}} \left(\frac{\partial k_{r,o}}{\partial S_w}\right)_{i,j,k-1} (\Phi_{w,i,j,k-1} - \Phi_{w,i,j,k}) - \left(T_w \frac{\partial p_c}{\partial S_w}\right)_{i,j,k-1} \right\}^{n+1},$$

$$\mathbf{P_2} = \frac{1}{(\Delta z)^2}\left\{ \left(\frac{KA\rho_w}{\triangle x \mu_w}\right)_{i,j,k-\frac{1}{2}} \left(\frac{\partial k_{r,o}}{\partial S_w}\right)_{i,j,k} (\Phi_{w,i,j,k-1} - \Phi_{w,i,j,k}) - \left(T_w \frac{\partial p_c}{\partial S_w}\right)_{i,j,k} \right\}^{n+1},$$

$$\mathbf{P_3} = \frac{1}{(\Delta z)^2}\left\{ \left(\frac{KA\rho_w}{\triangle x \mu_w}\right)_{i,j,k+\frac{1}{2}} \left(\frac{\partial k_{r,o}}{\partial S_w}\right)_{i,j,k} (\Phi_{w,i,j,k+1} - \Phi_{w,i,j,k}) - \left(T_w \frac{\partial p_c}{\partial S_w}\right)_{i,j,k} \right\}^{n+1},$$

$$\mathbf{P_4} = \frac{1}{(\Delta z)^2}\left\{ \left(\frac{KA\rho_w}{\triangle x \mu_w}\right)_{i,j,k+\frac{1}{2}} \left(\frac{\partial k_{r,o}}{\partial S_w}\right)_{i,j,k+1} (\Phi_{w,i,j,k+1} - \Phi_{w,i,j,k}) - \left(T_w \frac{\partial p_c}{\partial S_w}\right)_{i,j,k+1} \right\}^{n+1},$$

$$\mathbf{E_3} = \frac{V_b}{\Delta t}\left\{ S_w \left(\phi \frac{\partial \rho_w}{\partial p_w} + \rho_w \frac{\partial \phi}{\partial p_w}\right) \right\}^{n+1}, \quad \mathbf{E_4} = \frac{V_b}{\Delta t}\left\{ (\phi \rho_w) \right\}^{n+1}. \tag{2.47}$$

And the Eqs. 2.43 and 2.45 become

$$\begin{aligned}
&\mathbf{M_1}\delta p_{o,i,j,k-1} + \mathbf{N_1}\delta S_{w,i,j,k-1} \\
&\mathbf{I_1}\delta p_{o,i,j-1,k} + \mathbf{J_1}\delta S_{w,i,j-1,k} \\
&\mathbf{A_1}\delta p_{o,i-1,j,k} + \mathbf{C_1}\delta S_{w,i-1,j,k} \\
&+ (-\mathbf{A_1} - \mathbf{B_1} - \mathbf{I_1} - \mathbf{K_1} - \mathbf{M_1} - \mathbf{O_1} - \mathbf{E_1})\delta p_{o,i,j,k} \\
&+ (\mathbf{C_2} + \mathbf{C_3} + \mathbf{J_2} + \mathbf{J_3} + \mathbf{N_2} + \mathbf{N_3} - \mathbf{E_2})\delta S_{w,i,j,k} \\
&+ \mathbf{B_1}\delta p_{o,i+1,j,k} + \mathbf{C_4}\delta S_{w,i+1,j,k} \\
&+ \mathbf{K_1}\delta p_{o,i,j+1,k} + \mathbf{J_4}\delta S_{w,i,j+1,k} \\
&+ \mathbf{O_1}\delta p_{o,i,j,k+1} + \mathbf{N_4}\delta S_{w,i,j,k+1} \\
&= -R(\mathbf{X_{o,i,j,k}})
\end{aligned} \tag{2.48}$$

and

$$\begin{aligned}
&\mathbf{M_2}\delta p_{o,i,j,k-1} + \mathbf{P_1}\delta S_{w,i,j,k-1} \\
&\mathbf{I_2}\delta p_{o,i,j-1,k} + \mathbf{L_1}\delta S_{w,i,j-1,k} \\
&\mathbf{A_2}\delta p_{o,i-1,j,k} + \mathbf{D_1}\delta S_{w,i-1,j,k} \\
&+ (-\mathbf{A_2} - \mathbf{B_2} - \mathbf{I_2} - \mathbf{K_2} - \mathbf{M_2} - \mathbf{O_2} - \mathbf{E_3})\delta p_{o,i,j,k} \\
&+ (\mathbf{D_2} + \mathbf{D_3} + \mathbf{L_2} + \mathbf{L_3} + \mathbf{P_2} + \mathbf{P_3} - \mathbf{E_4})\delta S_{w,i,j,k} \\
&+ \mathbf{B_2}\delta p_{o,i+1,j,k} + \mathbf{D_4}\delta S_{w,i+1,j,k} \\
&+ \mathbf{K_2}\delta p_{o,i,j+1,k} + \mathbf{L_4}\delta S_{w,i,j+1,k} \\
&+ \mathbf{O_2}\delta p_{o,i,j,k+1} + \mathbf{P_4}\delta S_{w,i,j,k+1} \\
&= -R(\mathbf{X_{w,i,j,k}})
\end{aligned} \tag{2.49}$$

2. Expansion for the Blocks near the Boundary

For the blocks communicating with the boundary, the left hand side and right hand side expansions are slightly different. In an experimental study, total flow rate of one phase is specified at the inlet and certain pressure is maintained at the outlet face.

Specification of flow rate normally presents a special problem in numerical representation. If the actual boundary spans more than one grid blocks and if the total flow rate q_t is specified (see Figure 2), then this flow rate must be distributed, in an appropriate fashion over the boundary blocks.

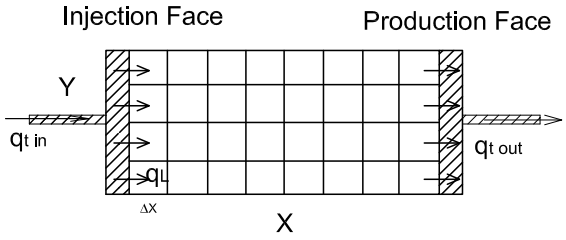

Fig. 2. Representation of a Rectangular Shaped Sample

According to Darcy equation, we have

$$v_f = -\frac{Kk_{r,f}}{\mu}(\nabla p_f - \rho_f g \nabla h) \tag{2.50}$$

$$q_f = v_f A = -\frac{Kk_{r,f}A}{\mu}(\nabla p_f - \rho_f g \nabla h), \quad f = w, nw. \tag{2.51}$$

A method developed by Nolen and Berry has been used in original two-dimensional SENDRA to perform the allocation of injected flow according to the total transmissi-

bility (Nolen and Berry, 1972). This method assumes that the difference of pressure between the injection face and the center of an adjacent block is the same for all blocks communicating with the boundary. Under this assumption, it can be shown that the allocated flow for any block near the boundary is approximated by

$$q_{f,l} = \frac{T_{f,l}}{\sum_{l=1}^{L} \left(T_{w,l} + T_{nw,l} \right)} q_t, \tag{2.52}$$

where L is the total number of blocks communicating with a given boundary. q_t is the total mass flow rate specified at this boundary, and $q_{f,l}$ is the mass flow rate allocated for the block l.

Wu et al. (1996) pointed out that Nolen and Berry scheme may result in physically incorrect solution because of the constant pressure drop assumption. The reason of the original two-dimensional SENDRA using this scheme is believed that the scheme is easy to implement. An appropriate approach to handling the allocation of the flow is required and modification of the numerical code according the appropriate approach is necessary. However, the objective of this work is extend the computer code into three dimensions. Therefore, the method of dealing with the allocation of injected flow used in original two-dimensional SENDRA is followed.

Both kinds of boundaries, total flow rate specified and pressure specified at boundary, have flow in and out of the sample. Aziz and Settari (1979) demonstrated that the actual flow boundary can be treated as no-flow boundary conditions by introducing the flow into or out of the system through source and sink terms because the numerical interpretations of both cases at finite difference level are equivalent. The detail will be discussed as following.

Figure 3 is presented to show the detail of flow boundary and no-flow boundary. In the figure, there is no flow across the boundary $\mathbf{T_2}$. According to Darcy equation,

the component of the velocity normal to the boundary surface must be zero,

$$\frac{Kk_{r,f}}{\mu}(\nabla p_f - \rho_f g \nabla h) \cdot \mathbf{n} = 0, \tag{2.53}$$

$$\frac{Kk_{r,f}}{\mu}(\frac{\partial p_f}{\partial x} - \rho_f g \frac{\partial h}{\partial x}) = 0 \quad \text{For all the boundaries of } T_2 \text{ normal to the x direction,} \tag{2.54}$$

$$\frac{Kk_{r,f}}{\mu}(\frac{\partial p_f}{\partial y} - \rho_f g \frac{\partial h}{\partial y}) = 0 \quad \text{For all the boundaries of } T_2 \text{ normal to the y direction.} \tag{2.55}$$

For boundaries $\mathbf{T_1}$ and $\mathbf{T_3}$, flow rate specified at the boundary and pressure specified at the boundary, there are flows across both of them. Then, the normal component of the velocity at the boundary must equal the flow rate,

$$\frac{Kk_{r,f}}{\mu}(\nabla p_f - \rho_f g \nabla h) \cdot \mathbf{n} = q(\mathbf{T}), \tag{2.56}$$

$$\int_{\mathbf{T_1}} q(\mathbf{T}) = q_T \tag{2.57}$$

$$p(\mathbf{T_3}) = p_{end} \tag{2.58}$$

For both kinds of boundaries $\mathbf{T_1}$ and $\mathbf{T_3}$, since $q(T)$ is nonzero, there have

$$\frac{Kk_{r,f}}{\mu}(\frac{\partial p_f}{\partial x} - \rho_f g \frac{\partial h}{\partial x}) \neq 0 \quad \text{For all the boundaries of } T_1 \text{ and } T_3 \text{ normal to the x direction,} \tag{2.59}$$

$$\frac{Kk_{r,f}}{\mu}(\frac{\partial p_f}{\partial y} - \rho_f g \frac{\partial h}{\partial y}) \neq 0 \quad \text{For all the boundaries of } T_1 \text{ and } T_3 \text{ normal to the y direction.} \tag{2.60}$$

According to Aziz and Settari (1979), we consider two cases as shown in Figure 4, case 1 is flow boundary with specified inlet flow rate with no fluid production (source)

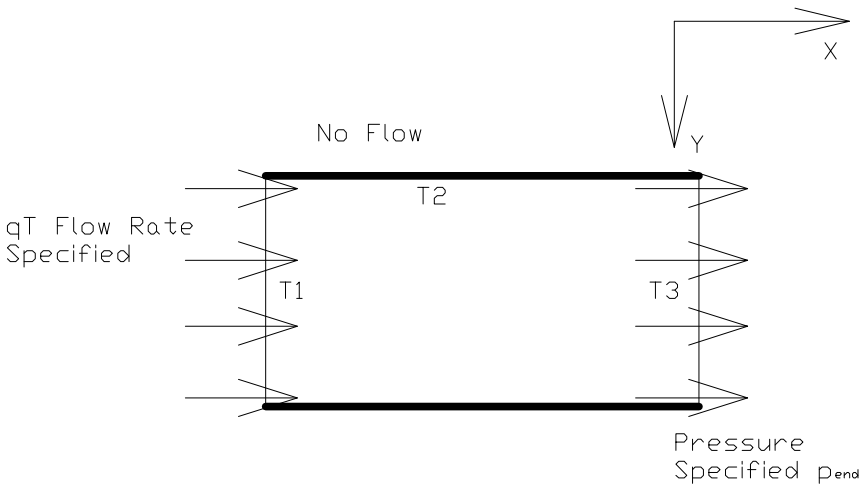

Fig. 3. Representation of the Flow Boundary and No-Flow Boundary

and case 2 is no-flow boundary with local fluid production (for example, there is fluid flowing into the block through a small hole). After integration Eqs. 2.1 and 2.2 over the volume of block, we will have

$$\triangle z \iint_A \left\{ \nabla \cdot \left[\frac{\rho_f K k_{r,f}}{\mu_f} (\nabla p_f - \rho_f g \nabla z) \right] \right\} dx\, dy + \triangle z \iint_A q_f\, dx\, dy = \triangle z \iint_A \left\{ \frac{\partial (\phi \rho_f S_f)}{\partial t} \right\} dx\, dy. \quad (2.61)$$

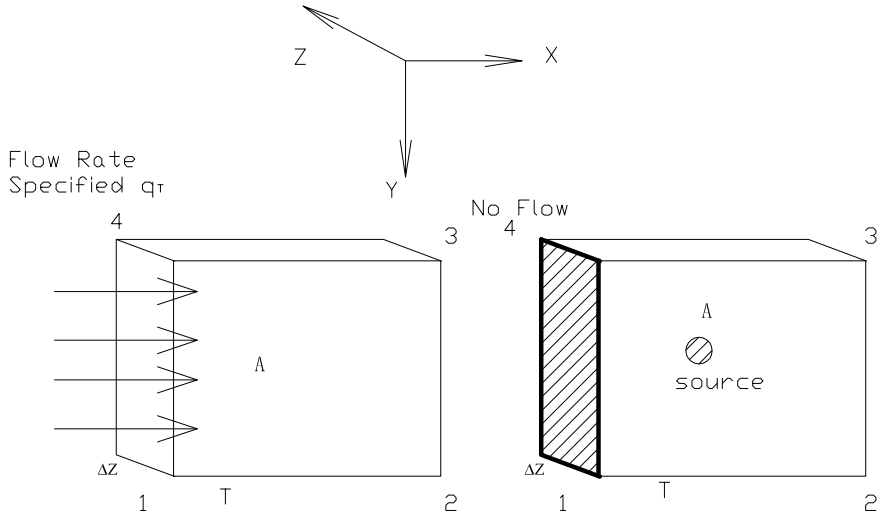

Fig. 4. Representation of No-Flow Boundary and Flow Boundary with Specified Flow Rate at Finite Difference Level

Using Green's theorem, The left side of Eq. 2.61 can be converted to a line

integral over the boundary T.

$$\triangle z \int_{\mathrm{T}} \Big\{ \Big[\frac{\rho_f K k_{r,f}}{\mu_f} \frac{\partial \Phi}{\partial y} \Big] dx - \Big[\frac{\rho_f K k_{r,f}}{\mu_f} \frac{\partial \Phi}{\partial x} \Big] dy \Big\} + \triangle z \iint_A q_f \, dx \, dy = \triangle z \iint_A \Big\{ \frac{\partial (\phi \rho_f S_f)}{\partial t} \Big\} \, dx \, dy. \quad (2.62)$$

For simplification, we define function

$$\mathbf{\Psi} = \Big[\frac{\rho_f K k_{r,f}}{\mu_f} \frac{\partial \Phi}{\partial y} \Big] dx - \Big[\frac{\rho_f K k_{r,f}}{\mu_f} \frac{\partial \Phi}{\partial x} \Big] dy \quad (2.63)$$

The boundary T can be divided into four segments, the segments 1-2,2-3,3-4 and 4-1. Then Eq. 2.62 becomes

$$\triangle z \Big\{ \int_1^2 \mathbf{\Psi} + \int_2^3 \mathbf{\Psi} + \int_3^4 \mathbf{\Psi} + \int_4^1 \mathbf{\Psi} \Big\} + \triangle z \iint_A q_f \, dx \, dy = \triangle z \iint_A \Big\{ \frac{\partial (\phi \rho_f S_f)}{\partial t} \Big\} \, dx \, dy. \quad (2.64)$$

The integral from 4 to 1 is the integral over the boundary we are interested. For case 1, there is no fluid production and total inlet fluid rate is specified,

$$\triangle z \iint_A q_f \, dx \, dy = 0, \quad (2.65)$$

$$\triangle z \int_4^1 \Big\{ - \Big[\frac{\rho_f K k_{r,f}}{\mu_f} \frac{\partial \Phi}{\partial x} \Big] dy \Big\} = q_t. \quad (2.66)$$

Therefore, Eq. 2.64 for case 1 becomes

$$\triangle z \Big\{ \int_1^2 \mathbf{\Psi} + \int_2^3 \mathbf{\Psi} + \int_3^4 \mathbf{\Psi} \Big\} + q_t = \triangle z \iint_A \Big\{ \frac{\partial (\phi \rho_f S_f)}{\partial t} \Big\} \, dx \, dy. \quad (2.67)$$

For case 2, since there is no-flow boundary and the total fluid production equals to the total inlet fluid rate in case 1, we have

$$\triangle z \iint_A q_f \, dx \, dy = q_t, \tag{2.68}$$

$$\triangle z \int_4^1 \Big\{ - \Big[\frac{\rho_f K k_{r,f}}{\mu_f} \frac{\partial \Phi}{\partial x} \Big] \, dy \Big\} = 0. \tag{2.69}$$

Eq. 2.64 for case 2 becomes

$$\triangle z \Big\{ \int_1^2 \mathbf{\Psi} + \int_2^3 \mathbf{\Psi} + \int_3^4 \mathbf{\Psi} \Big\} + q_t = \triangle z \iint_A \Big\{ \frac{\partial (\phi \rho_f S_f)}{\partial t} \Big\} \, dx \, dy. \tag{2.70}$$

Comparing Eqs. 2.67 and 2.70, we find these two equations are identical.

A similar situation will be found in pressure specified boundary. We consider two cases as shown in Figure 5, case 1 is flow boundary with specified outlet pressure with no fluid depletion (sink) and case 2 is no-flow boundary with local fluid depletion (for example, there is fluid flowing out of the block through a small hole). The integral from 4 to 1 of Eq. 2.64 is the integral over the boundary we are interested. For case 1, there is no fluid depletion and total outlet fluid rate can be calculate from pressure drop,

$$\triangle z \iint_A q_f \, dx \, dy = 0, \tag{2.71}$$

$$\triangle z \int_4^1 \Big\{ - \Big[\frac{\rho_f K k_{r,f}}{\mu_f} \frac{\partial \Phi}{\partial x} \Big] \, dy \Big\} = \triangle z \triangle y \Big\{ - \Big[\frac{\rho_f K k_{r,f}}{\mu_f} \frac{p - p_{end}}{\frac{1}{2} \Delta x} \Big] \Big\}. \tag{2.72}$$

Eq. 2.64 for case 1 becomes

$$\triangle z \Big\{ \int_1^2 \mathbf{\Psi} + \int_2^3 \mathbf{\Psi} + \int_3^4 \mathbf{\Psi} \Big\} + \triangle z \triangle y \Big\{ - \Big[\frac{\rho_f K k_{r,f}}{\mu_f} \frac{p - p_{end}}{\frac{1}{2} \Delta x} \Big] \Big\} = \triangle z \iint_A \Big\{ \frac{\partial (\phi \rho_f S_f)}{\partial t} \Big\} \, dx \, dy. \tag{2.73}$$

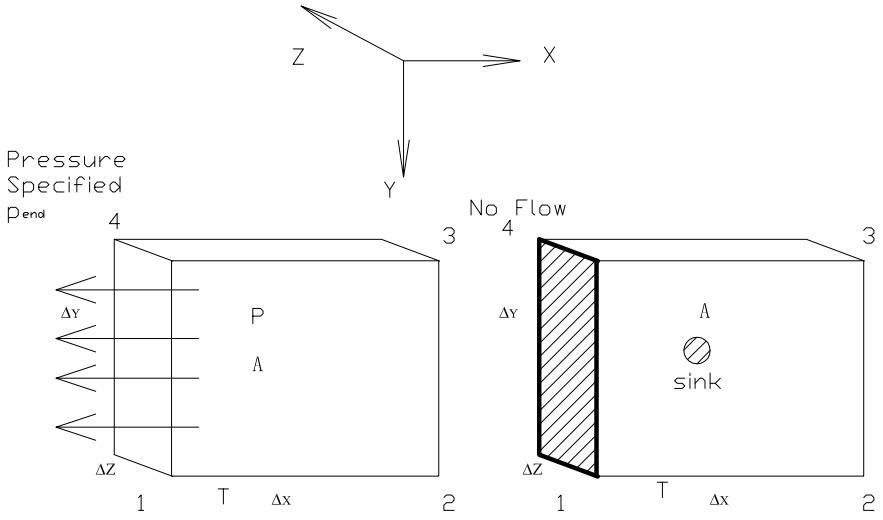

Fig. 5. Representation of No-Flow Boundary and Flow Boundary with Specified Outlet Pressure at Finite Difference Level

For case 2, since there is no-flow boundary and the total fluid depletion equals to the total outlet fluid rate in case 1, we have

$$\triangle z \iint_A q_f \, dx \, dy = \triangle z \triangle y \Big\{ - \Big[\frac{\rho_f K k_{r,f}}{\mu_f} \frac{(p - p_{end})}{\frac{1}{2}\Delta x} \Big] \Big\}, \tag{2.74}$$

$$\triangle z \int_4^1 \Big\{ - \Big[\frac{\rho_f K k_{r,f}}{\mu_f} \frac{\partial \Phi}{\partial x} \Big] \, dy \Big\} = 0. \tag{2.75}$$

Eq. 2.64 for case 2 becomes

$$\begin{aligned} \triangle z \Big\{ \int_1^2 \mathbf{\Psi} + \int_2^3 \mathbf{\Psi} + \int_3^4 \mathbf{\Psi} \Big\} + \triangle z \triangle y \Big\{ - \Big[\frac{\rho_f K k_{r,f}}{\mu_f} \frac{(p - p_{end})}{\frac{1}{2}\Delta x} \Big] \Big\} \\ = \triangle z \iint_A \Big\{ \frac{\partial (\phi \rho_f S_f)}{\partial t} \Big\} \, dx \, dy. \end{aligned} \tag{2.76}$$

Comparing Eqs. 2.73 and 2.76, we find these two equations are identical.

Therefore, for both kinds of boundaries, the actual flow boundary can be treated as no-flow boundary conditions by introducing the flow into or out of the system through source and sink terms at finite difference level. Since there are nonzero sink/source terms for the blocks communicating with the boundary, the numerical expansion for Eq. 2.30 is slightly different.

a. Total Flow Rate Specified at the Boundary

A three-dimension flow, pictured in Figure 6, is presented to show the detail of handling the boundary condition. Aziz and Settari (1979) demonstrated that the flow boundary can be treated as no-flow boundary conditions by introducing the flow into or out of the system through source and sink terms because the numerical interpretations of both cases at finite difference level are equivalent. Therefore, the actual flow is implemented as source term in the finite difference scheme. For the block $(1, 1, k)$, the source term equals to the flow rate transported through boundary for this block

which is calculated according to the transmissibilities (Nolen and Berry, 1972)

$$\left\{q_{f_{(1,1,k)}}\right\}^{n+1} = \left\{\frac{T_{f_{(1,1,k)}}}{\Sigma_{j=1}^{N_y}\,\Sigma_{k=1}^{N_z}\,T_{f_{(1,j,k)}}} q_{t,f}\right\}^{n+1}, \quad f = w, nw. \tag{2.77}$$

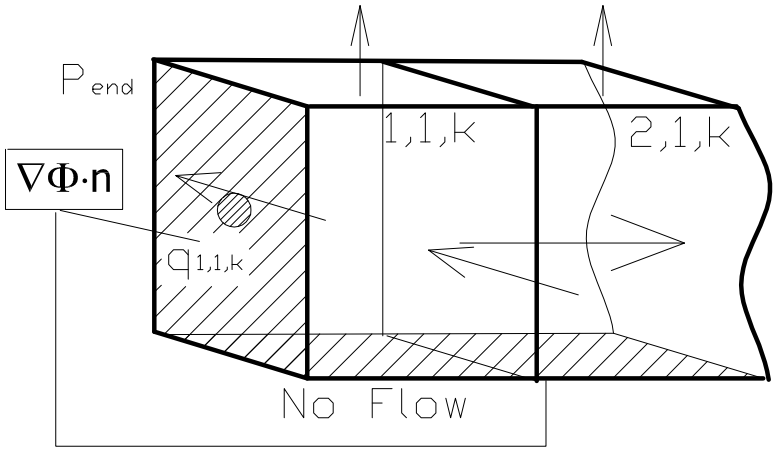

Fig. 6. Representation of the Sample Boundary (Flow Rate Specified at the Boundary)

For no-flow boundary, Darcy equation can be expressed as

$$\frac{Kk_{rf}}{\mu_f}(\nabla p_f - \rho_f g \nabla h) \cdot \mathbf{n} = 0,$$

$$\nabla \Phi \cdot \mathbf{n} = 0.$$

It is noticed that two sides of this block are no-flow boundaries so as that two

terms in the difference quotients 2.22-2.24 become zeros

$$\left.\frac{\partial}{\partial x}\left(T_f\frac{\partial \Phi_f}{\partial x}\right)\right|_{(1,1,k)} = \frac{T_{f_{(1+\frac{1}{2},1,k)}}\{\Phi_{f_{(2,1,k)}} - \Phi_{f_{(,1,1,k)}}\} - 0}{(\Delta x)^2},$$

$$\left.\frac{\partial}{\partial y}\left(T_f\frac{\partial \Phi_f}{\partial y}\right)\right|_{(1,1,k)} = \frac{T_{f_{(1,1+\frac{1}{2},k)}}\{\Phi_{f_{(1,2,k)}} - \Phi_{f_{(1,1,k)}}\} - 0}{(\Delta y)^2},$$

$$\left.\frac{\partial}{\partial z}\left(T_f\frac{\partial \Phi_f}{\partial z}\right)\right|_{(1,1,k)} = \frac{T_{f_{(1,1,k+\frac{1}{2})}}\{\Phi_{f_{(1,1,k+1)}} - \Phi_{f_{(1,1,k)}}\} - T_{f_{(1,1,k-\frac{1}{2})}}\{\Phi_{f_{(1,1,k)}} - \Phi_{f_{(1,1,k-1)}}\}}{(\Delta z)^2}.$$

Then the right hand side of the Eq. 2.30 for block $(1,1,k)$ is expressed as

$$\begin{aligned}
-\{R(\mathbf{X})\}_{1,1,k} &= -\Big\{\ \Delta_x\left(T_f\Delta_x\Phi_f\right) + \Delta_y\left(T_f\Delta_y\Phi_f\right) + \Delta_z\left(T_f\Delta_z\Phi_f\right)\ \Big\}_{1,1,k}^{n+1} \\
&+ \frac{V_b}{\Delta t}\Big\{\ (\phi\rho_f S_f)_{1,1,k}^{n+1} - (\phi\rho_f S_f)_{1,1,k}^{n}\ \Big\} - q_{f_{(1,1,k)}}^{n+1} \\
&= -\Big\{\ \frac{T_{f_{(1+\frac{1}{2},1,k)}}\{\Phi_{f_{(2,1,k)}} - \Phi_{f_{(1,1,k)}}\} - 0}{(\Delta x)^2} \\
&+ \frac{T_{f_{(1,1+\frac{1}{2},k)}}\{\Phi_{f_{(1,2,k)}} - \Phi_{f_{(1,1,k)}}\} - 0}{(\Delta y)^2} \\
&+ \frac{T_{f_{(1,1,k+\frac{1}{2})}}\{\Phi_{f_{(1,1,k+1)}} - \Phi_{f_{(1,1,k)}}\} - T_{f_{(1,1,k-\frac{1}{2})}}\{\Phi_{f_{(1,1,k)}} - \Phi_{f_{(1,1,k-1)}}\}}{(\Delta z)^2}\ \Big\}^{n+1} \\
&+ \frac{V_b}{\Delta t}\Big\{\ (\phi\rho_f S_f)_{1,1,k}^{n+1} - (\phi\rho_f S_f)_{1,1,k}^{n}\ \Big\} \\
&- \Big\{\frac{T_{f_{(1,1,k)}}}{\sum_{j=1}^{N_y}\sum_{k=1}^{N_z} T_{f_{(1,j,k)}}} q_{t,f}\Big\}^{n+1},
\end{aligned} \tag{2.78}$$

and the left hand side of the Eq. 2.30 is expressed as

$$\begin{aligned}
&\mathbf{M_1}\delta p_{o,1,1,k-1} + \mathbf{N_1}\delta S_{w,1,1,k-1} \\
&+ (-\mathbf{B_1} - \mathbf{K_1} - \mathbf{M_1} - \mathbf{O_1} - \mathbf{E_1})\delta p_{o,1,1,k} \\
&+ (\mathbf{C_3} + \mathbf{J_3} + \mathbf{N_2} + \mathbf{N_3} - \mathbf{E_2})\delta S_{w,1,1,k} \\
&+ \mathbf{B_1}\delta p_{o,2,1,k} + \mathbf{C_4}\delta S_{w,2,1,k} \\
&+ \mathbf{K_1}\delta p_{o,1,2,k} + \mathbf{J_4}\delta S_{w,1,2,k} \\
&+ \mathbf{O_1}\delta p_{o,1,1,k+1} + \mathbf{N_4}\delta S_{w,1,1,k+1}
\end{aligned} \tag{2.79}$$

and

$$\begin{aligned}
&\mathbf{M_2}\delta p_{o,1,1,k-1} + \mathbf{P_1}\delta S_{w,1,1,k-1} \\
&+ (-\mathbf{B_2} - \mathbf{K_2} - \mathbf{M_2} - \mathbf{O_2} - \mathbf{E_3})\delta p_{o,1,1,k} \\
&+ (\mathbf{D_3} + \mathbf{L_3} + \mathbf{P_2} + \mathbf{P_3} - \mathbf{E_4})\delta S_{w,1,1,k} \\
&+ \mathbf{B_2}\delta p_{o,2,1,k} + \mathbf{D_4}\delta S_{w,2,1,k} \\
&+ \mathbf{K_2}\delta p_{o,1,2,k} + \mathbf{L_4}\delta S_{w,1,2,k} \\
&+ \mathbf{O_2}\delta p_{o,1,1,k+1} + \mathbf{P_4}\delta S_{w,1,1,k+1}
\end{aligned} \tag{2.80}$$

b. Pressure Specified at the Boundary

Specification pressure at the boundary is straightforward. For example, one of the end faces is maintained with constant p_{end} (see Figure 7). Then, the pressure drop between blocks communicating the boundary and the boundary can be calculated by

$$\triangle p_{f_{(Nx,j,k)}} = p_{f_{(Nx,j,k)}} - p_{end}. \tag{2.81}$$

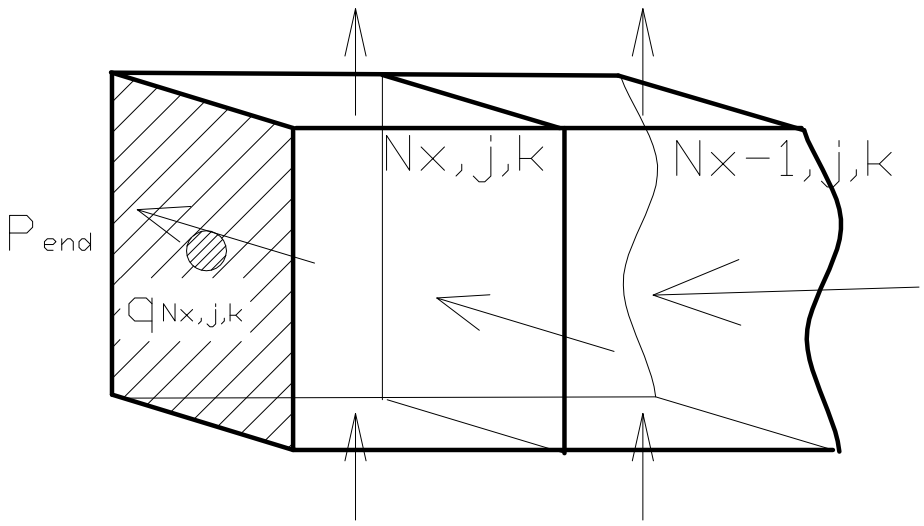

Fig. 7. Representation of the Sample Boundary (Pressure Specified at the Boundary)

According to Aziz and Settari (1979), the actual flow out of system are implemented as sinks term in the finite difference scheme. For the block (N_x, j, k), the sink term is calculated through the its transmissibility and pressure drop. Only under the condition of the potential of the fluid in this block greater than the outlet face pressure, the fluid can flow out of the sample:

$$\Big\{q_f\Big\}^{n+1}_{N_x,j,k} = \Big\{ -T_f(\Phi_f - p_{end})\Big\}^{n+1}_{N_x,j,k}, \qquad \text{if } \Phi_f - p_{end} > 0 \tag{2.82}$$

$$\Big\{q_f\Big\}^{n+1}_{N_x,j,k} = 0, \qquad \text{if } \Phi_f - p_{end} \leq 0. \tag{2.83}$$

The derivative for the sink term is calculated as

if $\Phi_f - p_{end} > 0$,

$$\Big\{\frac{\partial}{\partial p_o} q_o\Big\}^{n+1}_{N_x,j,k} = \Big\{ -T_o\Big\}^{n+1}_{N_x,j,k} = \mathbf{R_1} \tag{2.84}$$

$$\Big\{\frac{\partial}{\partial S_w} q_o\Big\}^{n+1}_{N_x,j,k} = \Big\{ -(\Phi_o - p_{end})\frac{\partial}{\partial S_w} T_o\Big\}^{n+1}_{N_x,j,k} = \mathbf{R_2} \tag{2.85}$$

$$\Big\{\frac{\partial}{\partial p_o} q_w\Big\}^{n+1}_{N_x,j,k} = \Big\{ -T_w\Big\}^{n+1}_{N_x,j,k} = \mathbf{R_3} \tag{2.86}$$

$$\Big\{\frac{\partial}{\partial S_w} q_w\Big\}^{n+1}_{N_x,j,k} = \Big\{ -(\Phi_w - p_{end})\frac{\partial}{\partial S_w} T_w + T_w \frac{\partial p_c}{\partial S_w}\Big\}^{n+1}_{N_x,j,k} = \mathbf{R_4} \tag{2.87}$$

For this block, only one side of this block is no-flow boundary so as that one term in the difference quotients 2.22-2.24 becomes zero. Then the right hand side of

Eq. 2.30 for block (N_x, j, k) is expressed as

$$
\begin{aligned}
-\{R(\mathbf{X})\}_{N_x,j,k} &= -\Big\{ \Delta_x \left(T_f \Delta_x \Phi_f\right) + \Delta_y \left(T_f \Delta_y \Phi_f\right) + \Delta_z \left(T_f \Delta_z \Phi_f\right) \Big\}_{N_x,j,k}^{n+1} \\
&+ \frac{V_b}{\Delta t}\Big\{ \left(\phi \rho_f S_f\right)_{N_x,j,k}^{n+1} - \left(\phi \rho_f S_f\right)_{N_x,j,k}^{n} \Big\} - q_{f_{(N_x,j,k)}}^{n+1} \\
&= -\Big\{ \frac{T_{f_{(N_x-\frac{1}{2},j,k)}} \{\Phi_{f_{(N_x,j,k)}} - \Phi_{f_{(N_x,j,k)}}\} - 0}{(\Delta x)^2} \\
&+ \frac{T_{f_{(N_x,j+\frac{1}{2},k)}} \{\Phi_{f_{(N_x,j+1,k)}} - \Phi_{f_{(N_x,j,k)}} - T_{f_{(N_x,j,k)}} \{\Phi_{f_{(N_x,j-\frac{1}{2},k)}} - \Phi_{f_{(N_x,j,k)}}\}}{(\Delta y)^2} \\
&+ \frac{T_{f_{(N_x,j,k+\frac{1}{2})}} \{\Phi_{f_{(N_x,j,k+1)}} - \Phi_{f_{(N_x,j,k)}}\} - T_{f_{(N_x,j,k-\frac{1}{2})}} \{\Phi_{f_{(N_x,j,k)}} - \Phi_{f_{(N_x,j,k-1)}}\}}{(\Delta z)^2} \Big\}^{n+1} \\
&+ \frac{V_b}{\Delta t}\Big\{ \left(\phi \rho_f S_f\right)_{N_x,j,k}^{n+1} - \left(\phi \rho_f S_f\right)_{N_x,j,k}^{n} \Big\} - q_{f_{(N_x,j,k)}}^{n+1},
\end{aligned}
\tag{2.88}
$$

and the left hand side of Eq. 2.30 is expressed as

$$
\begin{aligned}
&\mathbf{M_1}\delta p_{o,N_x,j,k-1} + \mathbf{N_1}\delta S_{w,N_x,j,k-1} \\
&\mathbf{I_1}\delta p_{o,N_x,j-1,k} + \mathbf{J_1}\delta S_{w,N_x,j-1,k} \\
&\mathbf{A_1}\delta p_{o,N_x-1,j,k} + \mathbf{C_1}\delta S_{w,N_x-1,j,k} \\
&+ (-\mathbf{A_1} - \mathbf{I_1} - \mathbf{K_1} - \mathbf{M_1} - \mathbf{O_1} - \mathbf{E_1} + \mathbf{R_1})\delta p_{o,N_x,j,k} \\
&+ (\mathbf{C_2} + \mathbf{J_2} + \mathbf{J_3} + \mathbf{N_2} + \mathbf{N_3} - \mathbf{E_2} + \mathbf{R_2})\delta S_{w,N_x,j,k} \\
&+ \mathbf{K_1}\delta p_{o,N_x,j+1,k} + \mathbf{J_4}\delta S_{w,N_x,j+1,k} \\
&+ \mathbf{O_1}\delta p_{o,N_x,j,k+1} + \mathbf{N_4}\delta S_{w,N_x,j,k+1}
\end{aligned}
\tag{2.89}
$$

and

$$\begin{aligned}
&\mathbf{M_2}\delta p_{o,N_x,j,k-1} + \mathbf{P_1}\delta S_{w,N_x,j,k-1} \\
&\mathbf{I_2}\delta p_{o,N_x,j-1,k} + \mathbf{L_1}\delta S_{w,N_x,j-1,k} \\
&\mathbf{A_2}\delta p_{o,N_x-1,j,k} + \mathbf{D_1}\delta S_{w,N_x-1,j,k} \\
&+ (-\mathbf{A_2} - \mathbf{I_2} - \mathbf{K_2} - \mathbf{M_2} - \mathbf{O_2} - \mathbf{E_3} + \mathbf{R_3})\delta p_{o,N_x,j,k} \\
&+ (\mathbf{D_2} + \mathbf{L_2} + \mathbf{L_3} + \mathbf{P_2} + \mathbf{P_3} - \mathbf{E_4} + \mathbf{R_4})\delta S_{w,N_x,j,k} \\
&+ \mathbf{K_2}\delta p_{o,N_x,j+1,k} + \mathbf{L_4}\delta S_{w,N_x,j,k} \\
&+ \mathbf{O_2}\delta p_{o,N_x,j,k+1} + \mathbf{P_4}\delta S_{w,N_x,j,k+1}
\end{aligned} \tag{2.90}$$

The total production is calculated by the summation of production of each blocks near the boundary:

$$q_t = \sum_{j=1}^{N_y}\sum_{k=1}^{N_z} q_{f_{(N_x,j,k)}} = \sum_{j=1}^{N_y}\sum_{k=1}^{N_z}\left\{T_{f_{(N_x,j,k)}} \triangle p_{f_{(N_x,j,k)}}\right\}. \tag{2.91}$$

Initialization of phase pressures and saturation is based on the actual initial conditions. In this model, initial wetting phase condition should be provided firstly. Then the pressure and saturation for the other phase is calculated from the saturation of the wetting phase and capillary pressure.

From above, it is found that each block have two unknowns $(p_o, S_w)_{i,j,k}$ and two equations (one for wetting phase and the other for non-wetting phase). Therefore, we totally have $(N_x \times N_y \times N_z \times 2)$ unknowns with $(N_x \times N_y \times N_z \times 2)$ equations. A iterative method is used to find the solution (Petec Software & Services, 2000). The variables of the left hand side and right hand side of Eq. 2.30, which should be evaluated at time t_{n+1}, initially use the value at t_n. The left hand side and right hand side are then updated according to the solution of Eq. 2.30. The iteration process converges

rapidly to a stable solution usually within 3-4 iterations. The solution is assumed to be found when the maximum change in the solution between two successive iterations is less than the preset tolerances.

The structure of the resulting coefficient matrix of Eq. 2.30 has a 'block' triangular form shown in Fig. 8. The matrix of order $N = N_x \cdot N_y \cdot N_z$ can be partitioned into $N_z \cdot N_z$ submatrices. Each submatrix can be further partitioned into $N_y \cdot N_y$ submatrices, where each submatrix is of order $N_x \cdot N_x$. For one-dimensional problems, SENDRA uses the Thomas algorithm to solve the block system equations. For two-dimensional problems, the technique of D4 ordering (Aziz and Settari, 1979) is applied in two-dimensional problems. The D4 technique provides the greatest advantage (Aziz and Settari, 1979) for two-dimensional reservoir simulation, especially for complex reservoir shapes. But our problem is the three-dimensional simulation for fluid flow through a sample that has a regular shape. We need to find a matrix solver to deal with the matrix equation that is yielded by the three-dimensional problem.

For the simulation involving many grid points, direct methods are too expensive to be practical, so iterative methods are good choices (Peaceman, 1977). SPLIB is a library of sparse iterative solvers, with preconditioners, for rapid prototyping of solvers for nonsymmetrical linear systems of equations (Bramley and Wang, 1995). The data structure of the coefficient matrix used in SPLIB is CSR, compressed sparse row. This is the transpose of the data structure used for the Harwell/Boeing collection of matrices, a set of standard test matrices for sparse matrix problems. Harwell/Boeing format is a standard format which can store the nonzeros of the matrix in an efficient way (Duff et al., 1992). SENDRA can only create the matrix in IJvalue format (also called coordinated format) (Alvarado, 1993) which can store the nonzero elements of the matrix in a format, for example, $\boxed{2\ 3\ 45.5}$, where the first two numbers representing the row and column indices of the nonzero element 45.5. A routine is supplied

by an important package SPARSKIT which can create a Harwell/Boeing (H/B) file from a matrix in any format (Saad, 1994). After the IJvalue format is converted into H/B format by implementing SPARSKIT, SPLIB provides us a fast and accurate solution method for the type of linear systems encountered in SENDRA.

D. Two-Dimensional Comparison Test

In this work, the code was extended to include all three spatial coordinate directions in order to account for spatial variations in the porosity and absolute permeability. The validity of SENDRA has been verified for the original two-dimensional system. The aim of this section is to demonstrate the validity of simulating fluid flow in three-dimensional geometry.

After extending SENDRA from two-dimensional to three-dimensional and compiling on our Linux workstation, the modified program needs to be tested and validated with the original two-dimensional SENDRA program. For the sake of the validation, we take the x-direction horizontal, two-dimensional flow as a test case to validate the extended code. In Fig. 9, the upper image presents a grid system with 10 blocks in x direction, 5 blocks in y direction, and 1 block in z direction as a vertical plane. The bottom image presents another grid system with 10 blocks in x direction, 1 block in y direction and 5 blocks in z direction as a horizontal plane. The rock heterogeneities (porosity and permeability) which are assigned to different blocks should satisfy the following relationship:

$$K_V(i,j,1) = K_H(i,1,j)$$

$$\phi_V(i,j,1) = \phi_H(i,1,j)$$

The subscripts H and V represent the horizontal and vertical plane, respectively.

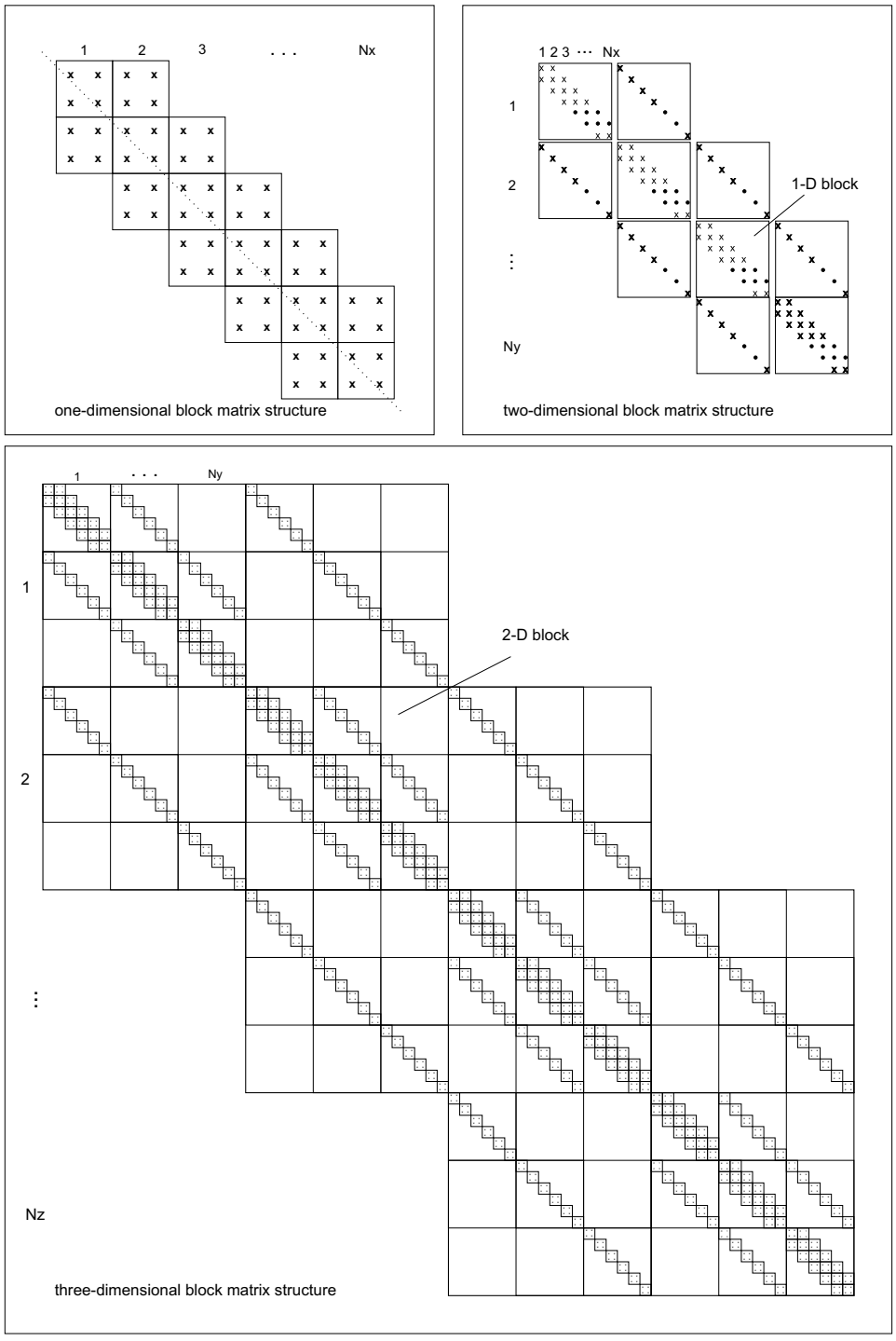

Fig. 8. The Block Matrix Structure

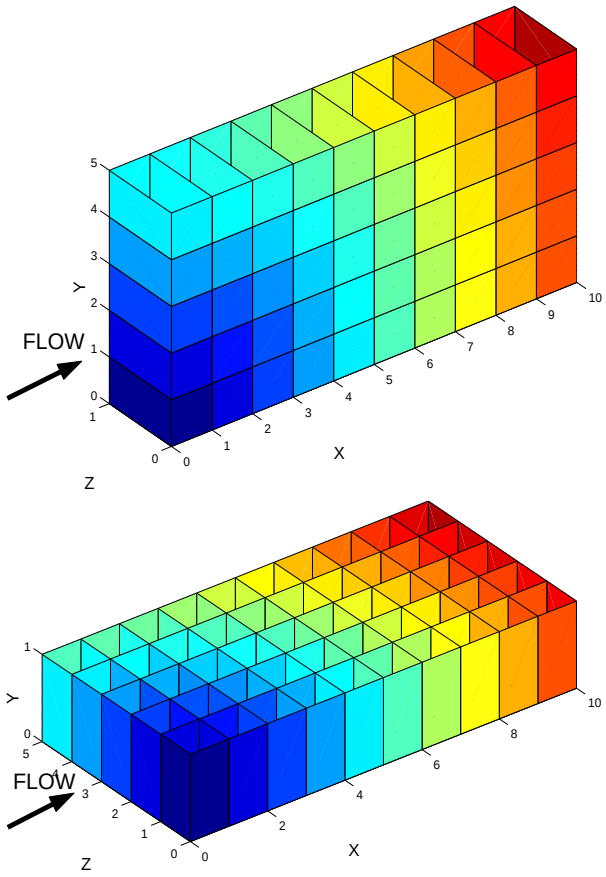

Fig. 9. 2-Dimensional Vertical Plane (left), 2-Dimensional Horizontal Plane (right)

The multiphase flow through the vertical plane is simulated by the original two-dimensional SENDRA code, and the one through the horizontal plane is simulated by the three-dimensional SENDRA code with only a single layer of grid blocks in the y-direction. The data listed in Table I and the flow functions were then implemented in SENDRA to simulate a displacement experiment. If gravity is neglected (g=0), the 2-dimensional horizontal plane should have the same results as 2-dimensional vertical plane.

Results for fluid flow through the two-dimensional horizontal plane are compared

Table I. The SENDRA Input for Horizontal and Vertical Plane

Core and Fluid Properties		
	Vertical Plane	Horizontal Plane
Porosity [%]	20	Same as Left
Permeability[mD]	1000, 900, 800, 700, 600	Same as Left
Core Size (X× Y× Z) [mm]	$40 \times 40 \times 10$	$40 \times 10 \times 40$
Oil Viscosity [cP]	0.75	0.75
Water Viscosity [cP]	0.339	0.339
Oil Density [kg/m^3]	800	800
Water Density [kg/m^3]	1,000	1,000
Data Defining Initial State and Grid Data		
Pressure [kPa]	33500	33500
Water Saturation [frac]	0.2	0.2
No. of Grid Blocks (X-Direction)	10	10
No. of Grid Blocks (Y-Direction)	5	1
No. of Grid Blocks (Z-Direction)	1	5
Two-Phase Experiment		
Water Injection Rates [ml/min]	1.0, 5.0	1.0, 5.0
Corresponding Times [min]	1000, 1500	1000, 1500
Total Experimental Time [min]	2000	2000

with the results from the vertical plane. The simulated water saturation profiles, oil productions, and differential pressures are found to be identical. The results for the two planes are shown in Figures 10-12.

After comparing all Figures 10-12, we find that the data in the z-direction is consistent with that of the original two-dimensional SENDRA in y-direction. Therefore, we concluded that the extended code works well.

E. Synthetic Experiments and Estimations

The motivation of extension of the code is that we believe taking sample heterogeneities into consideration will improve the accuracy of determination of flow functions. In this section, we will show how the homogeneity assumption influences the estimation of the flow functions. Several synthetic oil-water displacement experiments are performed and the synthetic results (the pressure drop and production) are then simulated by adjusting relative permeabilities and capillary pressure. Absolute permeability and porosity distributions are specified and used to generate synthetic data. Two scenarios are considered in synthetic data analysis stage: heterogeneous and homogeneous system. In the first scenario, a true absolute permeability and porosity used in generating synthetic data are applied. In the second scenario, we take the properties of the sample to be uniform. Three synthetic experiment results are analyzed by using the above two estimation scenarios. Two of these three experiments, a single-injection-rate experiment and a two-injection-rate experiment, are tested on a coarse scale system. The third experiment is a single-injection-rate experiment on a relative fine scale system.

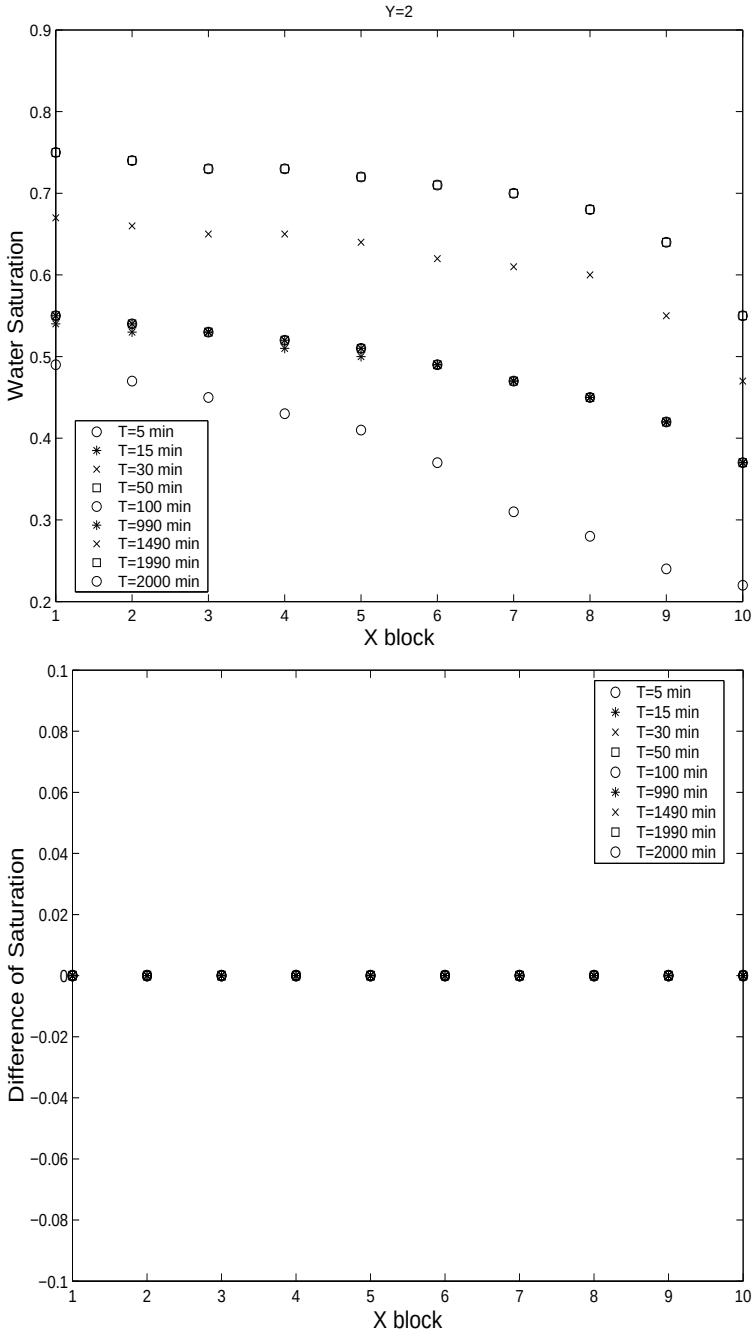

Fig. 10. Water Saturation Profiles for Both of 2-Dimensional Planes (top), the Saturation Difference between the 2-Dimensional Horizontal Plane and Vertical Plane (bottom)

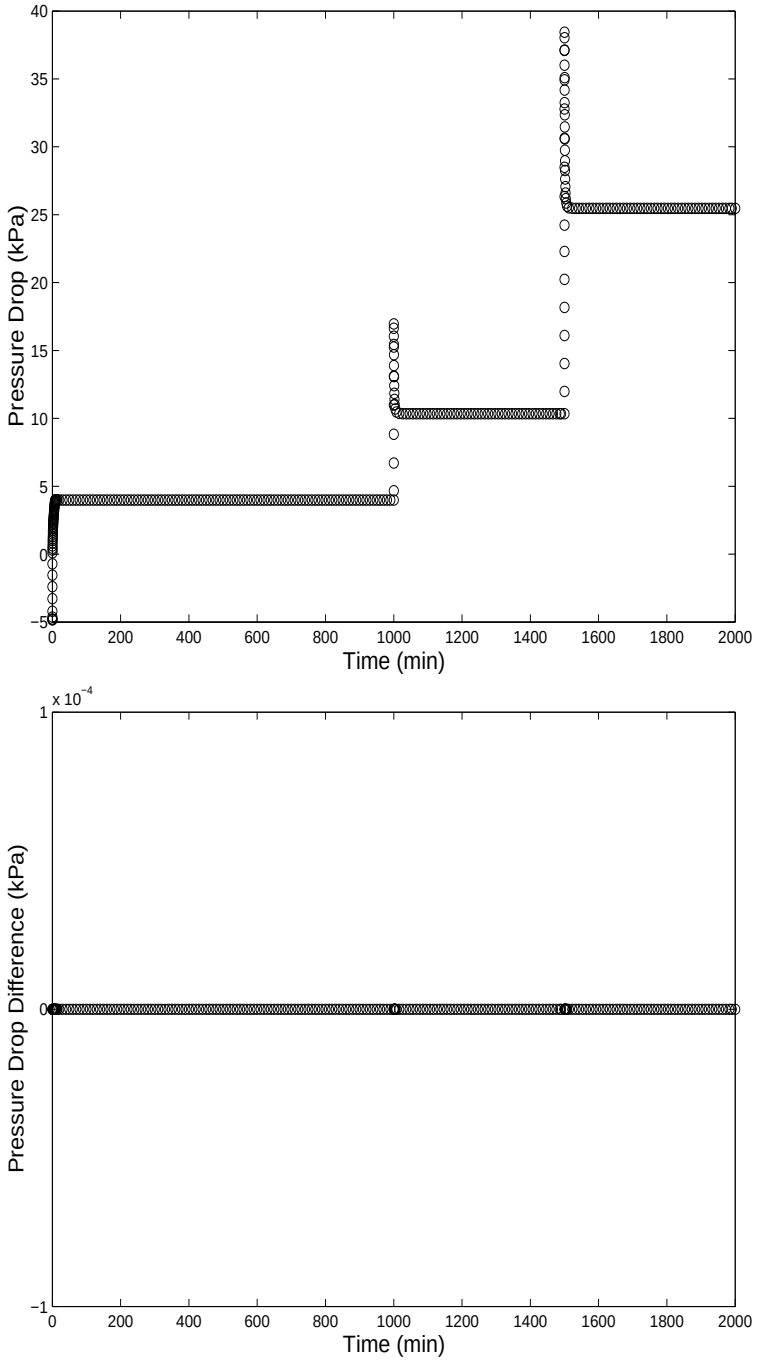

Fig. 11. Pressure Drop for the Two Planes (top), Pressure Drop Difference between the Two Planes (bottom)

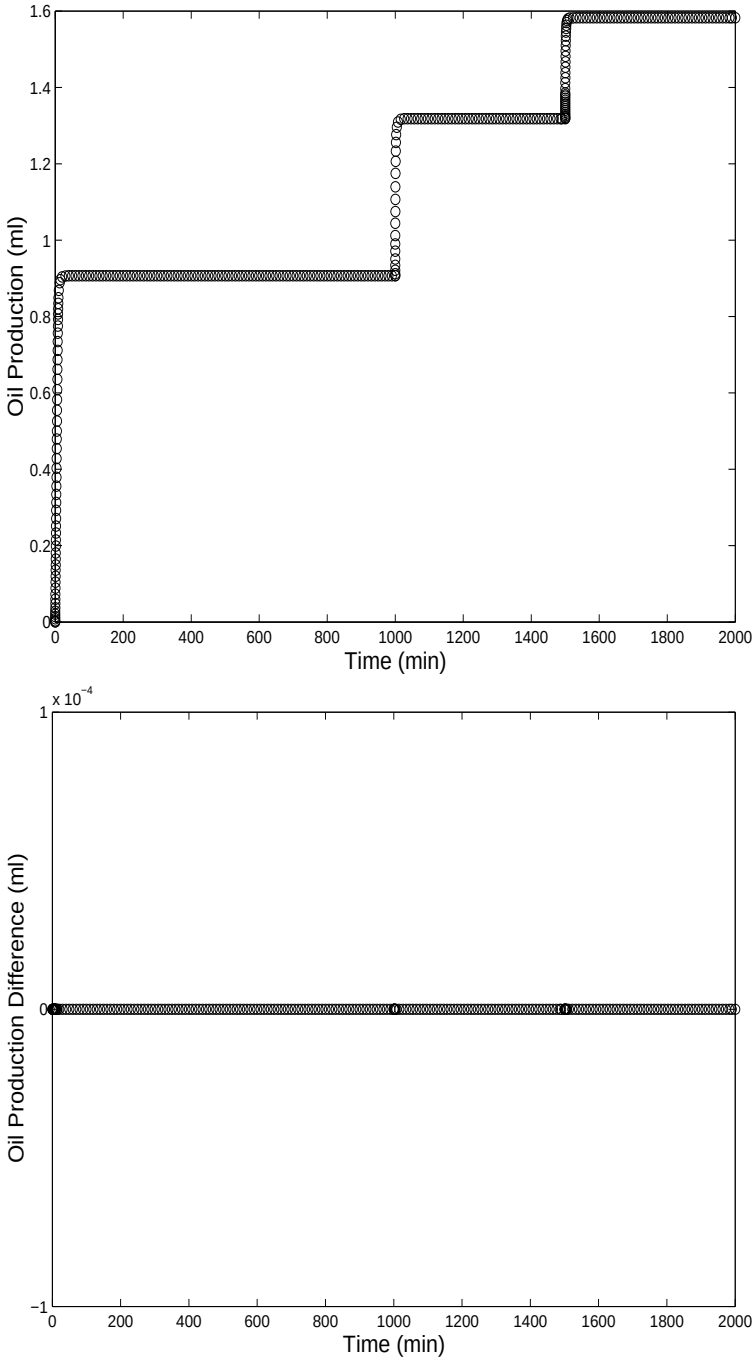

Fig. 12. Oil Production for the Two Planes (top), Oil Production Difference between the Two Planes (bottom)

1. Single-Rate Synthetic Experiment in Coarse Scale System

In the single rate synthetic experiment, water is injected at a constant flow rate into a core saturated with oil, and pressure drop and oil production data are generated by the simulator SENDRA. The whole core is divided into $2 \times 2 \times 2$ grid blocks. Each block is assigned a different absolute permeability and porosity value (see Table II). The relative permeabilities and capillary pressure are specified in terms of B-spline. The positions of knots and parameters of the B-spline are presented in Table III. The experimental conditions and properties of the fluids listed in Table IV are used in three-dimensional SENDRA to synthesize the pressure drop and production data.

These resulting synthetic data represent the true response which is noise free. Data actually used in the estimation are generated by adding random noise which is normally distributed with a mean of zero and a standard deviation based on the desired accuracy of the true response. We anticipate that 95% of the data lie between $\pm 0.5\%$ noise level. Here, the noise level is expressed as a percentage of the expected maximum magnitude of the data Y_{max}. The synthetic data, Y^{syn} is related to the exact data, Y^{exact}, as follows:

$$Y^{syn} = Y^{exact} + e. \tag{2.92}$$

The random variable e can be related to the standard normal distributed variable $\mathbf{X}$ by

$$e = \mathbf{X}\frac{\epsilon Y_{max}}{1.96}, \tag{2.93}$$

where $\epsilon = 0.5\%$. The details can be found in Appendix of Hollenshead's dissertation (Hollenshead, 2001).

Two scenarios are considered. One is based on heterogeneous assumption where the true absolute permeability and porosity distribution specified in the synthetic

Table II. Core Properties for Single-Rate Synthetic Experiment

Length(X-Direction) [mm]		60	
Height(Y-Direction) [mm]		40	
Width(Z-Direction) [mm]		40	
No. of Grid Blocks (X-Direction)		2	
No. of Grid Blocks (Y-Direction)		2	
No. of Grid Blocks (Z-Direction)		2	
Porosity [%]		X=1	X=2
Z=1	Y=1	0.18	0.22
Z=1	Y=2	0.23	0.28
Z=2	Y=1	0.15	0.24
Z=2	Y=2	0.20	0.28
Absolute Permeability[mD]		X=1	X=2
Z=1	Y=1	200	400
Z=1	Y=2	500	900
Z=2	Y=1	100	500
Z=2	Y=2	300	700

Table III. Multiphase Properties for the Single-Rate Synthetic Experiment

Water Relative Permeability	
Spline Order	3
Low Knot (S_w)	0.15
Interior Knots (S_w)	0.3, 0.5
High Knot (S_w)	0.8
Spline Parameters	0, 0.002, 0.01, 0.2, 0.6
Oil Relative Permeability	
Spline Order	3
Low Knot (S_w)	0.15
Interior Knots (S_w)	0.5, 0.7
High Knot (S_w)	0.8
Spline Parameters	1.0, 0.1, 0.001, 0.00004, 0.0
Capillary Pressure (KPa)	
Spline Order	3
Low Knot	0.15
Interior Knot	0.25, 0.4, 0.6, 0.7
High Knot	0.8
Spline Parameters	20, 0, -6, -9, -20, 80, -300

Table IV. Fluids Properties and Experimental Conditions for the Single-Rate Synthetic Experiment

Fluid Properties	
Oil Viscosity [cP]	1.121
Water Viscosity [cP]	1.11
Oil Density [kg/m^3]	750
Water Density [kg/m^3]	1000
Initial Conditions	
Pressure [KPa]	3500
Water Saturation [%]	0.15
Boundary Conditions	
Oil Injection Rates [ml/min]	0.0
Water Injection Rates [ml/min]	0.5

experiment as shown in Table II are used in the estimation. The other is a homogeneous system where a uniform absolute permeability and porosity are applied. An arithmetic mean is used for the porosity average. For absolute permeability, Cardwell (Carwell and Parsons, 1945) and Li (Li et al., 1999) had reported formulae to get the upper bound of the average permeability

$$K_{ave}^{+} = \frac{\Delta X}{\Delta Y \Delta Z \sum_{i=1}^{N_x} \frac{\Delta x_i}{\sum_{j=1}^{N_y} \sum_{k=1}^{N_z} \Delta y_j \Delta z_{i,j,k} K_{i,j,k}}} \tag{2.94}$$

and the lower bound of average permeability

$$K_{ave}^{-} = \frac{\Delta X}{\Delta Y \Delta Z} \sum_{j=1}^{N_y} \sum_{k=1}^{N_z} \frac{\Delta y_j}{\sum_{i=1}^{N_x} \frac{\Delta x_i}{\Delta z_{i,j,k} K_{i,j,k}}}. \tag{2.95}$$

The average permeability can be determined through an iteration procedure using the following formulae:

$$\begin{aligned}
K_{ave}^{-}(1) &= \sqrt{K_{ave}^{-} K_{ave}^{+}} \\
K_{ave}^{+}(1) &= \sqrt{K_{ave}^{-}(1) K_{ave}^{+}} \\
K_{ave}^{-}(i) &= \sqrt{K_{ave}^{-}(i-1) K_{ave}^{+}(i-1)}, i = 2, 3... \\
K_{ave}^{+}(i) &= \sqrt{K_{ave}^{-}(i) K_{ave}^{+}(i-1)}
\end{aligned}$$

Li et al. (Li et al., 1999) also indicated the third iteration is good enough for application purposes. The calculated uniform absolute permeability and porosity used in the second analysis scenario are provided in the Table V.

The methodology described in Section 3 is used to estimate the multiphase properties from the synthetic data. Starting with just one knot for B-spline representation of each flow function, successive parameter estimation problems are solved with increasing number of knots. The knot partition used in estimation is not necessarily the same as the knot partition used to define the true flow functions in the synthetic

Table V. Core Properties Used in Homogeneous System for the Single Rate Synthetic Experiment

Porosity [%]	0.22
Absolute Permeability[mD]	379.21

experiments. It is found that the performance index does not significantly decrease when more knots are added beyond representations with two interior knots each for the relative permeability and four interior knots for the capillary pressure representation. For the heterogeneous estimation scenario, the parameters and knot position used to represent flow functions chosen in the final step are provided in Table VI. Table VII gives the final representation of the flow functions for the homogeneous estimation scenario. The synthetic data with noise, the pressure drop and production data, along with the value simulated through three-dimensional SENDRA with the estimated multiphase properties from two scenarios, are shown in Figures 13 and 14. Figure 15 shows the plot of residuals for both heterogeneous and homogeneous cases. The sum of square residuals are provided in the figure. The saturation distributions determined from the heterogeneous estimation scenario are presented in Figure 16. The true flow functions, along with the estimated flow functions from the two scenarios are shown in Figures 17-18. The estimated flow functions from both scenarios with 95% confidence intervals are shown in Figures 19 and 20.

Although the production and pressure drop data calculated from SENDRA with the estimated multiphase properties from both scenarios show good consistency with the synthetic data in Figures 13-14 which may result from the coarse scale system used, the sum of square residuals which are provided in Figure 15 indicate that the heterogeneous scenario gives better matching than the homogeneous scenario. On the

Table VI. Estimated Multiphase Properties from the Single-Rate Synthetic Experiment (Heterogeneous)

Water Relative Permeability	
Spline Order	3
Low Knot (S_w)	0.15
Interior Knots (S_w)	0.3, 0.5, 0.7
High Knot (S_w)	0.8
Spline Parameters	0, 0.27e-4, 0.16e-1, 0.17e+0, 0.24e+0, 0.78e+0
Oil Relative Permeability	
Spline Order	3
Low Knot (S_w)	0.15
Interior Knots (S_w)	0.5, 0.7
High Knot (S_w)	0.8
Spline Parameters	0.24e+0, 0.19e-1, 0.53e-22, 0.53e-22, 0.0
Capillary Pressure (KPa)	
Spline Order	3
Low Knot	0.15
Interior Knot	0.25, 0.4, 0.6, 0.7
High Knot	0.8
Spline Parameters	0.20e+2, 0.12e+1, -0.26e+1
	-0.26e+1, -0.11e+3, -0.15e+3, -0.30e+3

Table VII. Estimated Multiphase Properties from the Single-Rate Synthetic Experiment (Homogeneous)

Water Relative Permeability	
Spline Order	3
Low Knot (S_w)	0.15
Interior Knots (S_w)	0.3, 0.7
High Knot (S_w)	0.8
Spline Parameters	0, 0.83e-18, 0.19e-1, 0.24e+0, 0.25e+0
Oil Relative Permeability	
Spline Order	3
Low Knot (S_w)	0.15
Interior Knots (S_w)	0.5, 0.7
High Knot (S_w)	0.8
Spline Parameters	0.80e+0, 0.43e-1, 0.43e-1, 0.22e-19, 0.0
Capillary Pressure (KPa)	
Spline Order	3
Low Knot	0.15
Interior Knot	0.25, 0.4, 0.6, 0.7
High Knot	0.8
Spline Parameters	0.20e+2, 0.63e+0, -0.71e+1
	-0.99e+1, -0.28e+2, -0.80e+2, -0.30e+3

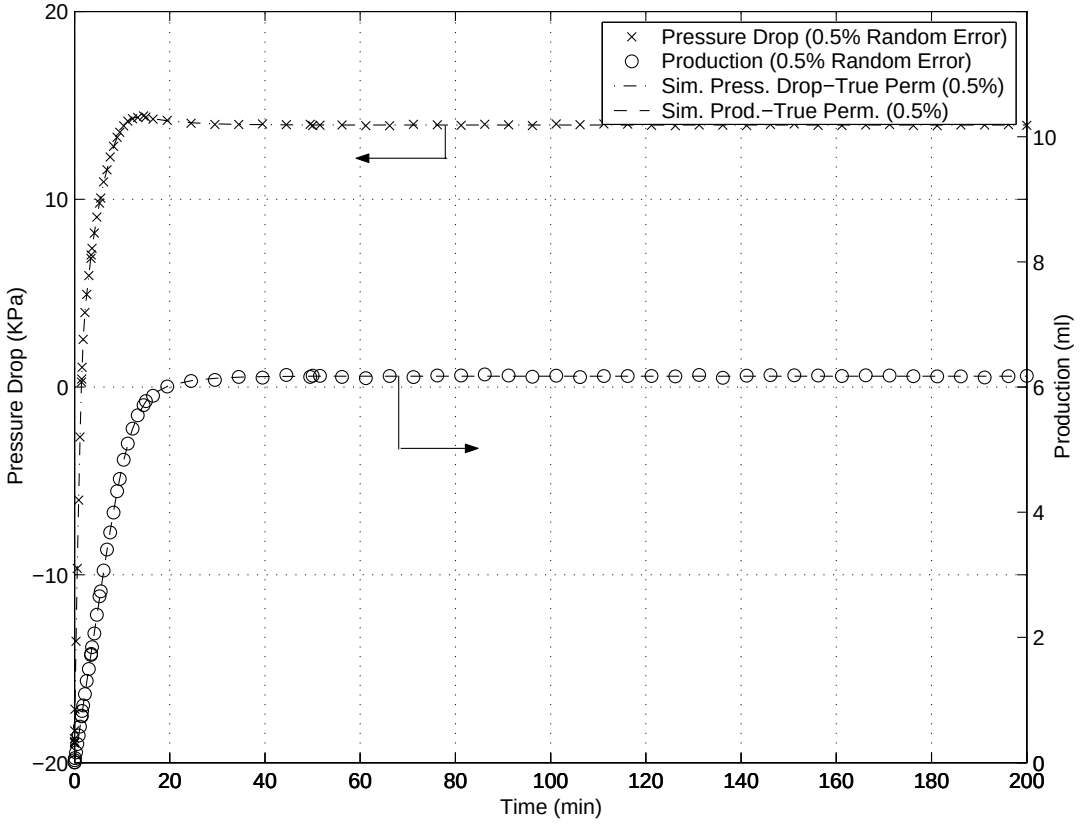

Fig. 13. Simulated and Synthetic Data in Single-Rate Experiments in Coarse Scale System (Heterogeneous)

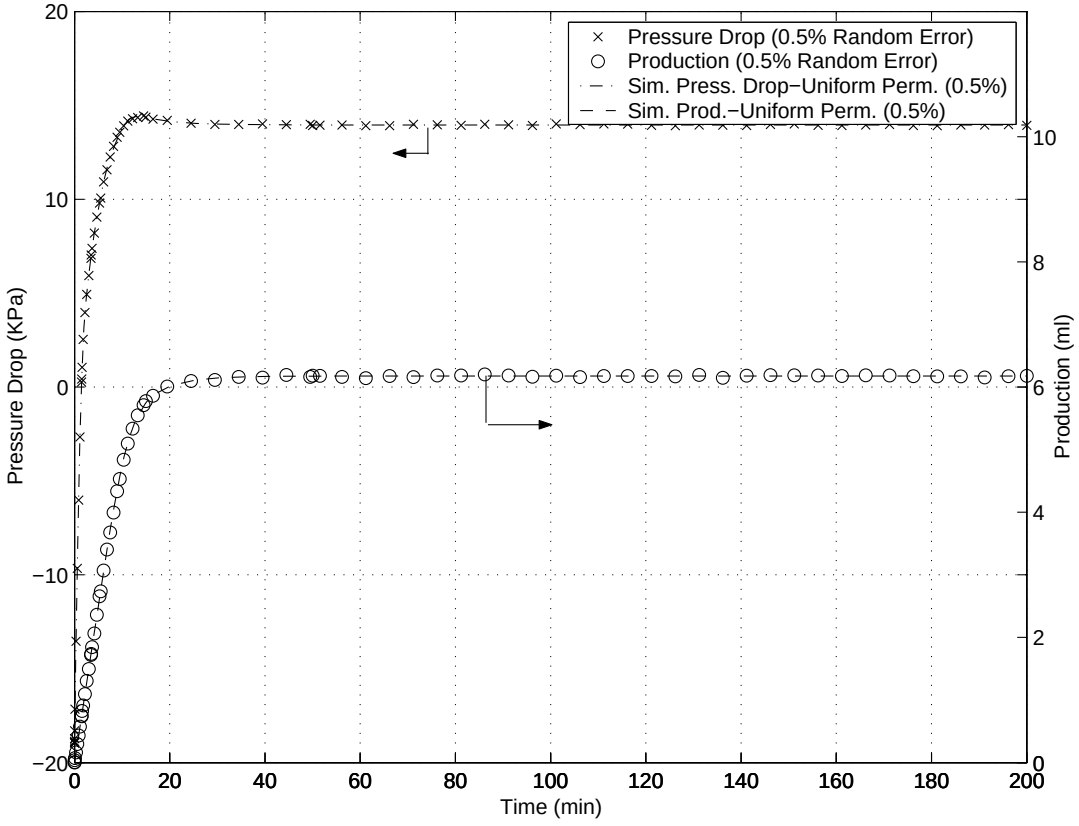

Fig. 14. Simulated and Synthetic Data in Single-Rate Experiments in Coarse Scale System (Homogeneous)

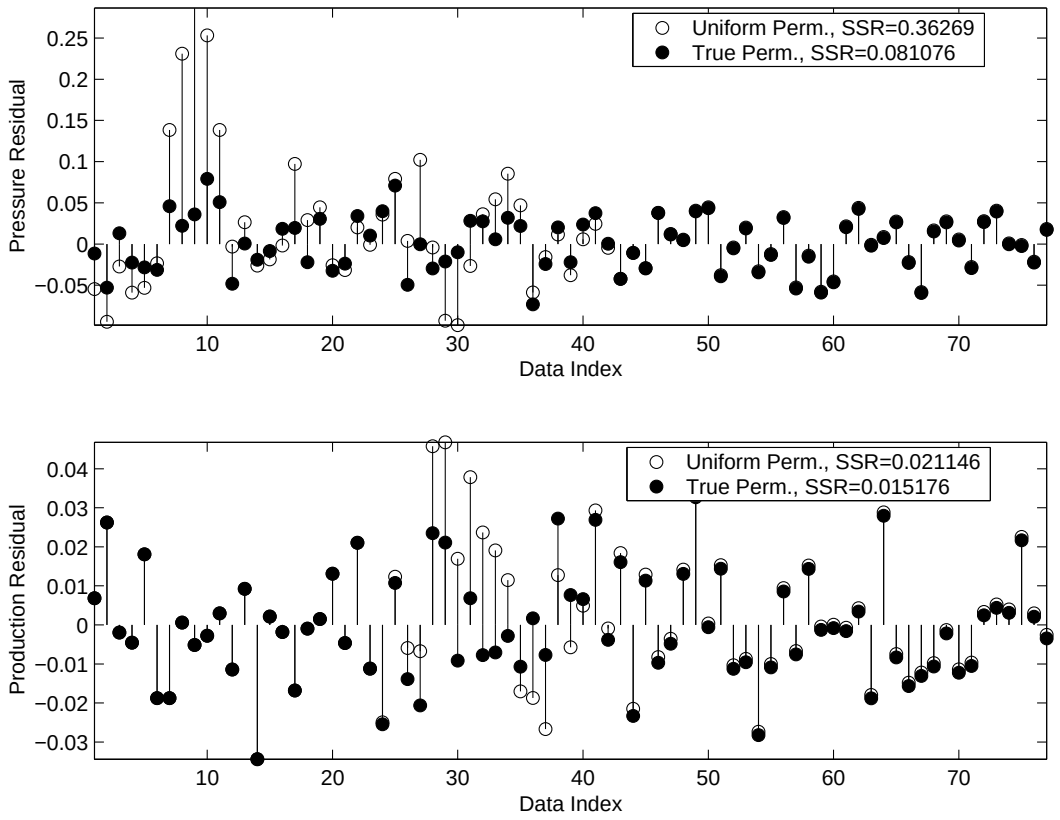

Fig. 15. Residual Plot Corresponding to Final Estimates for Single-Rate Experiments

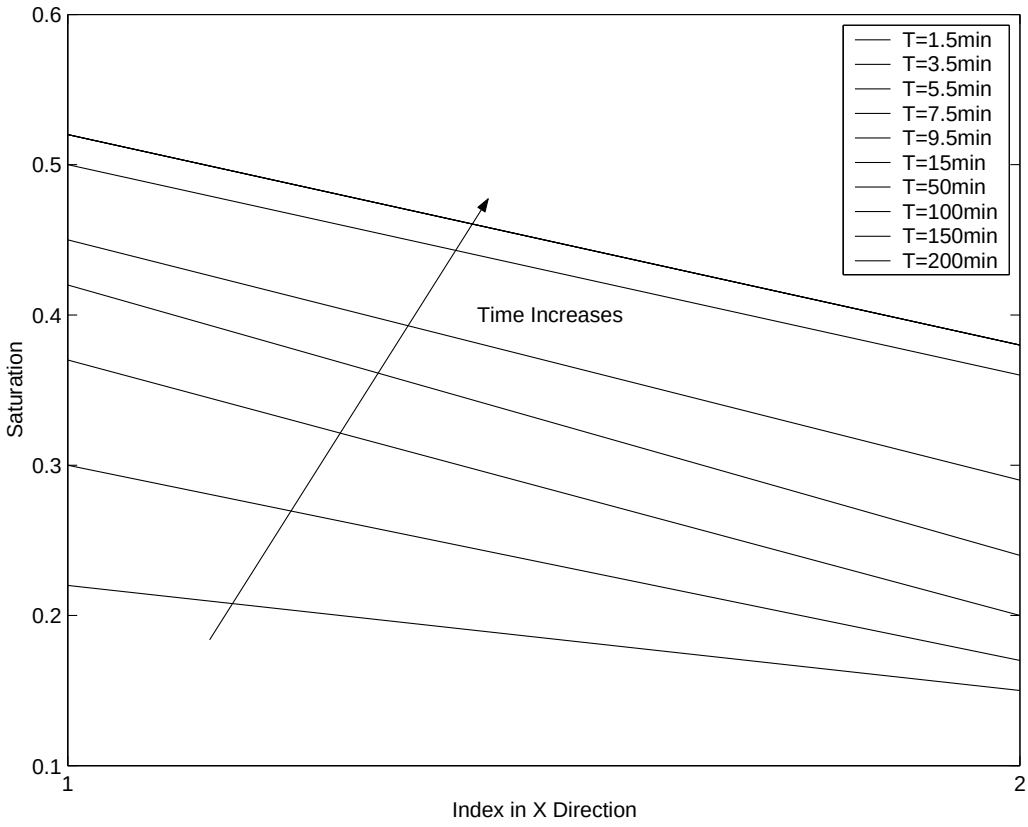

Fig. 16. Simulated Water Saturation Profiles in Single-Rate Experiments in Coarse Scale System at Slice Y=1 and Z=1 (Heterogeneous)

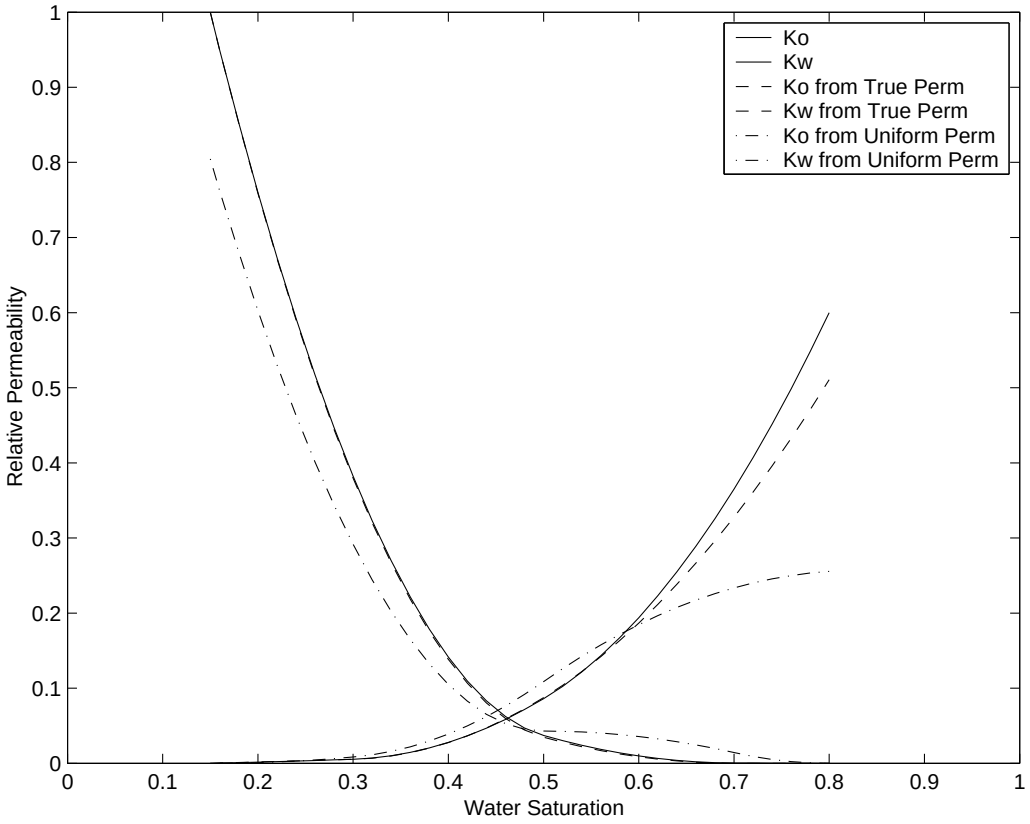

Fig. 17. True and Estimated Relative Permeabilities from Single-Rate Experiments in Coarse Scale System

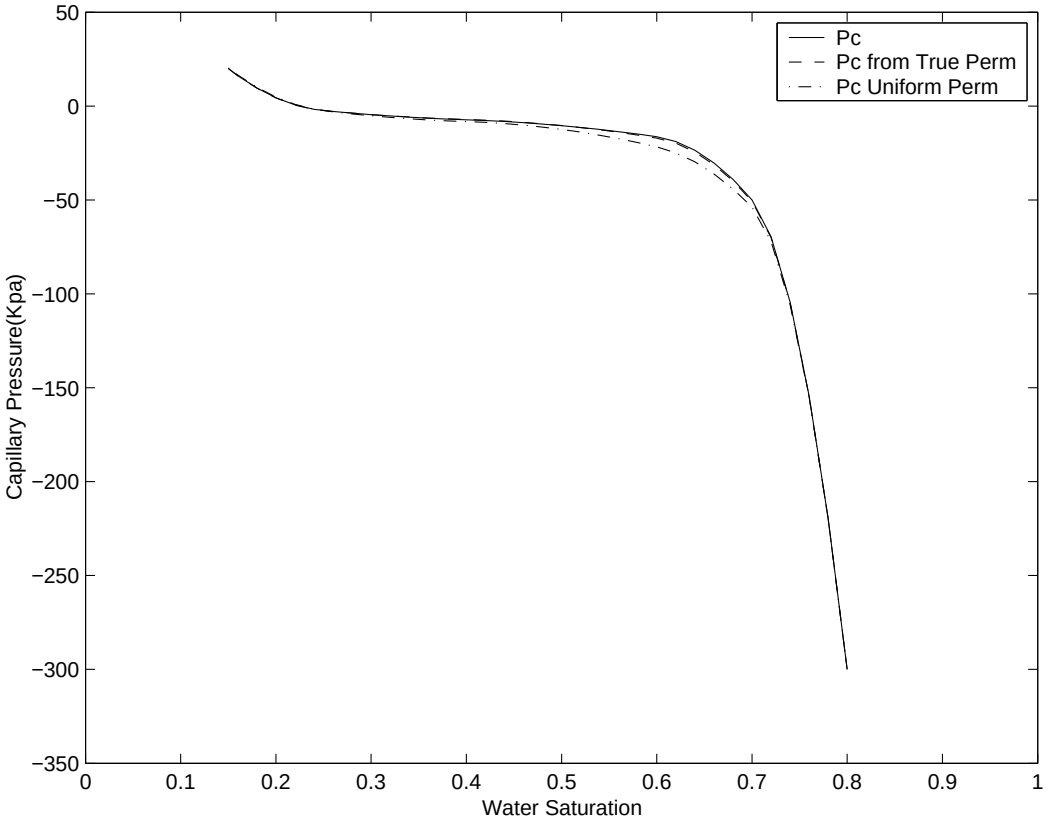

Fig. 18. True and Estimated Capillary Pressure from Single-Rate Experiments in Coarse Scale System

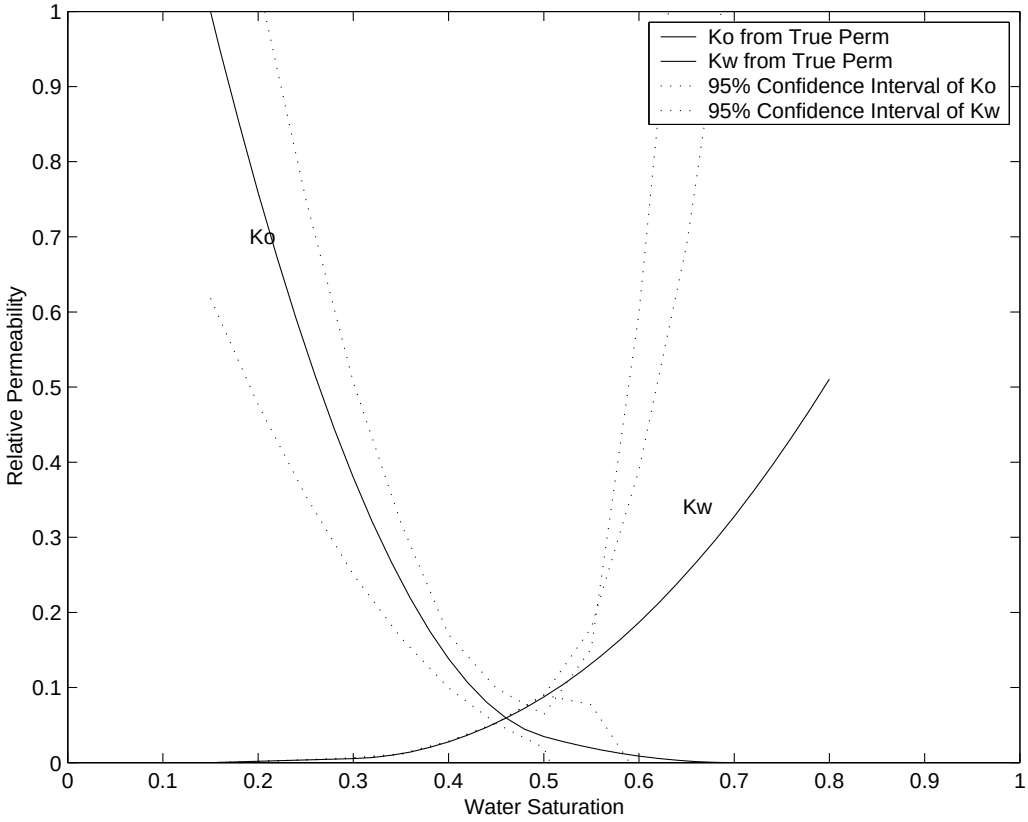

Fig. 19. Estimated Relative Permeabilities and 95% Confidence Intervals from Single-Rate Experiments in Coarse Scale System (Heterogeneous)

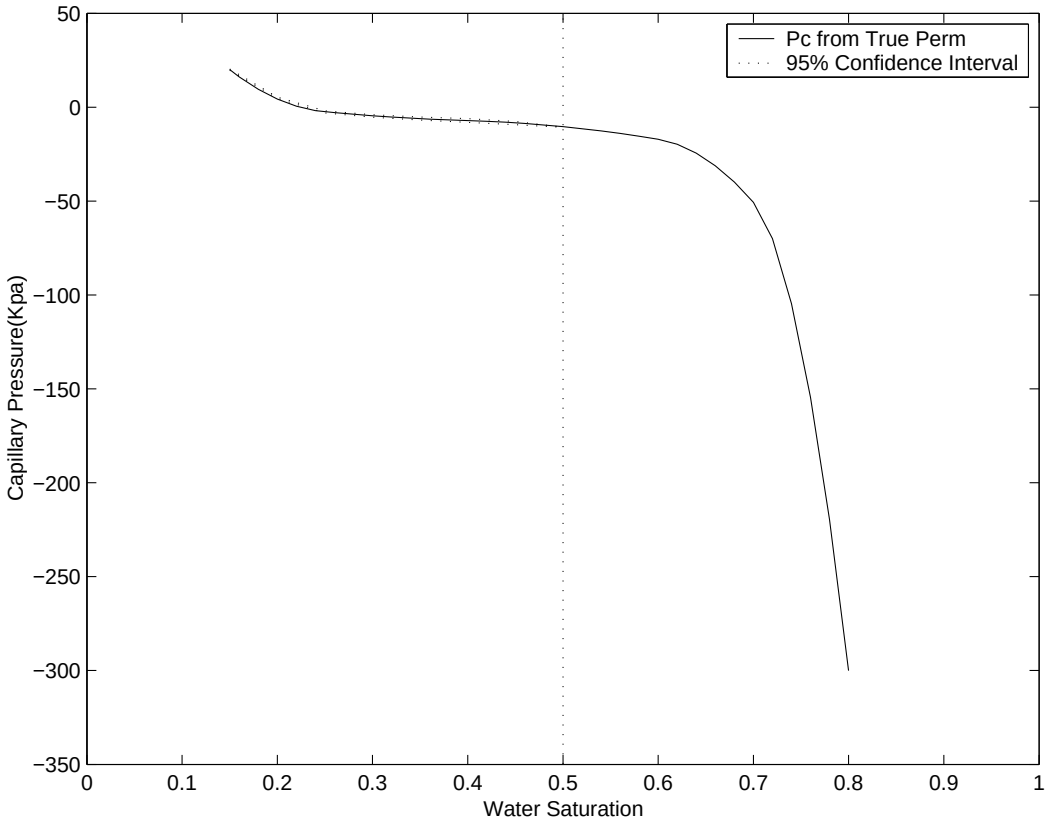

Fig. 20. Estimated Capillary Pressure and 95% Confidence Intervals from Single-Rate Experiments in Coarse Scale System (Heterogeneous)

other hand, the estimated multiphase properties from the two scenarios show different levels of agreement with the true properties. The estimated properties from the heterogeneous scenario by using the true absolute permeability and porosity show a better consistency with the true ones. The relative permeabilities from the heterogeneous scenario almost completely overlap the true curve except for the saturation range beyond 0.6. The curve from the homogenous scenario shows differences with the true curve over the whole range of the saturation. The capillary pressure curve from the heterogeneous case is closer to the true curve than the one from the homogeneous case. As we expected, both of the curves, the relative permeabilities and capillary pressure, indicate that using the true rock properties will give more reliable determination of the flow functions.

The confidence intervals are computed with a linearized covariance analysis (Petec Software & Services, 2000). The size of confidence regions indicates the relative sensitivity of the estimated functions to the specified level of measurement error and is related to the relative degree of information that is available for the estimation region (Kulkarni et al., 1998). For the single-rate experiment, a maximum water saturation of 0.5 as shown in Figure 16 is reached at the end of the experiment. Consequently, the flow function cannot be reliably estimated for water saturation greater than that value. The Figures 19 and 20 show an increase of the confidence interval when the saturation exceeds 0.5. It appears that the relative permeabilities and capillary pressure cannot be determined accurately in the higher wetting saturation region from the single-rate experiment data because of the lack of information. In order to get more information in the higher water saturation region, two-rate synthetic experiment is performed.

2. Two-Rate Synthetic Experiment in Coarse Scale System

A two-rate synthetic experiment is performed. The core properties and fluid properties are exactly the same as the properties used in the single-rate synthetic experiment. The experimental conditions are the same as for the single-rate experiment except that two water injection rates are used. Table VIII provides the details. The pressure drop and the oil production data are generated by the simulator SENDRA. 0.5% noise is added into the resulting data as has been described for the single-rate synthetic experiment. The estimation of the flow functions is determined from synthetic data for both, homogeneous and heterogeneous estimation scenarios. The analysis procedure is conducted in the same way as the previous experiment. Starting with just one knot for B-spline representation of each flow function, successive parameter estimation problems are solved with increasing number of knots. It is found that the performance index does not significantly decrease when more knots are added beyond representations with three interior knots each for the relative permeability and four interior knots for the capillary pressure representation. For the heterogeneous estimation scenario, the parameters and knot position used to represent flow functions chosen in the final step are provided in Table IX. Table X gives the final representation of the flow functions for the homogeneous estimation scenario.

Figure 21 gives the saturation distribution at slice Y=1 and Z=1. The observed time is indicated in the figure. It can be found that a maximum water saturation of 0.6 is achieved at the end of the experiment. The simulated and synthetic pressure drop and production data from both scenarios are shown in Figures 22 and 23. Again, there is excellent agreement between simulated and synthetic data for both scenarios. However, the residual plot shown in Figure 24 indicates that the heterogeneous scenario gives better matching than the homogeneous scenario. The true flow

Table VIII. Experiment Conditions for the Two-Rate Synthetic Experiment

Oil Injection Rates [ml/min]	0.0, 0
Water Injection Rates [ml/min]	0.5, 3
Injection Time [min]	0, 250

functions, along with the estimated flow functions from the two scenarios are shown in Figures 25-26.

The estimated flow functions from heterogeneous system show better agreement with the true functions than the results from the homogeneous do. Both the relative permeabilities and capillary pressure curves from the heterogeneous scenario is closer to the true curves than the ones from the homogeneous scenario. The estimated flow function from heterogeneous scenario with 95% confidence intervals are shown in Figures 27 and 28. The confidence intervals indicate that the relative permeabilities and capillary pressure are accurately estimated over most range of saturation below 0.6. This misfit above 0.6 explained by 0.6 being the maximum saturation obtained by this experiment and there is no information obtained beyond this value. It is apparent that the flow function cannot be reliably estimated when saturation exceeds 0.6. Compared with the results from the single-rate experiment (Figure 19 vs Figure 27), the confidence interval is narrower in the two-rate experiment and a larger range of information is obtained. It is obvious that the two-rate experiment can provide more reliable determination of the flow functions over a broader saturation range than the single-rate experiment does. Next, we will perform a single-rate experiment in a relative fine scale system to show the effect of the block size on the determination of flow functions.

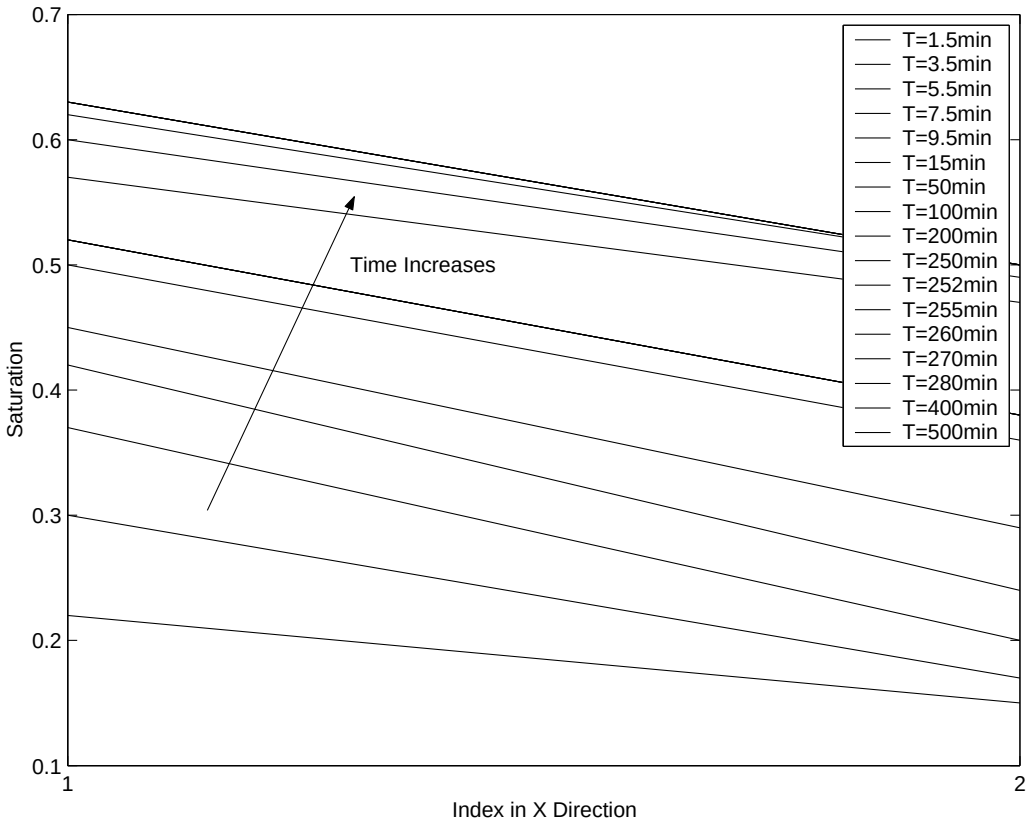

Fig. 21. Simulated Water Saturation Profiles in Two-Rate Experiments at Slice Y=1 and Z=1 (Heterogeneous)

Table IX. Estimated Multiphase Properties from the Two-Rate Synthetic Experiment (Heterogeneous)

Water Relative Permeability	
Spline Order	3
Low Knot (S_w)	0.15
Interior Knots (S_w)	0.3, 0.5, 0.7
High Knot (S_w)	0.8
Spline Parameters	0, 0.59e-3, 0.99e-2, 0.16e+0, 0.46e+0, 0.56e+0
Oil Relative Permeability	
Spline Order	3
Low Knot (S_w)	0.15
Interior Knots (S_w)	0.5, 0.6, 0.7
High Knot (S_w)	0.8
Spline Parameters	0.91e+0, 0.11e-0, 0.20e-1, 0.30e-37, 0.30e-37, 0.0
Capillary Pressure (KPa)	
Spline Order	3
Low Knot	0.15
Interior Knot	0.25, 0.4, 0.6, 0.7
High Knot	0.8
Spline Parameters	0.20e+2, 0.23e+0, -0.56e+1
	-0.97e+1, -0.19e+2, -0.86e+2, -0.46e+3

Table X. Estimated Multiphase Properties from the Two-Rate Synthetic Experiment (Homogeneous)

Water Relative Permeability	
Spline Order	3
Low Knot (S_w)	0.15
Interior Knots (S_w)	0.3, 0.5
High Knot (S_w)	0.8
Spline Parameters	0, 0.18e-2, 0.15e-1, 0.25e+0, 0.67e+0
Oil Relative Permeability	
Spline Order	3
Low Knot (S_w)	0.15
Interior Knots (S_w)	0.5, 0.7
High Knot (S_w)	0.8
Spline Parameters	0.52e+0, 0.99e-1, 0.63e-32, 0.31e-33, 0.0
Capillary Pressure (KPa)	
Spline Order	3
Low Knot	0.15
Interior Knot	0.25, 0.4, 0.6, 0.7
High Knot	0.8
Spline Parameters	0.21e+2, 0.11e+1, -0.62e+1
	-0.10e+2, -0.29e+2, -0.93e+2, -0.50e+3

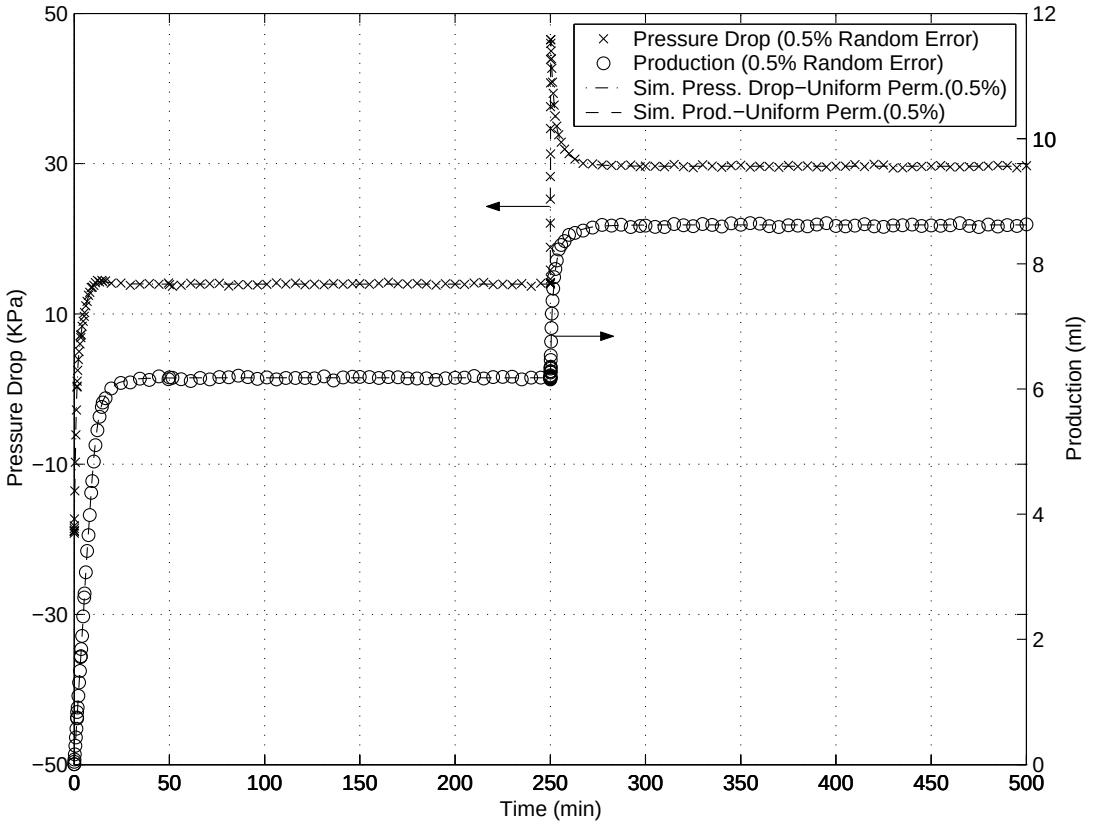

Fig. 22. Simulated and Synthetic Data in Two-Rate Experiments (Homogeneous)

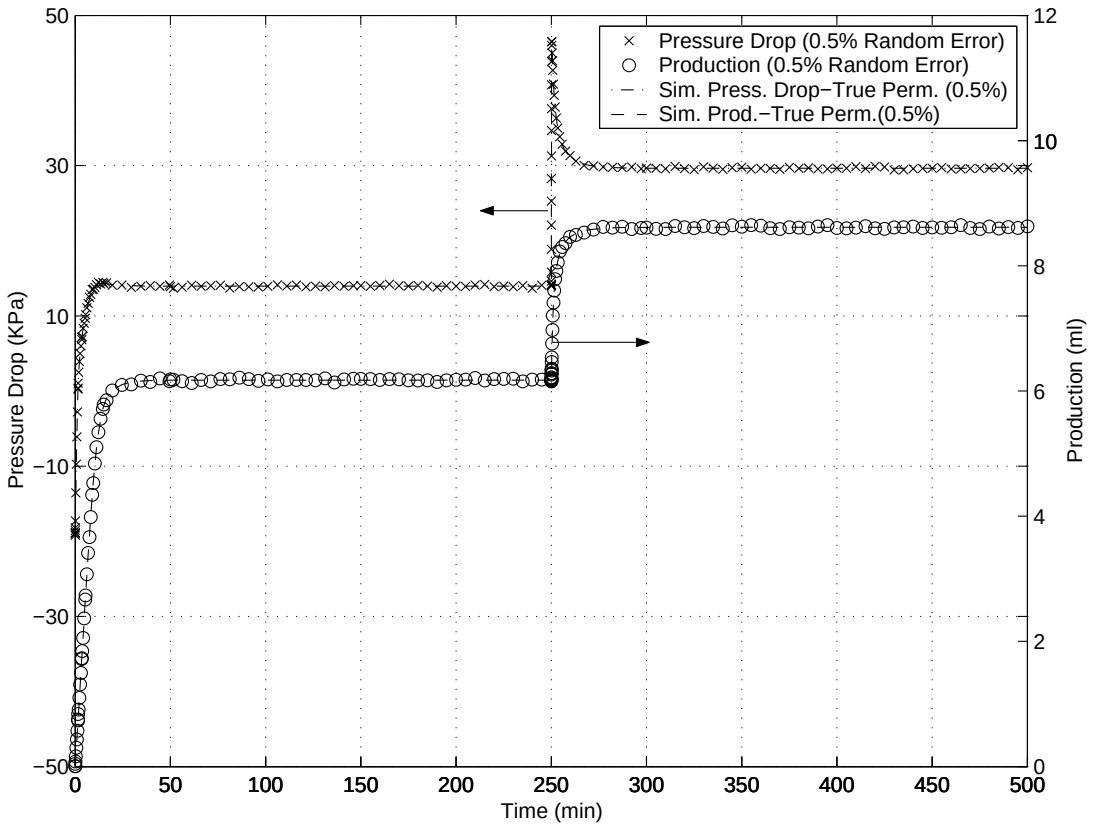

Fig. 23. Simulated and Synthetic Data in Two-Rate Experiments (Heterogeneous)

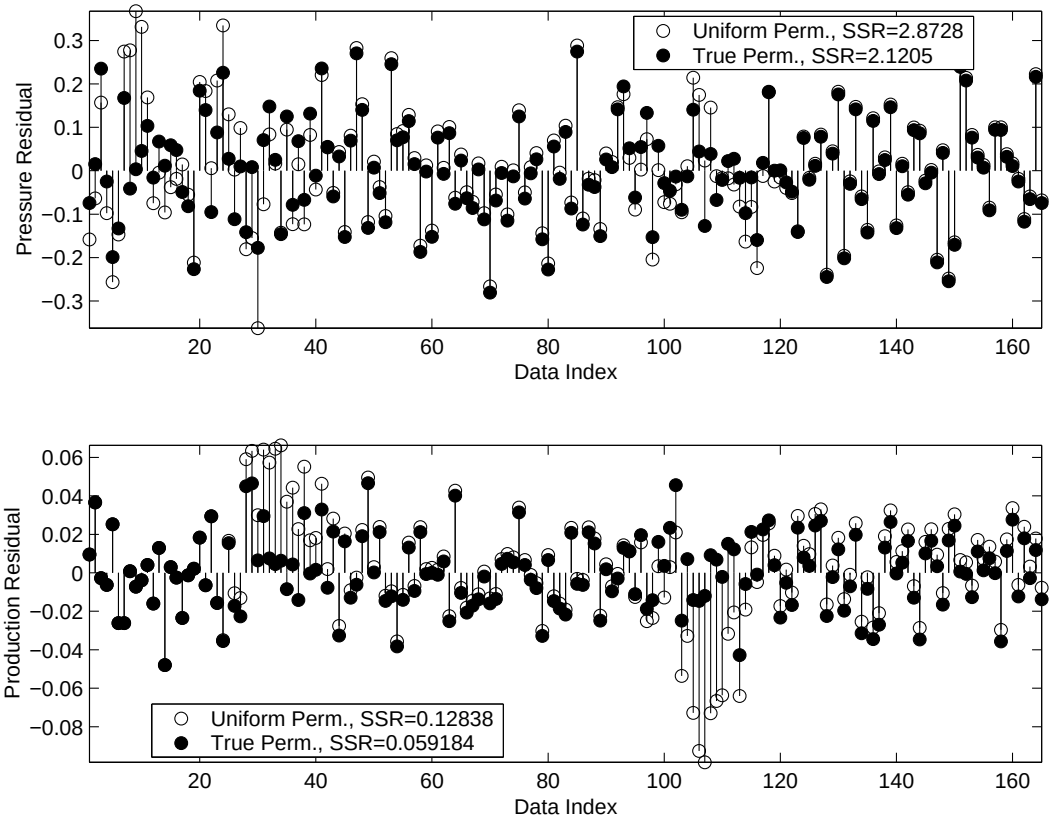

Fig. 24. Residual Plot Corresponding to Final Estimates for Two-Rate Experiments

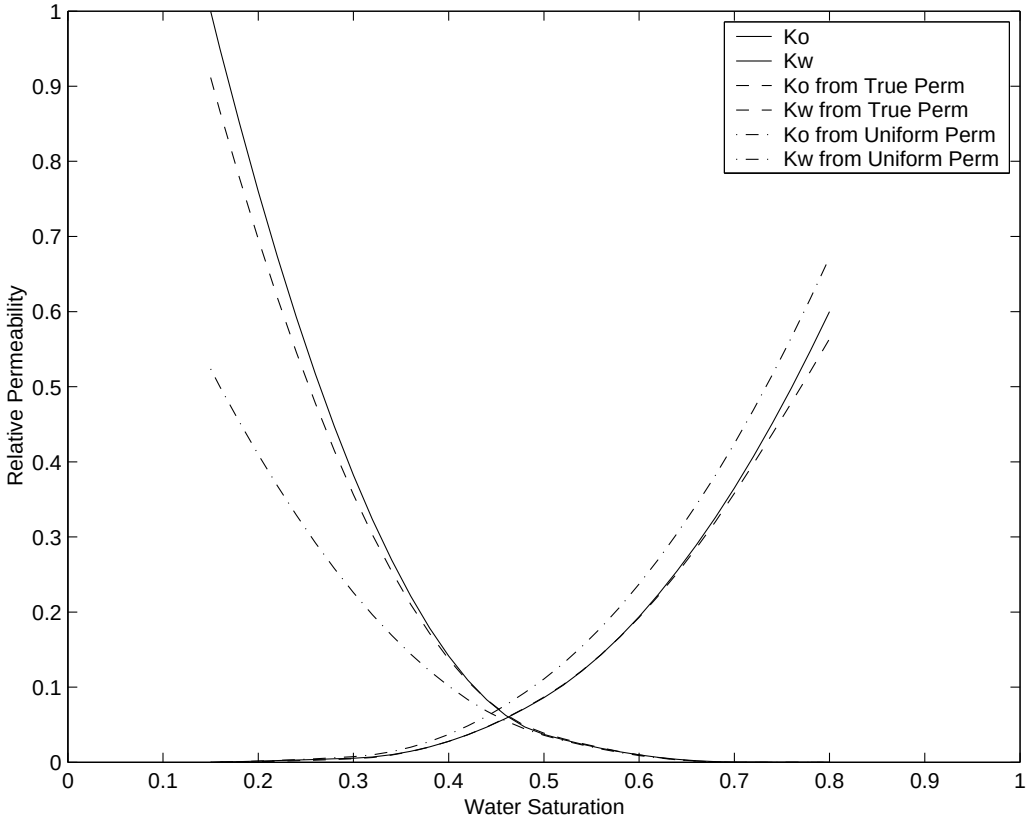

Fig. 25. True and Estimated Relative Permeabilities from Two-Rate Experiments

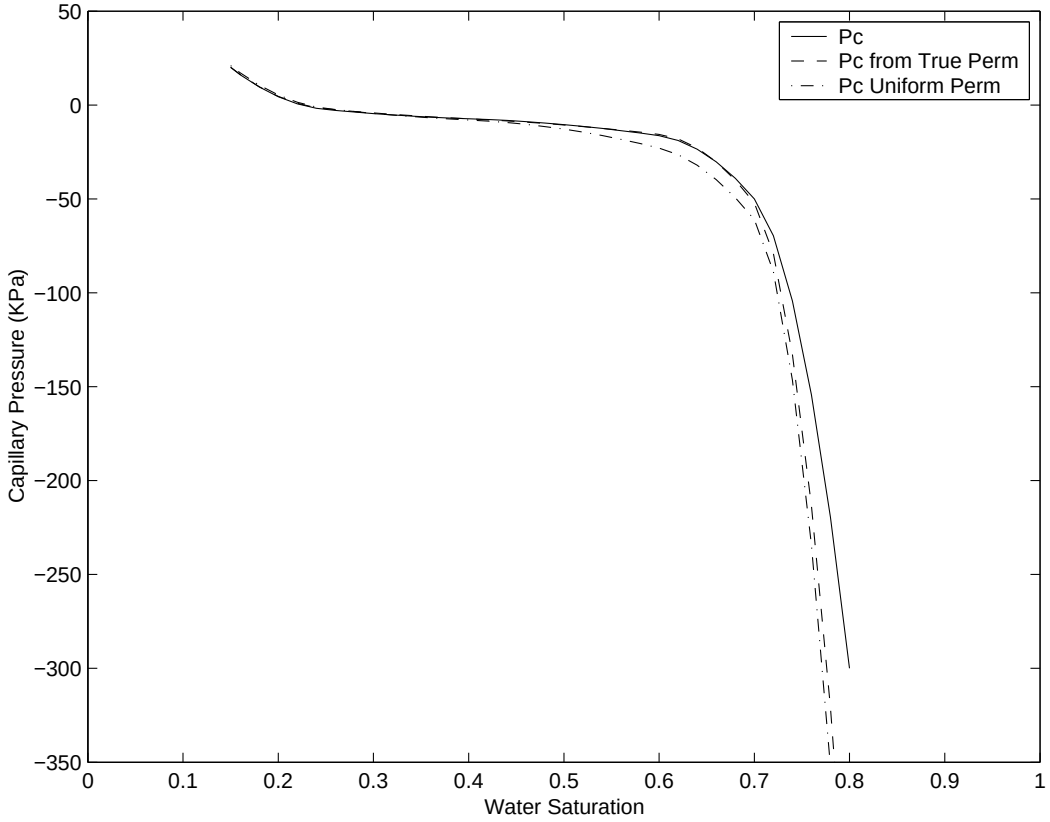

Fig. 26. True and Estimated Capillary Pressure from Two-Rate Experiments

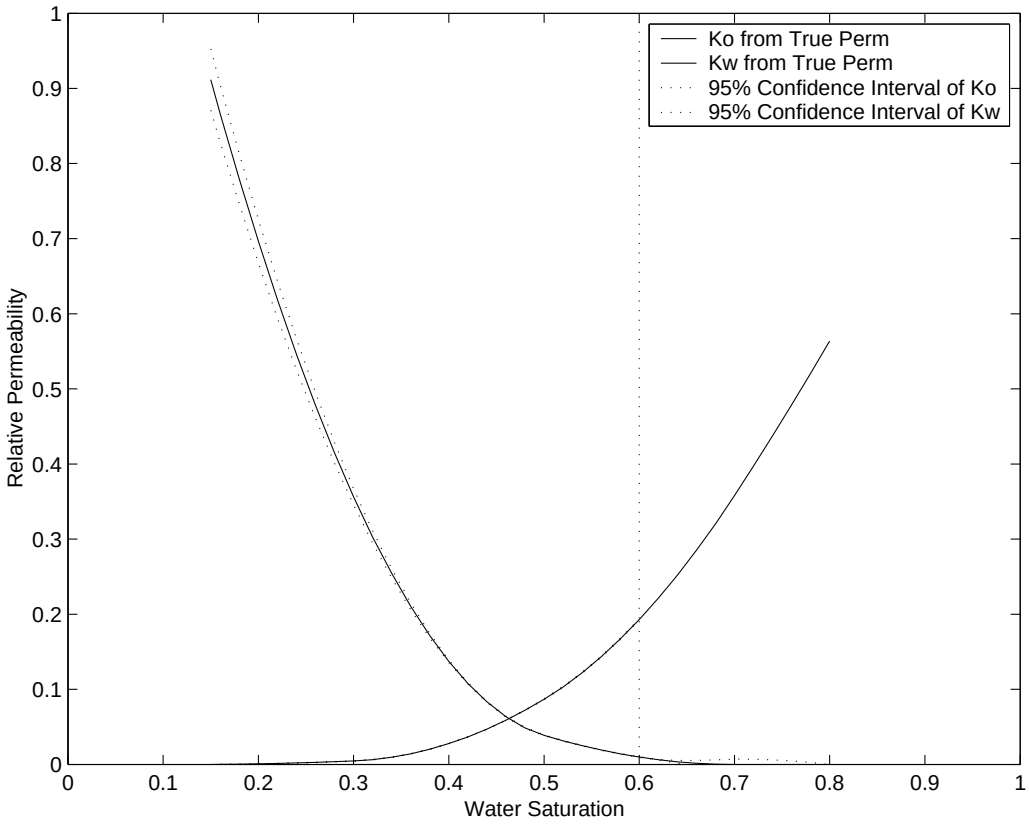

Fig. 27. Estimated Relative Permeabilities and 95% Confidence Intervals from Two-Rate Experiments (Heterogeneous)

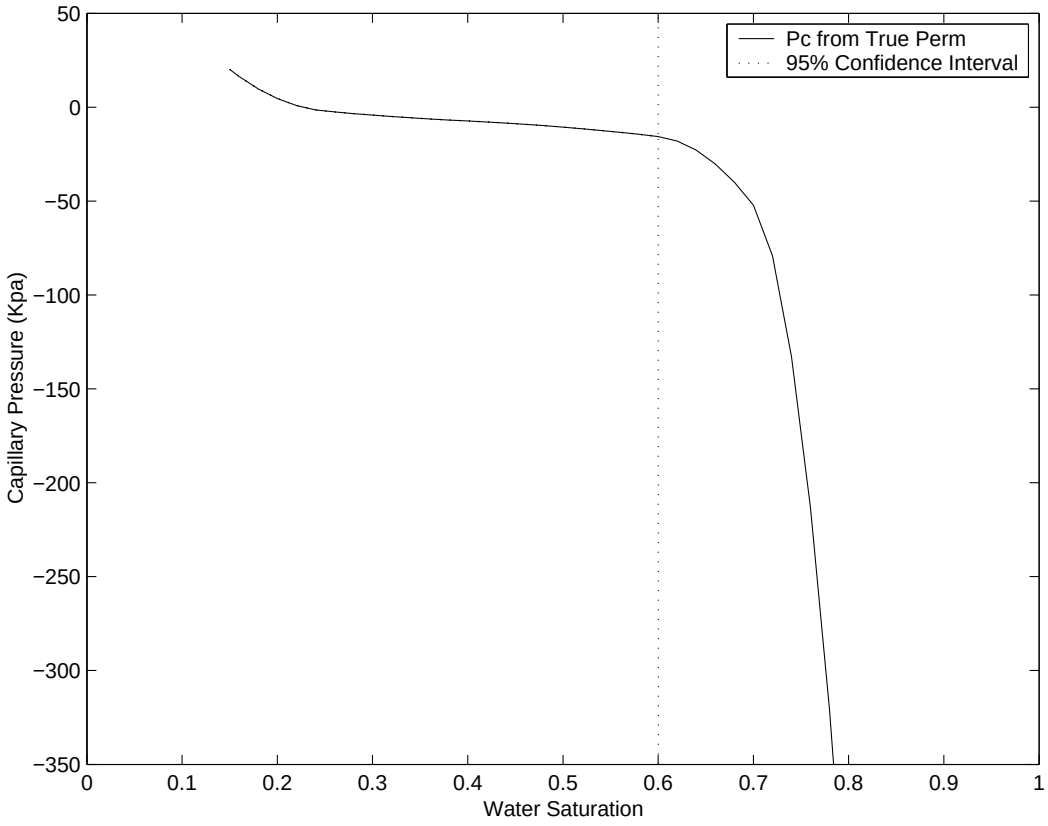

Fig. 28. Estimated Capillary Pressure and 95% Confidence Intervals from Two-Rate Experiments (Heterogeneous)

3. Single-Rate Synthetic Experiment in Relative Fine Scale System

A single rate synthetic experiment is performed in a core sample which is divided into $10 \times 5 \times 3$ grid blocks. The resolution of this system is still very rough and it is a comprise between computing time and the objective of investigation. The objective of the synthetic experiment is to show the improvement of the accuracy of determination of flow functions with consideration of sample heterogeneities and this resolution is able to show the effect. Each block is assigned a different absolute permeability and porosity value. The porosity distribution is randomly generated by computer with mean 0.15 and standard deviation 0.02. The absolute permeability is also randomly generated with mean 400 mD and standard deviation 200. The Figures 29 and 30 give the contour plots of the permeability and porosity distribution on different slices. The actual value of the permeability and porosity can be found in the color bar below the plots. Table XI provides more details. The average porosity and permeability is calculated through the method indicated in Subsection 1 of this section. The determined results are presented in Table XII. The fluid properties, multiphase properties and experimental conditions are exactly the same as provided in Subsection 1 of this section. Figures 31 and 32 show the simulated saturation distribution at slice Z=2 at time 1.5 minutes and 45 minutes. A maximum water saturation of 0.7 is observed at the end of experiment. 0.5% noise is added to the resulting data. The estimation of the flow functions is determined from synthetic data from both homogeneous and heterogeneous estimation scenarios. The parameters of determined flow functions are provided in the Tables XIII and XIV.

The simulated and synthetic pressure drop and oil production data from both homogeneous and heterogeneous system are shown in Figures 33 and 34. There are excellent agreements again between simulated and synthetic data for both scenarios

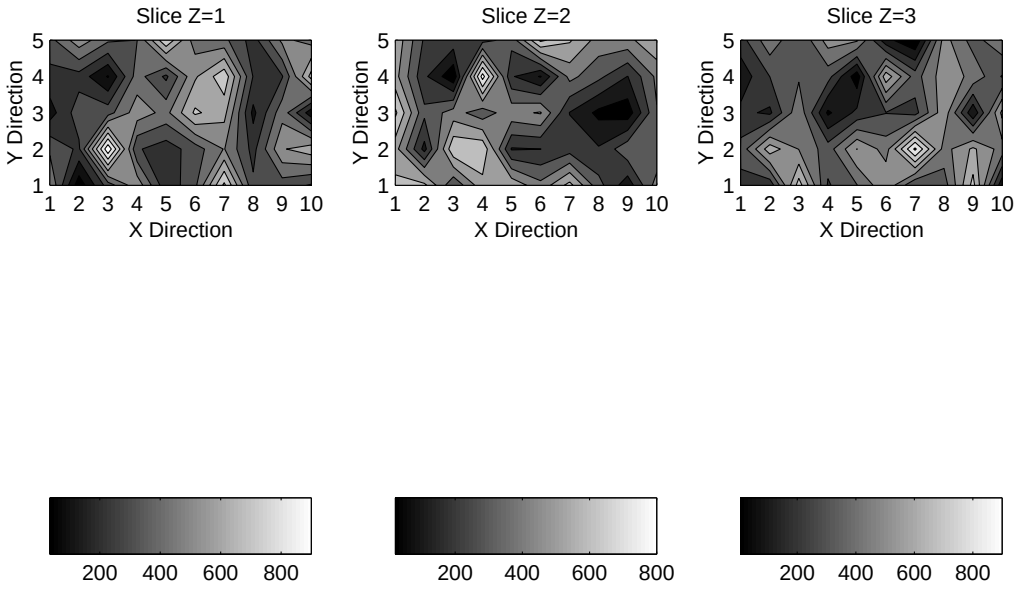

Fig. 29. Synthetic Permeability Distribution in Relative Fine Scale System (Heterogeneous)

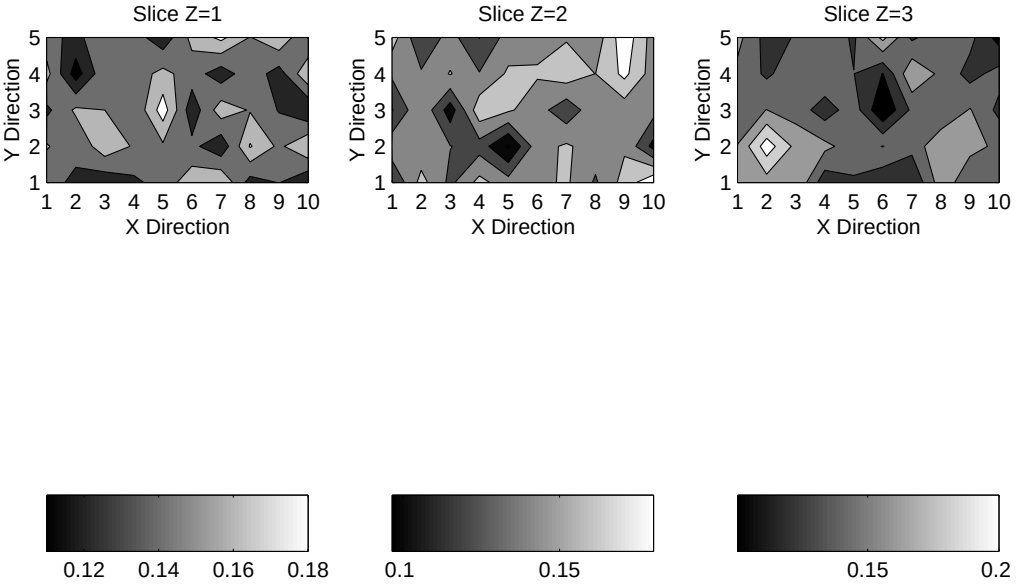

Fig. 30. Synthetic Porosity Distribution in Relative Fine Scale System (Heterogeneous)

Table XI. Core Properties for Single-Rate Synthetic Experiment in Relative Fine Scale System

Length(X-Direction) [mm]	50
Height(Y-Direction) [mm]	20
Width(Z-Direction) [mm]	24
No. of Grid Blocks (X-Direction)	10
No. of Grid Blocks (Y-Direction)	5
No. of Grid Blocks (Z-Direction)	3

Table XII. Core Properties Used in Homogeneous System for the Single Rate Synthetic Experiment in Relative Fine Scale System

Porosity [%]	0.15
Absolute Permeability[mD]	351.45

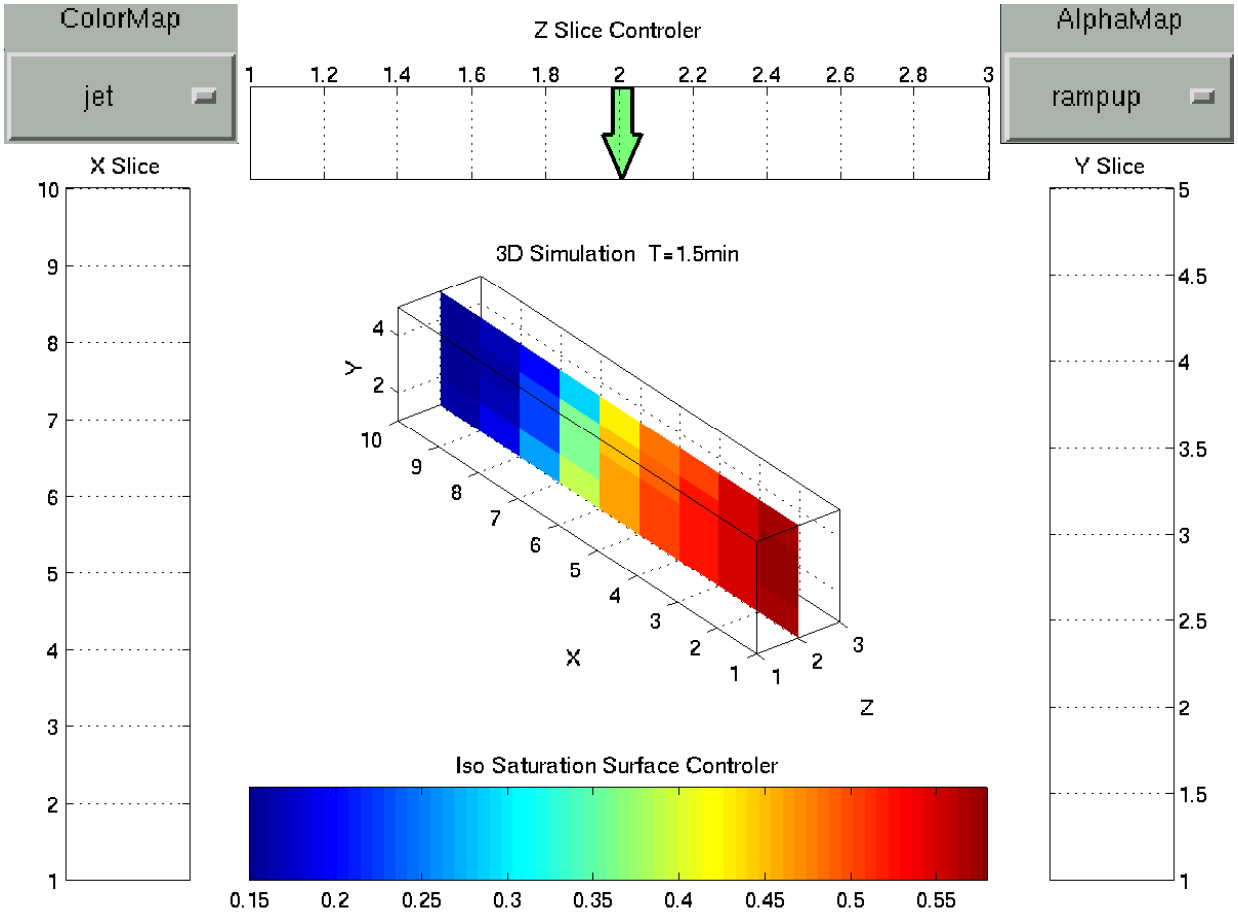

Fig. 31. Simulated Water Saturation Profiles in Relative Fine Scale System at Time=1.5 min (Heterogeneous)

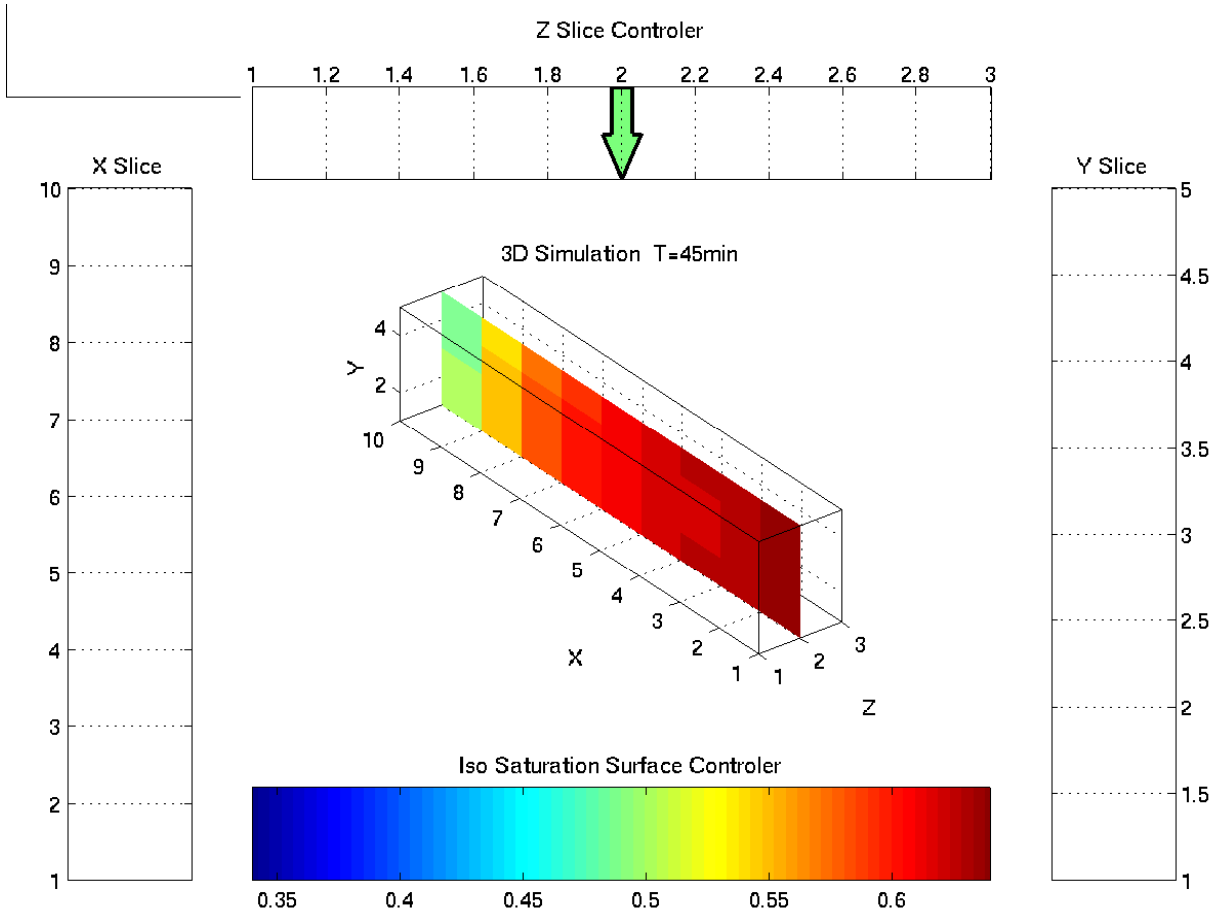

Fig. 32. Simulated Water Saturation Profiles in Relative Fine Scale System at Time=45 min (Heterogeneous)

Table XIII. Estimated Multiphase Properties from the Relative Fine Scale System (Heterogeneous)

Water Relative Permeability	
Spline Order	3
Low Knot (S_w)	0.15
Interior Knots (S_w)	0.3, 0.5, 0.7
High Knot (S_w)	0.8
Spline Parameters	0, 0.85e-3, 0.78e-2, 0.17e+0, 0.45e+0, 0.58e+0
Oil Relative Permeability	
Spline Order	3
Low Knot (S_w)	0.15
Interior Knots (S_w)	0.5, 0.6, 0.7
High Knot (S_w)	0.8
Spline Parameters	0.10e+1, 0.94e-1, 0.22e-1, 0.39e-35, 0.35e-35, 0.0
Capillary Pressure (KPa)	
Spline Order	3
Low Knot	0.15
Interior Knot	0.25, 0.4, 0.6, 0.7
High Knot	0.8
Spline Parameters	0.20e+2, 0.16e+0, -0.57e+1
	-0.89e+1, -0.21e+2, -0.44e+2, -0.30e+3

Table XIV. Estimated Multiphase Properties in Relative Fine Scale System (Homogeneous)

Water Relative Permeability	
Spline Order	3
Low Knot (S_w)	0.15
Interior Knots (S_w)	0.3, 0.5
High Knot (S_w)	0.8
Spline Parameters	0, 0.25e-2, 0.12e-1, 0.25e+0, 0.69e+0
Oil Relative Permeability	
Spline Order	3
Low Knot (S_w)	0.15
Interior Knots (S_w)	0.5, 0.7
High Knot (S_w)	0.8
Spline Parameters	0.99e+0, 0.13e+0, 0.46e-7, 0.0, 0.0
Capillary Pressure (KPa)	
Spline Order	3
Low Knot	0.15
Interior Knot	0.25, 0.4, 0.6, 0.7
High Knot	0.8
Spline Parameters	0.20e+2, -0.37e+1, -0.56e+1
	-0.12e+2, -0.19e+2, -0.11e+3, -0.30e+3

since the resolution in this system is still not big enough and the variances in porosity and permeability are not high. However, the residual plot shown in Figure 35 indicates that the heterogeneous scenario gives better matching than the homogeneous scenario. The true flow functions, along with the estimated flow functions from two scenarios are shown in Figures 36 and 37. Again, the estimated flow functions from heterogeneous system show better agreement with the true functions than the results from the homogeneous case do. Both the relative permeabilities and capillary pressure curves from the heterogeneous scenario are closer to the true curves than the ones from the homogeneous scenario.

The estimated flow functions from heterogeneous scenario with 95% confidence intervals are shown in Figures 38 and 39. The narrow confidence intervals indicate that the relative permeabilities and capillary pressure are accurately estimated over most range of the saturation below 0.7. Sudden increases of the confidence intervals for both relative permeabilities and capillary pressure curves show that the flow functions cannot be reliably estimated when saturation exceeds 0.7 since too little information is obtained.

In this section, three synthetic experiments were performed to investigate the effect of neglecting the sample heterogeneity on the multiphase property determination. All synthetic experiment show that, for heterogenous system, homogeneous scenario can result in erroneous estimates of flow functions. In order to access to greater range of the saturation, two-rate is used to obtain more accurate multiphase determination. The same situation is occurred in a relative fine scale system.

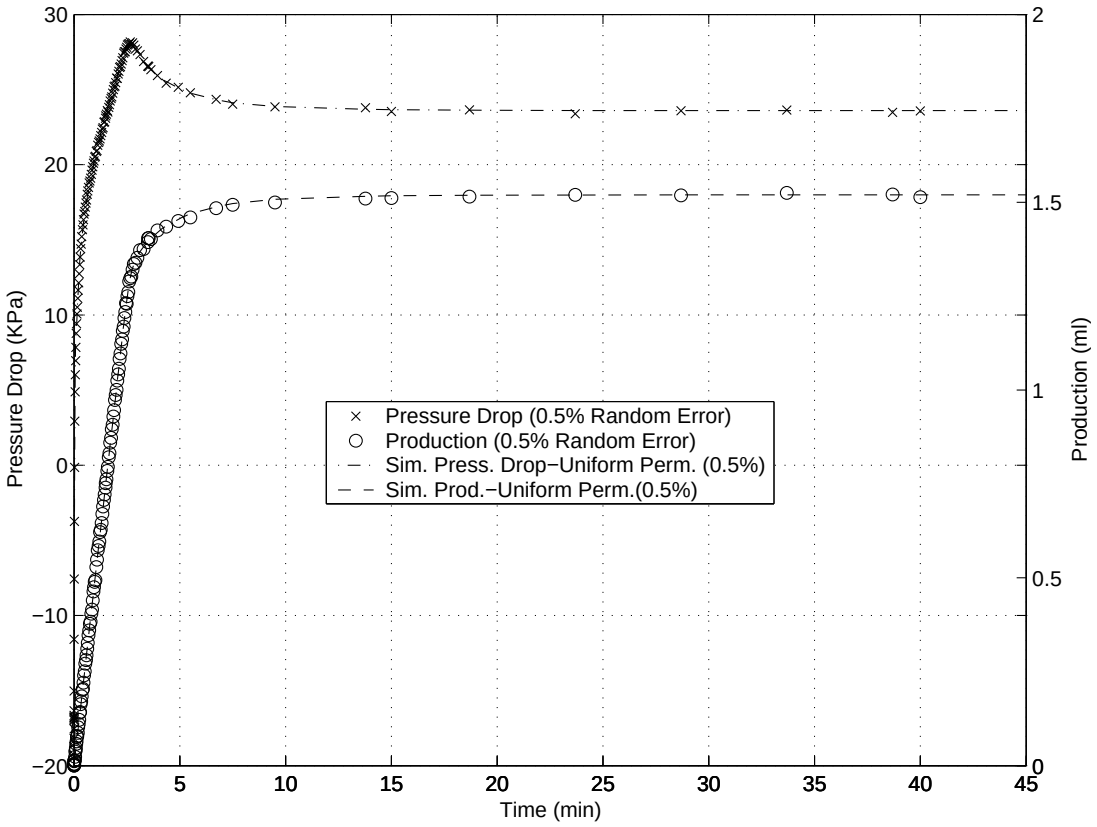

Fig. 33. Simulated and Synthetic Pressure Drop in Relative Fine Scale System (Heterogeneous)

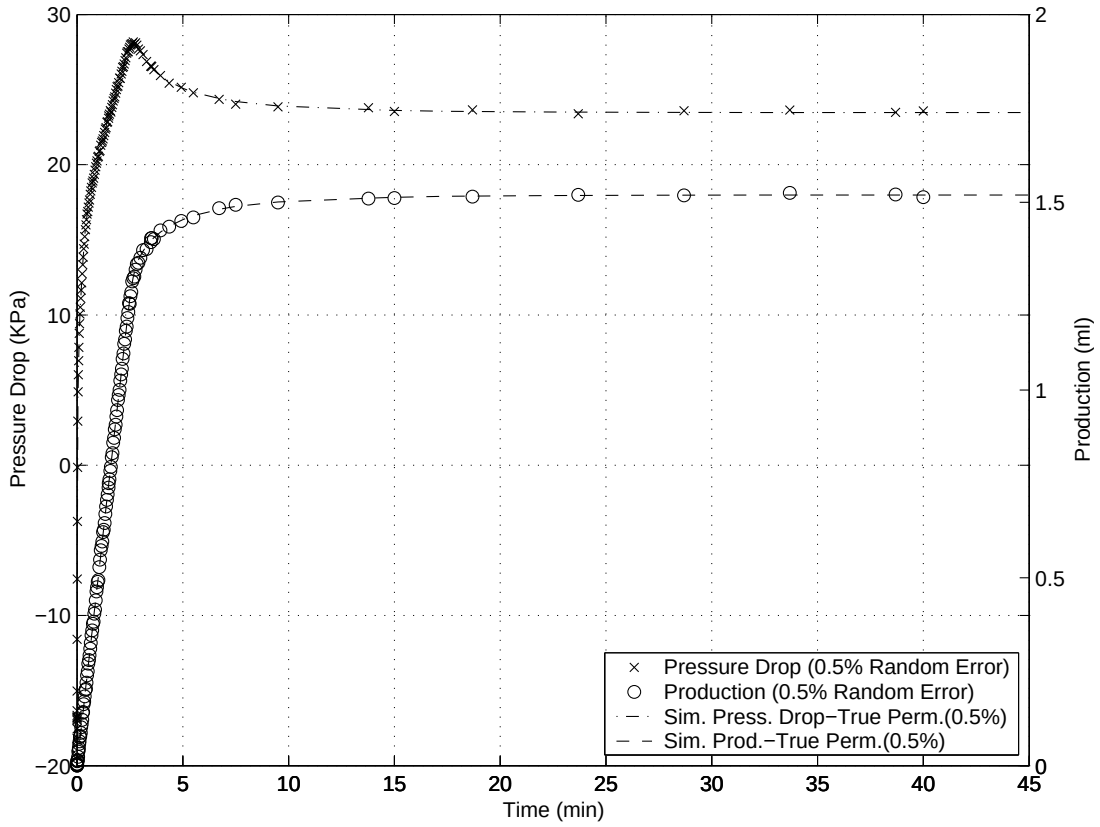

Fig. 34. Simulated and Synthetic Oil Production in Relative Fine Scale System (Heterogeneous)

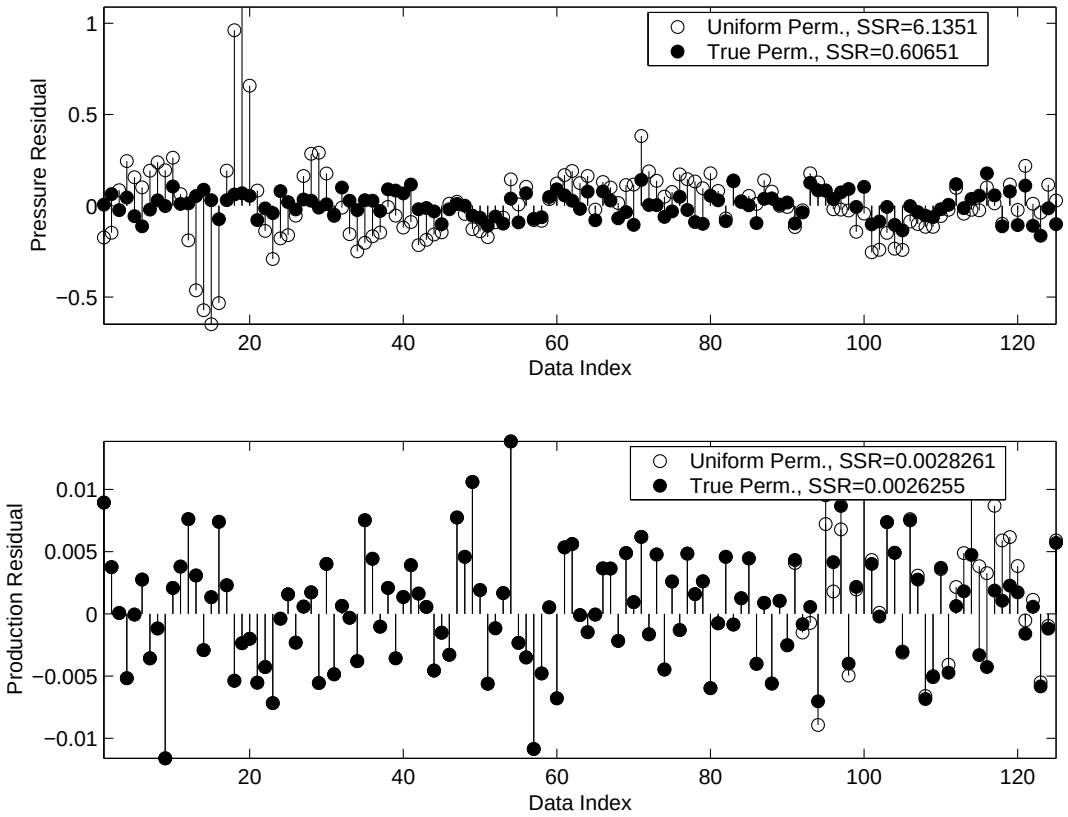

Fig. 35. Residual Plot Corresponding to Final Estimates for Single-Rate Experiments in Relative Fine Scale System

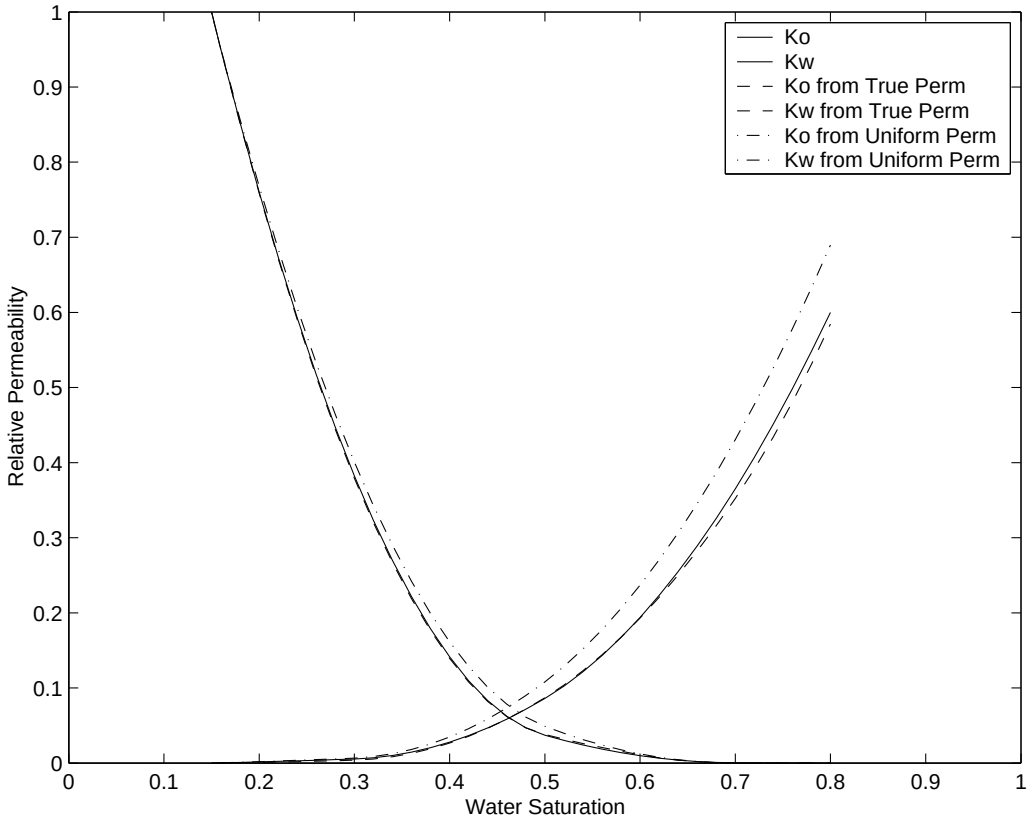

Fig. 36. True and Estimated Relative Permeabilities in Relative Fine Scale System

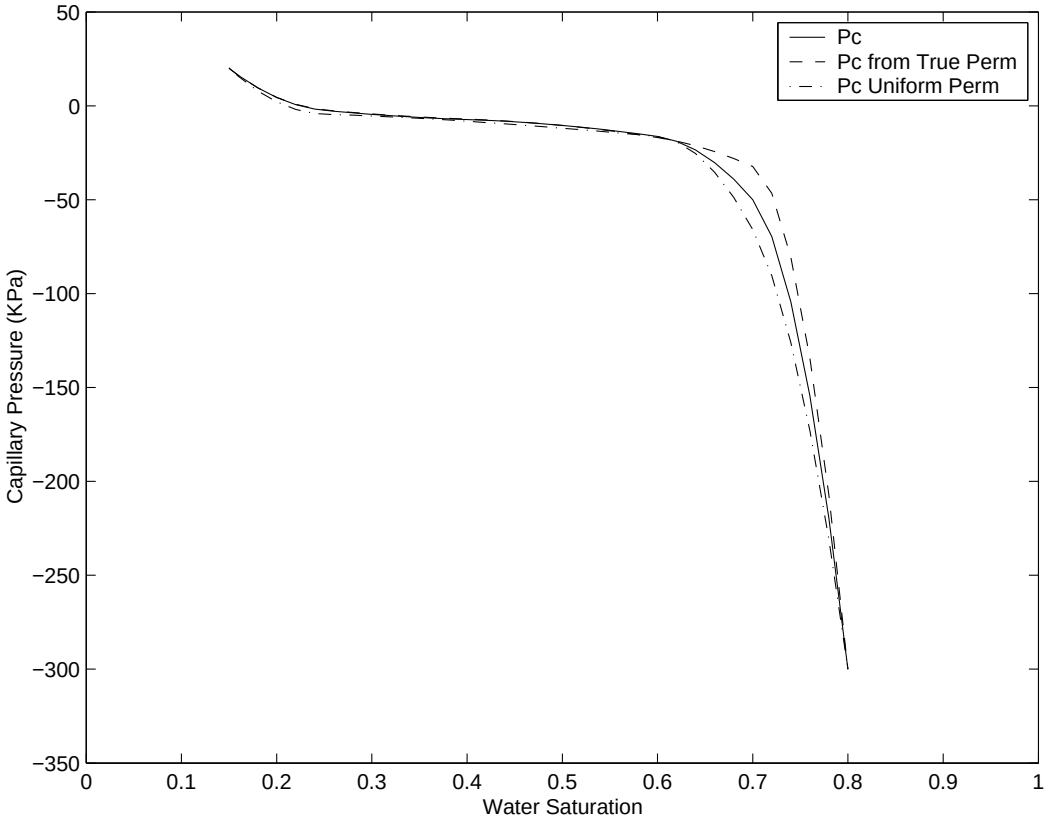

Fig. 37. True and Estimated Capillary Pressure in Relative Fine Scale System

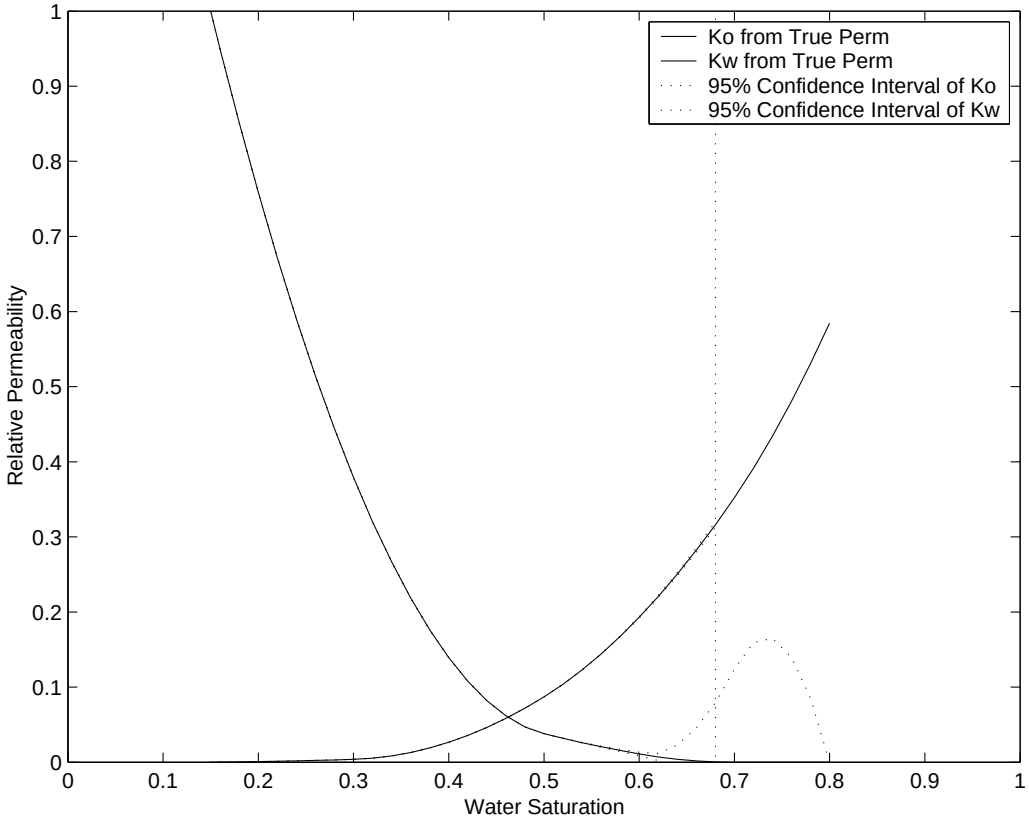

Fig. 38. Estimated Relative Permeabilities and 95% Confidence Intervals in Relative Fine Scale System (Heterogeneous)

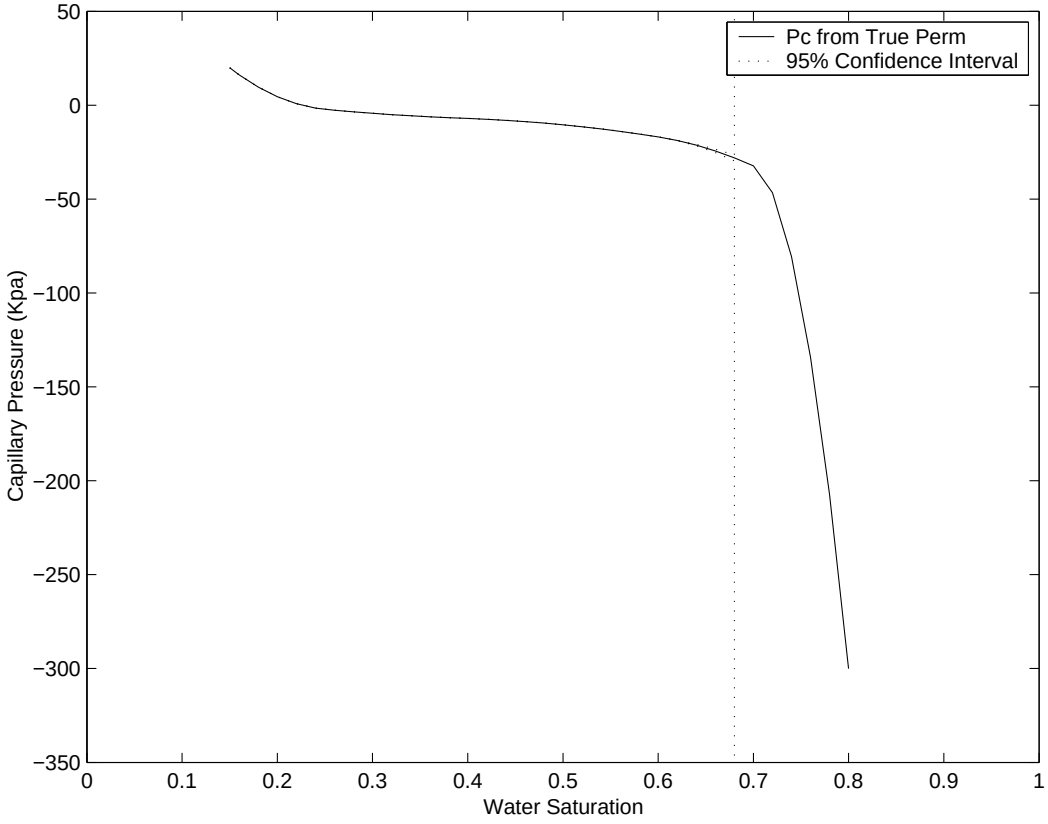

Fig. 39. Estimated Capillary Pressure and 95% Confidence Intervals in Relative Fine Scale System (Heterogeneous)

F. Summary

In this chapter, the methodology to estimate the multiphase properties has been described. The computer code SENDRA was extended to represent all three spatial coordinate directions so that the entire porosity and permeability distributions are accounted for in estimation of multiphase flow properties. The validity of the extended SENDRA code has been verified by showing the results' consistency between two two-dimensional systems. Three synthetic experiments were provided to demonstrate that taking the true spatial distributions of the absolute permeability and porosity into consideration gives more accurate estimation of the flow functions. The degree of available information plays a crucial role in the confidence interval behavior and reliability of the flow functions estimation.

CHAPTER III

PREDICTION OF RELATIVE PERMEABILITY OF THE WETTING PHASE

In this chapter, the proposal approach of predicting relative permeabilities of wetting phase using NMR relaxation data (Chen et al., 1994) is presented. The methodology which have been developed and used to determine multi-dimensional saturation and relaxation distribution in porous media (Hollenshead, 2001) is provided. Several sets of three-dimensional NMR experiments are performed on a fully and three partially saturated states for a rock sample. Quantitative analysis of NMR images is conducted to obtain the intrinsic magnetization and relaxation time at each position. The relative permeability is calculated from the determined three-dimensional saturation and relaxation data.

A. Introduction

Nuclear magnetic resonance (NMR) is an increasingly popular well-logging tool in petroleum industry because it can contribute to the *in situ* measurement of petrophysical properties of the porous media (Kleinberg and Jackson, 2001; Kleniberg, 2001). Modern NMR logging tools use permanent static magnets to create a static magnetic field B_o. In an NMR experiment, the magnetic moments of hydrogen nuclei of water first point along the static field direction. Then they are perturbed from their equilibrium state by a radio frequency pulse B_1 at the proton resonance frequency. B_1 is turned on for a while and then turned off. The rate at which the proton nuclei return to equilibrium after the pulse is known as the relaxation rate. The longitudinal magnetization recovered in an NMR experiment is characterized by the longitudinal magnetization relaxation time constant T_1, also known as spin-lattice relaxation time. The rate of signal decaying during the process of spin-spin relaxation is characterized

by the transverse magnetization relaxation time constant T_2, also known as spin-spin relaxation time. The transition back to equilibrium after the disturbance is monitored and recorded.

The effective relaxation rate in porous media depends on the bulk relaxation rate in the fluid and surface-relaxation rate, which is an environmental effect. Fluids near, or in contact with, grain surfaces relax at a much higher rate than the bulk fluid. Because of this nature, the relaxation decay time plays a significant role for well logging application. Laboratory NMR studies of fluids in porous media are thrived and the NMR measurements are used to estimate many important petrophysical properties of the porous media. There have been numerous attempts to establish correlations between nuclear magnetic resonance and the measured petrophysical properties. However, most of them are concerning absolute permeabilities (Banavar and Schwartz, 1987; Fleury et al., 2001; Hidajat et al., 2002), porosity, and saturation distributions (Timur, 1969; Chen et al., 1992). Using the approach of Katz and Thompson (1986) for the absolute permeability, $K \propto l_c^2 \sigma_0/\sigma_w$, and Archie's empirical relations (Archie, 1942) for the conductivity, $\sigma_0/\sigma_w = \phi^m$ and $\sigma_0/\sigma(S_w) = S_w^n$, Chen *et al.* (1994) proposed that the relative permeability of the wetting phase $k_{r,w}$ can be related to NMR spin-lattice relaxation time T_1 by

$$k_{r,w} = \left(\frac{\tau_1^2}{\tau_{1_0}^2}\right) S_w^n, \tag{3.1}$$

where l_c is some characteristic lenght of the pore space, σ_0 is the conductivity of the rock saturated with fluid of conductivity σ_w, and $n = 2$ is often approximately valid for many sandstones. τ_1 is a relaxation time defined as,

$$\frac{1}{\tau_1} = \frac{1}{T_1} - \frac{1}{T_{1b}}, \tag{3.2}$$

where T_1 is the spin-lattice relaxation time of wetting phase at saturation S_w and T_{1b}

is that in bulk fluid. τ_{1_0} is equal to τ_1 at $S_w = 1$.

Marck (1999) pointed out that there is a nonzero transport threshold existing. That means one fluid cease flowing at a nonzero saturation. Therefore, Archie equation should be modified by incorporation of irreducible saturation S_{wi} as $\sigma_0/\sigma(S_w) = (S_w - S_{wi})^n$. As a consequence, Eq. 3.1 becomes

$$k_{r,w} = \left(\frac{\tau_1^2}{\tau_{1_0}^2}\right)\left(\frac{S_w - S_{wi}}{1 - S_{wi}}\right)^n. \tag{3.3}$$

The inversion-recovery pulse sequence is usually used for T_1 measurement (Levitt, 2001). The basic part of an inversion recovery sequence is a 180-degree radio frequency (rf) pulse that inverts the magnetization followed by a 90-degree rf pulse that brings the residual longitudinal magnetization into the x-y or transverse plane where it can be detected by an rf coil (Schulthness and Smith, 1998).

A Carr-Purcell-Meiboom-Gill (CPMG) pulse sequence is applied for T_2 measurement and further used for the determination of saturation (Levitt, 2001). The CPMG sequence consists of a 90-degree pulse followed by an echo train consisting of successive 180 pulses. The 90^o pulse flips the longitudinal magnetization into the x-y or transverse plane where the magnetic moments which build the transverse magnetization start to lose their coherence due to the static magnetic field inhomogeneities. A train of 180^o pulses separated by a time interval serve to refocus the magnetization to generate signal echoes.

Several spatially resolved inversion-recovery and CPMG imaging experiments are performed on a wetting phase in porous media samples at different saturation levels. Then, spatially resolved T_1 distributions are estimated from the relaxation data for the different saturation levels of the wetting phase. From Eqs. (3.3) and (3.2), the relative permeability values are calculated with the estimated T_1 and determined S_w.

B. Background

1. Determination of Saturation and Porosity Distribution from CPMG Imaging Experiments

The use of NMR imaging techniques to determine saturation is based on the fact that the intrinsic magnetization M_o is proportional to the number of proton spins in the sample region subject to NMR excitation. In other words, the intrinsic magnetization is directly proportional to the mass of the water m. The relationship is expressed as:

$$M_o = km \tag{3.4}$$

where the proportionality factor, k, is affected by several experimental quantities such as receiver gain, the static magnetic field, and most importantly the rf coil quality factor Q, a measure of ratio of energy stored to energy dissipated in the receiving coil (Chen et al., 1992). The quantity of k may change during the experiments. It is desirable to include a reference standard in the imaged sample in order to determine the change of proportionality factor k during the saturation experiment. This is possible because the water mass in the reference remains constant. To determine the saturation, two subsequent images are required. The first is obtained when the sample is fully saturated with water. Next, the saturation level is obtained by blowing water out of the sample and the saturation distribution is determined by the following ratio:

$$S_w = \frac{k_1 M_{o,2}^{sample}}{k_2 M_{o,1}^{sample}} \tag{3.5}$$

where the ratio of two proportionality factors is determined by the reference magnetizations,

$$\frac{k_1}{k_2} = \frac{M_{o,1}^{ref}}{M_{o,2}^{ref}}. \tag{3.6}$$

Here, '1' represents the sample at the fully saturated state, and '2' represents the sample at the partially saturated state.

The porosity is determined by imaging at the fully saturated state. The fluid is assumed to completely fill the void space. The fluid mass determined in Eq. 3.4 is scaled to fluid volume using the fluid's density ρ_l. The porosity for the ith voxel is then given as

$$\phi_i = \frac{M_{oi}}{k\rho_l V_i} \tag{3.7}$$

where V_i is the volume of the ith voxel.

A CPMG pulse sequence can be used to determine the spatially resolved intrinsic magnetization M_o distribution (Levitt, 2001). The transverse magnetization observed for a bulk fluid having a spin-spin relaxation time of T_2, observed at echo time t_j, is

$$M(t) = M_o exp(-\frac{t_j}{T_2}). \tag{3.8}$$

For a real porous medium which comprises of pores of different sizes and shapes, we should introduce a distribution function $P(\tau)$ to deal with this situation since T_2 is pore size dependent (Hollenshead, 2001). The T_2 distribution function $P(\tau)$ is a function of nuclei for which relaxation times are between τ and $\tau + d\tau$. Then, Eq. 3.8 is rewritten as

$$\frac{M(t)}{M_o} = \int_0^\infty P(\tau) exp(-\frac{t_j}{\tau}) d\tau \tag{3.9}$$

Now, the goal is to determine the distribution function $P(\tau)$, and the solution will be revealed in the next Subsection 2.

2. Determination of Spin-Lattice Relaxation Distribution from Inversion-Recovery Experiment

The spin-lattice relaxation time T_1 can be measured by the inversion-recovery sequence. The longitudinal magnetization for a bulk fluid at the observation time t, is

$$M(t) = M_o[1.0 - 2exp(\frac{t}{T_1})] \tag{3.10}$$

With appropriate transformations, the longitudinal relaxation can be represented similar as the transverse relaxation:

$$\frac{M_o - M(t)}{2M_o} = exp(\frac{t}{T_1}) \tag{3.11}$$

For a porous medium, the relaxation time T_1 is pore size dependent. The T_1 distribution function $P(\tau)$ is a function of nuclei with relaxation times between τ and $\tau + d\tau$. Then, Eq. 3.11 is rewritten as

$$\frac{M_o - M(t)}{2M_o} = \int_0^\infty P(\tau)exp(-\frac{t}{\tau})d\tau \tag{3.12}$$

Considering the similar form of the Eqs. 3.9 and 3.12, a general approach is employed, with understanding that the same analysis is applicable to both transverse and longitudinal relaxation processes. The magnetization, observed at time t_j, is then found by integrating over all possible relaxation times:

$$Y(t_j) = \int_0^\infty P(\tau)K(t_j, \tau)d\tau, \tag{3.13}$$

where $Y(t_j)$ is the data, $P(\tau)$ is an unknown distribution and $K(t_j, \tau)$ is the kernel function. The goal is to determine the relaxation distribution function $P(\tau)$ from the measured magnetization data $Y(t_j)$. A non-parametric method is applied. The

distribution function $P(\tau)$ is expressed in terms of B-spline basis functions:

$$P(\tau) = \Sigma_j^N C_j B_j^m(\tau, \overrightarrow{y}), \tag{3.14}$$

where B_j^m are B-spline basis function, m is the order of the spline, and $\overrightarrow{y}$ represents the extended partition, the location of the knots. Once the partition is chosen, the distribution is specified by the complete set of coefficients, C_j. The coefficients are determined by solving a minimum problem:

$$\min_{\mathbf{C_j}} J = [\overrightarrow{Y_{obs}} - \overrightarrow{Y_{calc}}]^T \mathbf{W} [\overrightarrow{Y_{obs}} - \overrightarrow{Y_{calc}}] + n\lambda \int_{\tau_{min}}^{\tau_{max}} \left\{ \frac{d^2 P(\tau)}{d\tau^2} \right\}^2 d\tau. \tag{3.15}$$

The first term of the Eq. 3.15 is the performance index which reflects the precision of the fitting between calculated values Y_{calc} and observed data Y_{obs}. The second term is a regularization term. The regularization parameter λ controls the trade-off between the smoothness of the solution and the quality of the fitting. More details regarding the determination of λ can be found in Hollenshead's thesis (Hollenshead, 2001).

For the fast diffusion which means the time of a molecule crossing a pore and enter the surface layer is much less than that needed to relax at the surface, the harmonic mean can be used to calculate the average T_1 relaxation rate for fluid in each individual pore with the knowing distribution function $P(\tau)$ (Zimmerman and Brittin, 1957; Brownstein and Tarr, 1978)

$$\frac{1}{T_1^{ave}} = \int_0^\infty \frac{1}{\tau} P(\tau) d\tau. \tag{3.16}$$

The fast diffusion limit is valid if

$$T_1 > r_i/6D, \tag{3.17}$$

where r_i is the pore size and D is the fluid diffusion coefficient (Chen et al., 1993). This condition would be satisfied for pore size r_i up to the orders of $10^{-1} - 10^{-2}$ mm,

and is suitable for our investigated sandstone.

C. Experiment

A cylindrical porous rock sample, 4.1 cm in length and 2.54 cm in diameter, is sealed by epoxy (STYCAST® 2651) and surrounded by plexiglass to avoid fluid bypass and moisture evaporation, leaving the faces free for injection and production. As a reference standard, a tube full of water is placed on the top of the sample, and both ends of the tube are sealed by epoxy to avoid evaporation. Initially, the sample is fully saturated with water under 250 mmHg vacuum conditions. 5.28 g of water are absorbed and a bulk porosity of 0.25 is determined. Then, the sample with the reference standard is placed into a 3.5-cm-diameter birdcage rf coil and then inserted into a Buker BioSpec® 24/30 system operated at 100 MHz. The one end of the sample is connected to a pressurized N_2 gas line and the other end is open to the atmosphere. The Bruker system is equipped with ± 20 Gauss/cm gradient coil inside the 30 cm magnet bore.

Three-dimensional CPMG imaging and inversion-recovery pulse sequences are implemented in the ParaVision® system, which is the data acquisition and processing software. The parameter values associated with the imaging sequence are given in Table XV. Here, the matrix size $64 \times 8 \times 8$ is applied, where 64 is chosen to make sure that the signal from the reference is not overlapping the signal from water inside the sample yielding an undisturbed reference signal suitable for intensity calibration. The low resolutions used in the other two directions are based on the consideration of length of the experiment duration since the total length of experiment duration doubles when the matrix size doubles.

The three-dimensional CPMG imaging pulse sequence is used to acquire a total

Table XV. The Parameter Values for CPMG Imaging and Inversion-Recovery Sequences

Spectral Width	50000 Hz
Spatial Encoding	frequency-phase-phase encoding
Slice Orientation	transverse anterior-posterior
Excitation Pulse Length	50 μs
Refocusing Pulse Length	50 μs
Repetition Time	5 s
Number of Echoes (CPMG)	32
Number of Experiments (Inversion-Recovery)	30
Echo Spacing (CPMG)	3.6 ms
Field of View	4.8 cm $\times$ 4.8 cm $\times$ 6.4 cm
Matrix Size	64 $\times$ 8 $\times$ 8
Voxel Size	0.75 mm $\times$ 6 mm $\times$ 8 mm
Experiment Duration (CPMG)	30 min
Experiment Duration (Inversion-Recovery)	150 min

of 32 images at an echo spacing of 3.6 ms. As the experiment proceeds, the magnetization attenuates due to T_2 relaxation effects. The image files are then processed to obtain the intrinsic magnetization for each voxel. The left/right, head/foot and anterior/posterior coordinate axes system, as shown in Figure 40, are applied. The method used to determine the intrinsic magnetization intensity is described in Section B. After the CPMG imaging experiment is done, the three-dimensional inversion-recovery pulse sequence is immediately performed.

Three successive sets of CPMG and inversion-recovery images are taken after three different saturation levels in the sample were established. This is accomplished by injecting N_2 at one end of the sample and blowing some water out of the sample. The valve connected to the pressurized N_2 source is open for about 5 minutes to obtain a degree of saturation. Three different inlet pressures, 9.7 KPa, 19.3 KPa and 29.0 KPa, were applied to obtain different saturation. Then, the valve is closed and water redistribution might occur. After a sufficiently long time (half an hour), an equilibrium saturation is believed to be obtained because there are no further changes of the sample image MRI profile displayed. A set of CPMG and inversion-recovery images is immediately taken.

D. Results and Discussion

Figures 41-43 show the one-dimensional projection of three-dimensional magnetization on three axes from the first CPMG experiment on the fully saturated sample. Figures 44-52 show the results from the three successive CPMG experiments after three different saturation levels are obtained. The y-axis in these figures are indicated as magnetization intensity in arbitrary unit. The stacking curves in the figures represent the image profiles observed at multiples of the echo time. As the experiment

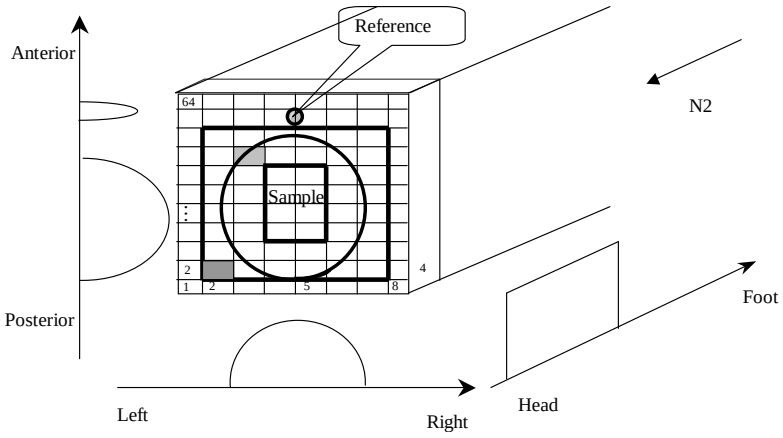

Fig. 40. Sample Orientation in NMR Experiments

proceeds, the intensity of magnetization becomes attenuated due to the T_2 relaxation effects. The determined intrinsic magnetization is shown as a darkened line at the top of each plot.

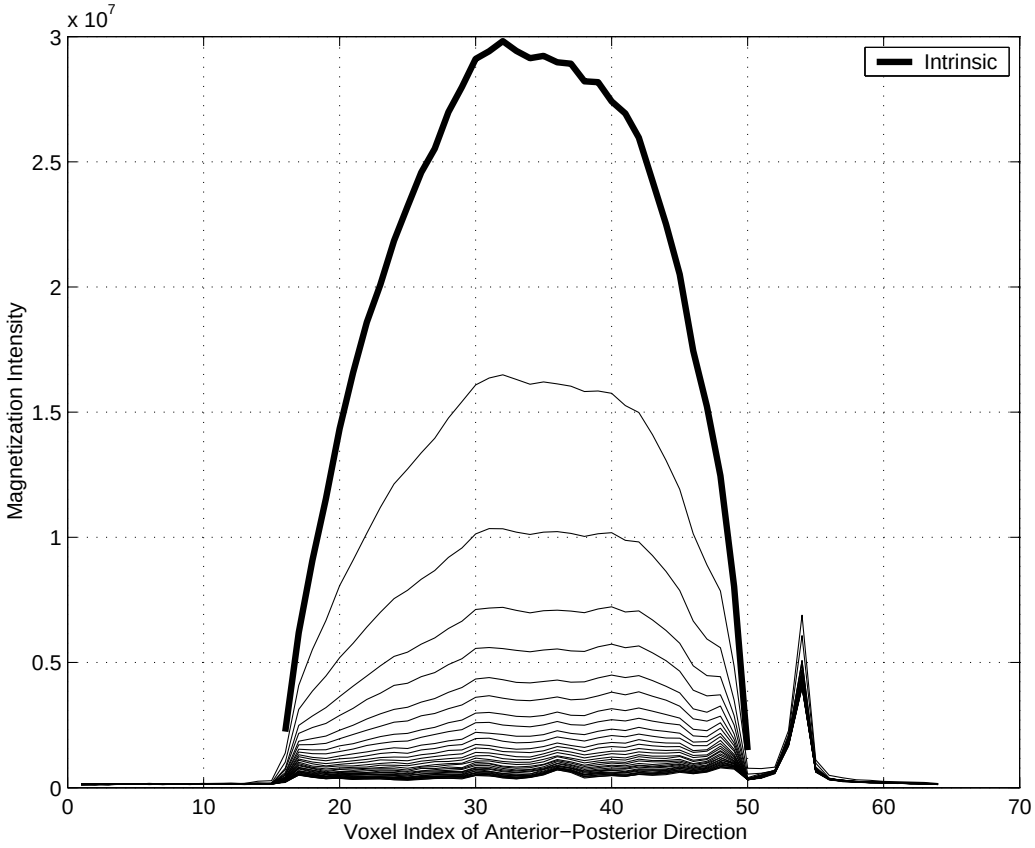

Fig. 41. One-Dimensional Projection of Three-Dimensional Image on Anterior-Posterior Axes by the First CPMG Experiment

The peaks shown beside the sample profile in the Figures 41, 44, 47 and 50 are originating from the reference standard. As expected, it is observed that the intensities of the Figures 44-46 are lower than the intensities of the Figures 41-43 since part of the water in the second CPMG images is pushed out of the sample by the N_2. This kind of behavior is observed again from figures of the third and fourth

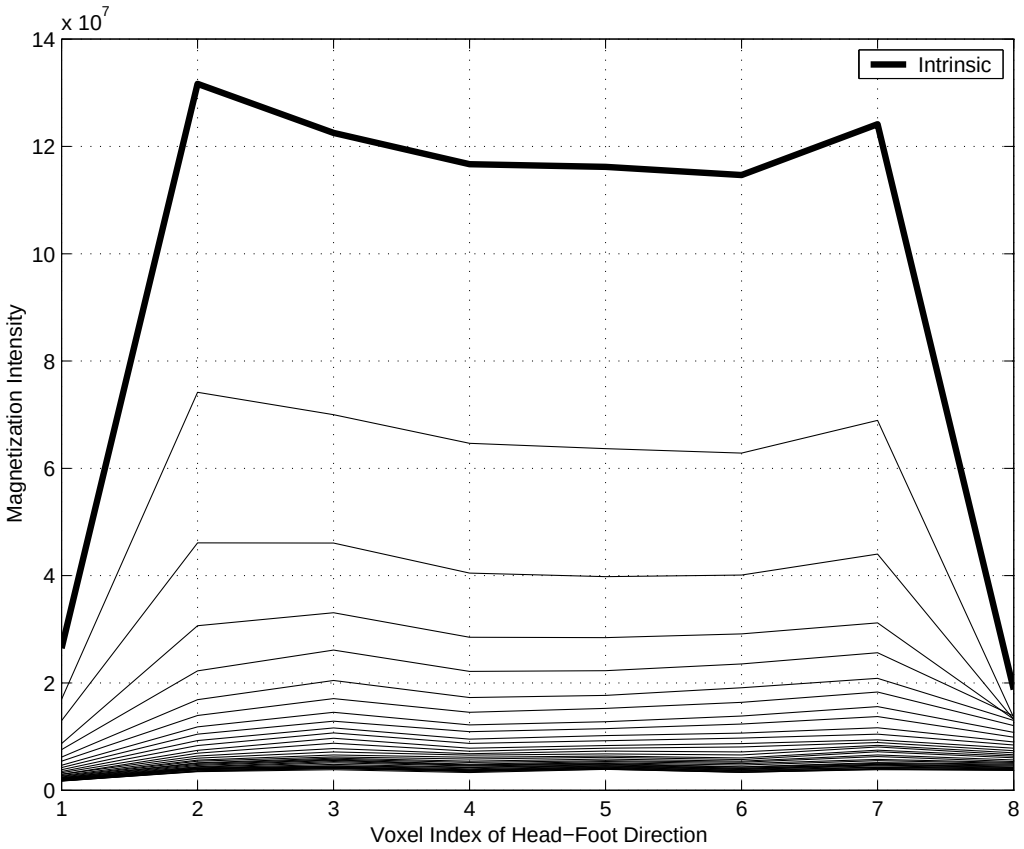

Fig. 42. One-Dimensional Projection of Three-Dimensional Image on Head-Foot Axes by the First CPMG Experiment

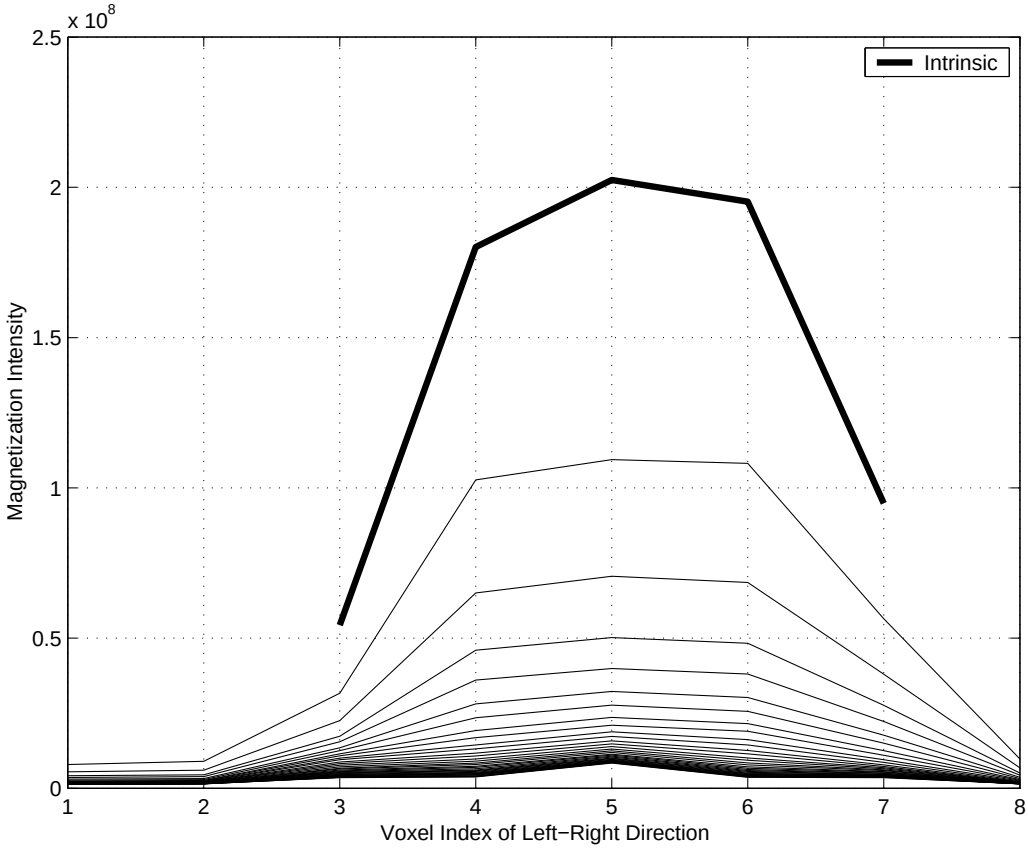

Fig. 43. One-Dimensional Projection of Three-Dimensional Image on Left-Right Axes by the First CPMG Experiment

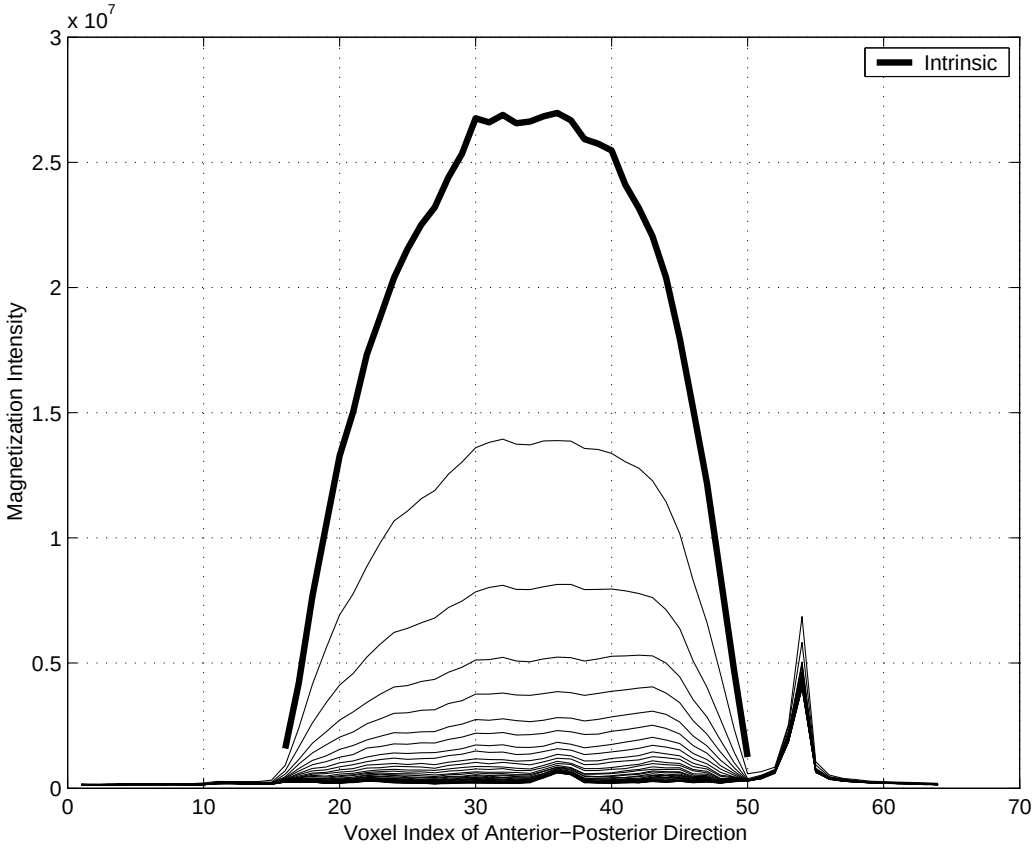

Fig. 44. One-Dimensional Projection of Three-Dimensional Image on Anterior-Posterior Axes by the Second CPMG Experiment

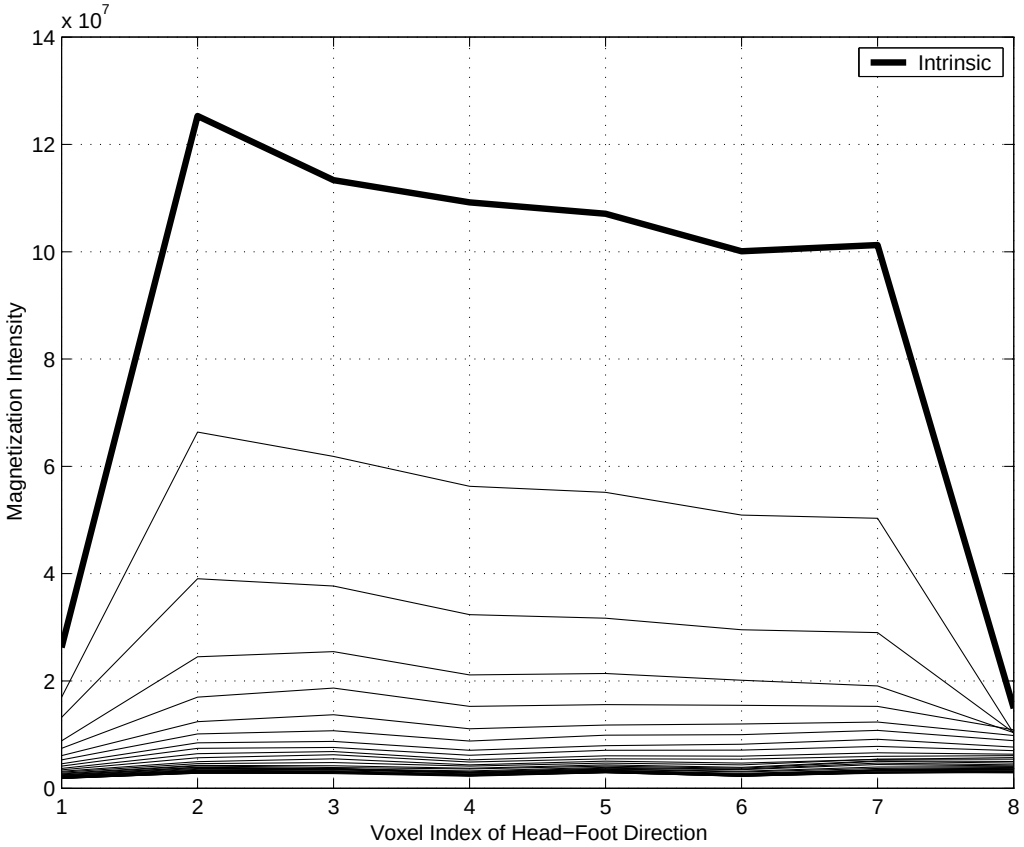

Fig. 45. One-Dimensional Projection of Three-Dimensional Image on Head-Foot Axes by the Second CPMG Experiment

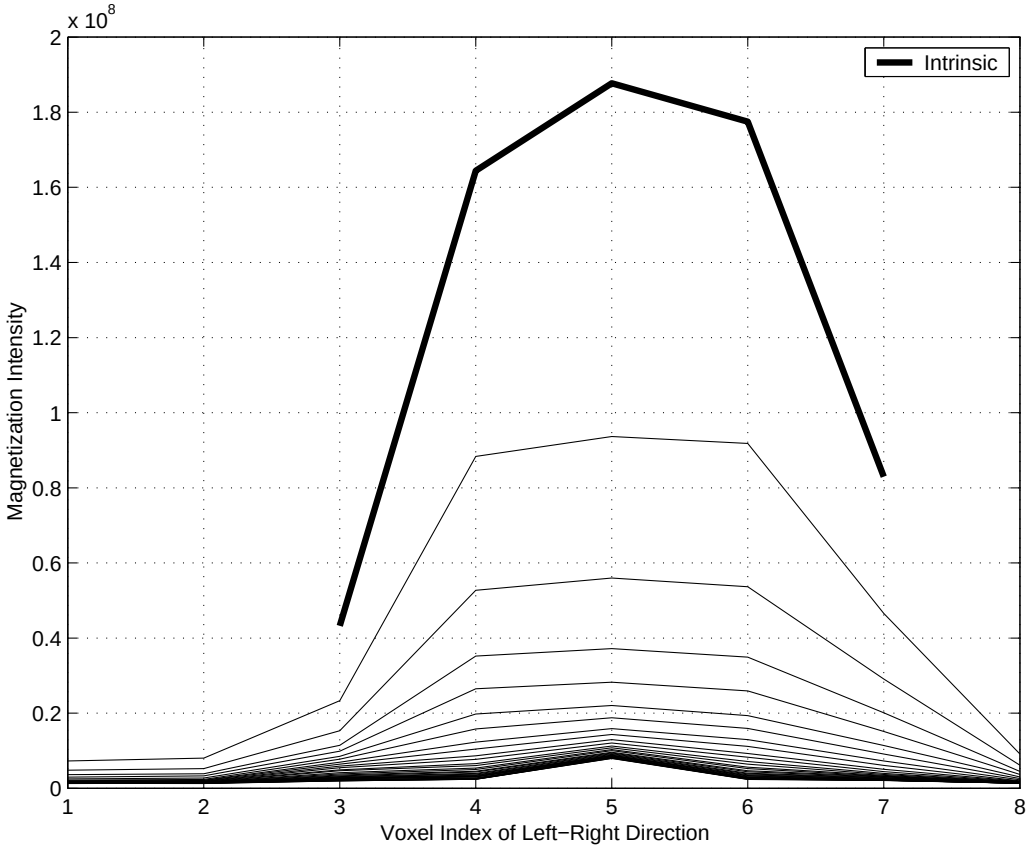

Fig. 46. One-Dimensional Projection of Three-Dimensional Image on Left-Right Axes by the Second CPMG Experiment

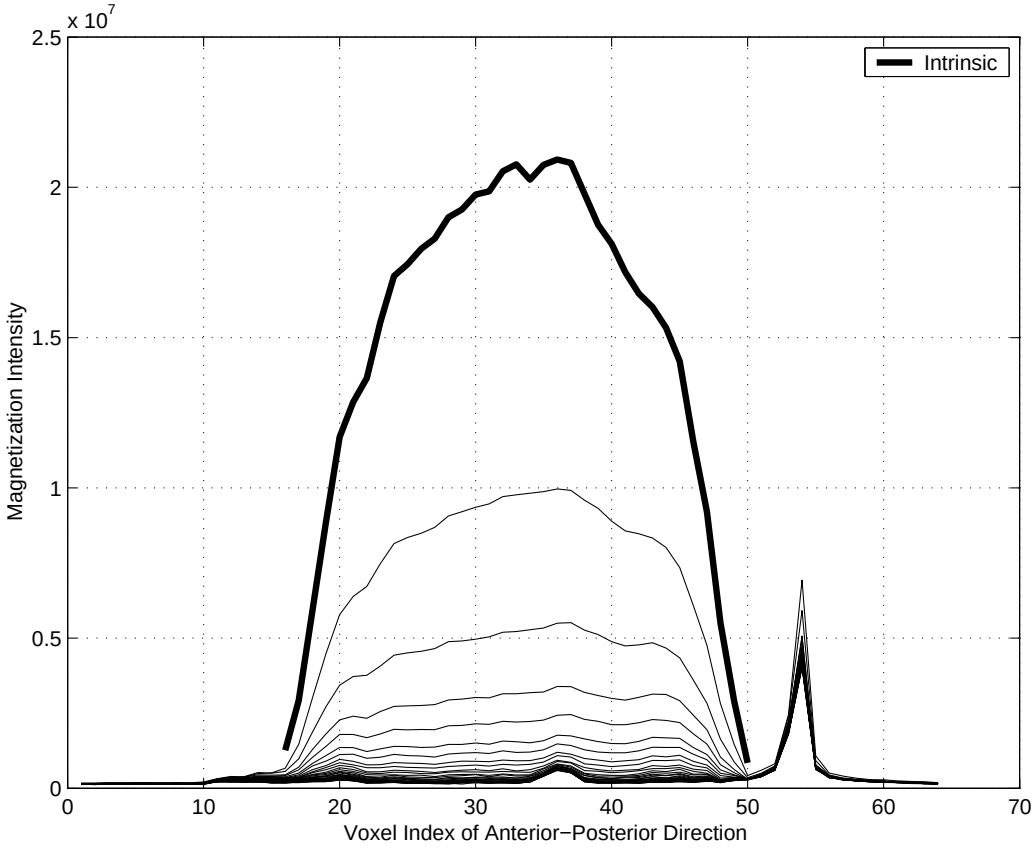

Fig. 47. One-Dimensional Projection of Three-Dimensional Image on Anterior-Posterior Axes by the Third CPMG Experiment

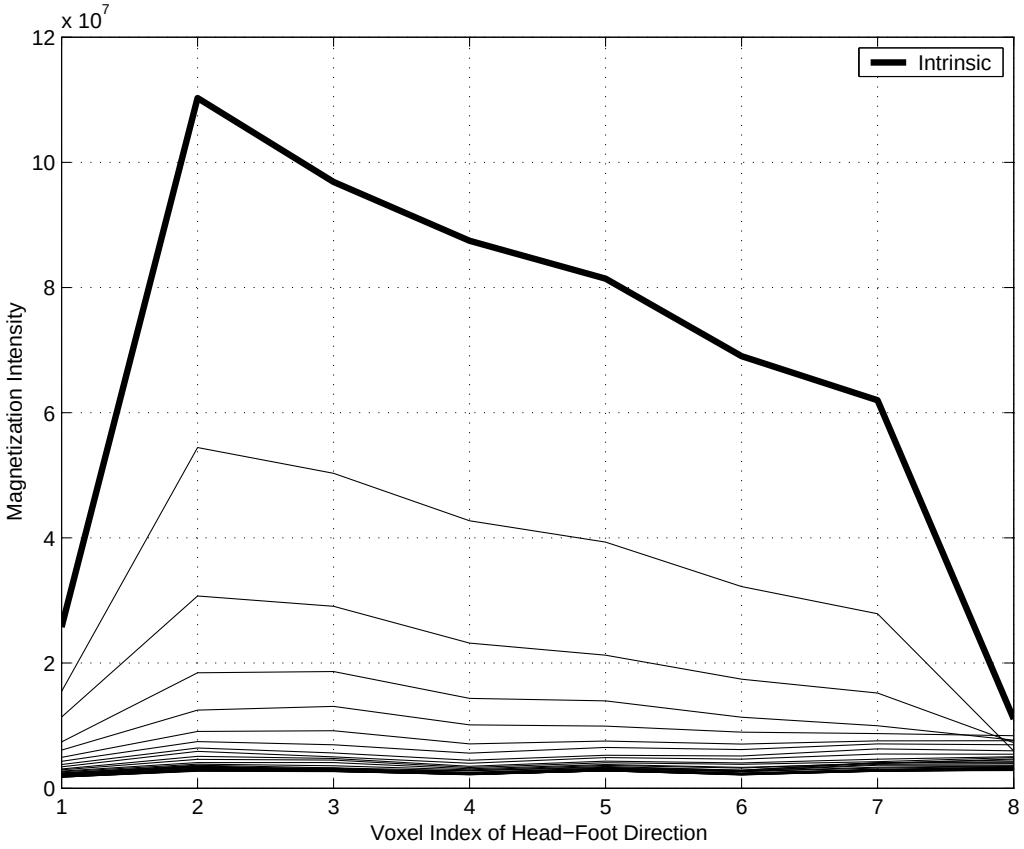

Fig. 48. One-Dimensional Projection of Three-Dimensional Image on Head-Foot Axes by the Third CPMG Experiment

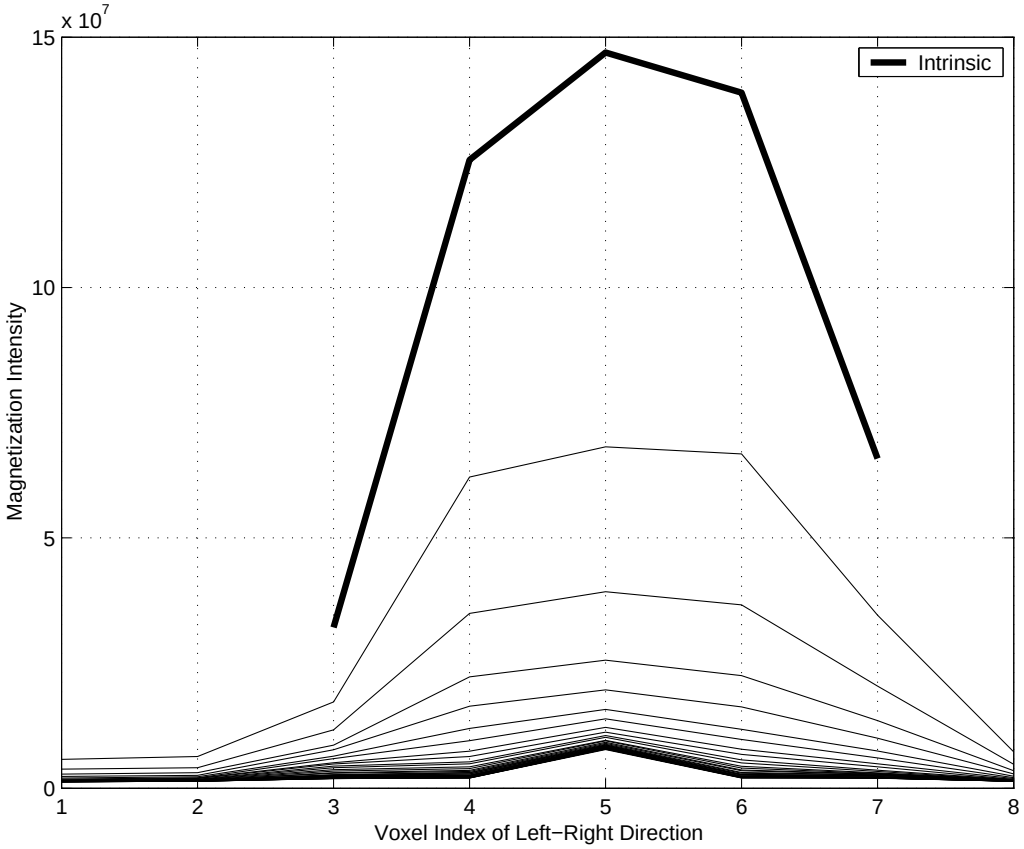

Fig. 49. One-Dimensional Projection of Three-Dimensional Image on Left-Right Axes by the Third CPMG Experiment

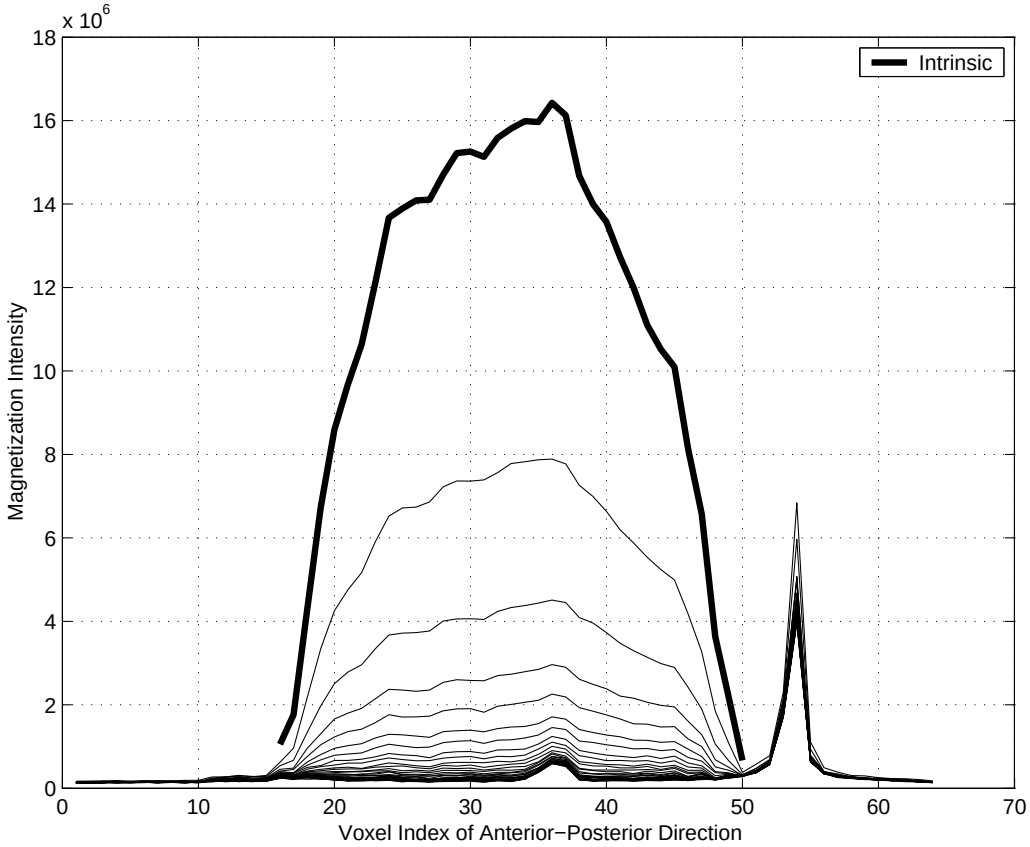

Fig. 50. One-Dimensional Projection of Three-Dimensional Image on Anterior-Posterior Axes by the Fourth CPMG Experiment

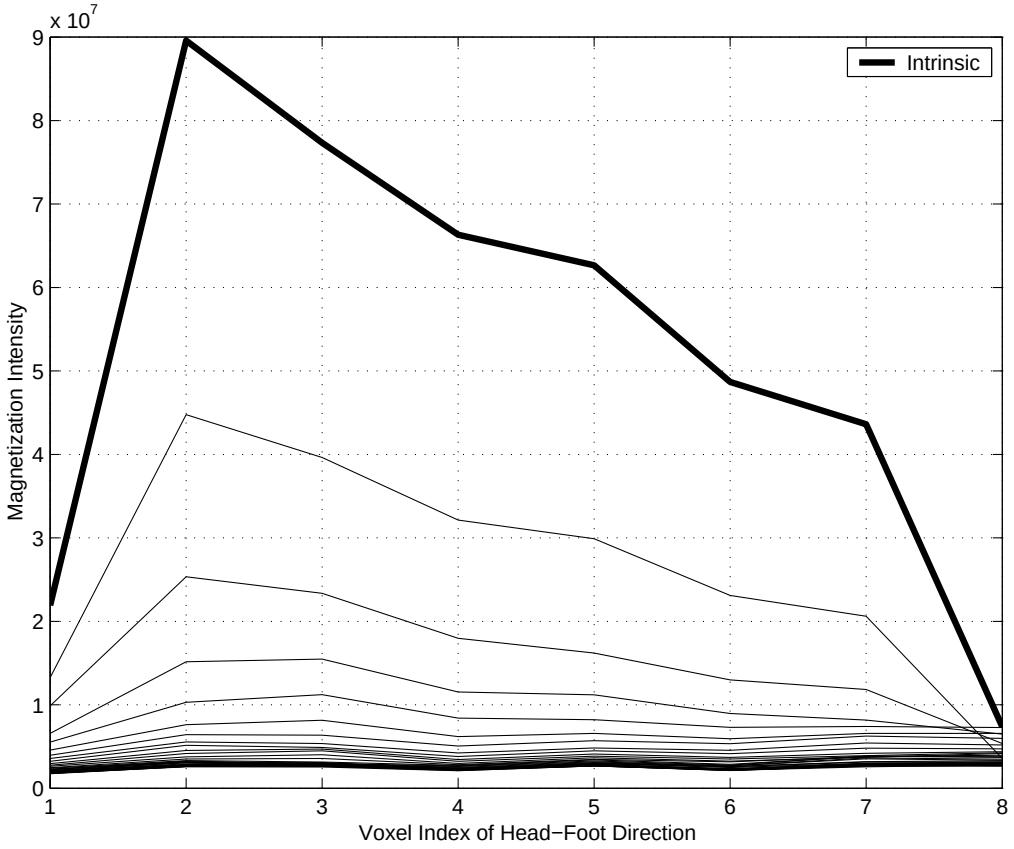

Fig. 51. One-Dimensional Projection of Three-Dimensional Image on Head-Foot Axes by the Fourth CPMG Experiment

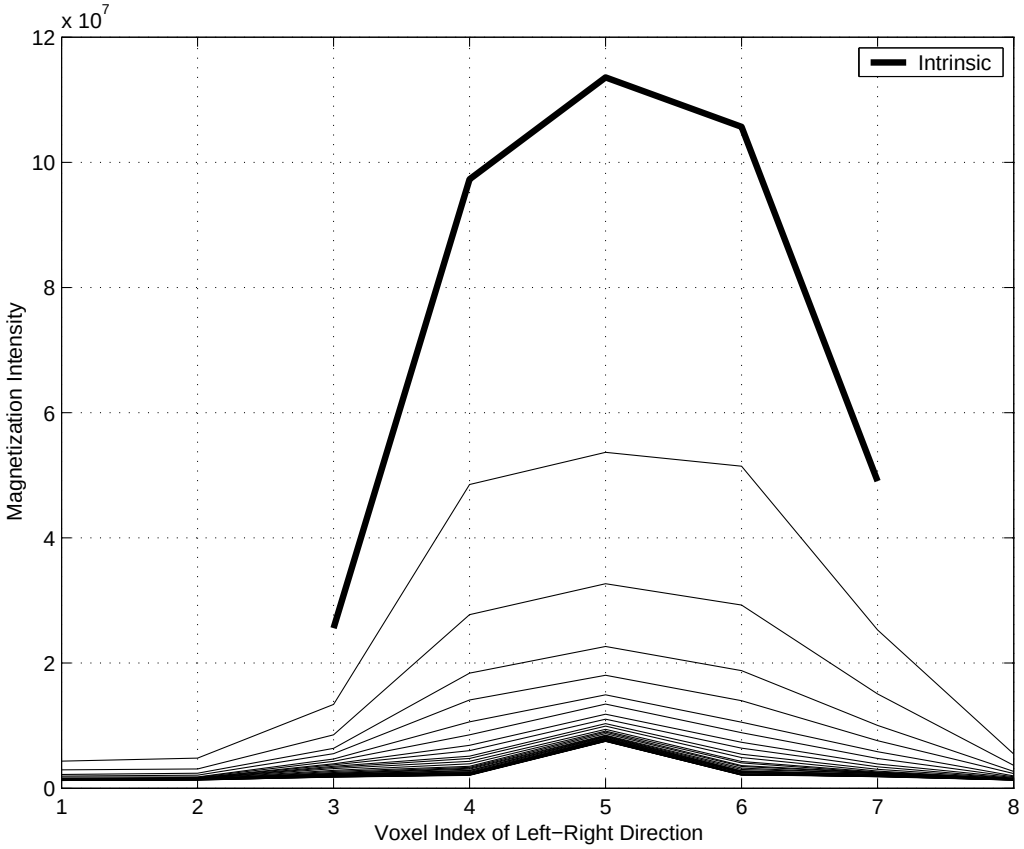

Fig. 52. One-Dimensional Projection of Three-Dimensional Image on Left-Right Axes by the Fourth CPMG Experiment

CPMG experiment results that the intensity keeps decreasing when the saturation is further lowered. The distribution along the main axis of the cylindrical sample becomes severely asymmetric in Figure 48, reflecting the geometry of the gas injection entrance. The N_2 is injected at the foot end and the signal intensity increases from foot to head. The slope shown in the Figure 48 thus displays that the saturation near the inlet is lower than the saturation near the outlet.

For careful analysis of the image profiles, the voxel ranges occupied by the sample and reference can be determined in the Table XVI so that the irrelevant noise region can be discarded. In order to determine the ratio of two proportionality factors ($\frac{k_1}{k_2}$) which defined in Eq. 3.6, the intensity of reference from each partially saturated experiment are compared with the reference intensity from the fully saturated sample. Then, the saturation of each voxel can be calculated through Eq. 3.5 with the determined intrinsic magnetization from both experiments. The saturation calculation of the example voxel (30, 5, 6) is given in Table XVI. Here, the first digit, 30, represents the 30th voxel in anterior-posterior (A-P) direction, 5 is the 5th voxel in head-foot (H-F) direction, and 6 is 6th voxel in left-right (L-R) direction.

In this manner, the three-dimensional water saturation distributions for three saturation levels have been obtained and are shown in Figures 53-70. There are six figures presented for each of three partially saturated levels. For each saturation level, the saturation distribution is shown as a series of two-dimensional images in axial, sagittal and coronal slices. A side view and front view are given for the slice's representation. The different colors within these slices are assigned by the different saturation values encoded according to the color bar on the right. The location of the voxel can be found from the reading in the axis.

Table XVI. Saturation Determination Experiment

Sample Limits in A-P Direction	16-50
Sample Limits in H-F Direction	1-8
Sample Limits in L-R Direction	3-7
Reference Limits (A-P)	51-57
Reference Limits (H-F)	2-7
Reference Limits (L-R)	5
Intensity from Reference (First)	6.56×10^6
Intensity from Reference(Third)	6.64×10^6
Ratio of Proportionality Factors $\frac{k_2}{k_1}$	1.01
Intensity from Voxel (30, 5, 6) (First)	1.07×10^6
Intensity from Voxel (30, 5, 6) (Third)	6.84×10^5
Determined Saturation for Voxel (30, 5, 6)	0.63

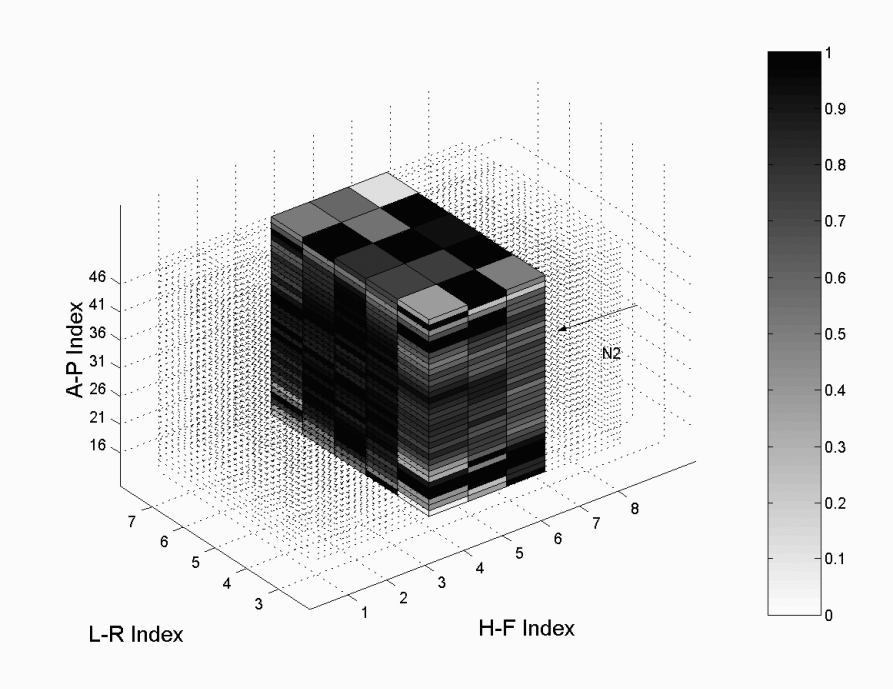

Fig. 53. Three-Dimensional Saturation Slice Distribution for the First Saturation Level (axial plane, side view)

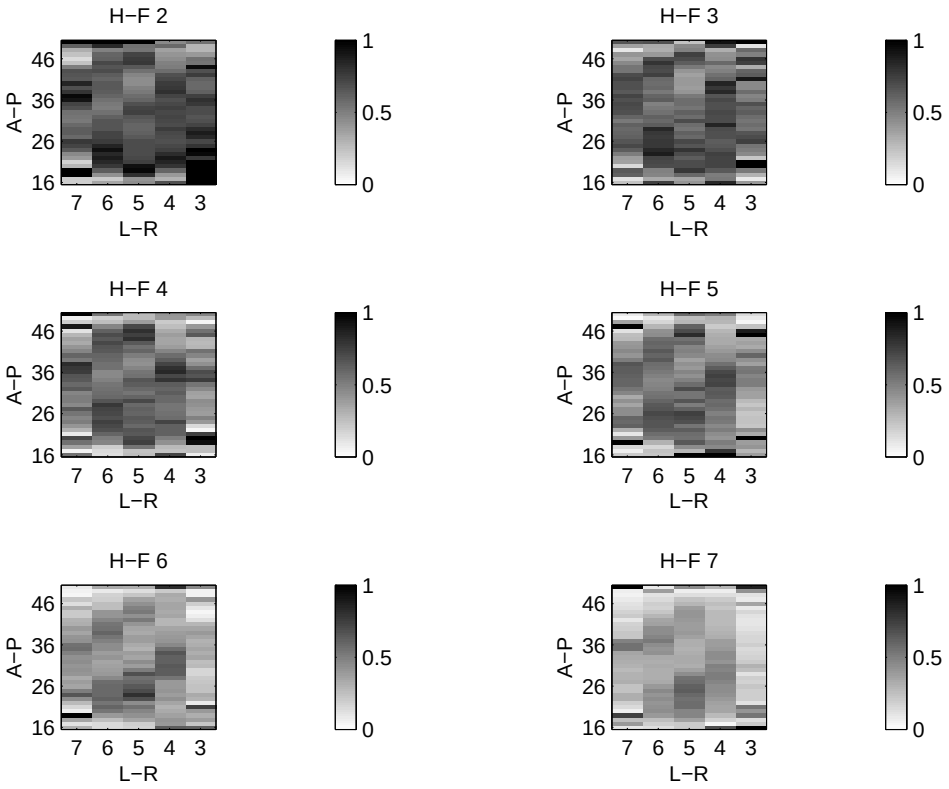

Fig. 54. Three-Dimensional Saturation Slice Distribution for the First Saturation Level (axial plane, front view)

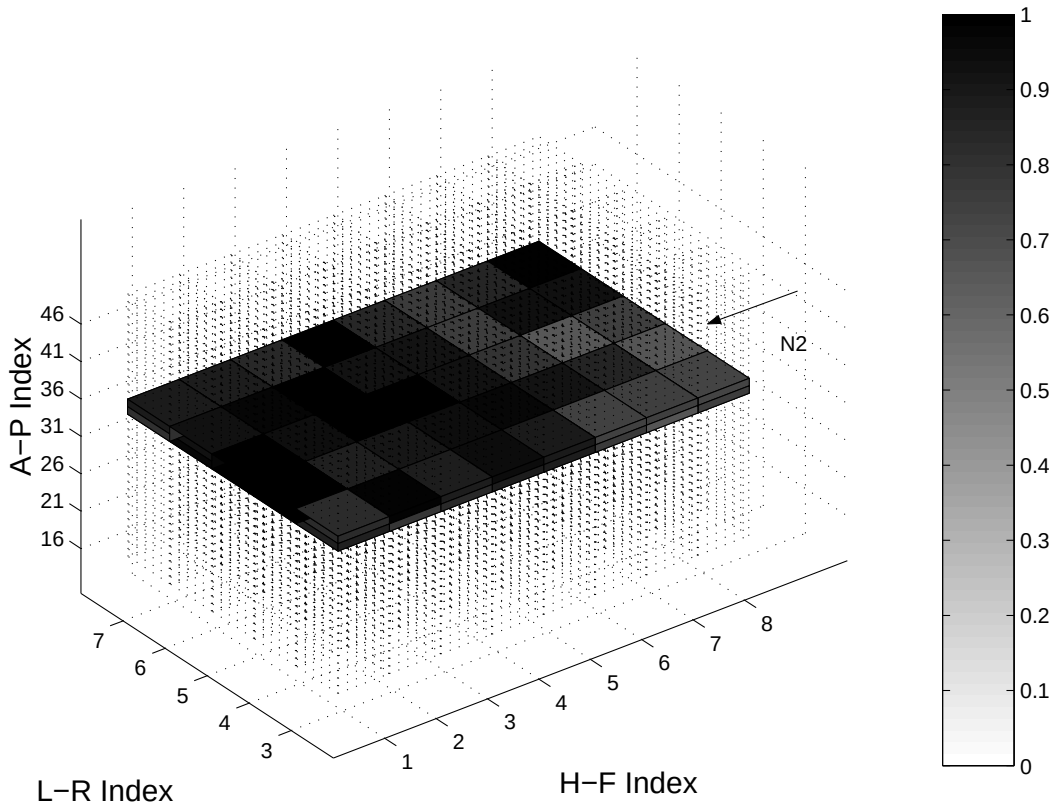

Fig. 55. Three-Dimensional Saturation Slice Distribution for the First Saturation Level (coronal plane, side view)

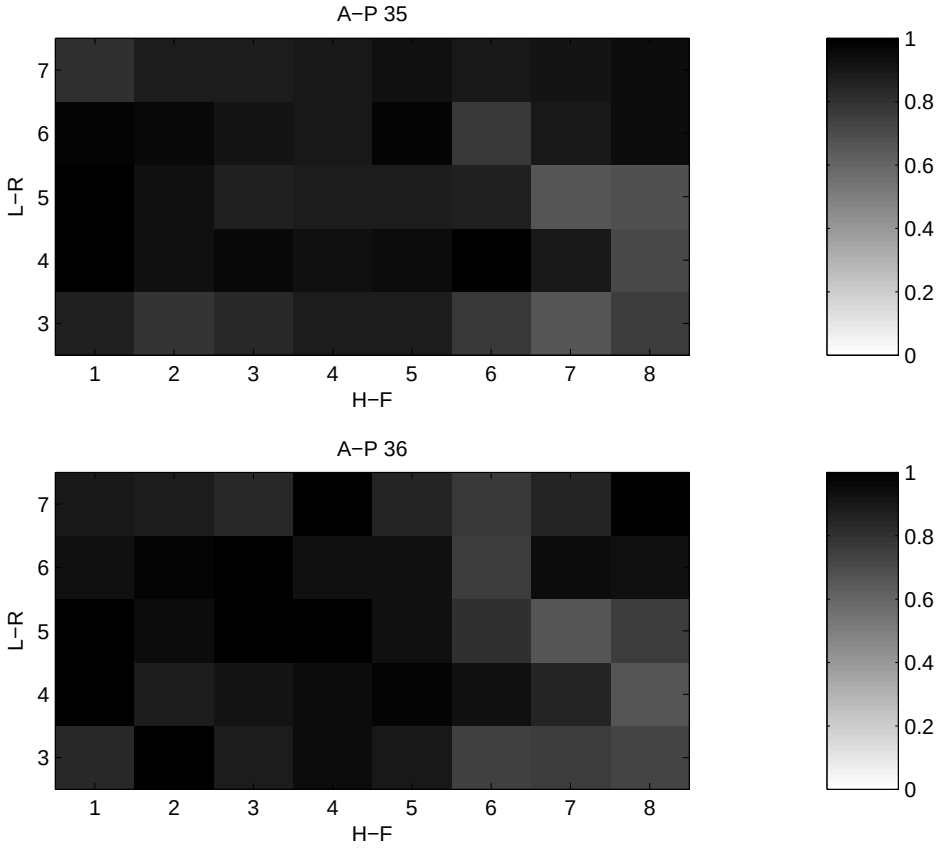

Fig. 56. Three-Dimensional Saturation Slice Distribution for the First Saturation Level (coronal plane, front view)

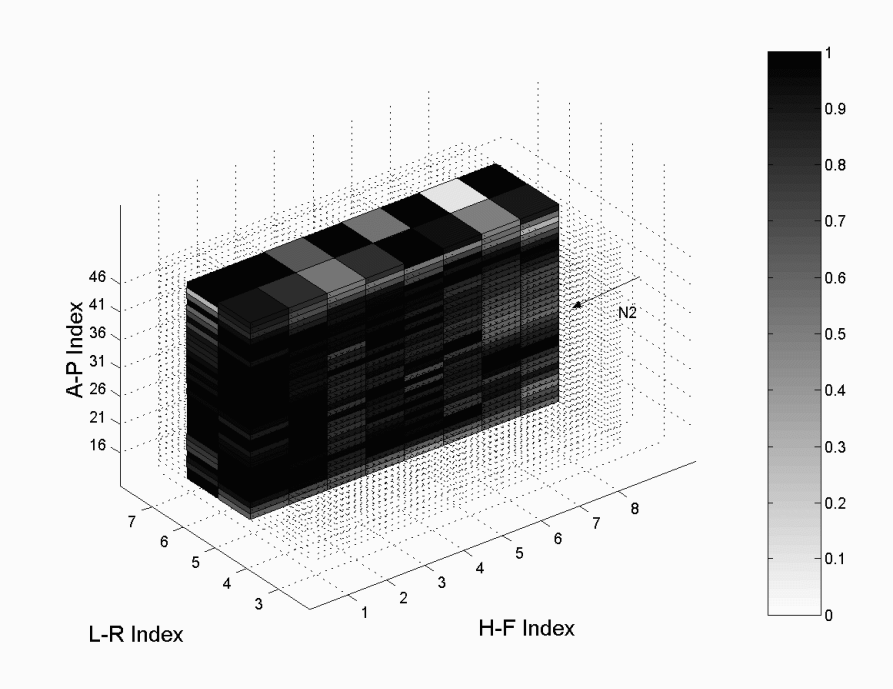

Fig. 57. Three-Dimensional Saturation Slice Distribution for the First Saturation Level (sagittal plane, side view)

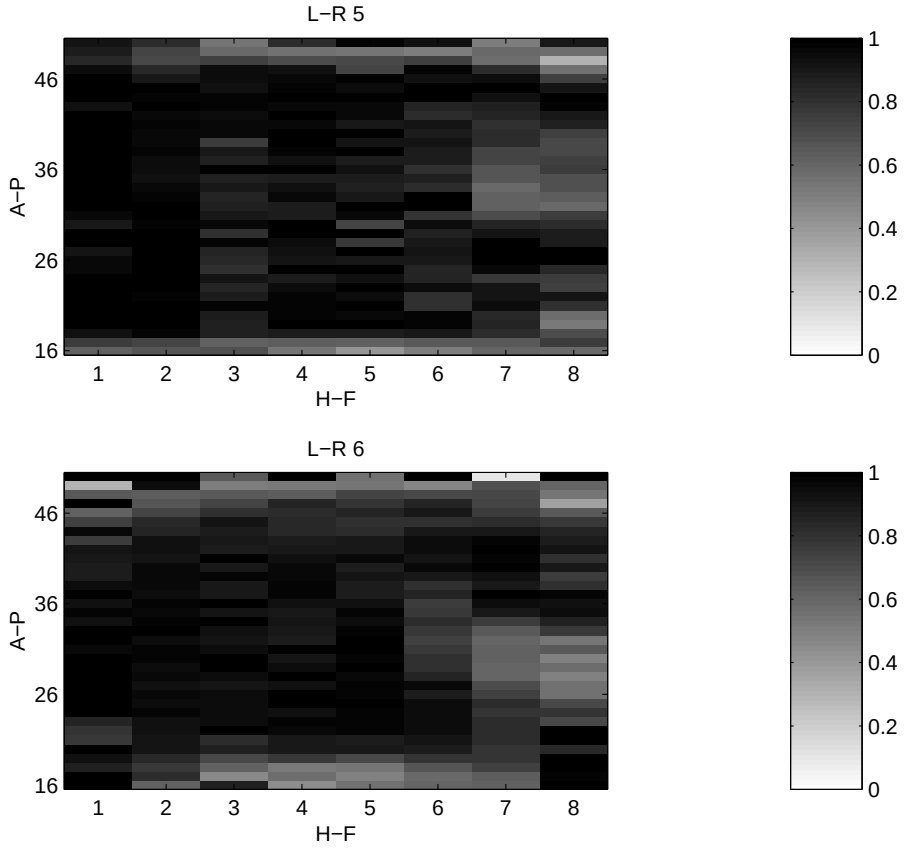

Fig. 58. Three-Dimensional Saturation Slice Distribution for the First Saturation Level (sagittal plane, front view)

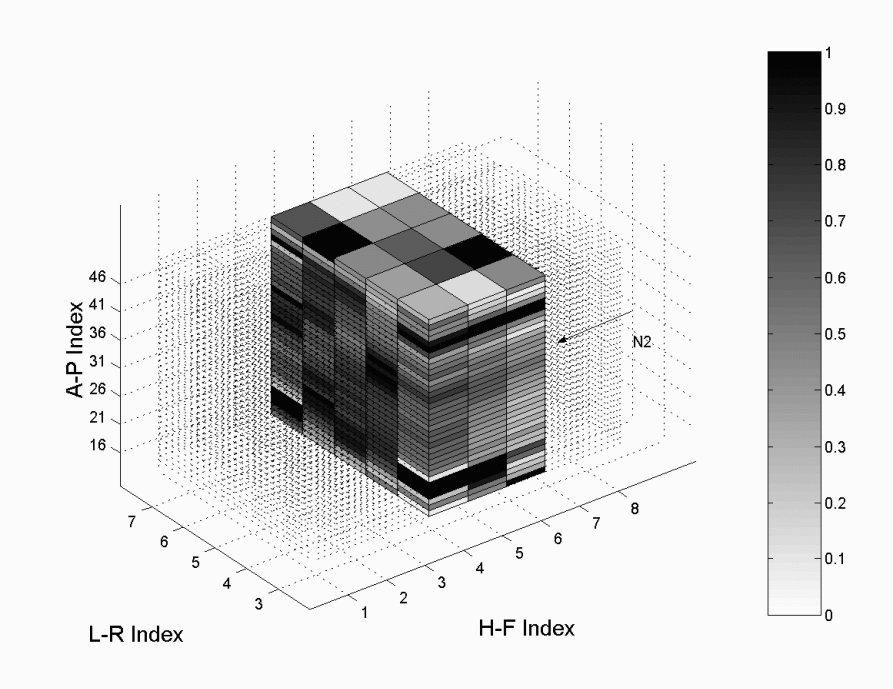

Fig. 59. Three-Dimensional Saturation Slice Distribution for the Second Saturation Level (axial plane, side view)

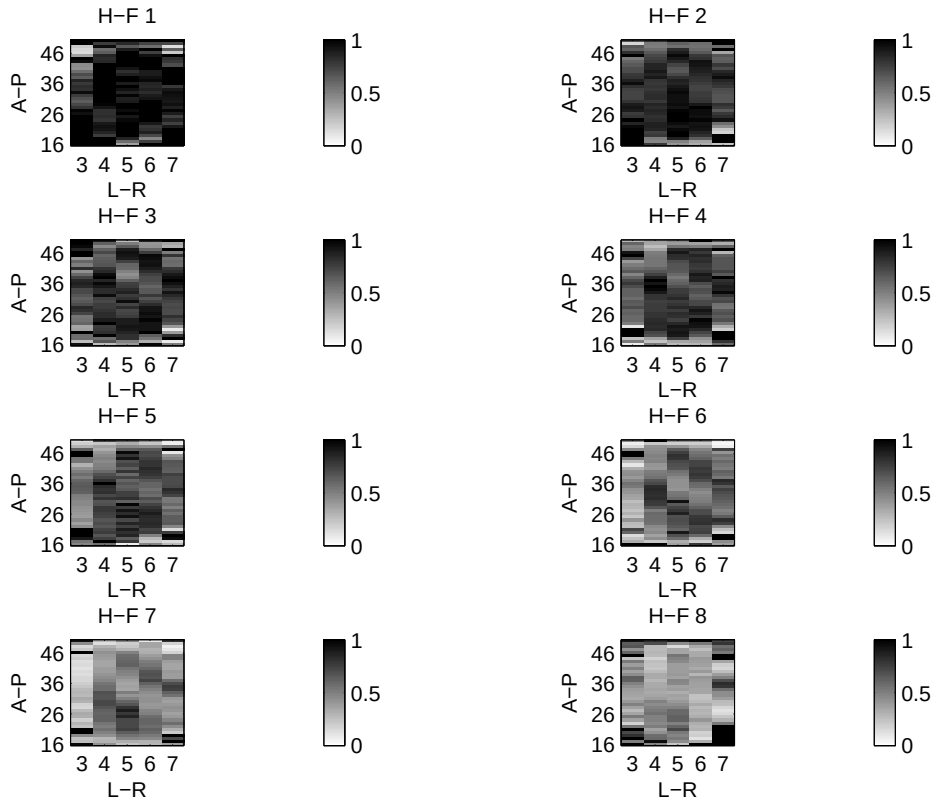

Fig. 60. Three-Dimensional Saturation Slice Distribution for the Second Saturation Level (axial plane, front view)

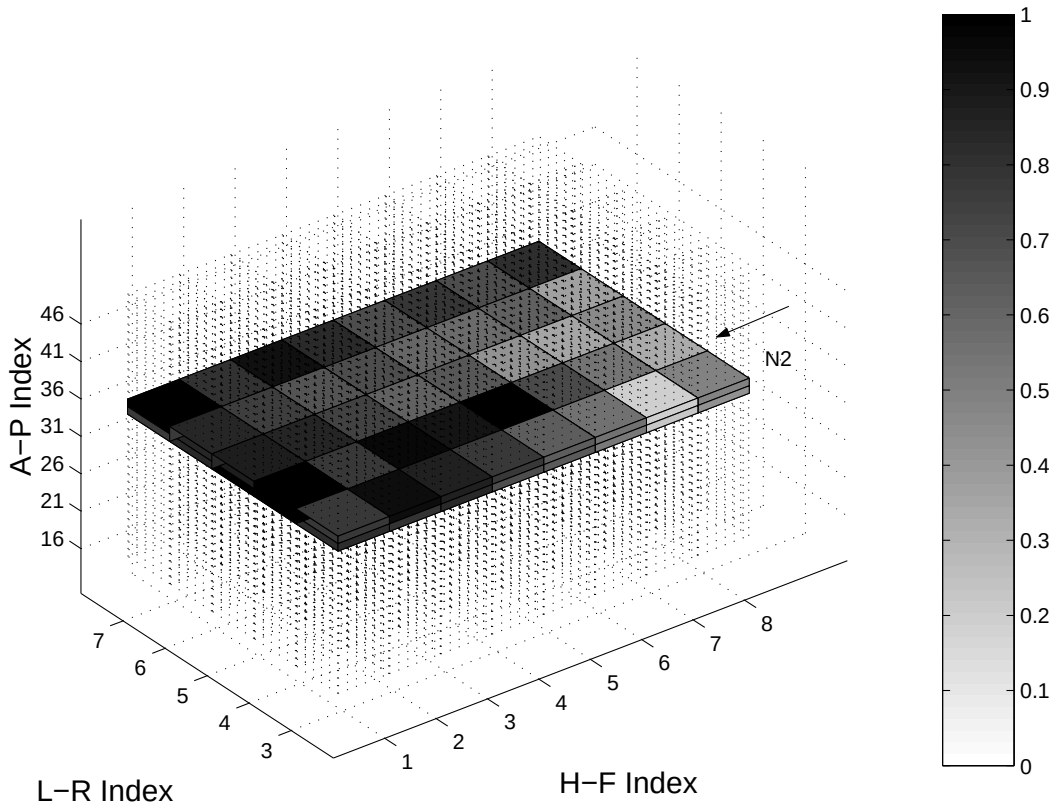

Fig. 61. Three-Dimensional Saturation Slice Distribution for the Second Saturation Level (coronal plane, side view)

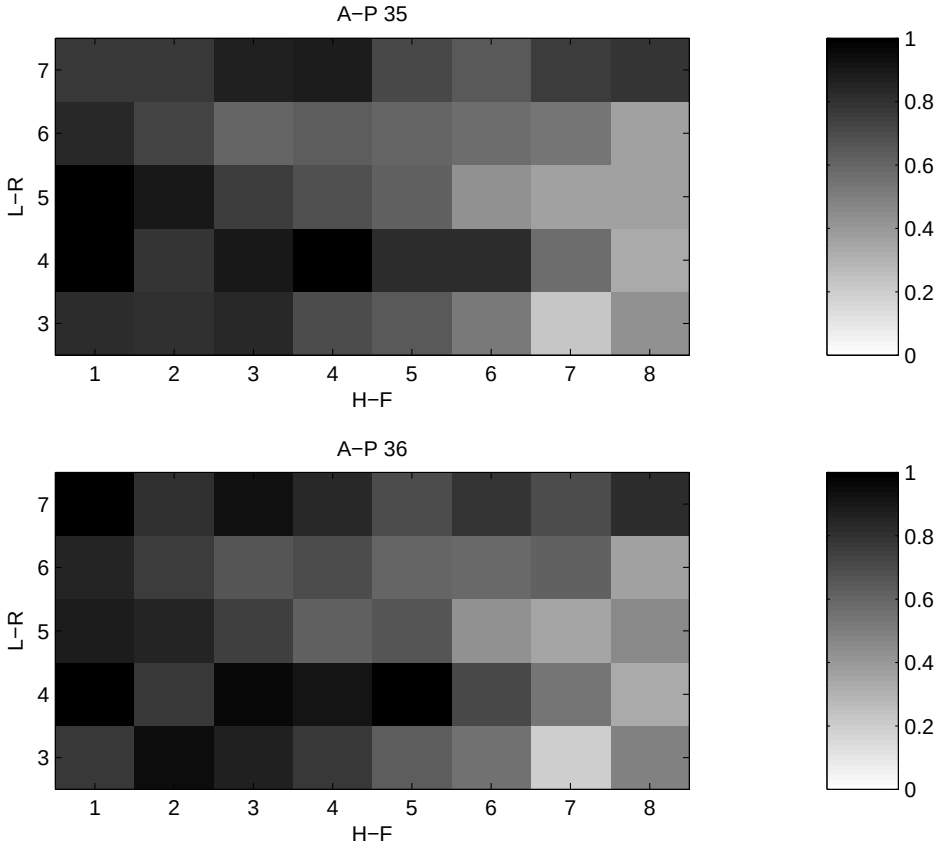

Fig. 62. Three-Dimensional Saturation Slice Distribution for the Second Saturation Level (coronal plane, front view)

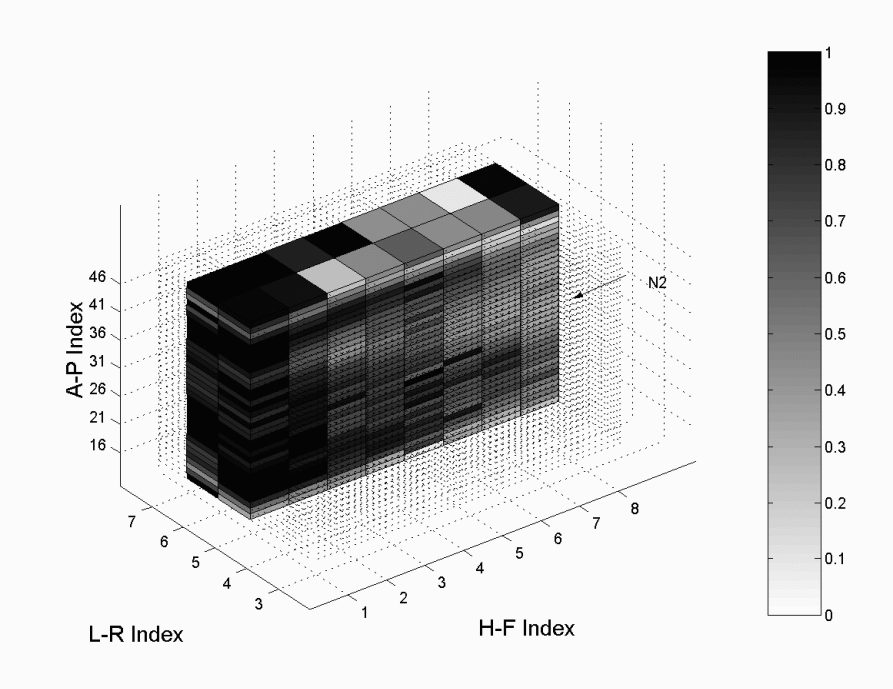

Fig. 63. Three-Dimensional Saturation Slice Distribution for the Second Saturation Level (sagittal plane, side view)

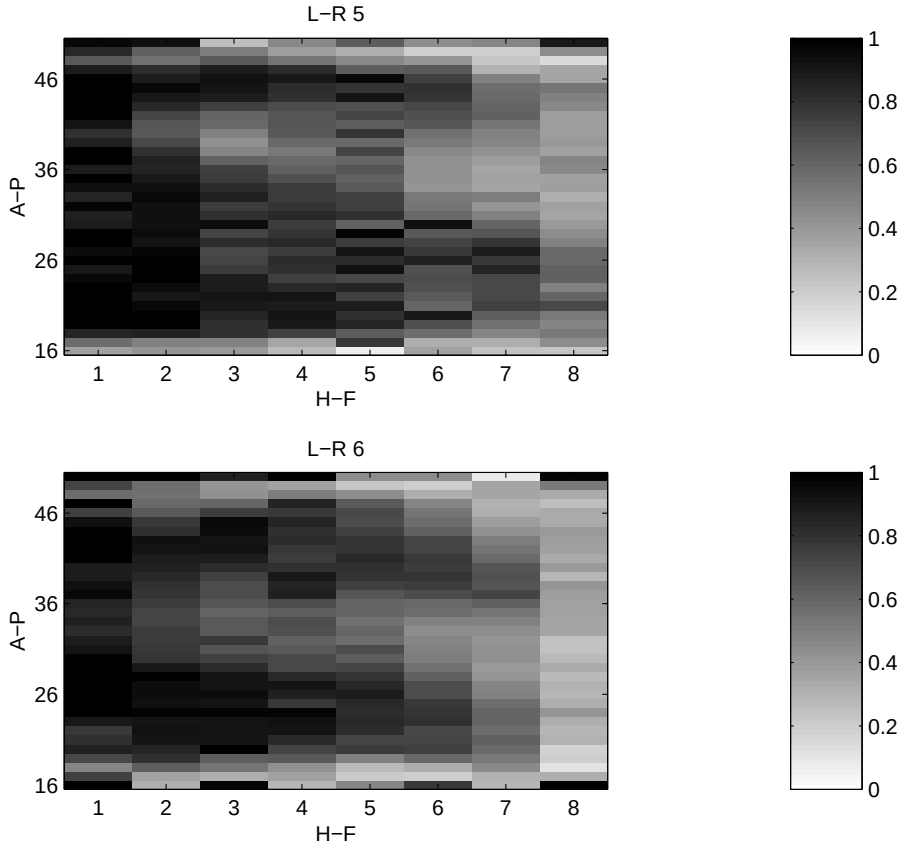

Fig. 64. Three-Dimensional Saturation Slice Distribution for the Second Saturation Level (sagittal plane, front view)

As can be expected, the overall saturation gradually decreases from the first saturation level to the third saturation level. From Figures 55, 57, 61, 63, 67 and 69, it can be observed that the saturation increases along the N_2 injection direction (see small arrow in figure). Figures 56, 58, 62, 64, 68 and 70 show a blurry preferential path for the fluid movement during the desaturation process, where the front of displacing phase is not planar, but fingerlike, which may caused by instability happened in immiscible displacement process (Aleman and Slattery, 1988; de Rooij, 2000).

From Figures 58, 64 and 70, the low saturation regions mainly distribute around the N_2 injection entrance and the brim of the sample. The explanation for the unusual low saturation on the edges is the inaccuracy in defining the sample edge relative to the voxel. The sample used in the experiment is cylindrical, however, the shape of the field of view defined in the NMR experiment can only be set rectangular. As a result, the voxels around the boundary of the sample are those which are located completely outside the sample region and partially outside the sample region (see the grey part of Figure 40). Then, the determined saturation values, for the blocks located completely outside the sample region, have no meaning since the obtained signal is pure noise.

Based on this reason, we further limit the sample voxels range. Figure 71 shows the relative position of the revised sample region in the sample and field of view (FOV). Figure 71 is plotted by assuming that the center of the sample overlaps with the center of the FOV and the sample is in perfect cylinder shape. The revised voxel range of the sample is provided in Table XVII and all the voxels in the revised range is completely in the sample region. Averaging the saturations from all the voxels in the revised range, the mean saturations we got for the three saturation level are provided in Table XVIII.

The three-dimensionally resolved porosity distribution is determined by three-

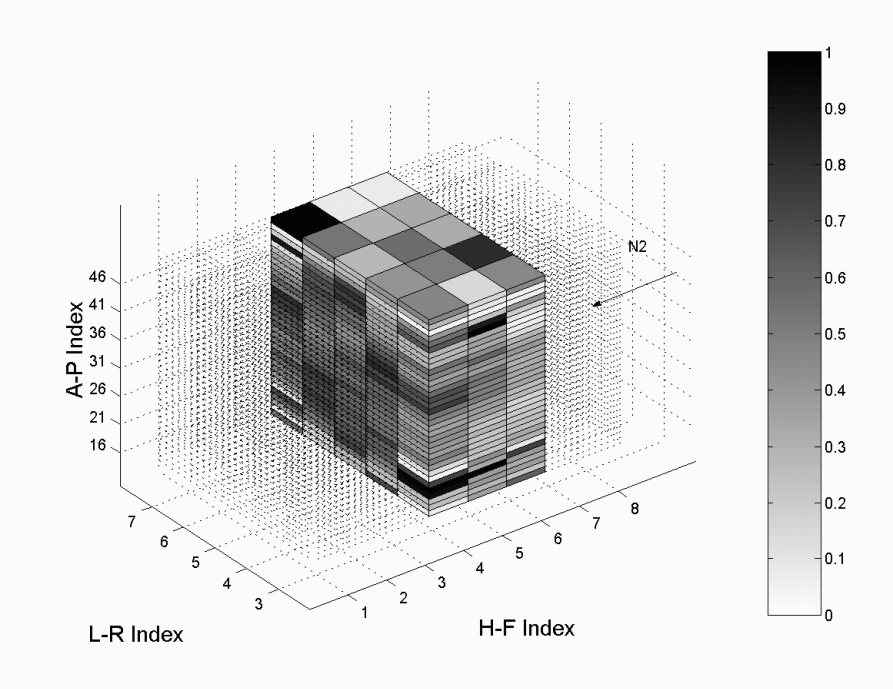

Fig. 65. Three-Dimensional Saturation Slice Distribution for the Third Saturation Level (axial plane, side view)

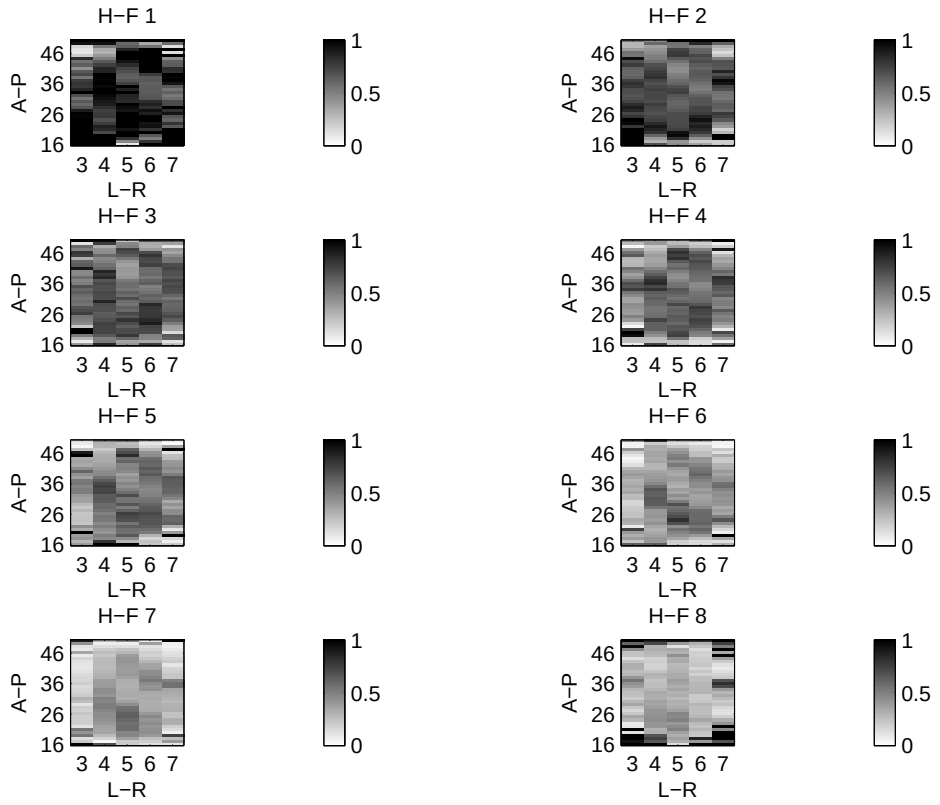

Fig. 66. Three-Dimensional Saturation Slice Distribution for the Third Saturation Level (axial plane, front view)

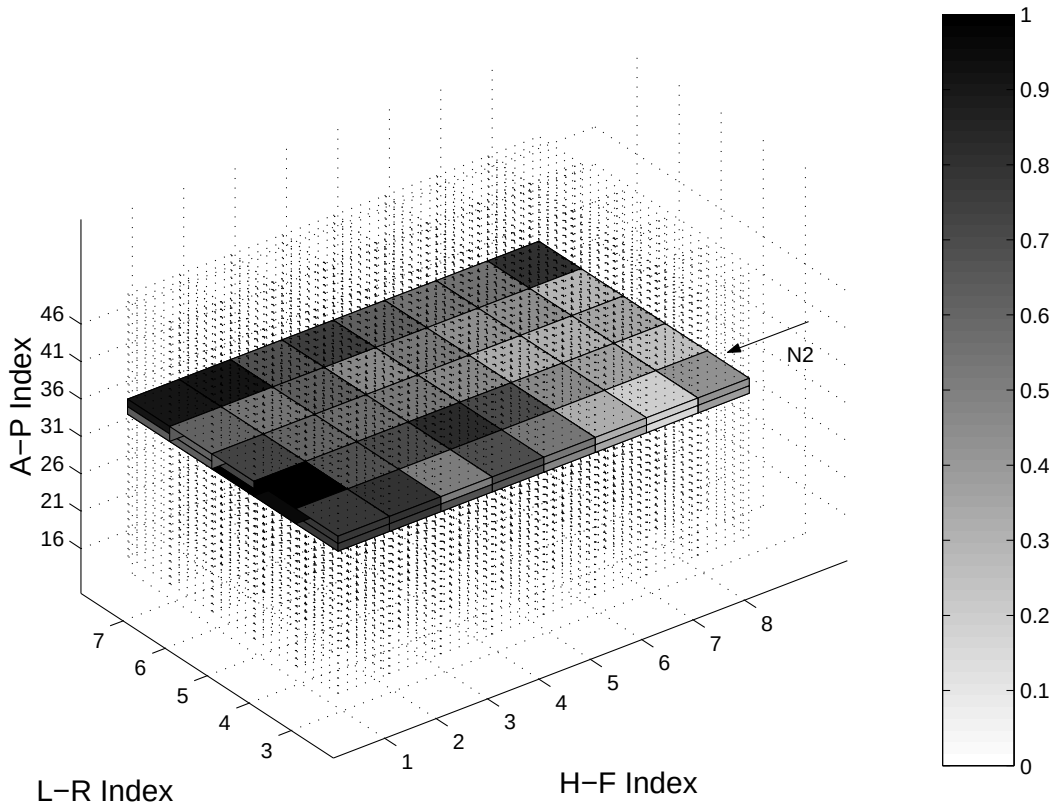

Fig. 67. Three-Dimensional Saturation Slice Distribution for the Third Saturation Level (coronal plane, side view)

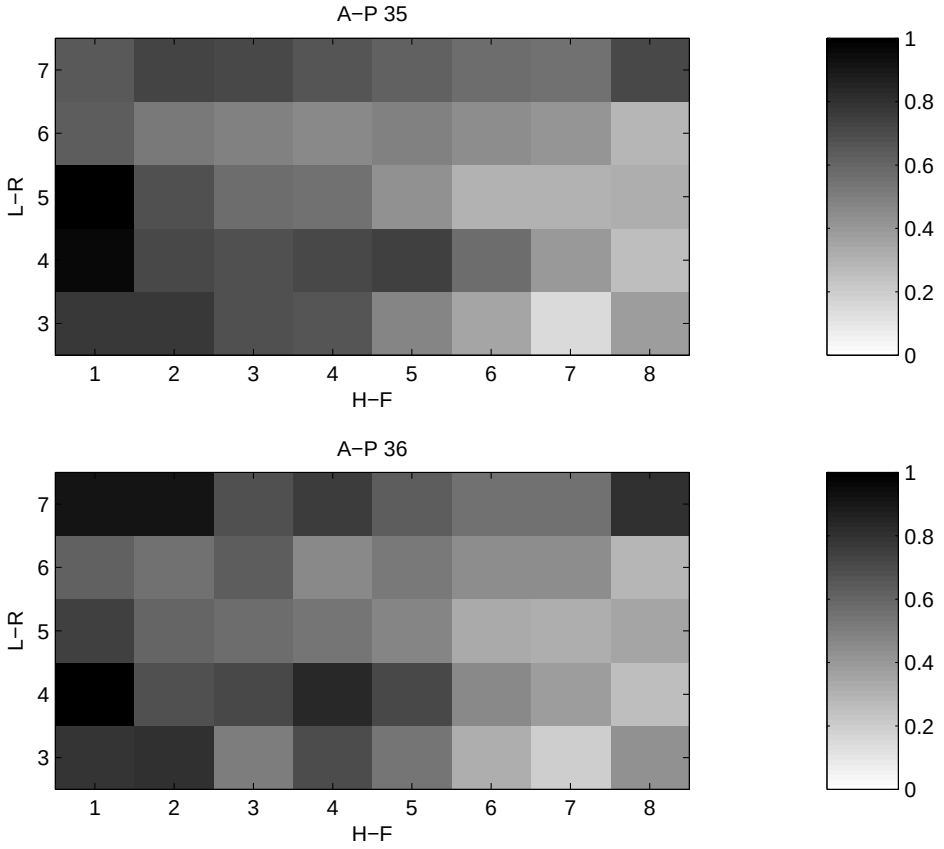

Fig. 68. Three-Dimensional Saturation Slice Distribution for the Third Saturation Level (coronal plane, front view)

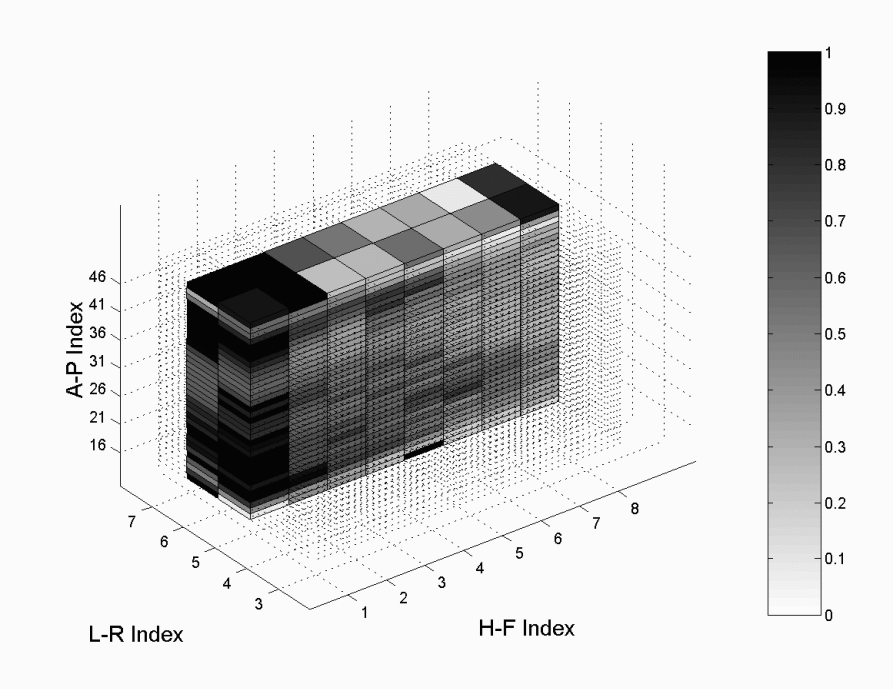

Fig. 69. Three-Dimensional Saturation Slice Distribution for the Third Saturation Level (sagittal plane, side view)

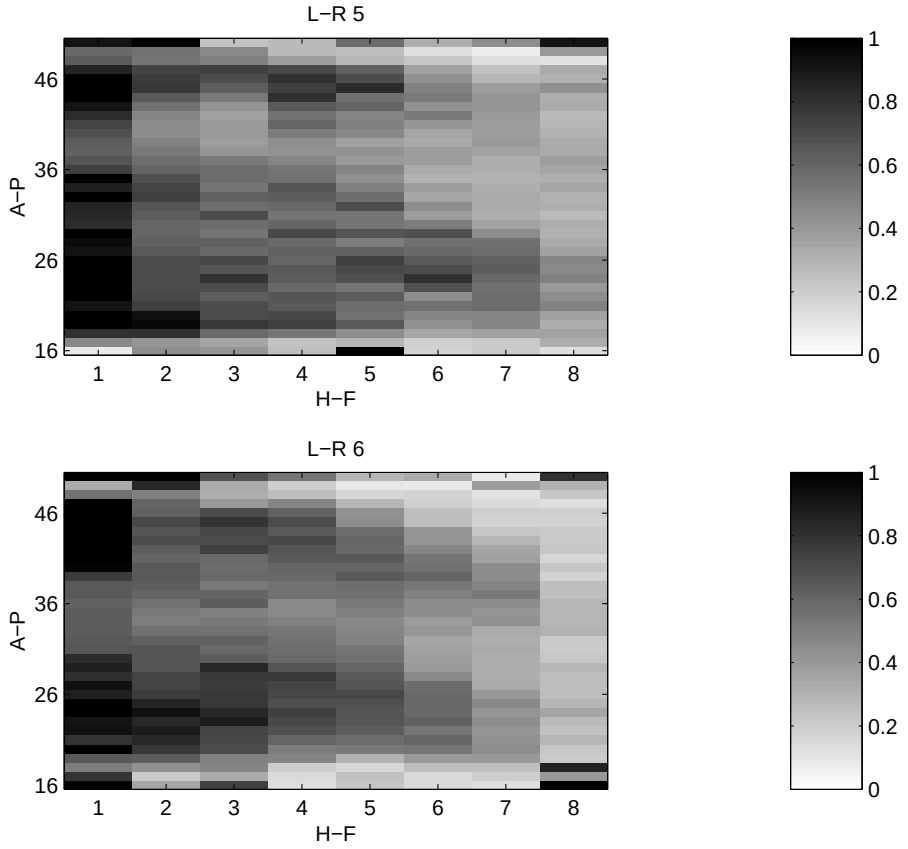

Fig. 70. Three-Dimensional Saturation Slice Distribution for the Third Saturation Level (sagittal plane, front view)

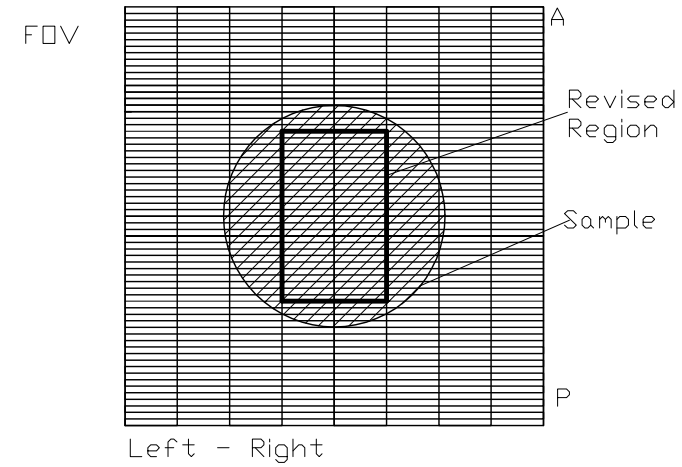

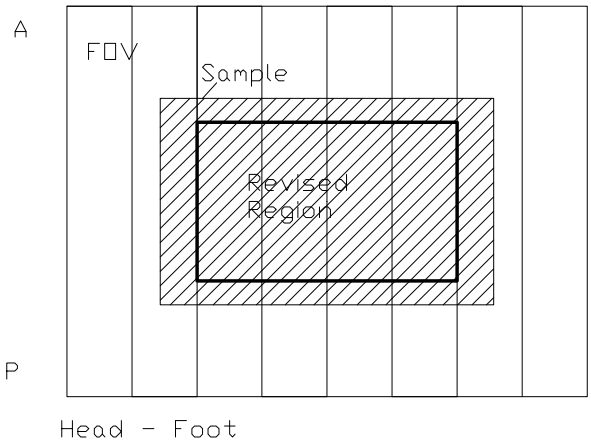

Fig. 71. Revised Region View

Table XVII. Revised Sample Voxels Range

Sample Limits in A-P Direction	20-45
Sample Limits in H-F Direction	3-6
Sample Limits in L-R Direction	4-5

Table XVIII. Average Saturations for Three Saturation Levels

Saturation for the First Saturation Level	0.9 ± 0.1
Saturation for the Second Saturation Level	0.7 ± 0.3
Saturation for the Third Saturation Level	0.6 ± 0.3

dimensional CPMG imaging according Eq. 3.7. The amount of the fluid in the sample are used to determine the proportionality k in Eq. 3.7. The porosity calculation of the example voxel (34, 3, 4) is given in Table XIX. Here, the porosities only located in the revised range are determined since we are unable to determine the fraction of voxel volume in which is partially occupied by the water. Averaging the porosity values from all the voxels in the revised range, the mean porosity with the range which contains 95% porosity values is provided in Table XIX. The determined average value is a little bit less than the gravimetrically determined value (0.25). The explanation is that gravimetrically determined value is the average porosity for the entire sample.

The three-dimensional porosity distribution is shown in Figures 72-77 as a series of two-dimensional images in axial, sagittal and coronal slices. A side view and front view are given for the slice's representation. The different colors within these slices are assigned by the different porosity values encoded according to the color bar on the right. The location of the voxel can be found from the reading in the axis.

Table XIX. Porosity Determination Experiment

Sample Limits in A-P Direction	16-50
Sample Limits in H-F Direction	1-8
Sample Limits in L-R Direction	3-7
Intensity from the Voxels in the Above Range (M_o)	7.02×10^8
Total Water in the Sample (m)	5.28 g
k=M_o/m	1.33×10^8 g^{-1}
Intensity from Voxel (34, 3, 4) (First)	9.35×10^5
Voxel Size	0.75 mm × 6 mm × 8 mm
Water Density	1 mg/mm^3
Determined Porosity for Voxel (34, 3, 4)	0.20
Average Porosity in the Revised Range	0.20±0.08

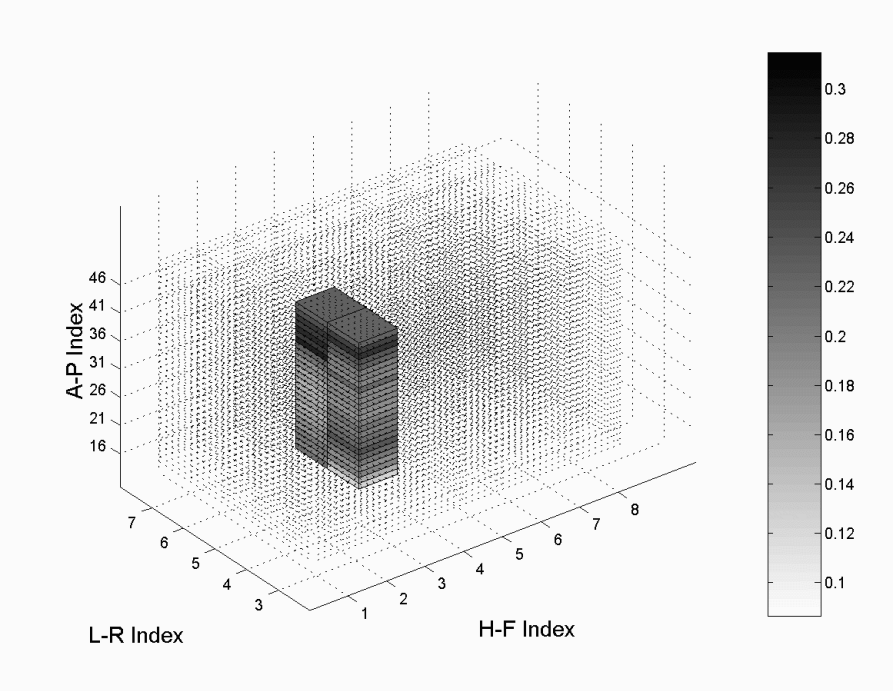

Fig. 72. Three-Dimensional Porosity Distribution (axial plane, side view)

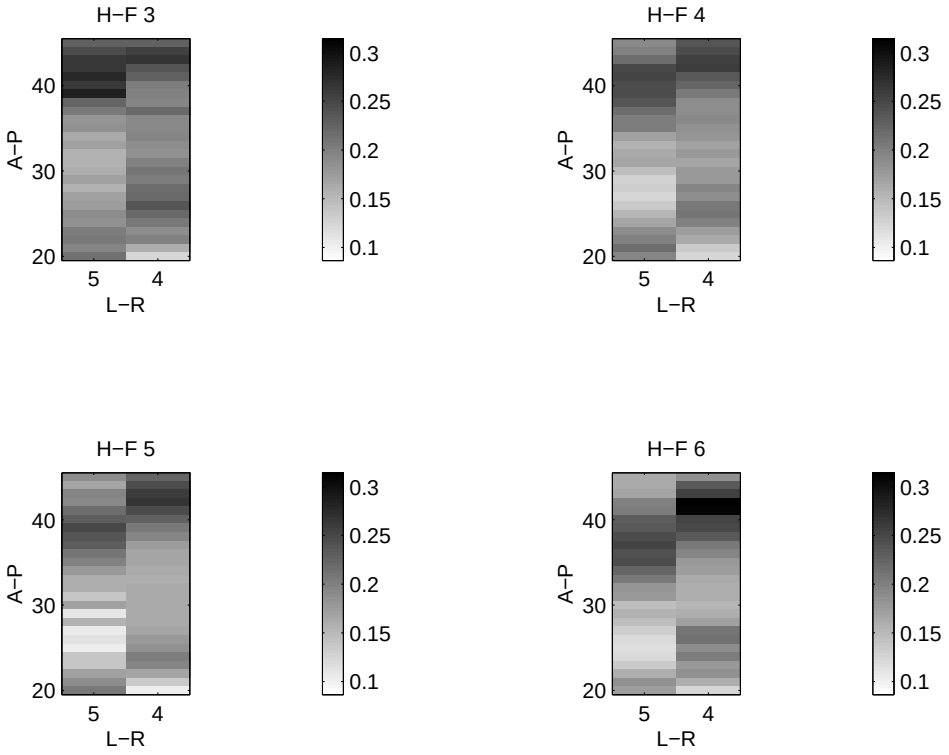

Fig. 73. Three-Dimensional Porosity Distribution (axial plane, front view)

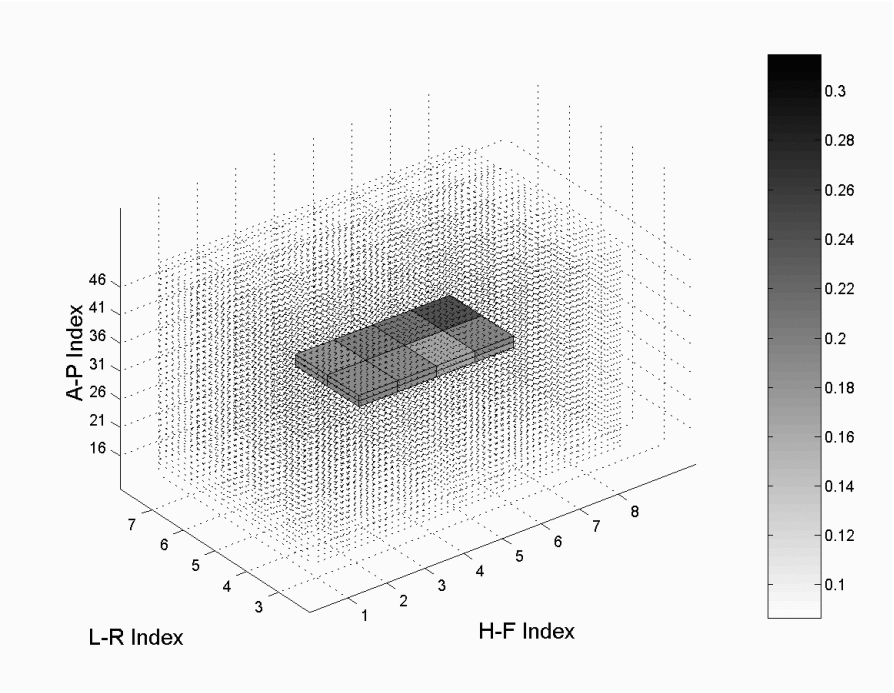

Fig. 74. Three-Dimensional Porosity Distribution (coronal plane, side view)

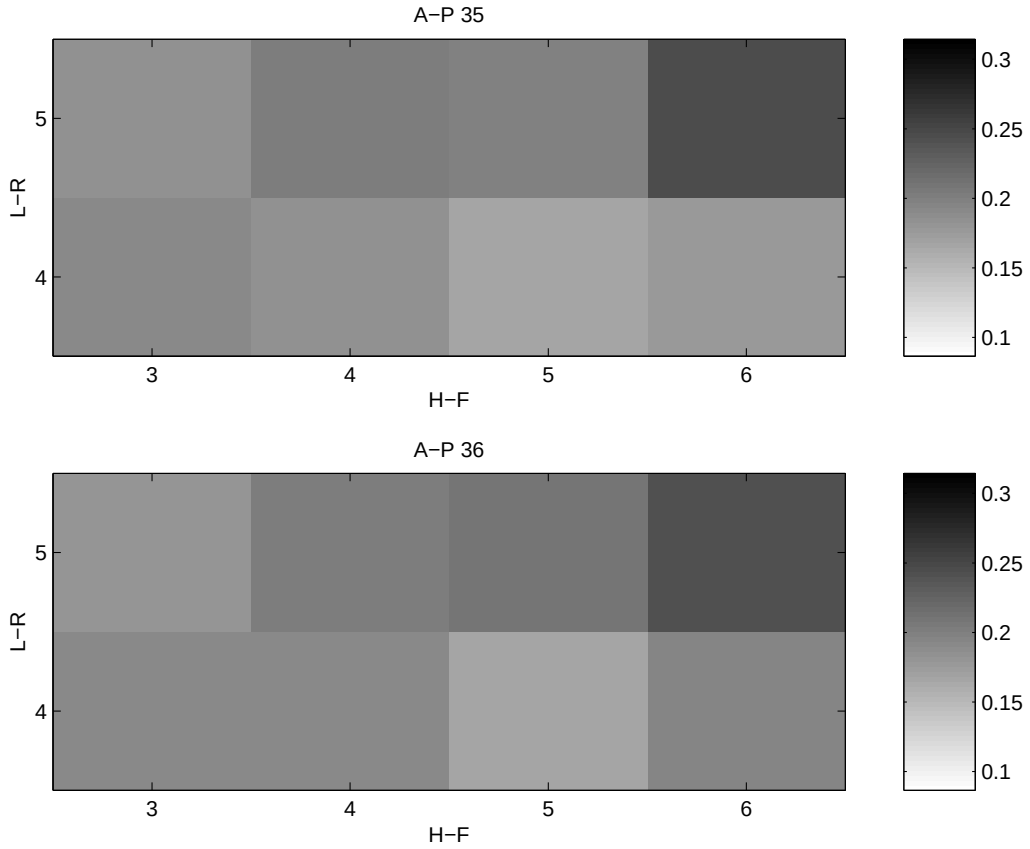

Fig. 75. Three-Dimensional Porosity Distribution (coronal plane, front view)

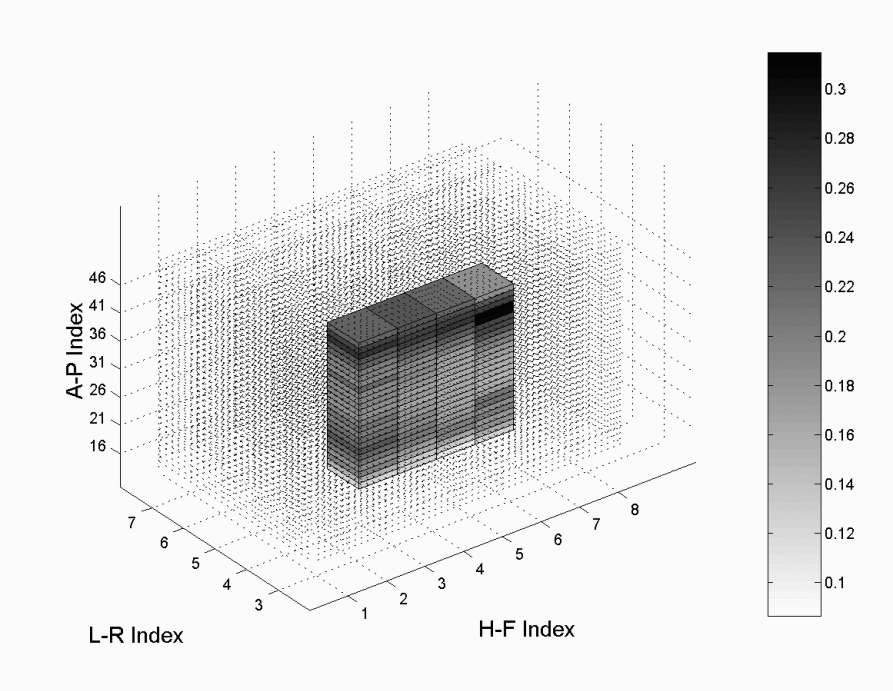

Fig. 76. Three-Dimensional Porosity Distribution (sagittal plane, side view)

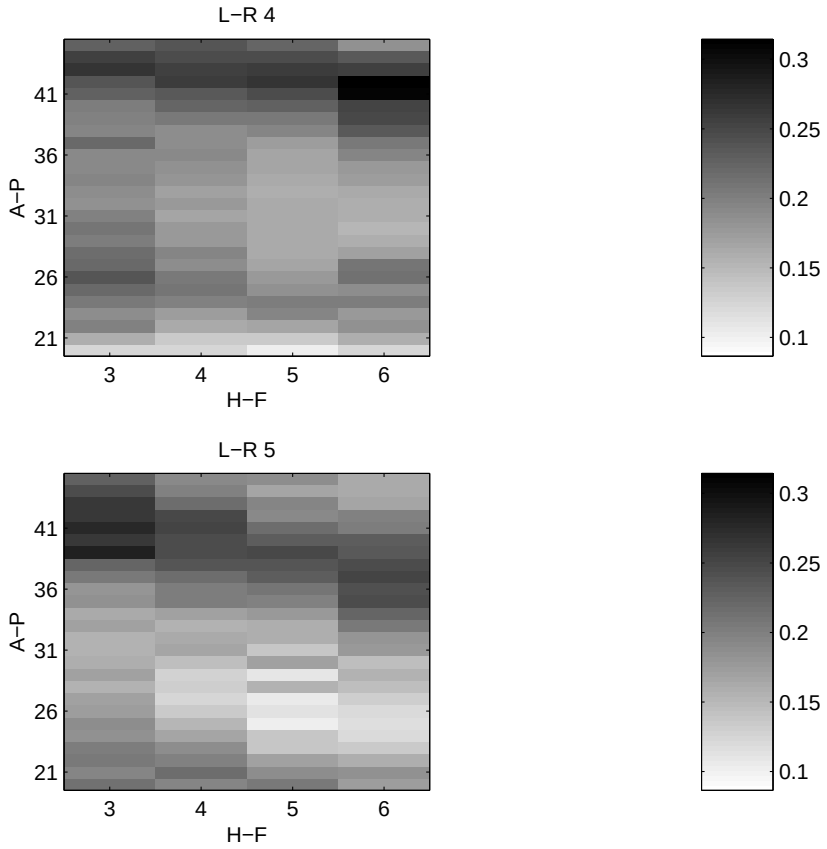

Fig. 77. Three-Dimensional Porosity Distribution (sagittal plane, front view)

Next, the results from inversion-recovery experiments are discussed. According to Eq. 3.10, the observed magnetization ranges from $-M_o$ at time t=0, back to M_o at $t = \infty$. For instance, the inversion recovery data of the voxel (35, 7, 6) from the first inversion-recovery experiment on the fully saturated sample and the three successive inversion recovery experiments on the partially saturated sample are shown in Figure 78. The relaxation of this voxel at different saturation levels are provided in the figure. All curves in the figure show a behavior as expected from the equation. The extrapolated equilibrium magnetization from the asymptotic value of the inversion-recovery data decreases when the saturation decreases. Similar behavior is observed for the voxel (30, 6, 6) which is shown in Figure 79. These two voxels represent typical phenomena according to observing all the voxels' results.

The determined T_1 distributions of all four inversion recovery experiments for the voxel (35, 7, 6) and (30, 6, 6) are shown in Figures 80 and 81. The area under the curves in the figures is proportional to the relative amount of water having the specific relaxation time. In the fully saturated state, the curve shows one peak. The relaxation rate of fluids in porous media depends on the relaxation rate of bulk-like fluid corresponding to region of fluid away from the pore boundaries, and a relaxation rate of surface fluid corresponding to a thin layer near the pore boundaries (Chen et al., 1993). The relaxation from both regimes cannot be distinguished from the curve and only an 'average' relaxation is observed. The T_1^{ave}s calculated from Eq. 3.16 for this voxel are provided in the Table XX. Chen et al. (1993) demonstrated that there is a linear relationship between pore size and characteristic relaxation time. In order to convert relaxation time distribution to pore-size distribution, a proportionality factor is required which could be determined from a surface relaxivity experiment by NMR diffusion measurement (Liaw et al., 1996). However, T_1 can be still regarded as a characteristic quantity representing the pore size. Larger pore has slow relaxation

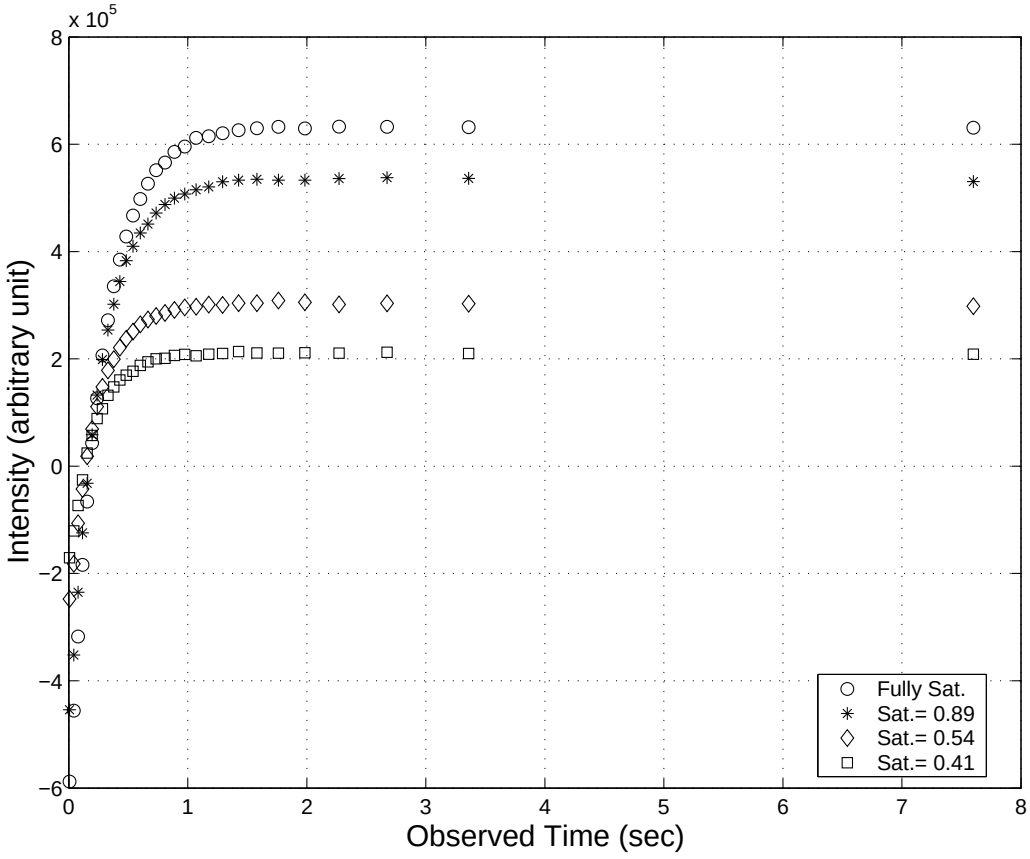

Fig. 78. Spin-Lattice Relaxation Data of Four Inversion-Recovery Experiments, Voxel (35, 7, 6)

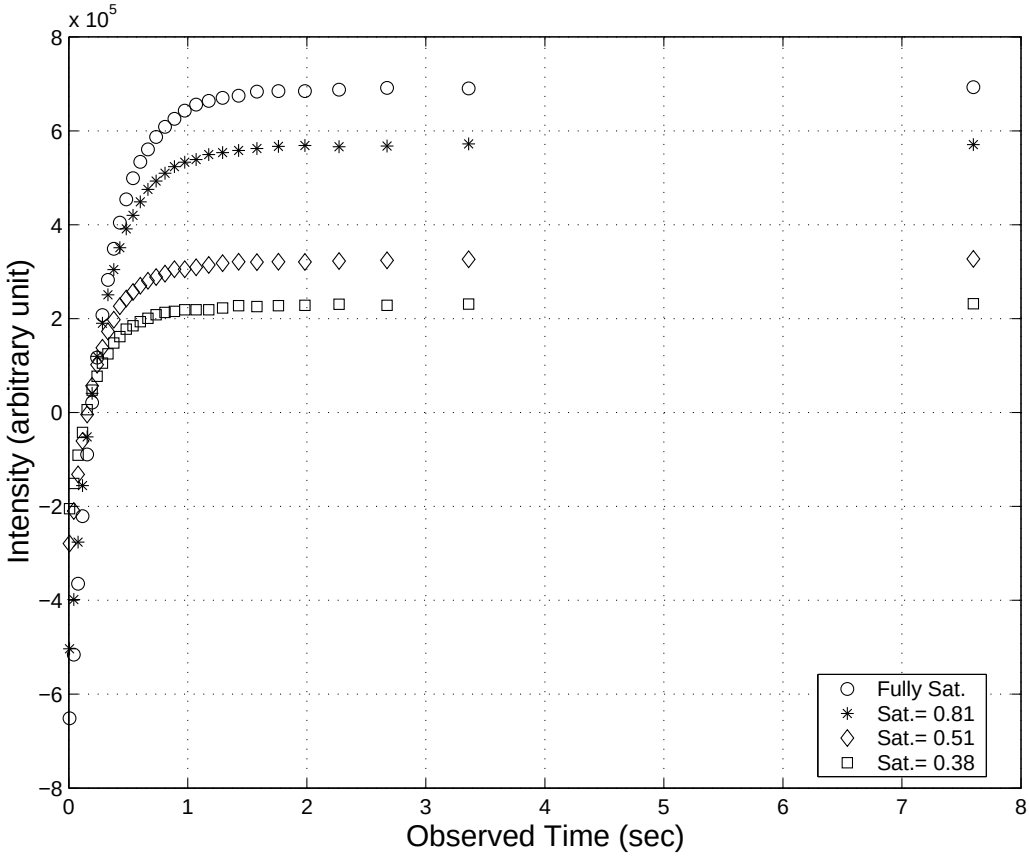

Fig. 79. Spin-Lattice Relaxation Data of Four Inversion-Recovery Experiments, Voxel (30, 6, 6)

due to the larger volume-to-surface ratio.

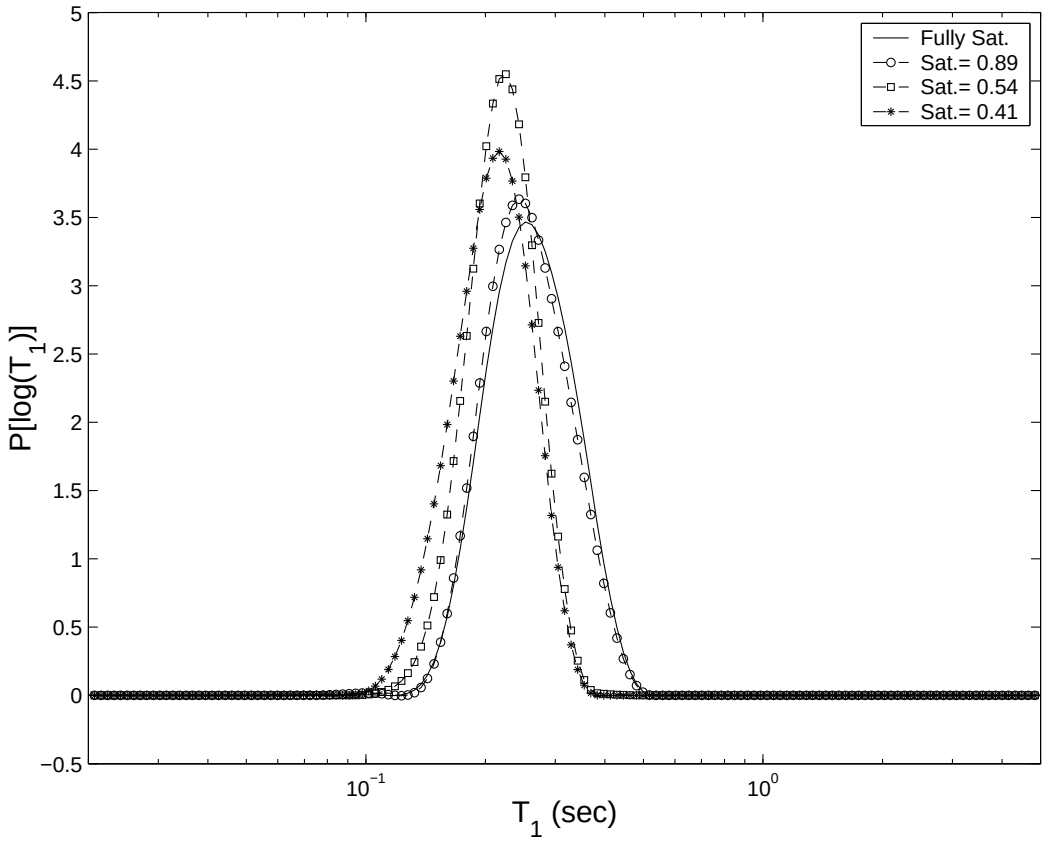

Fig. 80. Estimated T_1 Distribution of Four Inversion-Recovery Experiment, Voxel (35, 7, 6)

It is observed from the two Figures 80 and 81 that the peak shifts to the left, *i.e.*, towards the fast relaxation time region when the saturation decreases. This behavior gives a clear visualization of the desaturation process: most of the water leaves the larger pores. Since the larger pores have a slow relaxation, a larger fraction of its water which has the slow relaxation is replaced by gas when saturation decreases. As a result, the relaxation contributed from the fast relaxation increases and the 'average' relaxation time becomes less when saturation is lowered (see Table XX).

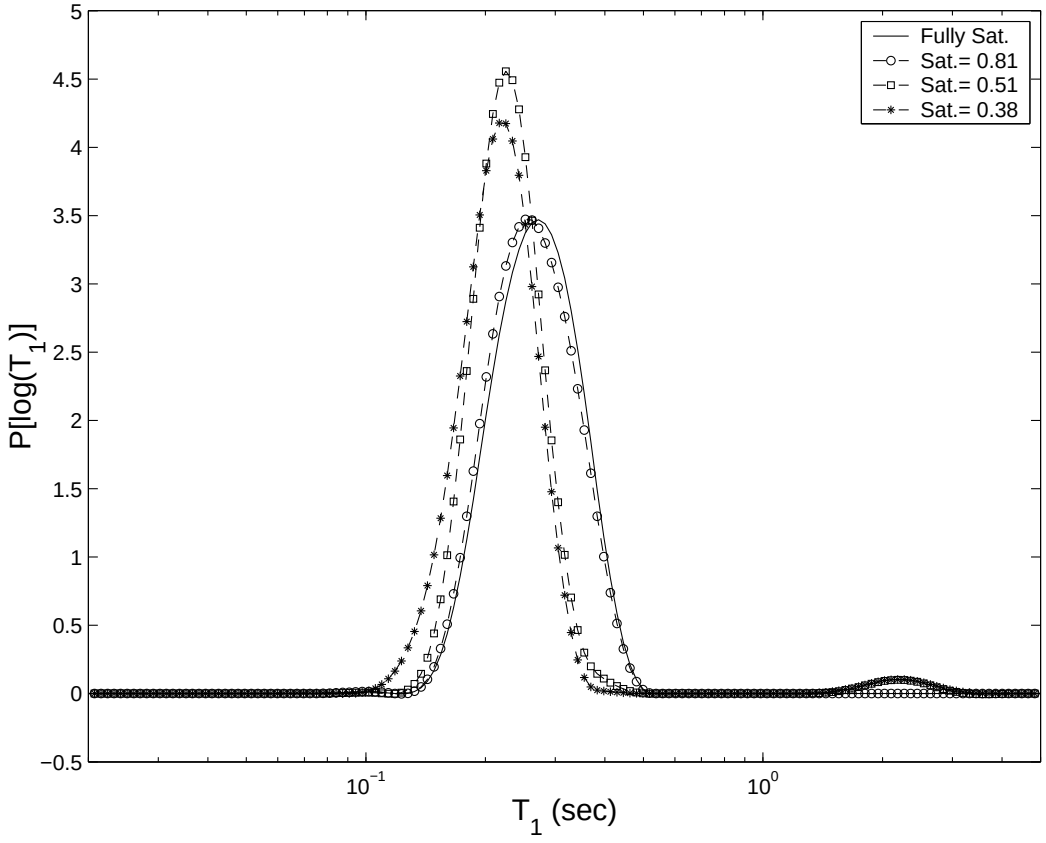

Fig. 81. Estimated T_1 Distribution of Four Inversion-Recovery Experiment, Voxel (30, 6, 6)

Table XX. Inversion-Recovery Experiments

Voxel (35, 7, 6)		
Inversion-Recovery Experiment No.	T_1^{ave}(sec)	Saturation
1	0.25	1
2	0.24	0.88
3	0.21	0.54
4	0.20	0.41
Voxel (30, 6, 6)		
Inversion-Recovery Experiment No.	T_1^{ave} (sec)	Saturation
1	0.26	1
2	0.25	0.81
3	0.23	0.51
4	0.21	0.38

In Figure 81, the curve of the third and fourth saturation states shows two peaks. The right peaks around 2 seconds T_1, we believe are artifacts. From the literature, even free bulk water does not have such a long T_1 unless it has been 'cleaned' of oxygen gas (Simpson and Carr, 1958). The reason for the occurrence of the small peak may come from the experimental data quality. There are indeed some fluctuations in the relaxation data around the 1 second for both of the third and fourth saturation levels in Figure 79. The distribution function $P(\tau)$ is determined from the regression methodology discussed in Section B. The quality of the experimental data influences the determined distribution function. Between the relaxation time $3s$ and $7.5s$, there is a big gap in Figures 78 and 79. It would be desirable to fill in more data points in

future experiment to get more accurate distribution results.

The three-dimensional average relaxation distribution for the fully saturated case is shown in Figures 82-87 as a series of two-dimensional images in axial, sagittal and coronal slices. The average relaxations only located in the revised range are presented since we want avoid trouble brought from the voxels which are located completely outside the sample. For these voxels, the signal is pure noise. A side view and front view are given for the slice's representation. The different colors within these slices are assigned by the different relaxation time in second encoded according to the color bar on the right. The mean of the average relaxation is calculated as 0.27 ± 0.07 second. The range contains 95% of relaxation data.

According to Eq. 3.2, the characteristic relaxation time τ is defined from the experimental relaxation value by elimination the bulk relaxation. Figures 88 and 89 plot the τ as function of saturation S_w for voxels (35, 7, 6) and (30, 6, 6). Figure 90 gives the τ as function of saturation S_w for all the voxels. The scattered behavior in the figure is due to the different relaxation rate at different voxel. In order to find the relation between the relaxation and saturation of each voxel, Figure 91 is presented. Each line in the plots of Figure 91 connects the data points for each voxel in the sample. To avoid the lines' overlapping, each plot in Figures 92 and 93 only gives 60 voxels. Monotonic decrease in relaxation times with S_w is observed for most of the voxels. This behavior indicates again that the fluid which has the fast relaxation rate prefers to stay when saturation decreases, whereas the larger fraction of fluid which has the slow relaxation rate is replaced by gas. There are indeed some fluctuations in these plots. The reason may come from the the inaccurate determination of the relaxation and saturation.

With the determined τ_1 and S_w, the wetting phase $k_{r,w}$ can be calculated through Eqs. 3.3 by assuming $S_{wi} = 0$. Figure 94 plots $k_{r,w}$ vs. S_w with assumption $S_{wi} = 0$.

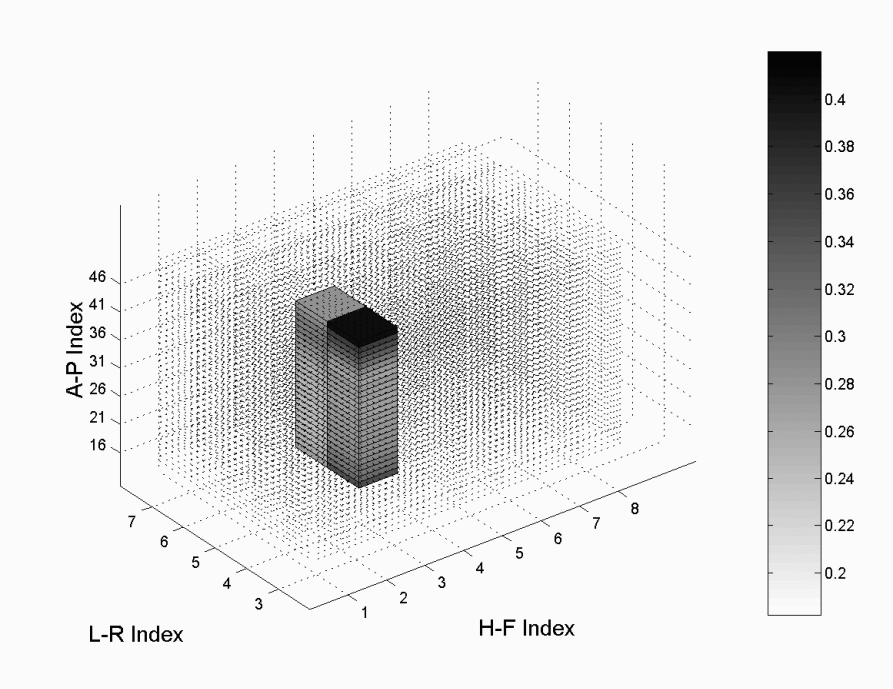

Fig. 82. Three-Dimensional Relaxation Distribution for the Fully Saturated State (axial plane, side view)

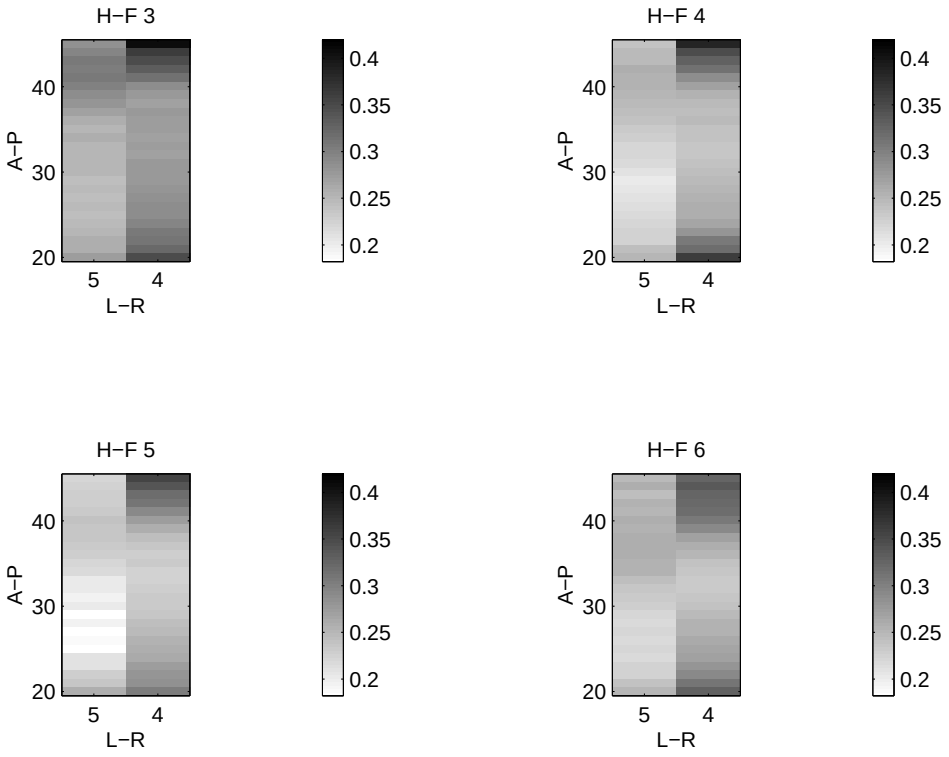

Fig. 83. Three-Dimensional Relaxation Distribution for the Fully Saturated State (axial plane, front view)

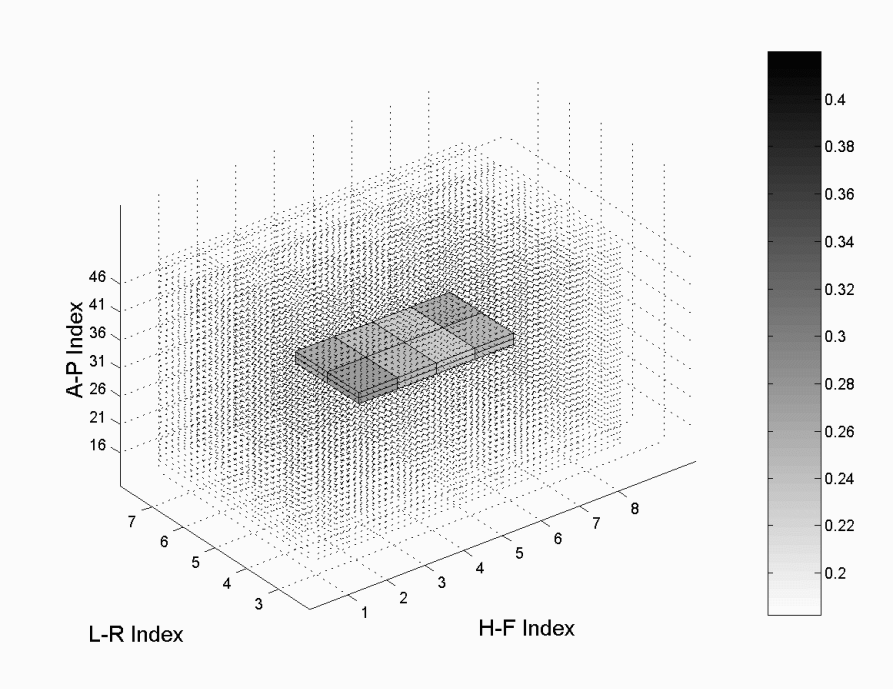

Fig. 84. Three-Dimensional Relaxation Distribution for the Fully Saturated State (coronal plane, side view)

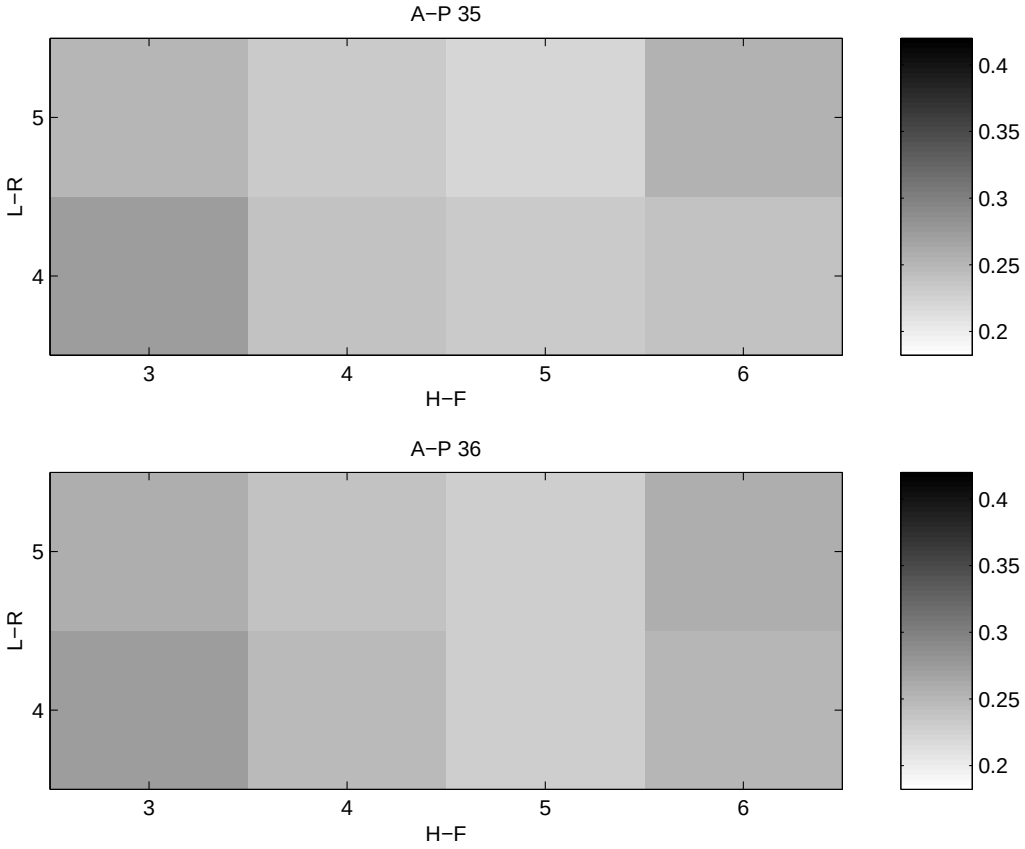

Fig. 85. Three-Dimensional Relaxation Distribution for the Fully Saturated State (coronal plane, front view)

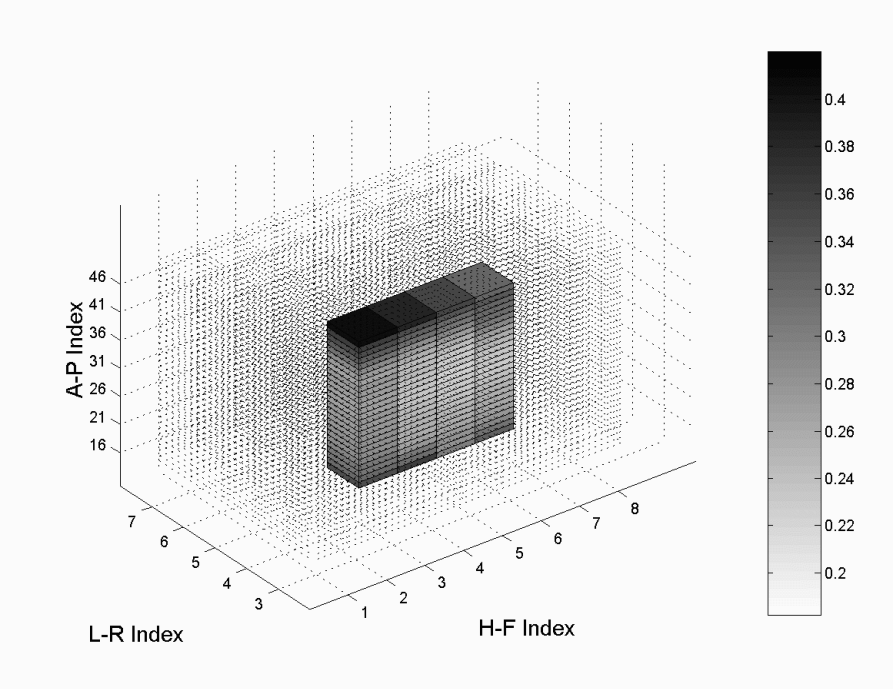

Fig. 86. Three-Dimensional Relaxation Distribution for the Fully Saturated State (sagittal plane, side view)

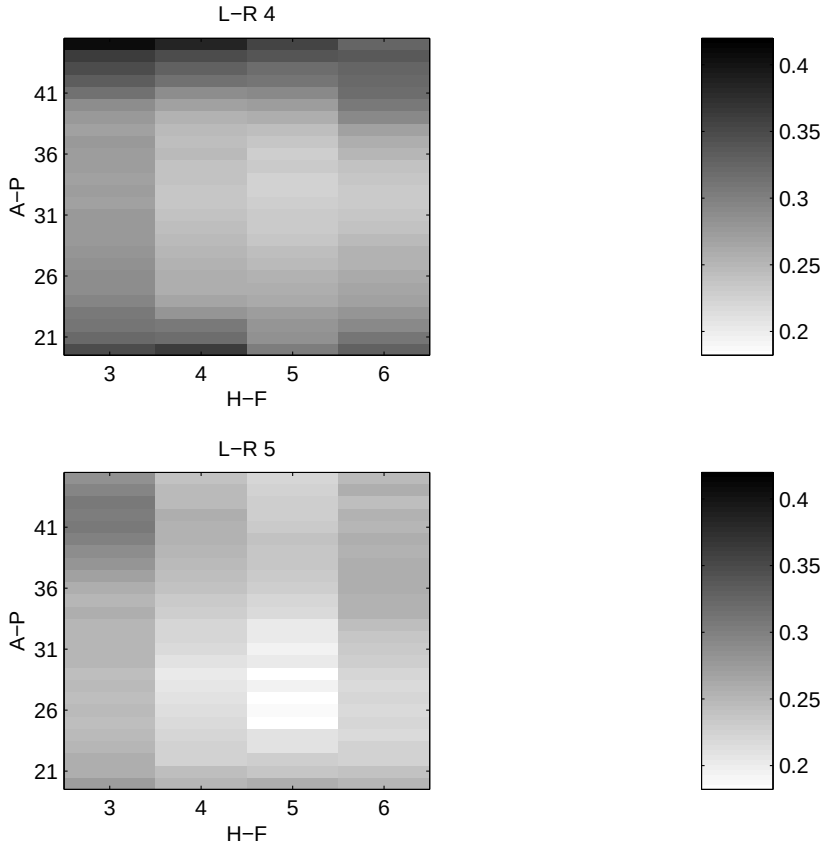

Fig. 87. Three-Dimensional Relaxation Distribution for the Fully Saturated State (sagittal plane, front view)

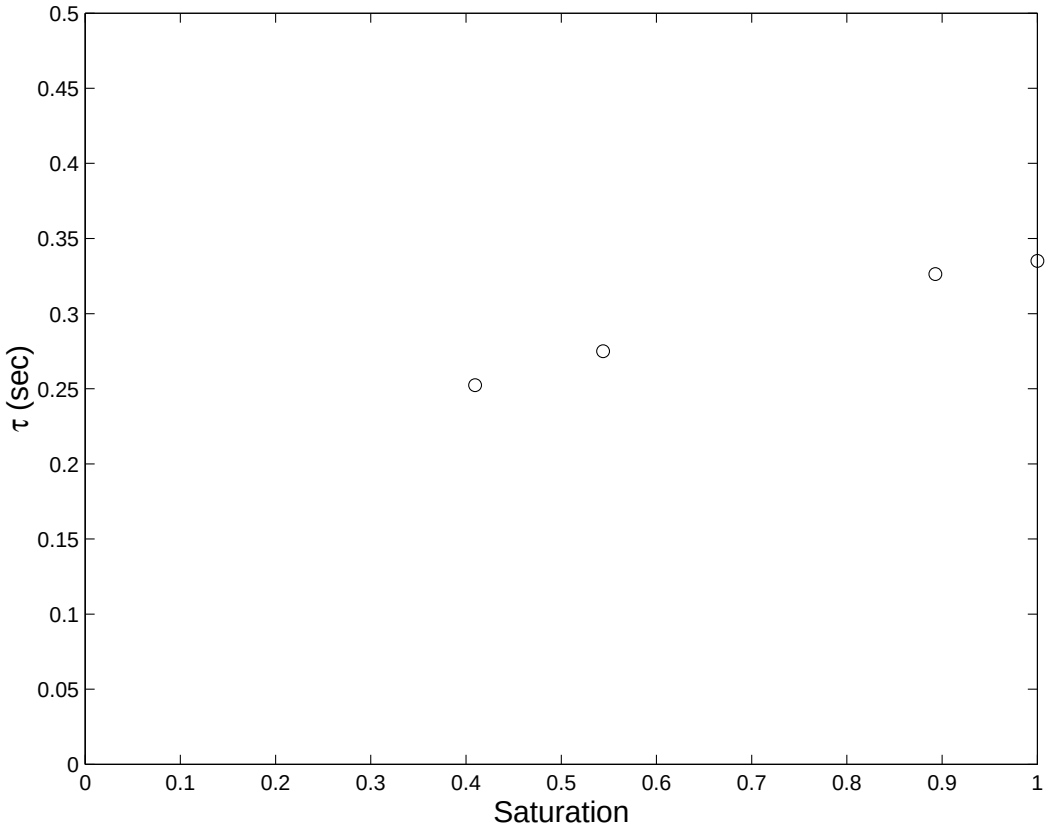

Fig. 88. τ vs. S_w for Voxel (35, 7, 6)

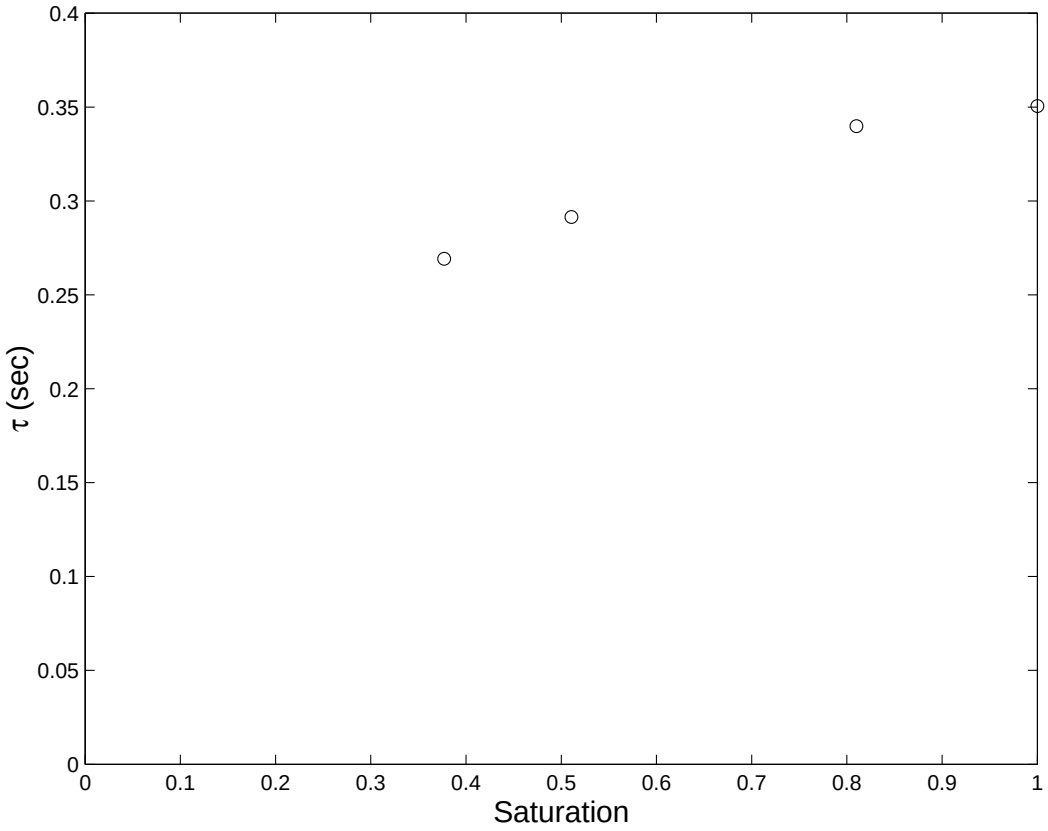

Fig. 89. τ vs. S_w for Voxel (30, 6, 6)

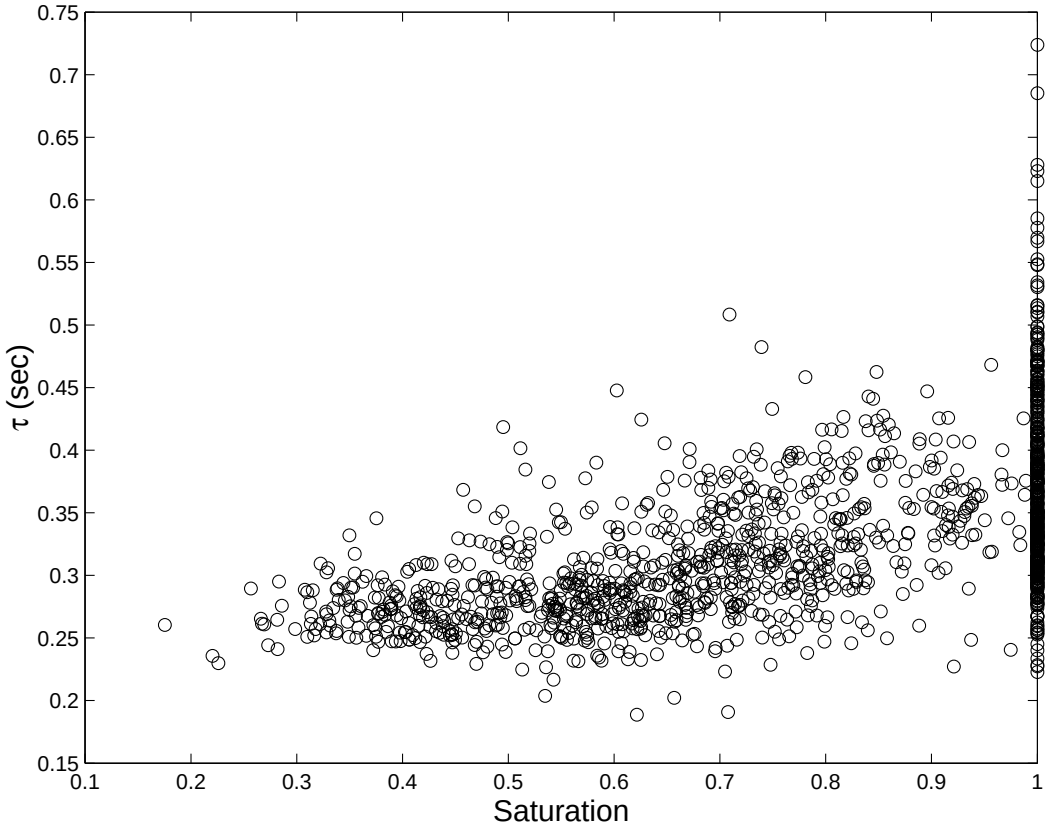

Fig. 90. τ vs. S_w for All Voxels

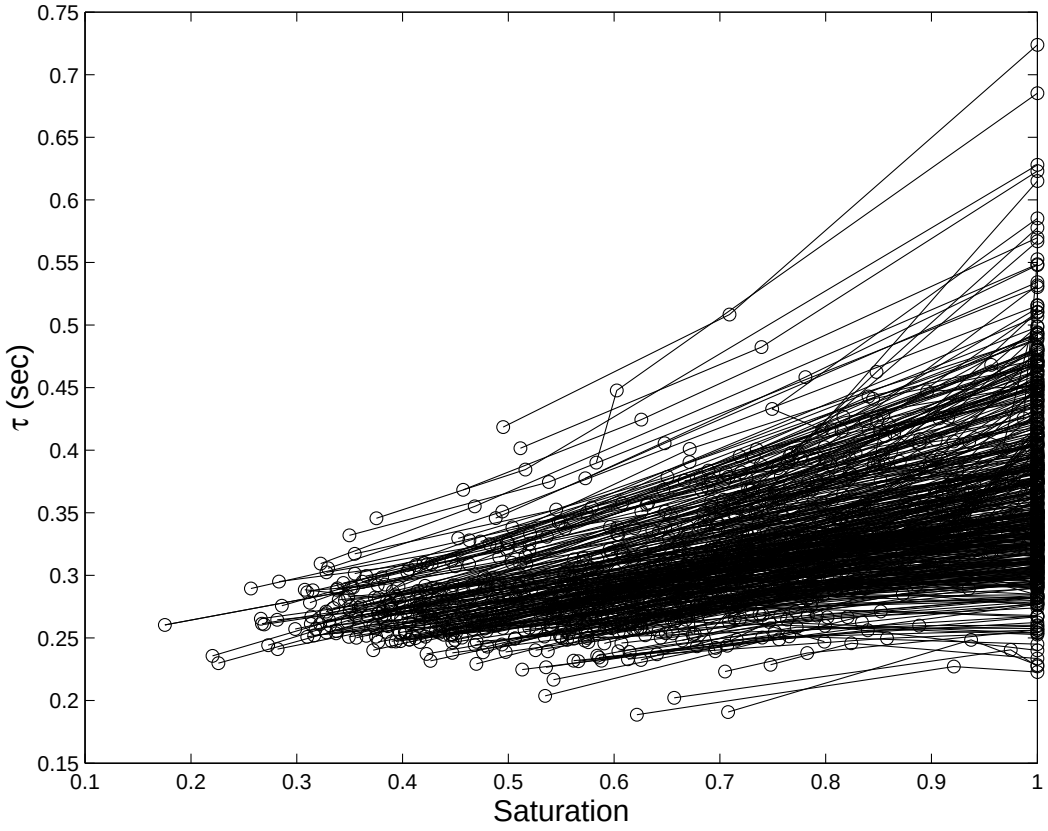

Fig. 91. τ vs. S_w for All Voxels Connected with Lines

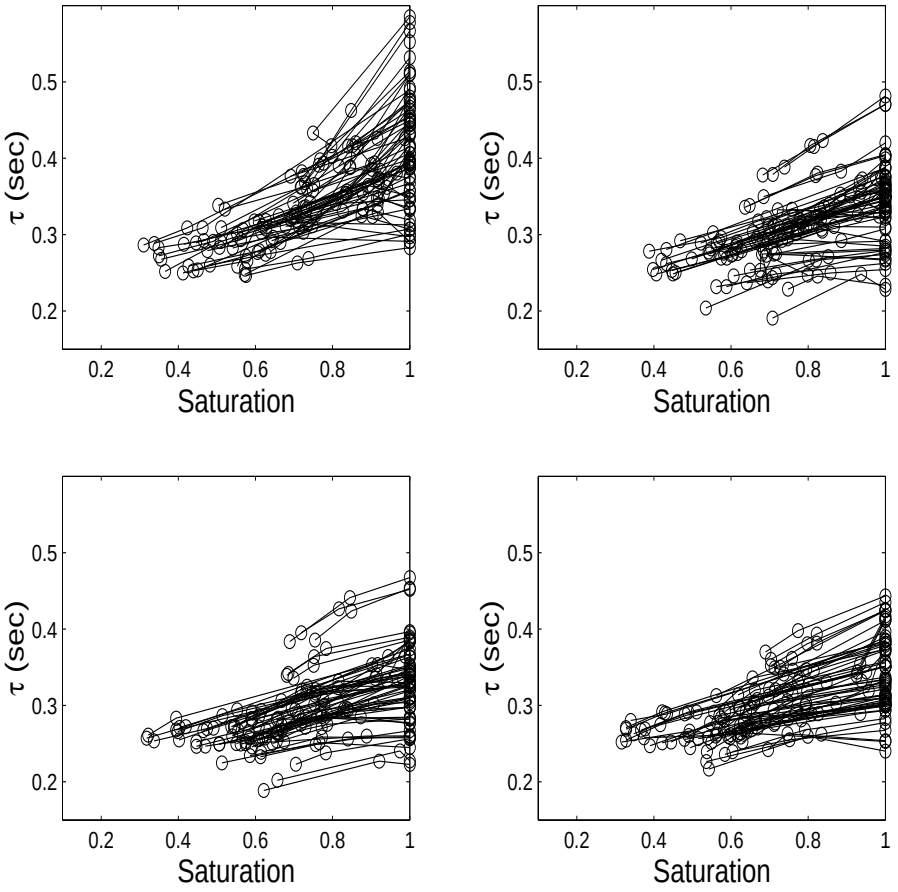

Fig. 92. Subplot for τ vs. S_w Connected with Lines

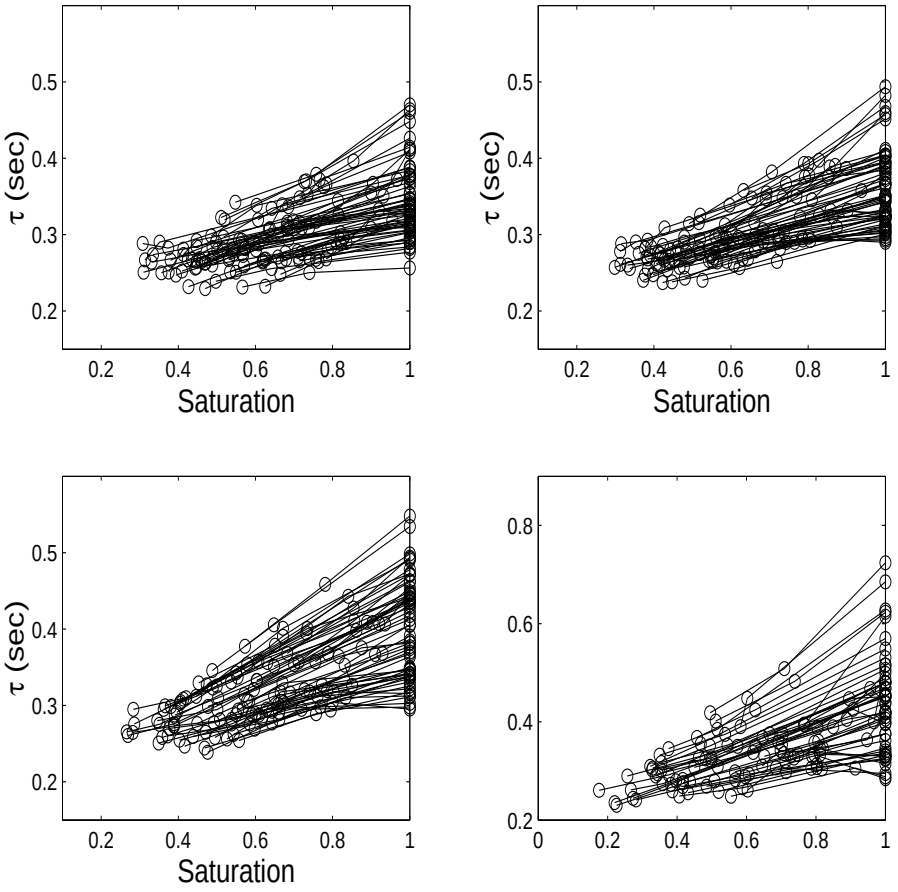

Fig. 93. Subplot for τ vs. S_w Connected with Lines

Each circle in the figure represents the calculated relative permeability of each voxel from the three saturated states. It can be observed that the relative permeability decreases with saturation decreasing. The scattered behavior in the figure is also due to the different relaxation rate at different voxel.

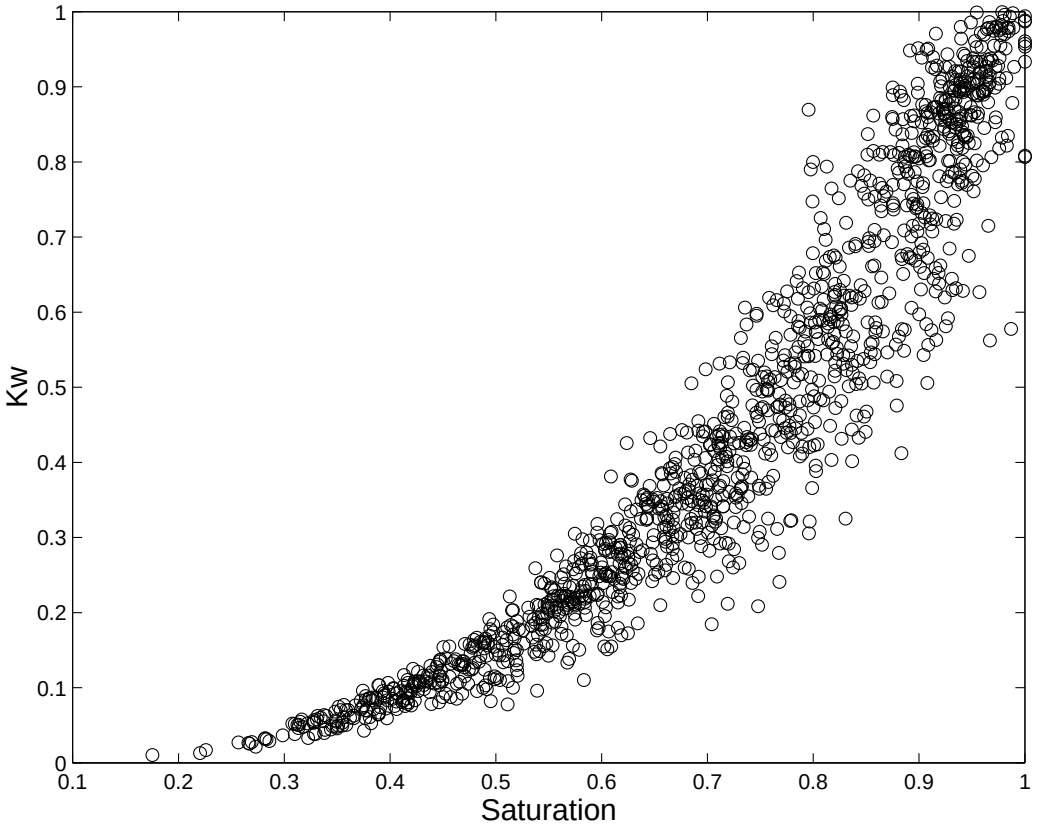

Fig. 94. Relative Permeability Obtained from NMR Experiment. ($S_{wi} = 0$)

In order to find the relationship between relative permeability and saturation for entire sample, further data analysis with averaging technique is required. We analyse the relaxation decay curves corresponding to each saturation state. As observed by the CPMG experiment, the water saturation has a broad variation range among the voxels. In order to do the analysis, we pick all the voxels which have the same

saturation level. For example, we collect all the voxels whose saturation falls in the saturation range from 0.50 to 0.55 in the third inversion recovery experiment. These voxels are listed in Table XXI. To determine the T_1^{ave} of all the listed voxels,

Table XXI. Voxel List with the Saturation in the Range 0.50-0.55 in the Third Inversion-Recovery

A-P Index	H-F Index	L-R Index	Saturation
027	006	004	0.51
032	006	005	0.55
033	006	005	0.52
038	004	005	0.52
039	006	004	0.52
039	006	005	0.52
040	006	004	0.50
040	006	005	0.55

distribution function $\overline{P}$ of all voxels in the table is required according to Eq. 3.16. As a matter of fact, the distribution function of the ith voxel P_i, the fraction of nuclei for which relaxation time are between τ and $\tau + d\tau$, has been normalized as

$$\int_0^\infty P_i(\tau)d\tau = 1. \tag{3.18}$$

Because different voxels have different porosity resulting in different amounts of water, the distribution function $\overline{P}$ of all voxels in the table should be determined through P_i with weighted coefficients ρ_i, the fraction of water in the ith voxel,

$$\overline{P}(\tau) = \sum_{i=1}^{N} \rho_i P_i(\tau). \tag{3.19}$$

Therefore, T_1^{ave} for all the list voxels can be calculated through

$$\frac{1}{T_1^{ave}} = \int_0^\infty \frac{1}{\tau}\overline{P}(\tau)d\tau, \tag{3.20}$$

where N is the total number of listed voxels. Considering the intrinsic magnetization is directly proportional to the mass of the water, the weighted coefficient can be determined by

$$\rho_i = \frac{M_{o,i}}{\sum_{i=1}^{N} M_{o,i}}. \tag{3.21}$$

The distribution function $\overline{P}(\tau)$ of all the listed voxels which have the same saturation level in the third inversion-recovery experiment, along with distribution function of all these voxels at the fully saturated state (the first inversion-recovery experiment) is shown in Figure 95.

In the same manner, we collect all the voxels whose saturation falls in the saturation range from 0.50 to 0.55 in the fourth inversion recovery experiment as listed in Table XXII. The distribution function $\overline{P}(\tau)$ of all the listed voxels which have the same saturation level in the fourth inversion-recovery experiment, along with distribution function of all these voxels at the fully saturated state (the first inversion-recovery experiment) is shown in Figure 96.

As expected, Figures 95 and 96 show similar behavior in that the peaks shift to the left when saturation decreases. That means contribution from the slow relaxation decreases. This can be explained in the same way as before by the fact that a larger fraction of the water, which represents the slow relaxation, is replace by the N_2 when saturated decreases. As a result, portion of the relaxation contributed from the fast relaxation increases. The T_1^{ave} can be calculated by applying Eq. 3.20. The same data processing procedure is applied for all the other saturation states with the same range $\Delta = 0.05$.

Table XXII. Voxel List with the Saturation in the Range 0.50-0.55 in the Fourth Inversion-Recovery

A-P Index	H-F Index	L-R Index	Saturation
025	005	004	0.54
026	004	004	0.55
027	004	004	0.54
028	004	004	0.54
028	005	005	0.51
028	006	004	0.54
029	003	005	0.55
030	005	005	0.54
030	006	005	0.52
031	004	005	0.54
031	005	005	0.54
034	003	005	0.54
035	004	005	0.55
036	004	005	0.53
037	003	005	0.52
038	002	005	0.52
040	004	005	0.51

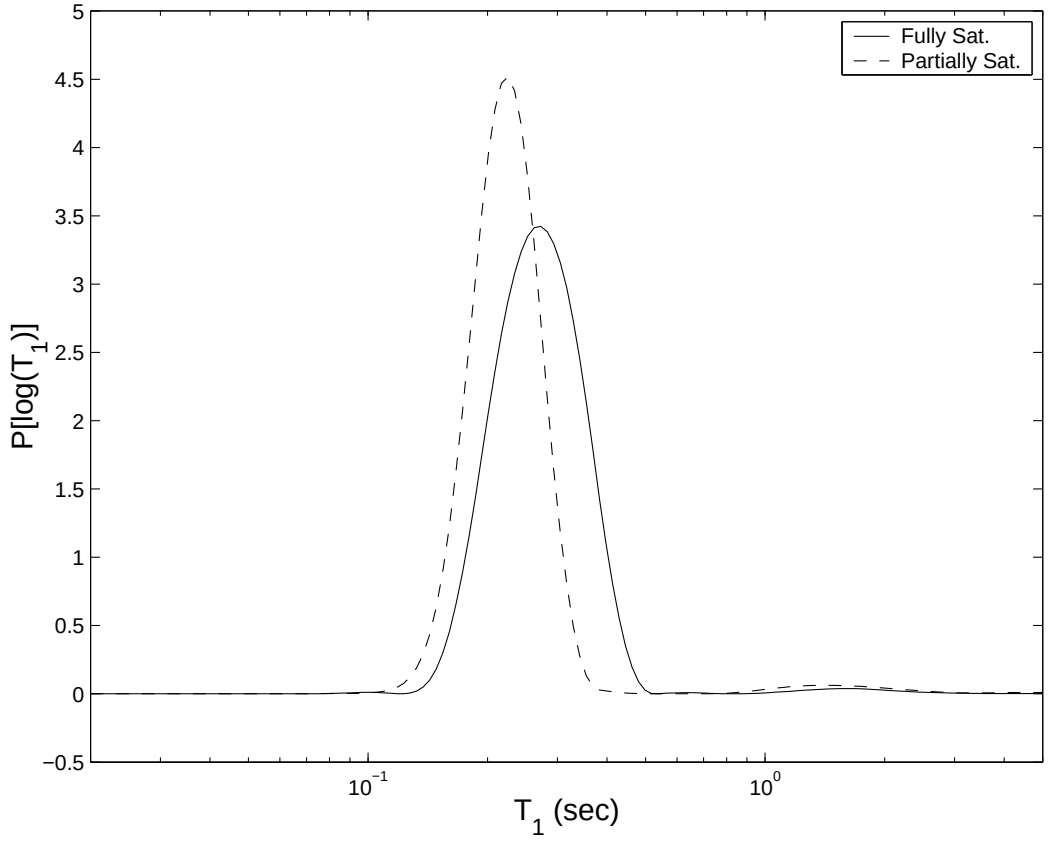

Fig. 95. T_1 Distribution for Voxels in Saturation Range 0.50-0.55 in Third Inversion-Recovery Experiment and in First Inversion-Recovery Experiment

Because we are able to determine the T_1^{ave} and S_w, the wetting phase $k_{r,w}$ can be calculated through Eqs. 3.3 and 3.2 by assuming $S_{wi} = 0$. Figure 97 plots $k_{r,w}$ vs. S_w with assumption $S_{wi} = 0$. The cross symbols in the figure represent the calculated data from the method mentioned above.

However, nonzero irreducible saturation S_{wi} may exist and is waiting for determination. In order to determine the irreducible saturation, the saturation distribution along the H-F direction of each saturation state is plotted in Figures 98-100. The open circles in the figure represent the determined saturations of a voxel in the sam-

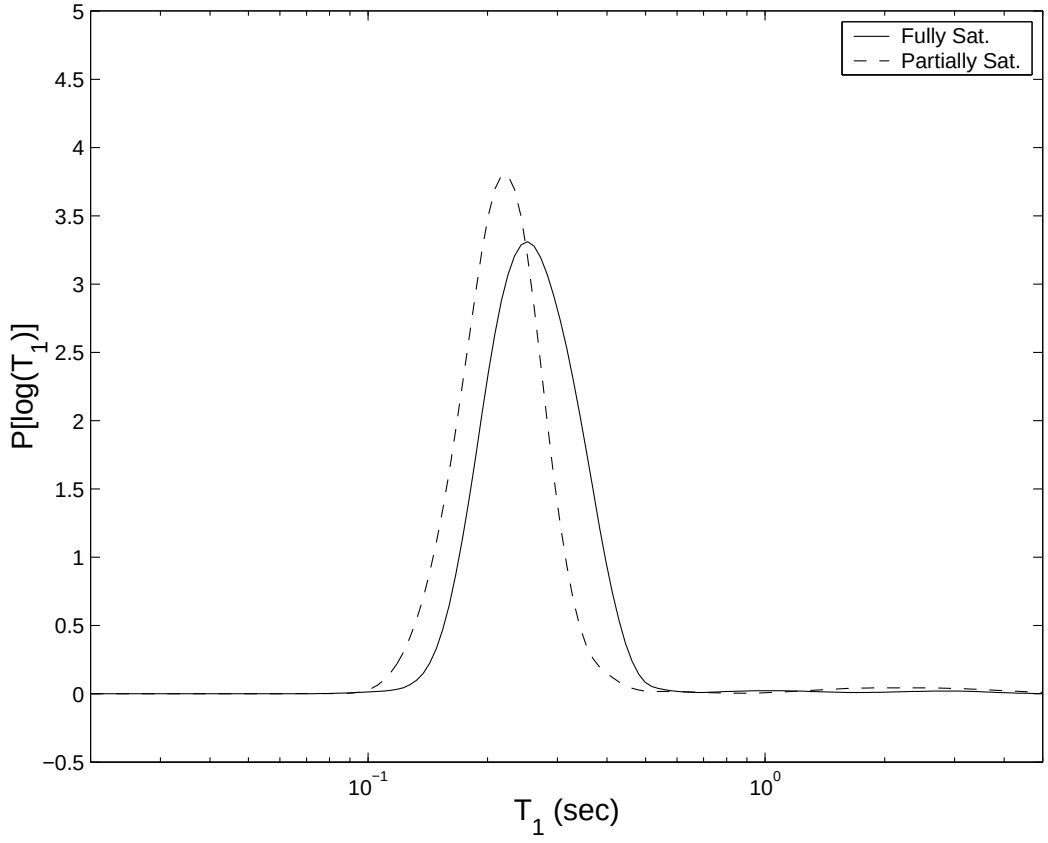

Fig. 96. T_1 Distribution for Voxels in Saturation Range 0.50-0.55 in Fourth Inversion-Recovery Experiment and in First Inversion-Recovery Experiment

ple. The x-axis gives the index of H-F direction of the voxel. From these figures, we can find the degree of variation of saturation within the same axial plane. The center line gives the mean of saturation in the plane. The the range between the upper line and bottom line contains 90% of the saturation values in the plane. It is observed that there is a quite big variation in saturation even in the same axial plane.

We are interested in the minimum saturation which can be achieved at each pressure step. The obtained minimum saturation is plotted as a function of inlet pressure in Figure 101. It is observed that the minimum saturation achieves to a

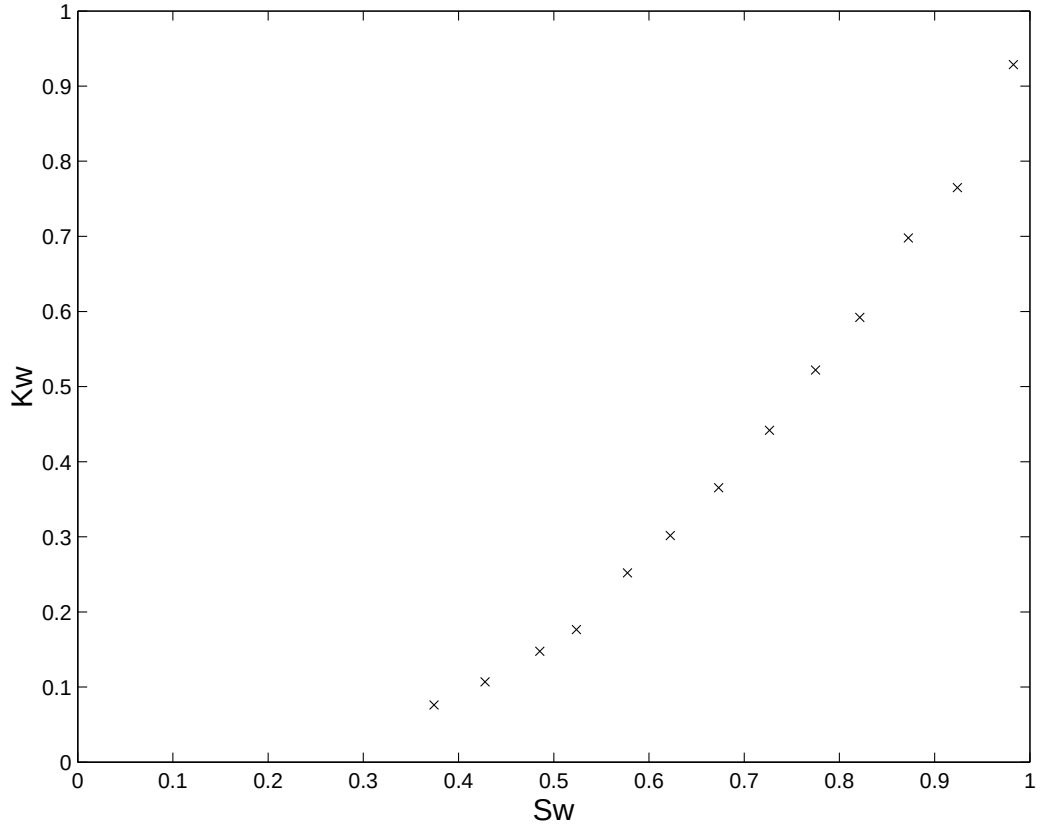

Fig. 97. Relative Permeability Obtained from NMR Experiment with Averaging. ($S_{wi} = 0$)

constant value when the pressure increases, and the irreducible saturation can be roughly determined to be 0.3.

With the $S_{wi} = 0.3$, Figure 102 plots $k_{r,w}$ vs. S_w. The cross symbols in the figure represent the calculated relative permeability. The relative permeability of water decreases with saturation decreasing.

According to the Eq. 3.3, the irreducible saturation affects the behavior of the calculated relative permeability. The method used to determine irreducible saturation only investigates a couple of pressure conditions. In order to accurately determine of the irreducible saturation, more pressures are desirable. Moreover, flow situation

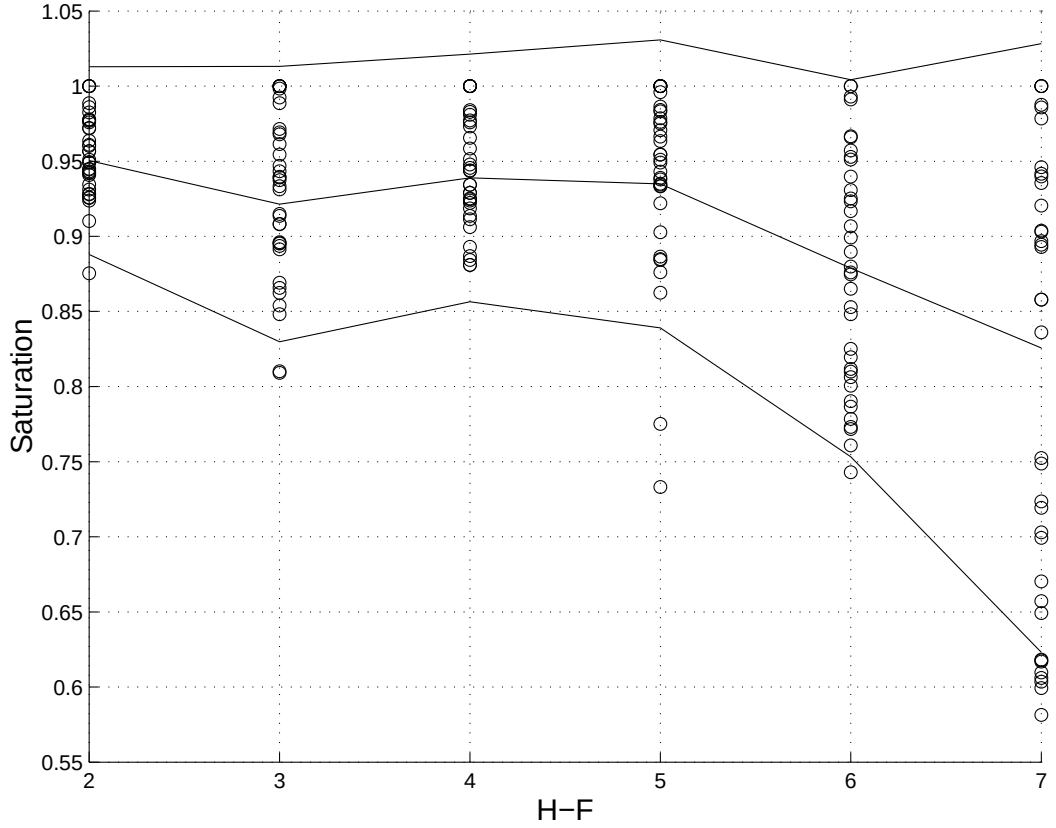

Fig. 98. Saturations of Voxels along the H-F Direction from the First Saturation State

may be unstable and the voxels in this study are huge compared to a single pore. This irreducible saturation is determined with a lot of suspicions.

In this chapter, several NMR experiments have been performed. Proton relaxation in the porous media is investigated through the step-by-step process of water desaturation. The relaxation behavior indicates the changes of water distribution in the porous media during the desaturaion process. For the first time, the three-dimensional resolved saturation and relaxation data are used to determine the relative permeability with incorporation the irreducible saturation. This method is more suitable than using single values of saturation and relaxation time for the whole sample

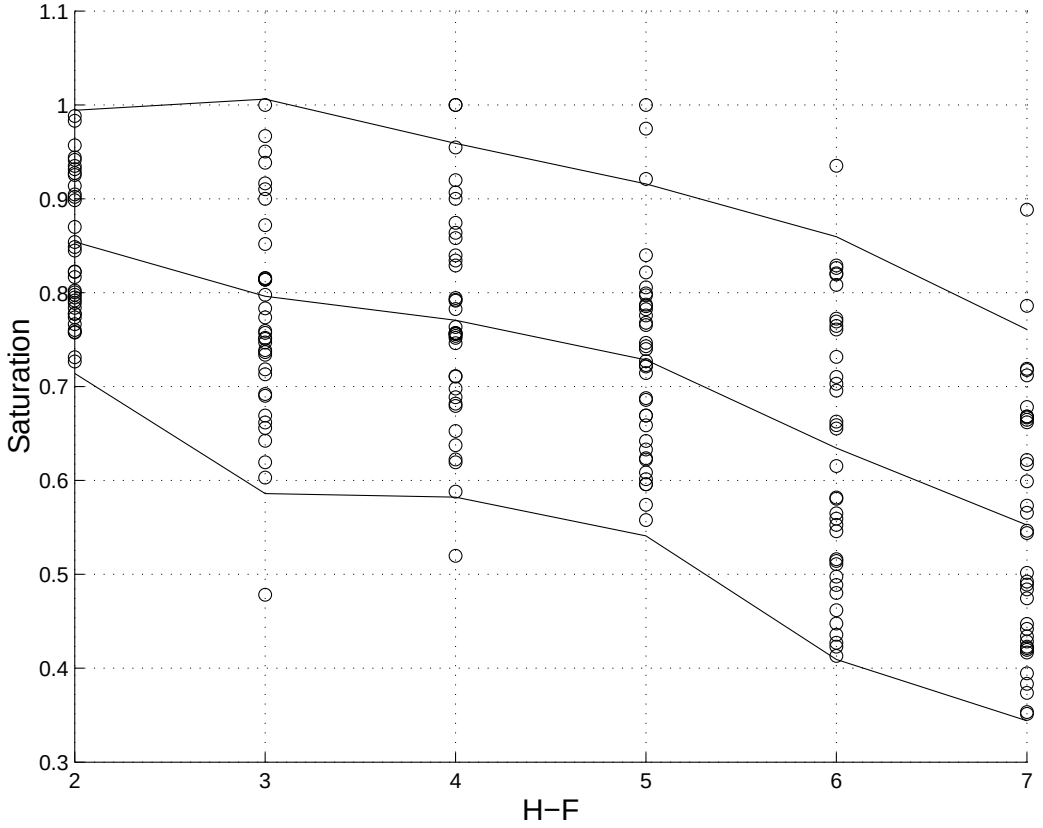

Fig. 99. Saturations of Voxels along the H-F Direction from the Second Saturation State

by assuming a uniform saturation (Chen et al., 1994). The three-dimensional saturation distribution indicates the preferential path for fluid movement that might result from the unstable flow. However, the predictive equation does not require the stable condition during the desaturation precess and the use of local saturation and relaxation measurement provides a way to predict the relative permeability, even if flow is unstable.

The empirical relation between wetting phase relative permeability and saturation could proven valuable in situ from well logging data. However, the validation of the relation has never been evaluated. Our group has already designed a N_2-water dis-

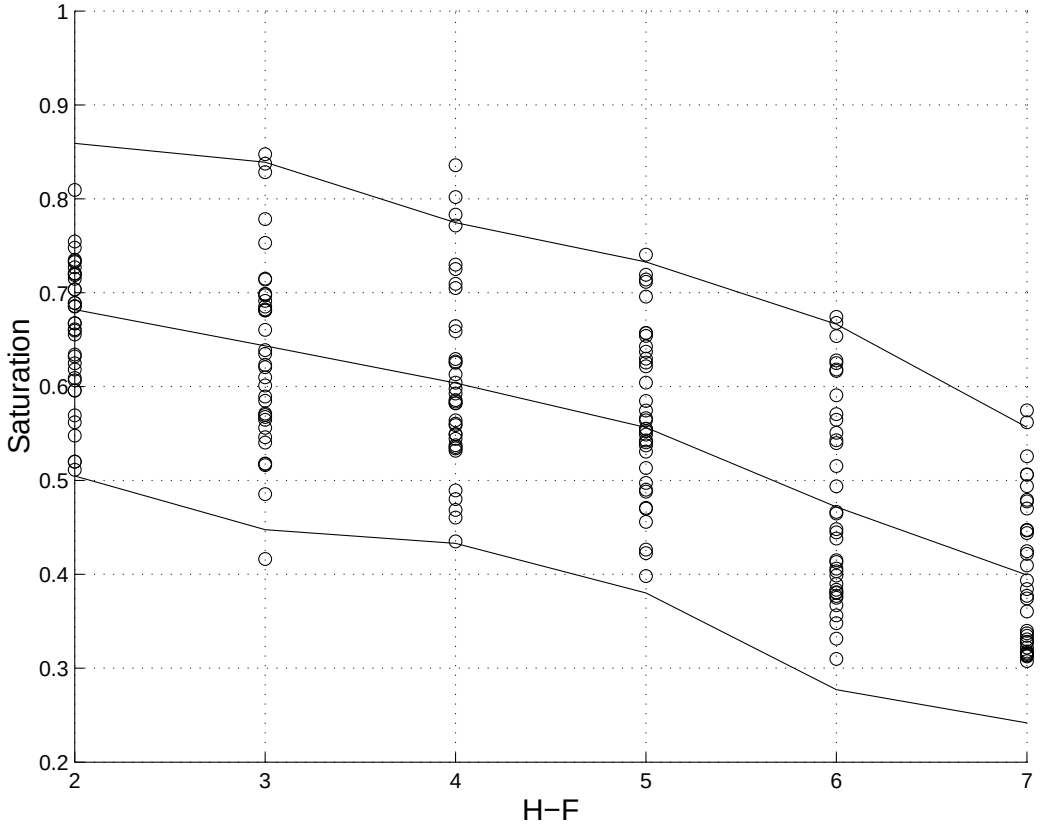

Fig. 100. Saturations of Voxels along the H-F Direction from the Third Saturation State

placement experiment in order to validate the relation. The detail of the experiment is provided in Appendix B.

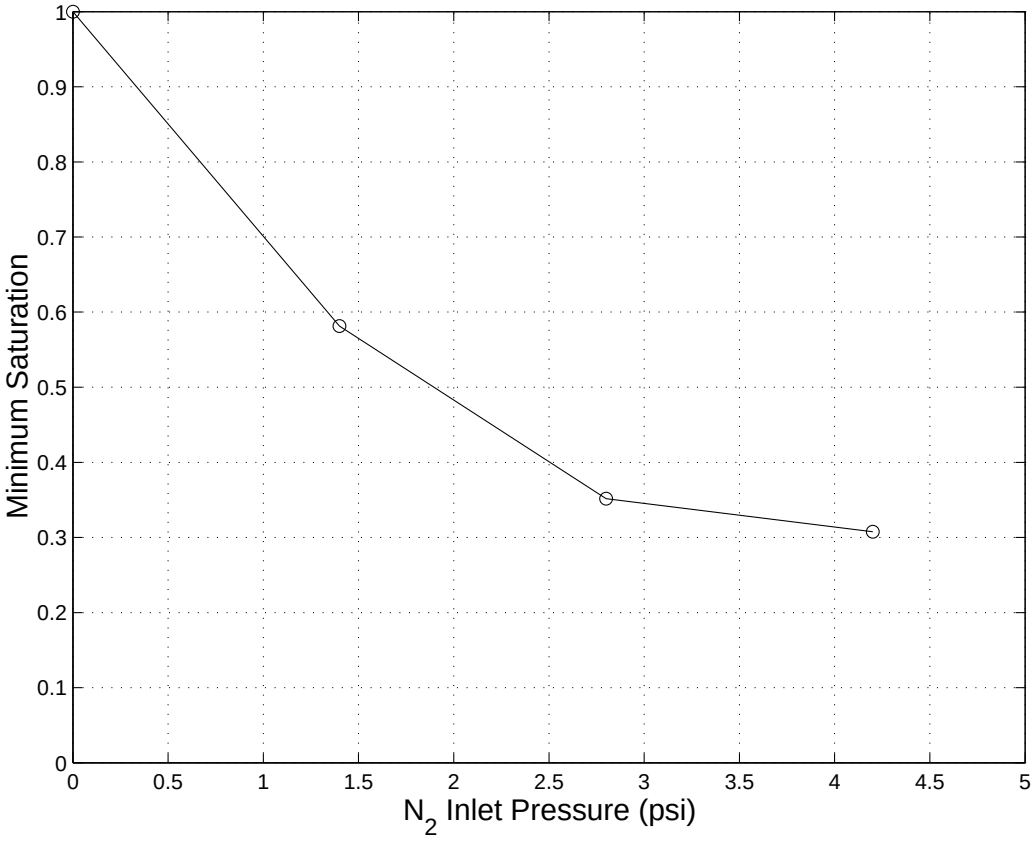

Fig. 101. Minimum Saturation with Different Inlet Gas Pressure

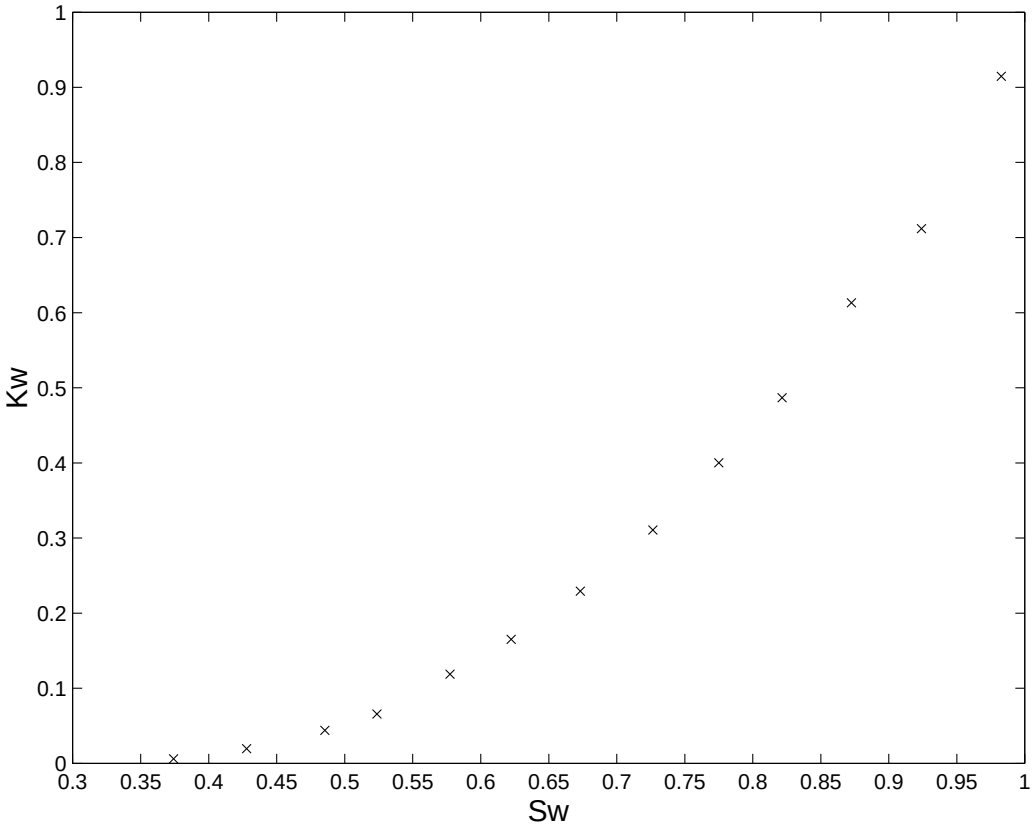

Fig. 102. Relative Permeability Obtained from NMR Experiment with Averaging. ($S_{wi} = 0.3$)

CHAPTER IV

CONCLUSIONS

The relative permeabilities and capillary pressure are saturation dependent functions of great importance for understanding the multiphase flow in porous media.

Chapter II describes the inverse estimation methodology used to determine the multiphase properties. The estimates of the multiphase properties are determined through matching experimental data and calculated results. The process for determining multiphase properties from experimental data is implemented with the computer program SENDRA. This program is built around a two-dimension, two-phase simulator. In this chapter the computer code is successfully extended to represent all three spatial coordinate directions so that the entire porosity and permeability distributions are accounted for in estimation of multiphase flow properties. Three synthetic experiment data are utilized to show the effect of sample heterogeneity on determination of flow functions. The erroneous estimates of flow functions associated with the homogeneity assumption are shown by all these three examples.

In Chapter III, the provided empirical relation used to predict the relative permeability of the wetting phase has been waiting for validation. Several sets of NMR experiments are performed on a rock sandstone sample. NMR relaxation data during the desaturaion processes are measured and analyzed. The change of water distribution at different saturations in a two-phase system is detected by NMR relaxation techniques. The preference of fluid distribution during the desaturation processes is observed. The irreducible saturation is necessary to be determined. The relative permeability of water is calculated from the empirical relation. This is the first time three-dimensional resolved saturation and relaxation data have been used to predict the relative permeability. The empirical relation is expected to be validated from

a nitrogen-water displacement experiment. However, the saturation distribution in Chapter III indicates the preferential path for fluid movement that might result from the unstable flow. If the displacement experiment is unstable, the analysis of water production data in order to estimate the multiphase properties through the method in Chapter II is meaningless. More investigation is required in order to clarify whether there is instability happened in immiscible displacement experiment.

NOMENCLATURE

B_j^m	–	the j^{th} B-spline basis function of order m
C_j	–	the B-spline coefficients
e	–	random measurement error
$\mathbf{G}$	–	matrix containing left hand side of linear inequality constraints
$\mathbf{g}$	–	matrix containing right hand side of linear inequality constraints
g	–	earth gravity acceleration
i	–	the ith iteration
J	–	objective function or performance criteria
K	–	absolute permeability
$K(t_j, \tau)$	–	the kernel function associated with t_j and τ
k	–	proportional factor between intrinsic magnetization and mass
$k_{r,f}$	–	relative permeability of the fluid, f=nw or w
$k_{r,nw}$	–	relative permeability of the non-wetting phase
$k_{r,w}$	–	relative permeability of the wetting phase
M_o	–	the total intrinsic magneitzation
m	–	mass of the observed region
$\mathbf{N}$	–	normal distribution
N	–	total number of coefficients used in B-spline
N_x	–	total number of blocks in x direction
N_y	–	total number of blocks in y direction
N_z	–	total number of blocks in z direction
n	–	number of experimental data

$\mathbf{p}$ – the vector of unknown parameters

P – the distribution function

$\overline{P}$ – the average distribution function

p_c – capillary pressure

p_{nw} – pressure of the non-wetting phase

p_w – pressure of the wetting phase

Q – flow rate at the boundary, $\frac{mass}{time}$

q_{nw} – sink or source term of the no-wetting phase inside the domain, $\frac{mass}{volumn \cdot time}$

q_w – sink or source term of the wetting phase inside the domain, $\frac{mass}{volumn \cdot time}$

S_{nw} – saturation of the non-wetting phase

S_w – saturation of the wetting phase

T – transmissibility

T_1 – characteristic time associated with longitudinal relaxation

T_2 – characteristic time associated with transverse relaxation

T_{1b} – T_1 of the bulk fluid

t – time

$\mathbf{W}$ – weighting matrix used in objective function

$\mathbf{X}$ – standard normal variable

$\overrightarrow{y}$ – the extended partitions used for spline basis functions

$\overrightarrow{Y_m}$ – measured experimental data

$\overrightarrow{Y_s}$ – calculated simulation data

$\overrightarrow{Y}^{exact}$	–	noise-free exact data
$\overrightarrow{Y}^{syn}$	–	synthetic data
x	–	length in x direction
y	–	length in y direction
z	–	length in z direction
ΔX	–	coarse-grid block length in x direction
ΔY	–	coarse-grid block length in y direction
ΔZ	–	coarse-grid block length in z direction
Δx	–	fine-grid block length in x direction
Δy	–	fine-grid block length in y direction
Δz	–	fine-grid block length in z direction

Greek Letters:

ϵ	–	the level of the experimental error expressed as a percentage of maximum magnitude of the data
λ	–	regularization parameter
μ_{nw}	–	viscosity of the no-wetting phase
μ_{nw}	–	viscosity of the wetting phase
ρ_i	–	weighted coefficient of ith voxel
ρ_{nw}	–	density of the no-wetting phase
ρ_w	–	density of the wetting phase
τ_1	–	a relaxation rate which eliminates the bulk relaxation rate
τ_{1_o}	–	τ_1 at $Sw = 1$
ϕ	–	porosity
Φ	–	potential
∇	–	the gradient operator

Superscripts:

ave	–	superscript denotes quantities associated with average
c	–	superscript denotes quantities associated with capillary pressure
$exact$	–	superscript denotes quantities associated with noise-free, exact data
f	–	superscript denotes quantities associated with fluids, f=nw or w
nw	–	superscript denotes quantities associated with the non-wetting phase
ref	–	superscript denotes quantities associated with the reference region
$sample$	–	superscript denotes quantities associated with the sample region
syn	–	superscript denotes quantities associated with the synthetic data
w	–	superscript denotes quantities associated with the wetting phase
$+$	–	superscript denotes upper bound
$-$	–	superscript denotes lower bound

Subscripts:

ave	–	subscript denotes quantities associated with average
c	–	subscript denotes quantities associated with capillary pressure
$calc$	–	subscript denotes the calculated data
e	–	subscript denotes effective quantities
f	–	subscript denotes quantities associated with fluids, f=nw or w
H	–	subscript denotes quantities associated with the horizontal plane
nw	–	subscript denotes quantities associated with the non-wetting phase

m – subscript denotes the measured experimental data

max – subscript denotes the maximum of experimental data

obs – subscript denotes the observed experimental data

s – subscript denotes the calculated simulation data

w – subscript denotes quantities associated with the wetting phase

V – subscript denotes quantities associated with the vertical plane

i – subscript denotes quantities associated with ith voxel in Chapter III

i – subscript denotes spatial index in x direction

j – subscript denotes spatial index in y direction

k – subscript denotes spatial index in z direction

x – subscript denotes the variable associate with the x direction coordinate

y – subscript denotes the variable associate with the y direction coordinate

z – subscript denotes the variable associate with the z direction coordinate

LITERATURE CITED

Akin, S. and B. Demiral, "Genetic Algorithm for Estimating Multiphase Flow Functions from Unsteady-State Displacement Experiment," *Com. & Geo.*, **24**, 251 (1998).

Aleman, M. A. and J. C. Slattery, "A Linear Stability Analysis for Immisicible Displacements," *Trans. in Por. Med.*, **3**, 455 (1988).

Alvarado, F. L., *The Sparse Matrix Manipulation System, User and Reference Manual.* The University of Wisconsin (1993). URL:http://www.cs.indiana.edu/ftp/techreports/TR454.html.

Archie, G. E., "The Electrical Resistivity Log as an Aid in Determining Some Reservoir Characteristics," *Trans. Am. Inst. Min. Metall. Pet. Eng.*, **146**, 54 (1942).

Aziz, K. and A. Settari, *Petroleum Reservoir Simulation.* Applied Science Publishers, London (1979).

Banavar, J. R. and L. M. Schwartz, "Magnetic Resonance as a Probe of Permeability in Porous Media," *Phy. Rev. Let.*, **58**, 1411 (1987).

Blunt, M. J., "Flow in Porous Media-Pore-Network Models and Multiphase Flow," *Cur. Opin. in Col. & Interf. Sci.*, **6**, 197 (2001).

Borgia, G. C., V. Bortolotti, P. Dattilo, P. Fantazzini, and G. Maddinelli, "Quantitative Determination of Porosity: A Local Assessment by NMR Imaging Techniques," *Mag. Res. Imag.*, **14**, 919 (1996).

Bramley, R. and X. Wang, *SPLIB: A Library of Iterative Methods for Sparse Linear Systems*. Indiana University, Bloomington (1995). URL:http://www.elk.itu.edu.tr/~dag/lssmc.html.

Brownstein, K. R. and C. E. Tarr, "Importance of Classical Diffusion in NMR Studies of Water in Biological Cells," *Phys. Rev. A.*, **19**, 2446 (1978).

Carwell, W. T. J. and R. L. Parsons, "Average Permeability of Heterogeneous Oil Sands," *Trans. Am. Inst. Min. Metall. Pet. Eng.*, **160**, 34 (1945).

Chen, S., H.-K. Liaw, and A. T. Watson, "Fluid-saturation-dependent Nuclear-Magnetic-Resonance Spin-Lattice Relaxation in Porous Media and Pore Structure Analysis," *J. of App. Phy.*, **74**(3), 1 (1993).

Chen, S., H.-K. K. Liaw, and A. T. Watson, "Measurements and Analysis of Fluid Saturation Dependent NMR Relaxation and Linebroadening in Porous Media," *Mag. Res. Imag.*, **12**, 815 (1994).

Chen, S., F. Qin, K.-H. Kim, and A. T. Watson, "NMR Imaging of Multiphase Flow in Porouse Media," *SPE Ann. Tech. Conf. and Exhib. Held in Washington, D.C., October 4-7*, 1 (1992). SPE 24760.

Dana, E. and F. Skoczylas, "Experiment Study of Two-Phase Flow in Three Sandstones. I. Measuring Relative Permeabilities During Two-phase Steady-State Experiments," *Int. J. of Multi. Flow*, **28**, 1719 (2002).

de Rooij, G. H., "Modeling Fingered Flow of Water in Soil Owing to Wetting Front Instability: A Review," *J. Hydrology*, **231-232**, 277 (2000).

Duff, I. S., R. G. Grimes, and J. G. Lewis, *Users' Guide for the Harwell-Boeing Sparse*

Matrix Collection. Research and Technology Division, Boeing Computer Services (1992).

Fleury, M., F. Deflandre, and S. Godefroy, "Validity of Permeability Prediction from NMR Measurements," *Chim./Chem.*, **4**, 869 (2001).

Fox, R. W., *Introduction to Fluid Mechanics*. John and Wiley, New York (1998).

Hidajat, I., M. Singh, J. Cooper, and K. K. Mohanty, "Permeability of Porous Media from Simulated NMR Response," *Trans. in Por. Med.*, **48**, 225 (2002).

Hirasaki, G. J., J. A. Gohan, and J. W. I. Dudley, "Interpretation of Oil/Water Relative Permeabilities from Centrifuge Displacement," *SPE Ann. Tech. Conf. and Exhib. Held in Washington, D.C., October 4-7*, 1 (1992). SPE 24879.

Hollenshead, J. T., Nuclear Magnetic Resonance Probes of Heterogeneous Media, Ph.D. dissertation, Texas A&M Univerisity (2001).

Johnson, E. F., D. P. Bossler, and V. O. Naumann, "Calculation of Relative Permeability from Displacement Experiment.," *Trans. Am. Inst. Min. Metall. Pet. Eng.*, **216**, 61 (1959).

Katz, A. J. and A. H. Thompson, "Quantitative Prediction of Permeability in Porous Rock," *Phys. Rev. B*, **34**, 8179 (1986).

Kleniberg, R. L., "Well Logging Overview," *Con. Mag. Res.*, **13**(6), 342 (2001).

Kleinberg, R. L. and J. A. Jackson, "An Introduction to the History of NMR Well Logging," *Con. Mag. Res.*, **13**(6), 340 (2001).

Kulkarni, R., A. T. Watson, J. E. Nordtvedt, and A. Sylte, "Two-Phase Flow in Porous Media: Property Identification and Model Validation," *AIChE J.*, **44**, 2337 (1998).

Levitt, M. H., *Spin Dynamics*. John Wiley & Sons, Ltd, England (2001).

Li, D., B. Bechner, and A. Kumar, "A New Efficient Averaging Technique for Scaleup of Multimillion-Cell Geologic Models," *SPE Ann. Tech. Conf. and Exhib. Held in Houston, Texas, October 3-6*, 1 (1999). SPE 56554.

Liaw, H.-K., R. Kulkarni, S. Chen, and A. T. Watson, "Characterization of Fluid Distribution in Porous Media by NMR Techniques," *AICHE J.*, **42**(2), 538 (1996).

Mani, V. and K. K. Mohanty, "Effect of Pore-Space Spatial Correlations on Two-Phase Flow in Porous Media," *J. of Pet. Sci. & Eng.*, **23**, 173 (1999).

Marck, S. C. V. D., "Evidence for a Nonzero Transport Threshold in Porous Media," *Wat. Res. Res.*, **35**(2), 595 (1999).

Maximenko, A. and V. V. Kadet, "Determination of Relative Permeability Using the Network Models of Porous Media," *J. Pet Sci. Eng.*, **28**, 145 (2000).

Mejia, G. M., K. K. Mohanty, and A. T. Watson, "Use of *in situ* Saturation Data in Estimation of Two-Phase Flow Functions in Porous Media," *J. Pet. Sci. Eng.*, **12**, 233 (1995).

Mitlin, V. S., J. D. McLennan, and S. G. Green, "Simultaneous Determination of Two-Phase Relative Permeability and Capillary Pressure of Porous Rock from Steady-State Flow Experiments: Accounting for Gravitational Forces and Fluid Compressibility," *J. Col. Interf. Sci.*, **204**, 205 (1998).

Nolen, J. S. and D. W. Berry, "Test of the Stability and Time-Step Sensitivity of Semi-Implicit Reservoir Simulation Techniques," *Soc. Pet. Engs. J.*, **12**, 263 (1972).

Nordtvedt, J. E., G. Mejia, P.-H. Yang, and A. T. Watson, "Estimation of Capillary Pressure and Relative Permeability Functions from Centrifuge Experiments," *SPE Res. Eng.*, **11**, 292 (1993).

Peaceman, D. W., *Fundamentals of Numerical Reservoir Simulation*. Elsevier Scientific Publishing Company, New York (1977).

Petec Software & Services, *CENDRA Verison 1.4 User's Manual*. Bergen, Norway (2000).

Reeves, P. C. and M. A. Celia, "Functional Relationship between Capillary Pressure, Saturation, and Interfacial Area as Realed by a Pore-scale Network Model," *Wat. Res. Res.*, **32**, 2345 (1996).

Richmond, P. C. and A. T. Watson, "Comparsion of Implicit and Explicit Methods for Interpreting Displacement Data," *SPE Res. Eng.*, **5**, 389 (1990).

Saad, Y., *SPARSKIT: A Basis Tool Kit for Sparse Matrix Computations, Version 2*. University of Illinois (1994). URL:http://www.cs.umn.edu/Research/arpa/SPARSKIT/sparskit.html.

Schulthness, G. K. V. and H.-J. Smith, The Encyclopaedia of Medical Imaging Volume I (1998). URL:http://www.amershamhealth.com/medcyclopaedia/index.asp.

Schumaker, L. L., *Spline Functions: Basic Theory*. John Wiley and Sons, New York (1981).

Seto, K., J. T. Hollenshead, A. T. Watson, C. T. P. Chang, and J. C. Slattery, "Determination Permeability Determinations Using NMR Velocity Imaging," *Trans. in Por. Med.*, **42**, 351–388 (2001).

Simpson, J. H. and H. Y. Carr, "Diffusion and Nuclear Spin Relaxation in Water," *Phy. Rev.*, **111**(5), 1201 (1958).

Slattery, J. C., *Momentum, Energy, and Mass Transfer in Continue*. Krieger, New York (1981).

Timur, A., "Pulsed Nuclear Magnetic Resonance Studies of Porosity, Movable Fluid, and Permeability of Sandstones," *J. Pet. Tech.*, **21**(6), 775 (1969).

Valestrand, R., A.-A. Grimstad, K. K. G. Nævdal, and J.-E. Nordtvedt, "Simutaneous Determination of Absolute and Relative Permeabilities," *Int. J. of Therm. Sci.*, **41**, 546 (2002).

Watson, A. T., G. R. Gavalas, and J. H. Seinfeld, "Identifiability of Estimates of Two-Phase Reservoir Properties in History Matching," *Soc. of Pet. Eng. J.*, **20**, 697 (1984).

Watson, A. T., J. T. Hollenshead, and C. T. P. Chang, "Developing Nuclear Magnetic Resonance Imaging for Engineering Application," *Inv. Prob. in Eng.*, **9**, 487 (2001).

Watson, A. T., J. T. Hollenshead, J. Uh, and C. T. P. Chang, "NMR Determination of Porous Media Property Distributions," *Annual Reports on NMR Spectroscopy*, **48**, 113 (2002).

Watson, A. T., R. Kulkarni, J.-E. Nordtvedt, A. Sylte, and H. Urkedal, "Estimation of Porous Media Flow Function," *Meas. Sci. & Tech.*, **9**, 898 (1998).

Watson, A. T., P. C. Richmond, P. D. Kerig, and T. M. Tao, "A Regression-Based Method for Estimating Relative Permeabilities from Displacement Experiments," *SPE Res. Eng.*, **3**, 953 (1988).

Wu, Y. S., P. A. Forsyth, and H. Jiang, "A Consistent Approach for Applying Numerical Boundary Conditions for Multiphpase Subsurface Flow," *J. of Cont. Hyd.*, **23**, 157 (1996).

Zimmerman, J. R. and W. E. Brittin, "Nuclear Magnetic Resonance Studies in Multiple Phase Systems: Lifetime of a Water Molecule in an Adsobing Phase on Silica Gel," *J. Phy. Chem.*, **61**, 1328 (1957).

APPENDIX A

MEASUREMENT OF AVERAGE ABSOLUTE PERMEABILITY

Average absolute permeability determination is based on the assumption that the samples were homogeneous. Although the samples are clearly not homogeneous, this step is necessary because the permeability is needed as an input parameter for the estimation of the multiphase flow functions, relative permeability and capillary pressure curves, which are required to simulate the flow of multiple fluid phases through porous media.

Permeability is a property of a porous material which is defined in Darcy's law. If horizontal linear flow of an incompressible fluid is established through a sample of porous material of length L_{sample} in the direction of flow, and cross sectional area A_{sample}, then the permeability, K, is determined as

$$K = \frac{v_{sample}\mu}{\Delta P / L_{sample}}. \tag{A.1}$$

Here v_{sample} is the superficial velocity in the sample, μ is the viscosity of the fluid and ΔP is the applied pressure difference across the length of the sample. Usually, the measured pressure drop consists of the pressure loss from the sample and a portion of the tube line as shown in Figure 103. Then,

$$\Delta P_{measured} = \Delta P_{sample} + \Delta P_{tube} \tag{A.2}$$

The pressure loss from the tube line is typically divided into two types: major and minor loss.

$$\Delta P_{tube} = \Delta P_{major} + \Delta P_{minor} \tag{A.3}$$

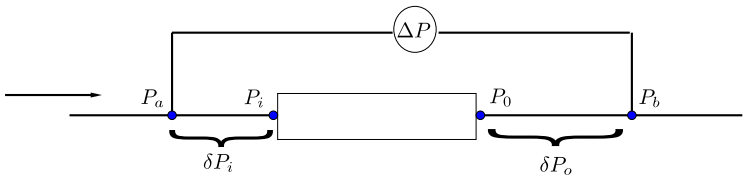

Fig. 103. Pressure Measurement

The Major loss comes from the friction in the tubes, and the minor loss is due to fittings and valves. The major loss can be calculated according to equation A.4 when the flow is considered to be laminar at a Reynolds number of 2000 or less (Fox, 1998).

$$\Delta P_{major} = 32\frac{L_{tube}\mu v_{tube}}{D_{tube}^2} \tag{A.4}$$

Minor loss is determined according to equation A.5 (Fox, 1998),

$$\Delta P_{minor} = K_{loss}\frac{\rho v_{tube}^2}{2}, \qquad \text{where } K_{loss} \text{ is a loss coefficient.} \tag{A.5}$$

Then, the pressure drop is given by

$$\Delta P_{calculated} = (\frac{\mu L_{sample}}{K}\frac{A_{tube}}{A_{sample}} + 32\frac{L_{tube}\mu}{D_{tube}^2})v_{tube} + \frac{K_{loss}\rho}{2}v_{tube}^2 \tag{A.6}$$

$$= \alpha v_{tube} + \beta v_{tube}^2. \tag{A.7}$$

The coefficients α and β in the above equation can be determined through a minimization problem,

$$\min_{\alpha,\beta} J(\alpha,\beta) = [\overrightarrow{\Delta P}_{measured} - \overrightarrow{\Delta P}_{calculated}]^T [\overrightarrow{\Delta P}_{mesured} - \overrightarrow{\Delta P}_{calculated}] \tag{A.8}$$

$$\alpha \geq 0 \tag{A.9}$$

$$\beta \geq 0. \tag{A.10}$$

The permeability of the sample is then determined as

$$K = \frac{A_{tube}\mu L_{sample}}{A_{sample}(\alpha - 32\frac{L_{tube}\mu}{D^2_{tube}})}. \tag{A.11}$$

A cylindrical (4.1 cm in length and 2.54 cm in diameter) rock sample is fully saturated with water. A Vindum QL-700 pump supplied a constant water flow rate into the sample. Two differential pressure transducers were used to measure the absolute pressure at the inlet of the core sample and the pressure drop across the sample. Measurements of the pressures are taken while the water is injected at several different constant volumetric flow rates.

The average permeabilities have been determined by the method mentioned above. Figure 104 shows the experimental pressure drop data, with the corresponding computed values by using the determined average permeabilities. The calculated pressure curve provide adequate representations of the experiment. The determined average permeabilities of two samples are listed in Table XXIII.

Table XXIII. Determined Average Permeability of the Samples

Samples Property	
Average Permeability [Darcy]	0.42

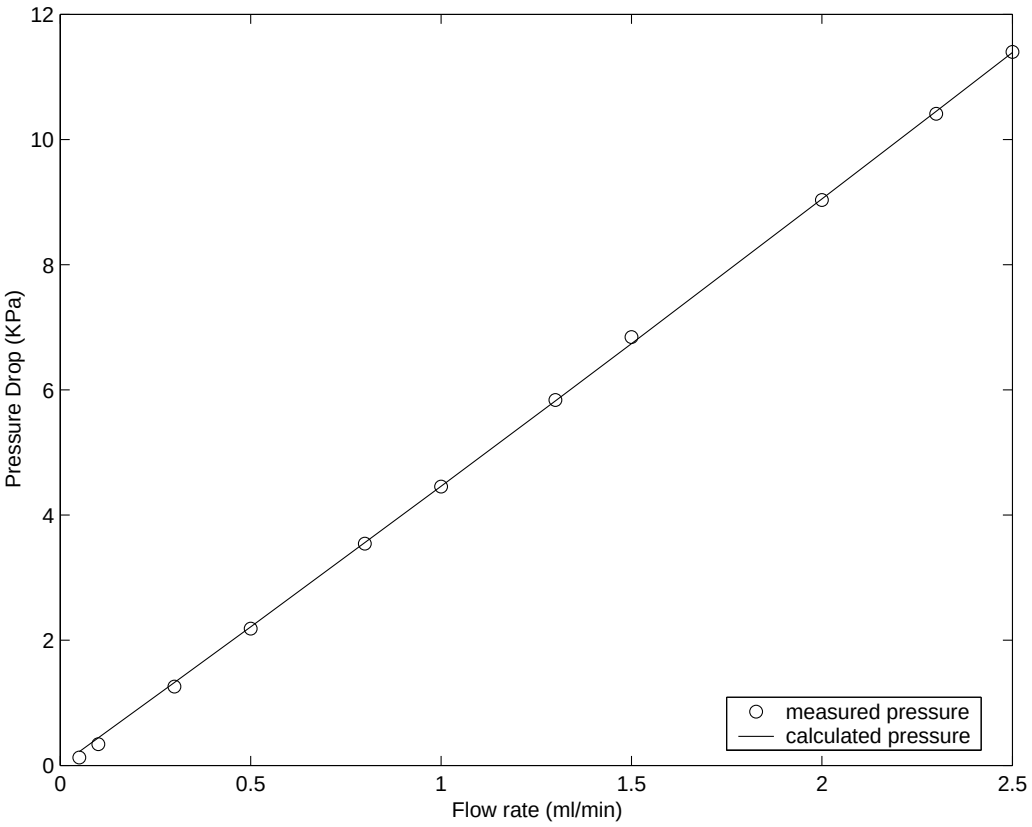

Fig. 104. Calculated and Measured Pressure Drop

APPENDIX B

NITROGEN-WATER DISPLACEMENT EXPERIMENT

Introduction

The method to predict wetting phase relative permeabilities from relaxation data obtained through NMR imaging has been discussed in Chapter III. A nitrogen-water[1] displacement experiment is designed in order to validate the relation in Chapter III.

Experimental Design

The rock sample used in Chapter III is used in this nitrogen-water displacement experiment. The sample is dried in an oven, fully resaturated under 250 mmHg vacuum conditions, and then is placed on a balance to monitor the weight of the sample during the experiment. The inlet of the sample is connected to a pressurized N_2 gas line. The outlet of the sample is open to the atmosphere. A pressure sensor is used to measure the inlet pressure. Figure 105 is a schematic of the experimental setup for the displacement experiment. In order to avoid evaporation of water in the sample by N_2 flow, we saturated N_2 with water before injection into the sample by bubbling N_2 through a moisturizer. The custom made moisturizer shown in Figure 106 is filled with glass beads and porous rock plates to enhance contact between N_2 bubbles and water. All equipment is kept at a regulated room temperature (21^oC). A series of four inlet gas pressures are applied to establish different saturation levels in the sample. A steady state is established at each fixed inlet pressure after half an hour.

---

[1]Water in this Appendix refers to brine solution which consists of $0.3\%NaN_3$, $3\%NaCl$ and $96.7\%H_2O$.

Table XXIV provides the details of the operation conditions. The average absolute permeability of the sample is known from a method discussed in Appendix A. The average porosity is gravimetrically determined.

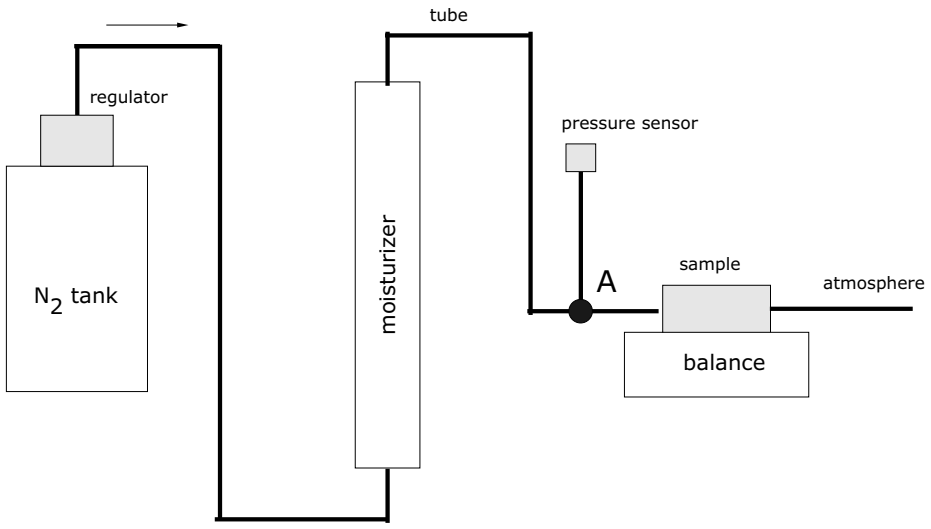

Fig. 105. Experiment Setup

Results and Discussion

The water production data is expected to be used in the regression-based approach, which is discussed in Chapter II, to estimate the relative permeability and capillary pressure functions. The measured water production is shown in Figure 107. The values on the y-axis represent the percentage of the water which is pushed out of the sample compared with the total water inside the sample.

By checking the production data carefully, it is observed that the curve does not continuously and smoothly increase for each pressure step, especially for the second and the third step, where the data holds for a while and then increases. This is due to the fact that the water which is pushed out by the gas stays in the transport tube for

Table XXIV. Sample Properties and Operating Conditions

Water Viscosity	1.0 cP
Nitrogen Viscosity	0.0177 cP
Average Porosity	0.21
Average Absolute Permeability	0.42 Darcy
Initial Fluid Saturation	1.0

Time (min)	Inlet pressure (KPa)
0	6.89
27.2	11.7
60.0	15.1
95.0	17.9

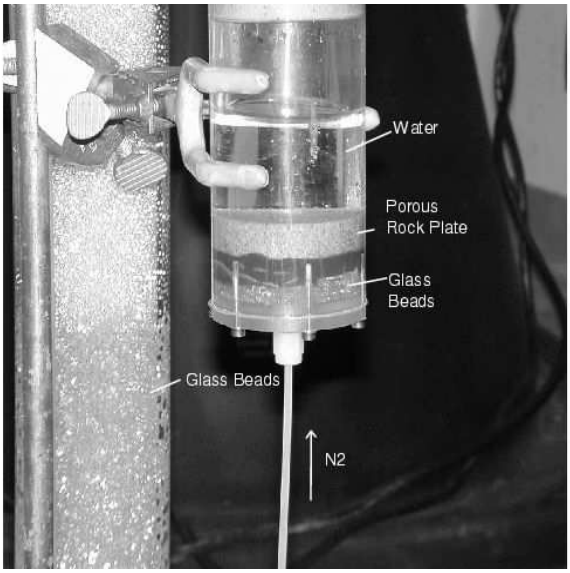

Fig. 106. Moisturer Used for Gas-Water Experiment

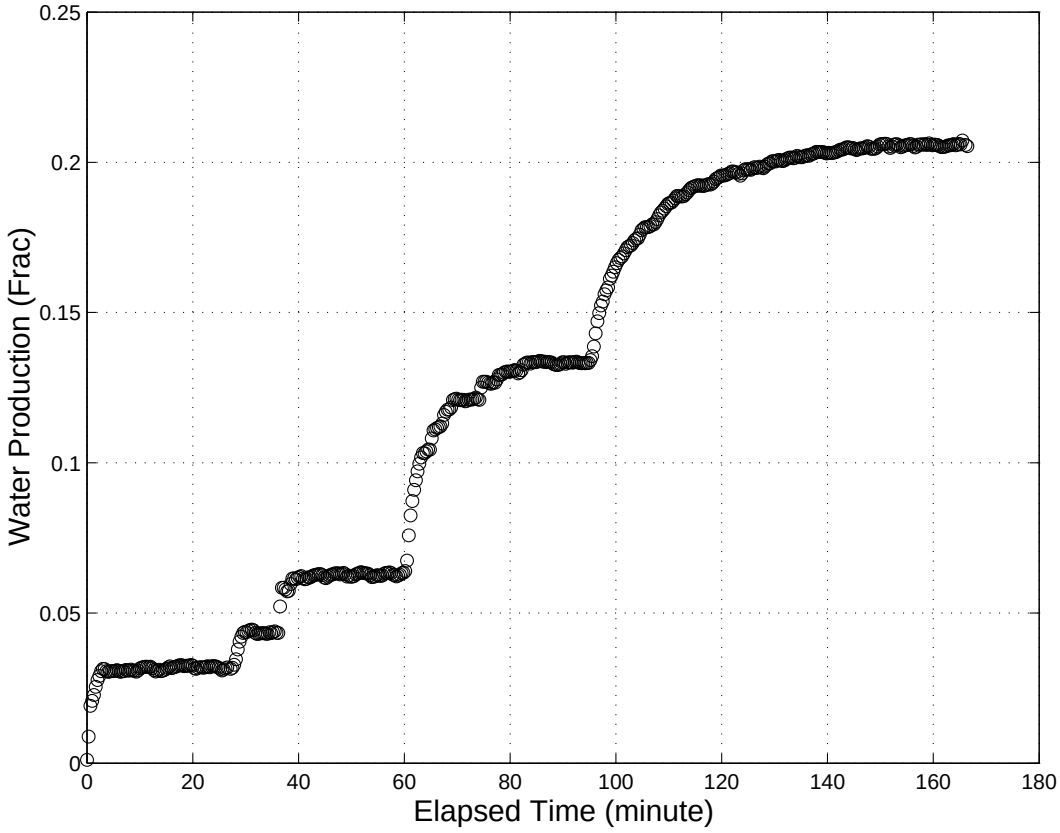

Fig. 107. Measured Water Production Data in N_2-Water Displacement Experiment

a while so that the decrease of the sample weight is not seen by the balance instantly. The anomaly in the second step is so large which is believed to be an occasionally happened extreme case.

Note, that only 20% water is pushed out of the sample during the whole experiment (see Figure 107). Consequently, we get the information only in the region of average saturation from 0.8 to 1.0. From the discussion of Section E in Chapter II, the degree of available information plays a crucial role in the confidence interval behavior and reliability of the flow functions estimation. It is desirable to design an experiment that gets more information. This could perhaps be achieved by increasing the N_2 inlet pressure to lower the saturation in the final step. In Chapter III, the irreducible saturation is approximately determined to be 0.3. That means the minimum saturation which can be obtained is 0.3 despite the increasing pressure.

The saturation distribution in Chapter III indicates the preferential path for fluid movement that might result from the unstable flow. If the displacement experiment is unstable, the analysis of water production data in order to estimate the multiphase properties through the method in Chapter II is meaningless since the mathematic model does not include the mechanism to simulate the instability. More investigation is required in order to clarify whether there is instability happened in immiscible displacement experiment.

In addition to the production data, the spatially resolved saturation profile of the steady state can be used to estimate relative permeability. The method of using NMR CPMG imaging to determine the saturation distribution has been proved applicable in Chapter III. The use of saturation profiles as well as production data will give us more reliable estimation of relative permeabilities. Further improvements in the accuracy of the estimates can be made when the permeability and porosity distribution are taken into account.

VITA

Song Xue received her B.S. and M.S. in chemical engineering from Zhejiang University in China. Ms. Xue was a graduate student in Texas A&M University Chemical Engineering Department since August 2000. She worked for Dr. Watson in the field of mathematical simulation of the flow of multiple fluid phases through porous media. She received a M.S. degree in May 2004.

Ms. Xue can be reached at 239 S Madison Ave., Apt. #12, Pasadena, CA 91101 or 1-626-564-2796. Her email address is xue_song@hotmail.com.

The typist for this thesis was the author.